Multimetallic Nanoparticles for Fuel Cell Electrocatalysts: Considerations of Their Formation and Thin-Film Inspired Compositions

by Mark Dreibelbis

MULTIMETALLIC NANOPARTICLES FOR FUEL CELL ELECTROCATALYSTS: CONSIDERATIONS OF THEIR FORMATION AND THIN-FILM INSPIRED COMPOSITIONS

A Dissertation

Presented to the Faculty of the Graduate School

of Cornell University

In Partial Fulfillment of the Requirements for the Degree of

Doctor of Philosophy

by

Mark Dreibelbis

August 2010

MULTIMETALLIC NANOPARTICLES FOR FUEL CELL ELECTROCATALYSTS: MECHANISTIC CONSIDERATIONS AND THIN-FILM INSPIRED COMPOSITIONS

Mark Dreibelbis, Ph. D.

Cornell University 2010

As part of collaborative efforts to develop new materials for use in polymer electrolyte membrane fuel cells, techniques for the high throughput synthesis and evaluation of thin films have been developed. These studies have revealed several multimetallic systems (both disordered alloys and ordered intermetallics) that are potential candidates for improved anode and cathode electrocatalysts. However, if those complex metallic materials are to be used as fuel cell electrocatalysts, they must be prepared as high surface area nanoparticles, typically as small as 3 to 5 nm in diameter. This dissertation describes efforts to understand intermetallic nanoparticle formation, and an example of preparing one of those promising thin film compositions as nanoparticles.

Intermetallic PtPb is known to be an active anode electrocatalyst for formic acid oxidation and is much less sensitive to poisoning by CO and sulfur-containing compounds than the typical Pt catalyst. Solution-phase synthesis of this compound from organometallic precursors co-reduced *via* sodium naphthalide has produced nanoparticles that retain this activity, and varying reaction conditions provides insight as to how they form. Hydrocarbon adsorption is shown to be a likely inhibitor of intermetallic nanoparticle formation. Single- and double-potential step

chronoamperometry methods are also used to investigate the first step of this synthesis- the rates at which the metal precursors are reduced and dissociate in solution. Under the assumptions of the electroanalytical measurements, the co-reduced precursors do appear to reduce near the same rate.

A promising thin film composition for oxygen reduction is palladium alloyed with tungsten and vanadium. Results are shown for the synthesis of ternary alloys near the composition $Pd_{0.88}W_{0.6}V_{0.06}$ as nanoparticles which retain some of their oxygen reduction activity from that of the initial thin film used in the screening protocols. Powder x-ray diffraction (pXRD), electron microscopy (SEM and TEM), energy dispersive x-ray spectroscopy (EDS), and rotating disk electrode (RDE) experiments serve as the primary means of characterizing these nanoparticle catalysts.

BIOGRAPHICAL SKETCH

Mark Lee Dreibelbis was born March 20th, 1983 in Lewisburg PA, to Curtis and Pamela Dreibelbis. The author was raised in rural central Pennsylvania, where he grew up in a happy environment that nurtured his scientific curiosity and enjoyment of athletics. He graduated valedictorian of Mifflintown, PA's Juniata High School in 2001, and enrolled at Susquehanna University in Selinsgrove PA as a chemistry major. After four years of studying chemistry, Spanish, and javelin throwing, the author graduated *magna cum laude* with a B.S. in chemistry. His interest in higher learning in chemistry was cemented during two Research Experience for Undergraduates programs at Penn State University and Cornell University in the summers of 2003 and 2004, respectively. Having enjoyed Cornell and the Ithaca area, the author enrolled in Cornell University's Department of Chemistry and Chemical Biology in 2005, and joined the Frank DiSalvo research group. Once he arrived at graduate school, the author renewed a relationship with Ellen Keene, whom he had met at Cornell the previous summer, and had also enrolled at Cornell in the department of Materials Science and Engineering. The two were married in July 2008. Upon completing his doctoral degree, the author (and his wife) will begin employment at the Dow Chemical Company in Midland MI, where the author will try to cope with being far away from his extended family and his beloved Philadelphia sports teams.

ACKNOWLEDGMENTS

I thank all the people who made my five years of graduate school both possible and enjoyable. First among those is my advisor Frank DiSalvo. Every graduate student should be so fortunate to learn under as knowledgeable, pleasant, and generous a boss. I hope to achieve a similar level of success in life as he has, first as a friend and human being, and then maybe as a scientist. I also thank my other committee members, Prof. Abruña and Prof. Wolczanski for their availability so I could seek advice on electrochemistry and organometallic chemistry from world-class sources.

I thank my former and current group mates for an environment that I looked forward to being part of every day. I'd like to thank the folks who helped shape my first years in grad school: Laif Alden, Chandrani Roy Chowdhury, Neal Abrams, Michael McGuire, Tanushree Ghosh, and Jesse Reiherzer. You taught me how to be a chemist, and more accurately, a grad student. I'd then like to acknowledge those who came somewhere along the way and helped see me to the end: Brian Leonard, Tracy Zhou, Chinmayee Subban, Hao Chen, Minh Ngyuen, and most recently Doug Desario, Spencer Robbins, and Tiju Thomas. I'm glad to know you all, and wish you all the best of luck as we part ways. I thank the group members who were constants in the group with me from Day 1 through Day 1678 (give or take a few days): Heather Edvenson, Morgan Stefik, Kelly Case, and Paul Mutolo. Special thanks go to Kelly and Paul for accompanying me on more walks for coffee than I care to admit. Finally, I thank the undergraduates who worked under me: Liz Rappoport, Tammer Yamany, and REU student Priscilla Cristi. Not everyone enjoys every minute with the undergrads they're paired with, but I did.

Thanks also go to Cornell researchers who were not in my group. I thank facility managers John Grazul, Mick Thomas, and John Hunt for teaching me electron

microscopy, and Maura Weathers for her immeasurable assistance in my battles with our old Scintag X-ray diffractometer. On that note, I thank Dave and Larry from building services for their help over the years in tearing apart our lab and putting it back together for our remodeling, and for their assistance in moving out the Scintag. I thank my collaborators Michael Lowe, Futoshi Matsumoto, Tiju Thomas, and Jonathan Petrie for their contributions to the research in this dissertation.

My classmates were also a great part of grad school. I'd like to especially recognize Rob Berger, Alex Hoepker, Eric Moore, Kevin Sylvester, Scott Gruenbaum, Doris Pun, Ben Strangfeld, Seán O'Leary, Josie Gruver, Amelia Anderson, Brenda Frazier, Emily Volpe, Elliott Hulley, Jon Dorando and Chris Sgro. We spent so much time together first year that I'm convinced the Crooked Board Tavern went out of business only because we grew too busy to go anymore.

Lastly, I thank my family, the most important people in my life. I thank my parents for supporting me all along the way in my 23 years of formal education. I thank my brother Adam and his wife Aileen for their visits to Ithaca for a few weekends every year. I'm thankful that my grad school was close enough to home to still attend holidays with my extended family, and that they were good enough sports to ask "how my grades were". But most importantly, I thank my wife Ellen. Not only has she been everything I could ask for in a companion, but also has been a source of excellent discussions about materials science and characterization techniques, and for helping me with Raman microscopy. I look forward to starting our careers together, and staying in the same location for more than two years.

TABLE OF CONTENTS

Biographical Sketch……...iii

Acknowledgements……iv

List of Figures……ix

List of Tables……xx

List of Equations……...……...xxi

CHAPTER 1: Introduction 1

1.1 Fuel Cells: Function and Requirements 1

1.2 Nanoparticles as Fuel Cell Electrocatalysts 4

1.3 Nanoparticle Synthesis 8

1.4 Fuel Cell Catalyst Research at the Energy Materials Center at Cornell (emc^2) 14

1.5 Outline of the Dissertation 19

REFERENCES 21

CHAPTER 2: PtPb *via* Sodium Naphthalide Reduction 32

2.1 Introduction 32

2.2 Variations in Solution Concentration and Excess Reducing Agent 38

2.2.1 Experimental 40

2.2.2 Characterization 41

2.2.3 Results and Discussion 42

2.3 In-Solution Hydrogen Treatments After Sodium Naphthalide Reduction 47

2.3.1 Experimental 48

2.3.2 Characterization 49

2.3.3 Results and discussion 49

2.4 Other Mechanistic Clues: Attempted Characterization of Side Products 59

2.4.1 Experimental 60

2.4.2 Results and Discussion 61
2.5 Commentary on the Aging of PtPb Nanoparticles in Air 66
REFERENCES 69
CHAPTER 3: Electroanalytical Studies of Metal Precursor Reduction 75
3.1 Introduction 75
3.2 Single Potential Step Chronoamperometry 76
3.2.1 Experimental 79
3.2.2 Results and Discussion 80
3.2.2.1 Lead (II) 2-ethylhexanoate 80
3.2.2.2 Dimethyl Platinum Cyclooctadiene and Platinum (II) Acetylacetonate SSCA 87
3.3 Double Potential Step Chronoamperometry 90
3.3.1 Experimental 91
3.3.2 Results and Discussion 92
3.3.2.1 Iron (III) acetylacetonate DSCA 103
3.4 Comparison of the Two PtPb Precursors Measured by Different Techniques. 106
REFERENCES 111
CHAPTER 4: Thin-Film Inspired Palladium Alloy Nanoparticle Electrocatalysts for Oxygen Reduction 116
4.1 Introduction 116
4.2 Pd and W Nanoparticles Synthesized by Different Reducing Agents 120
4.2.1 Experimental 121
4.2.2 Characterization 123
4.2.3 Results and discussion 124
4.3 Pd-W Nanoparticles Synthesized by Different Reducing Agents 134
4.3.1 Experimental 134

4.3.2 Results and Discussion 135
4.4 Pd-W-V Nanoparticles via Sodium Naphthalide Reduction 143
4.4.1 Experimental 143
4.4.2 Results and discussion 144
4.5 Arc-Melt Synthesis of a Bulk Pd-W-V Slug 157
4.5.1 Experimental 157
4.5.2 Results and Discussion 158
REFERENCES 162
CHAPTER 5: Projects Outside the Sphere of Fuel Cell Research 166
5.1 Transition Metal Carbide Synthesis by Sodium Naphthalide Reduction 166
5.1.1 Experimental 168
5.1.2 Results and Discussion 169
5.2 Synthesis of High-T_c Superconductor Host Lattices: LaFePO and LaFeAsO 177
5.2.1 Experimental 178
5.2.2 Results and Discussion 179
5.3 Synthesis of Rare Earth-Doped Gallium as a GaN Precursor 186
REFERENCES 190
CHAPTER 6: Conclusions and Suggestions for Future Work 192
6.1 PtPb via Sodium Naphthalide Reduction 192
6.2 Kinetic Electroanalysis of Metal Precursors 193
6.3 Thin-Film Inspired Pd Ternary Alloy Nanoparticles 193
6.4 Transition Metal Carbides via Sodium Naphthalide 195
REFERENCES 196
Appendix 1: Chemical and Electrochemical Reduction of Tin Alkoxides 198
Appendix 2: Attempted Synthesis of Carbon-Supported Pd-W Alloy Nanoparticles 204

LIST OF FIGURES

Figure 1.1 Cartoon of a PEMFC (polymer electrolyte or proton exchange membrane fuel cell). 3

Figure 2.1 Powder X-ray diffraction patterns for PtPb samples reduced with 100% excess sodium naphthalide down to 0% excess. The domain sizes (top to bottom) are 19, 22, 20, 25, 23, 21 and 25 nm. The relative low intensities of the 10% excess pattern make the peaks look broader than they actually are. The starred peaks in the 0% excess pattern index to PbO. 43

Figure 2.2 Energy-dispersive X-ray spectrum of PtPb. The Pt:Pb ratio is 52:48; the source of the shoulder in the Pb M_α peak at 2.34 keV is not known, but has been seen in other well-characerized PtPb samples [6]. 44

Figure 2.3 Energy-dispersive X-ray spectrum of PtPb where the Pt:Pb ratio was not 1:1. Here it was 30:69, presumably because PbO had phase separated from PtPb, and was the crystallite analyzed in this spectrum. 45

Figure 2.4 Powder X-ray diffraction pattern of two PtPb products synthesized at 135°C. The top pattern was 16mM with respect to each metal precursor after injection, and had a domain size of 24 nm, while the bottom was 3.3mM with 25 nm domains. 46

Figure 2.5 Powder X-ray diffraction patterns of PtPb nanoparticles treated with forming gas and heated in solution at the listed temperatures. Overlaid lines are the reported PtPb peaks. 50

Figure 2.6 Crystallite domain sizes for the diffraction patterns shown in Figure 2.5 compared to similar products without forming gas treatment [1]. 50

Figure 2.7 Powder X-ray diffraction patterns of PtPb products synthesized under identical conditions as Figures 2.5 and 2.6, but with argon treatment instead of

forming gas. The top pattern was from a product heated to 115°C, while the bottom pattern was heated to 100°C. 52

Figure 2.8 TEM of PtPb particles treated with forming gas and heated to 80°C during synthesis. 53

Figure 2.9 TEM of PtPb particles treated with forming gas and heated to 110°C during synthesis 54

Figure 2.10 TEM of PtPb particles treated with forming gas and heated to 130°C during synthesis. Lattice fringes are visible in the particles aggregated near the center. 55

Figure 2.11 Representative weight loss of PtPb nanoparticles from forming gas samples upon heating under argon. 56

Figure 2.12 Brunauer-Emmett-Teller isotherm surface area of forming gas-treated and non-forming gas treated (two triangles) PtPb as a function of preparation temperature. 57

Figure 2.13 Formic acid polarization curves under experimental conditions listed.... 58

Figure 2.14 Mass spectrum of headspace gas of room temperature reaction of $Pt(COD)Me_2$ and Pb(ethex)2 with NaNp. 62

Figure 2.15 Timed mass spectrum traces of the headspace of a room temperature NaNp reduction of $Pt(COD)ME_2$ and Pb(2-ethylhexanoate)$_2$ in THF. The traces for 58 and 59 amu remained at 0 Torr for the duration of the experiment. 63

Figure 2.16 Idealized representation of the hypothetical order of reaction steps to form binary intermetallic nanoparticles. 65

Figure 2.17 Powder X-ray diffraction pattern for PtPb sample which aged three years in air in a closed vial. Inset shows original (upper) pattern with PtPb structure, and lower pattern is duplicated in the main window. Peaks index mostly to $Pb_{10}(CO_3)_6(OH)_6O$. Pt and PtPb peaks are shown to provide reference. 68

Figure 3.1 Diagram of the expected shape of the chronoamperogram for classical electrodeposition..... 78

Figure 3.2 Cyclic voltammogram of approximately 7.5 mM lead (II) 2-ethylhexanoate in THF with 0.1 M TBAP. Scan rate = 100 mV s^{-1}. Note the change in reduction potential on the second cathodic scan. 81

Figure 3.3 Cyclic voltammogram s at 100 mV s^{-1} for the same solution as in Figure 3.2, but after the sweeps in that figure. The cathodic peak at -0.8 vs. Ag/Ag^{+} remains. 82

Figure 3.4 Single potential step **c**hronoamperograms of 7.5 mM lead (II) 2-ethylhexanoate in THF with 0.1 M TBAP. at – 750, -800, -825, -850, -875, and -900 mV vs. Ag/Ag^{+}. 83

Figure 3.5 Fit of sample chronoamperometric trace to Equation 3.1. Inset shows the ln(nucleation rate) as a function of applied potential, and the slope which gives the critical nucleus size. Error bars reflect the goodness of fit for the chronoamperograms at each potential; absent error bars are implied as being smaller than the data point. 84

Figure 3.6 Single potential step **c**hronoamperogram of 5.0 mM $Pt(acac)_2$ in THF with 0.1 M TBAP at -2.9 V vs. Ag/Ag^{+}. Faradaic electron transfer is occurring, as the current does not decay to zero, but the expected hump from electrodeposition is not present. 88

Figure 3.7 Cyclic voltammogram of 5.0 mM Pt(COD)Me2 in THF with 0.1 M TBAP. Sweep rate = 500 mVs-1. 240μm diameter Pt working electrode, Pt wire counter 89

Figure 3.8 Cyclic voltammograms of 0.1 M TBAP in THF, and 0.1 M TBAP and 5.0 mM $Pt(acac)_2$ in THF, both at 50 mV s^{-1}. 94

Figure 3.9 Diagram of a double step chronoamperometry experiment. The dark line is the applied potential, and the light line is the current response. Conventions for current and time values are labeled. 95

Figure 3.10 DSCA traces for $Pt(acac)_2$ at different values of τ. The applied potential steps from -0.5 V to -2.9 V and back. 98

Figure 3.11. i_a/i_c ratios vs. τ for the traces in Figure 3.9, with fit to Equation 3.6. 98

Figure 3.12. i_a/i_c ratios vs. τ for DSCA traces of 10 mM $Pt(acac)_2$ at 240 μm Pt electrode. The analysis curve is not shown, and the time constants are shown in milliseconds instead of the dimensionless $k\tau$. 100

Figure 3.13. i_a/i_c ratios vs. τ for 10 mM $Pt(acac)_2$ at 1 mm diameter electrode. Switching times in milliseconds are 20, 50, 80 and 160 ms, with a step potential of 0 V to -2.75 V and back to 0 V, all vs. Ag/Ag^+. Line represents prediction by theory. 101

Figure 3.14 i_a/i_c ratio vs. switching time plot for 5.0 mM lead (II) 2-ethylhexanoate and 0.1 M TBAP at a step potential of 0 V to -1.0 V and back to 0 V, all vs. Ag/Ag^+. 102

Figure 3.15 Cyclic voltammogram of 5.0 mM $Fe(acac)_3$ and 0.1 M TBAP in THF at 20 mV s^{-1}. 104

Figure 3.16 i_a/i_c vs τ for $Fe(acac)_3$. Applied potential was -0.6V at the beginning, then stepped to -1.65V and back to -0.6V, all vs. Ag/Ag+. 105

Figure 4.1 Current density at 0.85V vs. RHE of an air-saturated 0.1M sulfuric acid solution in a 1 cm^2 scanning cell over sputtered thin film electrodes. Each element listed represents a thin film continuous composition spread co-sputtered with Pd and W, and each point corresponds to the current density at the most active area on those films. 118

Figure 4.2 Current density at 0.85V vs. RHE of an air-saturated 0.1M sulfuric acid solution in a 1 cm^2 scanning cell over a thin film electrode of co-sputtered Pd, W and V, versus the Pd lattice constant of different spots on the film. Dashed lines mark the current density benchmarks for thin film Pd, thin film Pt, and alloys of Pd-W and Pd-W-V with the approximate compositions $Pd_{0.90}W_{0.10}$ and $Pd_{0.88}W_{0.06}V_{0.06}$. 119

Figure 4.3 Powder X-ray diffraction pattern of palladium nanoparticles synthesized by injection into sodium naphthalide in diglyme at room temperature, then stirring at 150°C. 124

Figure 4.4 Powder X-ray diffraction pattern of palladium nanoparticles synthesized by sodium borohydride reduction in methanol at 25°C..... 125

Figure 4.5 Powder X-ray diffraction pattern of annealed product of $KB(Et)_3H$ reduction of WCl_6. The powder is composed of KCl (lowest window containing reported peaks) and WO_2 (middle), but may or may not contain W metal (upper window). 127

Figure 4.6 Transmission electron micrograph of palladium nanoparticles synthesized by sodium naphthalide reduction in diglyme at 150°C. 128

Figure 4.7 Transmission electron micrograph of palladium nanoparticles synthesized by sodium borohydride reduction in methanol at 25°C..... 129

Figure 4.8 Energy-dispersive X-ray spectrum of palladium nanoparticles synthesized by sodium naphthalide reduction in diglyme at 150°C. 130

Figure 4.9 Energy-dispersive X-ray spectrum of palladium nanoparticles synthesized by sodium borohydride reduction in methanol at 25°C..... 131

Figure 4.10 Thermogravimetric analysis of palladium nanoparticles synthesized by sodium naphthalide reduction in diglyme at 150°C and by sodium borohydride reduction in methanol at 25°C. 132

Figure 4.11 Oxygen polarization curves of palladium nanoparticles synthesized by sodium naphthalide reduction in diglyme at 150°C and by sodium borohydride reduction in methanol at 25°C. Conditions were oxygen-saturated aqueous 0.1 M $HClO_4$, 1600 rpm rotation, and a sweep rate of 5 mVs^{-1}..... 133

Figure 4.12 Powder X-ray diffraction pattern of nominally $Pd_{0.90}W_{0.10}$ nanoparticles synthesized by sodium naphthalide reduction in diglyme at 150°C. The top pattern is the as-made product, and the bottom is after washing with distilled water, where most of the salt is removed. 137

Figure 4.13 Energy-dispersive X-ray spectrum of nominally Pd0.90W0.10 nanoparticles synthesized by sodium naphthalide reduction in diglyme at 150°C. The small peaks on either side of the 8.4 keV W peak are from the brass sample holder..... 137

Figure 4.14 Energy-dispersive X-ray spectrum of nominally $Pd_{0.90}W_{0.10}$ nanoparticles synthesized by sodium borohydride reduction in methanol at 25°C. Note the decrease in Na intensity with respect to the sample made by sodium naphthalide reduction (Figure 4.13). 138

Figure 4.15 Transmission electron micrographs of Pd-W nanoparticles synthesized by sodium naphthalide reduction in diglyme at 150°C. 139

Figure 4.16 Transmission electron micrographs of Pd-W nanoparticles synthesized by sodium borohydride reduction in methanol at 25°C..... 140

Figure 4.17 Thermogravimetric analysis of nominally $Pd_{0.90}W_{0.10}$ nanoparticles synthesized by sodium naphthalide reduction in diglyme at 150°C and by sodium borohydride reduction in methanol at 25°C. 141

Figure 4.18 Oxygen polarization curves of nominally $Pd_{0.90}W_{0.10}$ nanoparticles synthesized by sodium naphthalide reduction in diglyme at 150°C and by sodium borohydride reduction in methanol at 25°C. Conditions were oxygen-saturated

aqueous 0.1M $HClO_4$, 1600 rpm, 5 mVs^{-1}. The sodium naphthalide-reduced catalyst was approximately the target composition, while the sodium-borohydride-reduced catalyst was closer to $Pd_{0.95}W_{0.05}$. 142

Figure 4.19 Powder X-ray diffraction pattern of nominally $Pd_{0.9}W_{0.04}V_{0.06}$ nanoparticles synthesized by sodium naphthalide reduction in diglyme at 150°C.146

Figure 4.20 Energy-dispersive X-ray spectrum of nominally $Pd_{0.88}W_{0.06}V_{0.06}$ nanoparticles synthesized by sodium naphthalide reduction in diglyme at 150°C. The composition from this spectrum was 90 at% Pd, 5 at% W, and 5 at% V. 147

Figure 4.21 Energy-dispersive X-ray spectrum of nominally $Pd_{0.9}W_{0.04}V_{0.06}$ nanoparticles synthesized by sodium naphthalide reduction in diglyme at 150°C. The 5 keV vanadium peak is not seen, as the composition from this spectrum was 7 at% Pd, and 2 at% W (for a 77:23 Pd:W ratio) with 57% sodium and 33% chlorine. 148

Figure 4.22 Scanning electron micrograph of an aggregate of nominally $Pd_{0.90}W_{0.04}V_{0.06}$ nanoparticles. EDX spectra for Points 1 and 2 are shown in Figure 4.23..... 149

Figure 4.23 Energy-dispersive X-ray spectra from the two points in Figure 4.22. Point one is clearly a sodium chloride crystal, while point two is rich in vanadium, showing the micron-level phase separation. 150

Figure 4.24 Transmission electron micrograph of nominally $Pd_{0.9}W_{0.04}V_{0.06}$ nanoparticles agglomerated into a ~100nm aggregate. 151

Figure 4.25 Zoomed in transmission electron micrograph of Figure 4.24 151

Figure 4.26 Thermogravimetric analysis of several Pd ternary alloys nanoparticles. Nominal ternary compositions are labeled in the form “Pd-W-V”. 153

Figure 4.27 ORR polarization curves of nominally $Pd_{0.90}W_{0.04}V_{0.06}$ nanoparticles synthesized by sodium naphthalide reduction in diglyme at 150°C. First and

second ORR scans are shown, along with the curve for an analogous commercial platinum nanoparticle sample, and a sweep in Ar-saturated perchloric acid. Conditions were oxygen-saturated aqueous 0.1 M $HClO_4$, 1600 rpm, 5 mVs^{-1}. 154

Figure 4.28 ORR polarization curves progressing from Pd only, to nominally $Pd_{0.90}W_{0.10}$, to nominally $Pd_{0.90}W_{0.04}V_{0.06}$, all synthesized by sodium naphthalide reduction. Conditions were oxygen-saturated aqueous 0.1 M $HClO_4$, 1600 rpm, 5 mVs^{-1}. The first sweeps for all three are plotted on the left while the second sweeps are on the right. In both cases, the materials follow the trend expected from thin film results. 155

Figure 4.29. ORR polarization curves of five different samples of nominally $Pd_{0.90}W_{0.04}V_{0.06}$ nanoparticles synthesized by sodium naphthalide reduction in diglyme at 150°C. The first sweeps for all five are plotted on the left while the second sweeps are on the right. Conditions were oxygen-saturated aqueous 0.1M $HClO_4$, 1600 rpm, 5 mVs^{-1}. 156

Figure 4.30 Representative EDX spectrum of Pd-W-V alloy slug, after machining but before embedding in Teflon and polishing. 159

Figure 4.31 Scanning electron micrograph overlaid with the relative results of an EDX line scan. The metal counts in the line scan correspond to 85% Pd (top signal), 11% W (middle signal), and 4% V (bottom signal). 159

Figure 4.32 Oxygen polarization curves of Pd-W-V alloy slug, after embedding in Teflon and polishing. 160

Figure 5.1. Powder X-ray diffraction pattern of carbon product of CBr_4 reduced by sodium naphthalide. Peaks index to octacarbon (top reported pattern) and diamond (middle), as well as a small amount of sodium bromide (bottom). 171

Figure 5.2. Raman spectrum under 488 nm excitation. Raw data (bottom) is shown with the smoothed curve (top), where the D and G peaks are in approximately a 1:1 ratio. 172

Figure 5.3. Powder X-ray diffraction pattern of as-formed product of $FeCl_3$ and CBr_4 reduced by sodium naphthalide. Peaks index to Fe_2O_3 and NaCl; even though there should be a mixed NaCl/Br salt of approximately 25% Br, the peaks have not shifted from NaCl. 173

Figure 5.4. Powder X-ray diffraction pattern of annealed product of FeCl3 and CBr4 reduced by sodium naphthalide. In contrast to Figure 5.3, the peaks now index to a chloride-rich NaCl/NaBr solid solution and magnetite 174

Figure 5.5. Raman spectrum of Fe-C product under 488nm excitation. Peaks attributed to carbon are found at 1358.4cm^{-1} and 1589.6cm^{-1}. The I(D)/(G) ratio is 1.0. 175

Figure 5.6. Powder X-ray diffraction pattern of mixture of tantalum carbide and carbon from annealed TaC product. 176

Figure 5.7. Raman spectrum of TaC sample under 488nm excitation, with peaks at 1363.3cm^{-1} and 1583.1cm^{-1} and a I(D)/(G) ratio of 0.863. This spectrum is attributed to carbon content also seen by XRD. Note the similarity with the spectrum from the Fe-C product in Figure 5.5. 177

Figure 5.8. Powder X-ray diffraction pattern of LaFePO. Fe_2P (Baringerite, bottom reported pattern) is also present. 180

Figure 5.9. Scanning electron micrographs of LaFePO crystals. The tetragonal platelets have been etched at the corners by HCl during the removal of the Sn mineralizer. Scale bars = 1 μm. 181

Figure 5.10. EDX spectrum of LaFePO. The Si peak is from the mounting substrate and the Sn peak is from undissolved mineralizer. The stoichiometric ratio was precisely the desired composition (Table 5.1). 181

Figure 5.11. Scanning electron micrograph of an FeP crystal found in a LaFePO synthesis. Scale bar = 10μm. 183

Figure 5.12. EDX spectrum of FeP in Figure 5.11. A peak from the aluminum sample holder is visible at 1.487keV. The elemental ratio was precisely 1:1 Fe:P within the limits of the detector. 183

Figure 5.13. Powder X-ray diffraction pattern of LaFeAsO. Fe_3O_4 and Na/KCl are also present. 184

Figure 5.14. Scanning electron micrographs of LaFeAsO crystals. Both hexagonal and octagonal crystals are seen. Scale bar = 10 μm 185

Figure 5.15. Broad-range EDX spectrum of Figure 5.14. The composition in atomic percent was 18% La, 14% As, 14% Fe, 43% O, 6%Cl, and 3% each Si (from tube fragments) and Al (from sample mount). 186

Figure A1.1 Cyclic voltammograms of 0.005 M $Sn(iPrO)_4$ and Sn(tBuO)4 in methanol with 0.1 M TBAP. Sweep rate was 50 mV s^{-1} on an electrode made from a carbon fiber with a 30 μm diameter. 200

Figure A1.2 Powder X-ray diffraction pattern of tin product from reduction of $Sn(iPrO)_4$ by by $LiB(Et)_3H$ in THF at room temperature..... 202

Figure A1.3 Cyclic voltammogram of 0.005 M tin (IV) isopropoxide in THF with 0.1 M TBAP on a 125 μm Pt electrode at 50 mV s^{-1}. The redox behavior for the t-butoxide shows similar unacceptable variations with increasing sweeps. 203

Figure A2.1 SEM of the same area of the Pd-W/C product under normal mode (left) and high-contrast composition mode (right). The bright speck in the center of the right image is visible in the left, and corresponds to high W content. 206

Figure A2.2 ORR polarization curves for Pd-W/C product with oxygen-saturated 0.1M HClO4 solution at 5 mVs^{-1} and 1600 rpm. Cycling the potential between the upper and lower potential boundaries at 50 mVs^{-1} for 20 minutes increases the activity to the values for as-purchased Pd/C (not shown). 207

LIST OF TABLES

Table 3.1. Kinetic parameters obtained from fits of curves in Figure 3.4. 85

Table 3.2. Results for values calculated at different time constants from Figure 3.1199

Table 3.3. Reduction potentials measured for the metal precursors in this chapter . 107

Table 5.1 Results of EDX quantification from Figure 5.10..... 182

Table 5.2 Results from quantification of Figure 5.12..... 183

LIST OF EQUATIONS

Equation 1.1 Chemical reaction for oxidation of hydrogen……4

Equation 1.2 Chemical reaction for oxidation of methanol.……4

Equation 1.3 Chemical reaction for oxidation of formic acid……..……4

Equation 1.4 Half-cell reaction for reduction of oxygen……..7

Equation 2.1 Chemical reaction for reduction of Pt(COD)Me_2 by NaNp……..34

Equation 2.2 Chemical reaction for reduction of Pb(2-ethylhexanoate)$_2$ by NaNp…34

Equation 3.1 Current expression for diffusion-limited nucleation and growth on an electrode surface……...84

Equations 3.2 and 3.3 Exponential expressions used in Equation 3.1 for the determination of nucleation rate constants……85

Equation 3.4 Polynomial which approximates the quotient of Equations 3.2 and 3.3 × $t^{-1/2}$……..……85

Equation 3.5 Confluent hypergeometric function used to express current as a function of time in DSCA experiments……..96

Equation 3.6 Expression for the ratio of anodic current to cathodic current in a DSCA experiment…….96

Equation 4.1 Chemical reaction of sodium borohydride with methanol……...125

Equations 4.2 and 4.3 Two-step hypothetical reaction to give sodium tungstate…. 126

Equation 5.1 Generic chemical reaction for reduction of metal chloride and carbon tetrabromide with sodium naphthalide……...167

CHAPTER 1

Introduction

1.1 Fuel Cells: Function and Requirements

It is rare in 2010 for one to need to convince others of the need for more energy efficient devices to power our society, given the widespread awareness of the limits of fossil fuel reserves and the mostly accepted prospect of global warming from human-released carbon dioxide. A chief target for better energy efficiency and decreased CO_2 emissions is in automotive applications, where countless researchers are working to replace the standard internal combustion engine. Electrochemical devices are at the forefront of these efforts, mainly in the form of lithium ion batteries and fuel cells, and to a lesser extent, supercapacitors. All three of these are means of delivering electric charge to devices. Batteries and supercapacitors store charge in the form of ions and electrons, respectively, while fuel cells use chemical energy captured during electron transfer reactions of small molecules. Fuel cells are best thought of as "efficiency devices". They do not generate energy, and they do not even really store it, as the fuel itself accomplishes the energy storage. An effective metaphor [1] is that a fuel cell is a factory; raw materials (fuel and oxidant) go in, are consumed in an active process, and a product (electricity) goes out to the consumer. While the same can be said about a combustion engine, the attraction of fuel cells is that several of the inefficient energy conversion steps in a combustion engine are skipped. Each of the electrochemical devices listed above is in its own state of development, and none are yet ready for widespread implementation and deployment in automobiles. This work focuses on fuel cells, so it is appropriate to begin with a description of the architecture

and materials at work for the fuel cell commonly associated with automobiles and consumer electronics: the polymer electrolyte membrane fuel cell (PEMFC) [2].

PEMFC's are usually depicted with a cartoon similar to the one shown in Figure 1.1. The similarities with a battery are immediately apparent, as both consist of two electrodes sandwiching an ionic conductor. The main structural difference is that while a battery is self-contained, with all the reactants inside the battery housing and in a finite amount, a fuel cell's reactants are on the outside and fed into the cell as needed. Both devices have an anode and a cathode, where oxidation and reduction, respectively, take place. In a standard polymer electrolyte membrane fuel cell, the fuel, which is often hydrogen, is fed to the anode where it is electrooxidized, liberating electrons and hydrogen ions. The electrons travel through the external circuit and power some device, and the protons go through the proton-conducting (yet electrically insulating) polymer electrolyte membrane to reach the cathode. There, the electrons that have traversed the circuit reduce oxygen and combine with the hydrogen ions to produce water. The whole process is an elegant and satisfying reaction, in which a net "combustion" reaction occurs without Carnot heat engine limitations, and where the only waste products are water and heat. If a carbon-containing species such as methanol is used as a fuel, CO_2 would also be a byproduct. However, if efficient methanol oxidation catalysts could be found, the amount of electrical energy released per unit of CO_2 would theoretically be much greater than that obtained from a Carnot process.

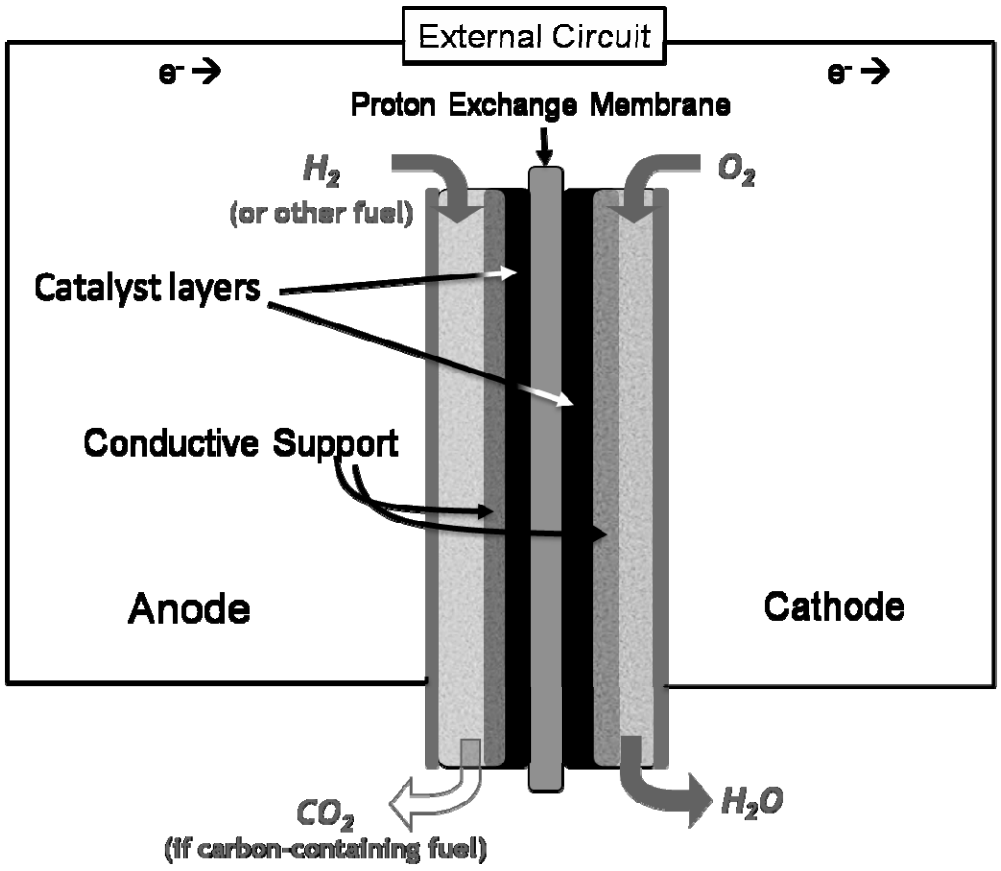

Figure 1.1 Cartoon of a PEMFC (polymer electrolyte or proton exchange membrane fuel cell).

The benefit of utilizing fuel cells in modern "green" technologies is clear, but fuel cell-powered cars are hardly rolling off assembly lines and into everyone's garage [2]. The disconnect between reality and the cartoon in Figure 1.1 is due to materials limitations: catalysts are inefficient and expensive, catalyst supports corrode, and proton membranes degrade. Since the research described in this dissertation mostly pertains to electrode catalysts, only their requirements and outstanding problems will be discussed, while, in truth, all aspects of the membrane electrode assembly (such as the catalyst supports, the proton exchange membrane, and fuel, water, and heat management) are in some way deficient [3, 4]. This introduction also excludes the

lengthy dialogue about the feasibility of efficiently generating the "fuels" under discussion, since molecular hydrogen does not exist as a natural resource. Rather, hydrogen is currently derived from steam reformation of natural gas or electrolysis of water. Thus, some energy source must be used to produce H_2. Unless the generation of hydrogen can be done in a carbon-neutral manner, and unless a hydrogen infrastructure is built, the "hydrogen economy" will not be feasible. Even then, hydrogen will certainly never replace automotive gasoline if efficient, affordable fuel cells are not available for use.

1.2 Nanoparticles as Fuel Cell Electrocatalysts

The fuel cell anode, like any anode in an electrochemical cell, is where oxidation occurs. The most common fuels used in PEMFC research are hydrogen, methanol, and formic acid, and the full-cell reactions for each, when oxygen is the oxidant, are shown in Equations 1.1-1.3.

$$2\ H_{2(g)} + O_{2(g)} \rightarrow 2\ H_2O_{(l)} \qquad E^o = 1.18\ V \qquad (1.1)$$

$$2\ CH_3OH_{(l)} + 3\ O_{2\,(g)} \rightarrow 2\ CO_{2(g)} + 4\ H_2O_{(l)} \qquad E^o = 1.21\ V \qquad (1.2)$$

$$2\ HCOOH_{(l)} + O_{2(g)} \rightarrow 2CO_{2(g)} + 2H_2O_{(l)} \qquad E^o = 1.20\ V \qquad (1.3)$$

When the anode reactions are coupled with oxygen reduction at the cathode, the standard reaction potential is around 1.2 V vs. NHE. Since methanol and formic acid are liquids, they are the most convenient for use in real cells, but formic acid is not as dense in energy since it undergoes a two electron oxidation compared to methanol's four electron reduction. Formic acid has a modest oxidation overpotential, and methanol a high overpotential due to the need to break three C-H bonds, instead of one for formic acid, and none for hydrogen. Although both gaseous and liquid hydrogen

are inconvenient in automotive applications, the electrooxidation of pure H_2 on Pt is a fast electrocatalytic reaction, and certainly gives a high enough current density at low overpotentials (a few 10's of mV's) for fuel cell purposes. However, platinum is easily poisoned by irreversible (at least under typical PEM fuel cell operation conditions) adsorption of species which are common in hydrogen made by methane reformation. The presence of more than 0.1-10 ppm CO and 10-100 ppb sulfur species like H_2S [3, 5] are enough to effectively passivate the Pt surface from performing electrooxidation.

The requirements for an effective anode in a PEMFC are specific to the fuel being used, and the state of the art technology meets them to varying degrees. The anode catalyst must be comprised of high surface area nanoparticles to attain high reaction rates and high gravimetric and volumetric power output, since only the surface of a catalyst is active. Nanoparticles maximize the surface to volume ratio, lowering the cost of expensive catalysts. Those particles must be bound to an electronically conductive support which then connects to a macroscopic electrode, and both the catalyst and support must be stable in acid near pH = 1. The catalyst must resist poisoning by impurities, and catalyze fuel oxidation near the thermodynamic limit of ~0 V vs. NHE at low overpotentials. Reaction kinetics are enhanced at higher temperatures, so higher power PEMFC's are operated at 80°C. Heat management engineering would be improved if the cell could be operated at 120°C, but at that temperature membrane dehydration and failure are still problematic. High surface area carbon black is usually the catalyst support, since it is conductive and reasonably stable under anode conditions. More exotic support materials than carbon are being investigated for both the anode and cathode, and the long-term stability of the support is a topic of intense research [3].

The list of materials which have been investigated as electrocatalysts for hydrogen and small organic molecule oxidation is extensive, but the most common are based on Pt and platinum group metals. This research usually falls in two categories: changing the catalyst composition or morphology. By modifying Pt to make alloys and compounds, researchers hope to retain the high activity for fuel oxidation yet avoid the poisoning problems. Pt-Ru alloys are the prototypical example of such a material. PtRu is the standard for methanol oxidation [6-8], because it is not deactivated during the reaction which produces CO as an intermediate, CO having already been mentioned as a poison on Pt. Alloying a more oxophilic metal like ruthenium with platinum enhances H_2O adsorption to the surface in close proximity to bound CO, promoting the oxidation of that CO to CO_2 and making the material resistant to poisoning [9]. Other metals have also been investigated in Pt alloys for anode catalysts, most notably Ni, Co, Sn, Ti, W, Pb and Bi. For any electrocatalyst to be of practical use in a fuel cell, it must be a high surface area nanoparticle, ideally with a diameter of 3-5 nm [10]. If particles are larger than that, too many of the metal atoms are isolated in the bulk, rather than on the surface and available to perform electrocatalysis.

Modifying the catalyst morphology rather than composition is the other common method for enhancing electrocatalytic activity. This line of research attempts not to discover a new catalyst material, but rather to improve on the efficacy and availability in the cell of known catalysts (most often Pt). By preferentially enhancing certain facets, as in synthesis of Pt nanocubes [11-14], the same amount of noble metal catalyst can be made more effective in catalyzing fuel oxidation [15, 16]. This line of thinking has also been used for Pt-transition metal alloys [11, 17]. As an alternative to direct catalyst morphology control, nanostructured architectures are being explored which direct nanoparticles' locations and can enhance the triple-phase boundaries

among catalyst, support, and membrane [18-21], where all fuel cell electrocatalysis must occur.

Unlike the fuel cell anode, in conventional PEMFC's the cathode focuses only on catalyzing one reaction, but it is a notoriously sluggish electrochemical reaction to catalyze: the oxygen reduction reaction (ORR, Equation 1.4).

$$O_{2(g)} + 4\ H^{+}_{(aq)} + 4e^{-} \rightarrow 2\ H_2O_{(g)} \qquad E^{o} = 1.23\ V \qquad (1.4)$$

Since one dissolved O_2 molecule must be joined at the catalyst with four protons and four electrons, passing through several reaction steps, each with its own activation barrier, it is not surprising that the rate of reaction is slow. Platinum is the best ORR catalyst we have, but the slow reduction rate leads to large overpotentials when operating at reasonable current densities. As reported by GM [22], the working potential of a fuel cell at useful current densities deviates greatly from the theoretical working potential (1.169V under actual partial pressures of H_2 and O_2 in a real system). 120mV is lost to mass transport-related overpotential (due to diffusion gradients in reactant and oxidant concentration), 70mV is lost to Ohmic contact resistances, and a dreadful 400mV loss is due to the ORR overpotential. The platinum ORR catalyst is barely even passable in a viable fuel cell, as nearly one third the cell potential is used to speed up the reduction of oxygen. If this overpotential is coupled with a possible anode overpotential (such as in methanol oxidation), the efficiency of the fuel cell plummets.

Many of the requirements that were listed for the anode carry over to the cathode, but there is the additional requirement for the cathode to withstand constant working potentials from 0.8 V to 1.5 V vs. NHE. This high potential coupled with the low pH causes most metals to dissolve, and causes the usual conductive carbon support to corrode to CO_2, a process that is catalyzed by Pt. Ideally the onset of oxygen reduction would occur at +1.2 V, but since even platinum is incapable of

catalyzing that reaction without a *ca.* 400 mV overpotential, the search for new catalysts and better utilization of current catalysts is a high priority. Improving on the kinetics of oxygen reduction on platinum would be a great advance in fuel cell technology, but since the cost of platinum is so high, researchers are willing to sacrifice performance for cost. Pt-free ORR catalysts are highly sought [23], and the most common research along those avenues involves Pd and Pd alloys [24-33], transition metal carbides [3], oxides and oxynitrides [3], and iron or cobalt-containing porphyrin-type macrocycle complexes [22]. Even though these catalysts have some activity for ORR and are much cheaper than platinum, studies have shown that an essentially zero-cost catalyst material (like iron, for example) would only be viable in a fuel cell if its activity is at least 10% that of Pt, but this challenge still has not been met [22]. Oxygen reduction kinetics are enhanced in base, but only the development of alkaline membranes will allow for the development of that technology.

The full challenge of fuel cell electrocatalysis is brought to the fore when one stops to consider the particular reactions and the potentials at which they are expected to occur. Fuel ideally is oxidized at 0 V vs. NHE, which can hardly be considered a very oxidizing potential, and reduction of oxygen is expected to occur at a potential (+1.2 V) that would almost never be considered reducing. Catalyzing both those processes is the challenge at hand, which makes even fuel cells' current performance seem remarkable. Significant improvements are a quite daunting challenge.

1.3 Nanoparticle Synthesis

Since both electrodes utilize nanoparticle electrocatalysts, it is useful to discuss some methods used to prepare nanoparticles of individual elements, alloys and

compounds. Many papers and review articles [13, 14, 34-38] have been written on the subject, and this brief introduction will only give the reader a small taste of the types of inorganic materials which can be synthesized as nanoparticles, a few of the methods by which that is accomplished, and some recommended reading for more complete treatments. The simplest and best-understood type of nanoparticle preparations are those of single metals, most notably the coin metals Pt, Au, and Ag, and to a lesser extent, the rest of the platinum group metals (Pd, Ir, Rh, Ru, Os) [35, 37]. These elements are amenable to a wide variety of preparation methods [35], such as solution-phase reduction of their corresponding salts or organometallics, reduction by flowing hydrogen, thermal decomposition of organometallics [34], microwave or gamma radiation-assisted precipitation, and ultrasonication. Solution-phase synthesis can be accomplished in either aqueous or non-aqueous solvents, since these electronegative metals are stable in water, unlike early transition or most main-group metals. Reduction in aqueous solution has also been reported for Co, Ni, and Cu [35], and is the preferred reaction medium in large-scale industrial applications where the use of organic solvents may present environmental challenges.

Synthesis of more electropositive elements than the ones listed above, such as early transition metals and main group elements, limits the field of methods and media available. Most methods other than solution-phase chemical reduction are not able to reduce these elements to their zero-valent state; for instance, the radicals generated by microwave radiation techniques [35] are sufficiently reducing to make silver nanoparticles, but not elemental vanadium. Non-aqueous solvents such as THF, glymes and other ethers, toluene, and dimethylformamide [35] are commonly used since they resist reaction with many of the reduced metal species under discussion, unlike, for instance, methanol, which oxidizes many electropositive metals. The reducing agents considered here are quite strong (< -1.0 V vs. NHE), which are much

more reducing than hydrogen gas, for example. James Dye has pioneered the use of alkalides (cryptand ligand-stabilized alkali metals which then form alkali metal anions), and has reported the synthesis of nanoparticles of Au, Pt, Cu, Te, Ni, Fe, Zn, Ga, Si, Mo, W, In, Sn, Sb, and Ti [35]. These reducing agents are able to reduce an amazing variety of elements, but their use is not widespread due to lack of commercial availability and difficulty in preparation and handling. A more commonly used group of reducing agents in non-aqueous solvents are the triethylborohydrides, $AB(Et)_3H$, where A is an alkali metal cation. These agents increase in reduction power from K < Na < Li, and are able to reduce Cr^{III}, Mn^{III}, Zn^{II}, Cd^{II}, In^{3+}, Sn^{II}, Mo^{III}, W^{IV}, all the Pt group metals, and the rest of the elements listed earlier under aqueous chemistry [35].

Of course, single element nanoparticles have finite utility in technological applications, and many materials with more than one element have been synthesized. One can divide these materials into two basic categories: ones which have a large negative enthalpy of formation, and ones whose $\Delta H°_f$ is small. For the purpose of this discussion, we will take this cutoff to be between -15 and -20 kcal mol^{-1}. The compounds with the enthalpy of formation more negative than -20 kcal mol^{-1} (and therefore the more negative $\Delta G°_f$, since the entropic $T\Delta S$ term in the formation of solids tends to be much smaller than the ΔH) include oxides, chalcogenides, carbides, and nitrides, some of which have technological utility. Oxides are often synthesized in water, since oxidation is not a concern in a fully oxidized material, and post-synthesis annealing or calcination is usually necessary [35]. The most common method of preparing oxide nanoparticles is simple co-precipitation of water-soluble precursors in base followed by drying and annealing in air, but more complex methods such as sol-gel chemistry and its subcategory of the Pechini method [39] are routinely used to yield multimetallic metal oxides as well as nitrides and oxynitrides. Metal carbides have been synthesized in solution by alkalide and trialkylborohydride reduction, and

transition metal nitrides have been synthesized by reaction with urea [40]. Semiconductor chalcogenide nanoparticles have been extensively studied [36] in the field of quantum dot technology, most notably as CdSe, CdTe, and PbSe.

The multi-component nanoparticles most germane to this dissertation are ones with small to modest enthalpies of formation: metal alloys and intermetallic compounds. These multimetallic compositions have usually ΔH_f's of -15 kcal mol^{-1} or less, though there are notable large-ΔH_f exceptions among intermetallics. Alloy nanoparticles are not quite as pervasively studied as single-component Pt group metals, but there is still an extensive alloy nanoparticle literature. The most common of these are binary alloys of coinage and Pt group metals prepared by liquid-phase co-reduction, since they are a natural extension of the methods established for those same single elements. One can find examples of these alloy nanoparticles by picking any pair of elements from the list of Pt, Au, Ag, Cu, Fe, Co, Ni, Ru, and Pd, and to a lesser extent Ir, Os and Rh. Such a list of pairs generated from the elements above is skewed in favor of Pt and Pd alloys for catalytic purposes, and there is ample publication of Pt alloys with Fe, Co, and Ni for their magnetic properties. A noteworthy accomplishment that illustrates that nanoparticles can be kinetic products, rather than only thermodynamic, is represented by the synthesis of Fe-Cu nanoparticles. Iron and copper are not normally soluble in one another in bulk, yet the binary alloy has been prepared as nanoparticles [35]. All the metals discussed in this paragraph still reduce fairly easily from molecular precursors (the most negative standard reduction potential of the Pt – Pd elements listed earlier in this paragraph is for Fe^{II} to Fe^0 at only -0.44V vs. NHE), and the number of reported nanoparticle alloys drop off rapidly as more and more electropositive elements are considered.

The difference between an alloy and an intermetallic compound is distinguished by their atomic order. In a binary alloy like 1:1 PtRu, the atomic sites

adopt the face-centered cubic crystal structure of Pt, but the actual occupancy of those sites by either a Pt or Ru atom is random, governed by probability based only on the Pt:Ru composition. In short, you know where the atoms are, but the identity of the atoms is only probabilistically known. However in an ordered intermetallic compound like PtPb, each element fully occupies different crystallographic positions.

PtPb adopts a hexagonal crystal structure in which both the crystallographic locations and the elemental identities are completely determined. This tendency for some metals to form ordered intermetallics mostly stems from differences in electronegativity, which manifests as a modestly negative ΔH_f. A classic alloy like Cu-Ni only has a slight difference in Pauling electronegativity between the two elements (Cu is 1.9 and Ni is 1.8 [41]), and therefore the alloy has a negligible enthalpy of formation. These similar electronegativities also tend to give rise to similar reduction potentials; for the pair listed above, E° for Cu^{II} to Cu^0 is +0.340 V, and Ni^{II} to Ni^0 is −0.25 V. This approximate 600 mV difference is not negligible, but is nowhere near as large as the 3.81 V difference between Pt (Pt^{II} to Pt^0 at + 1.18V) and Ti (Ti^{II} to Ti^0 at - 1.63V). The Pt-Ti phase diagram indicates that at least five intermetallic phases can be prepared at different mole ration of Pt and Ti. The Pauling electronegativities are 2.2 for Pt and 1.5 for Ti. The disparity in reduction potentials that usually accompanies elements that form intermetallics, especially when including early transition metals, must be considered when selecting a reducing agent for co-reduction, as will be discussed later.

Intermetallic compounds are even rarer in the literature than alloys. Schaak has published extensively [38, 42-54] on the synthesis of intermetallic nanoparticles, having synthesized binary intermetallics, pseudo-ternaries (a compound with three metals that adopts a structure type identical to a known binary), and true ternaries (a trimetallic compound whose structure type cannot be attained without all three of

those metals). Schaak's work often describes stepwise reduction of metal precursors [38, 50, 53, 55] and the conversion of as-made nanoparticles to different structures and compositions by annealing [45, 48, 49, 51]. Work in the DiSalvo group from *ca.* 2005- present [56-61] of course concerns the synthesis of intermetallic nanoparticles, and the methods used in the group and in this dissertation will be specifically addressed in a later section.

So far this discussion of nanoparticle synthesis has not included the reagents and methods used to prevent particle agglomeration, so they will be briefly discussed here. In order to prevent the high surface energy particles from aggregating together, capping agents must be employed to keep the particles stabilized in a (usually) monodisperse form. This can be accomplished by adsorbing charged species to the surface of the particles and letting electrostatic repulsion keep them separate, but the more common method is to rely on bulky aliphatic ligands or coordinating polymers to employ steric separation. These ligands are often referred to as surfactants (a misnomer when no polar/non-polar dual phase solvent is in use), and use varieties of long-chain alkyls branching from an electron donor heteroatom (O, N, S, P) that coordinates in a dative or even covalent bond to the particle's surface. The excellent 2004 review by Cushing et al. [35] of liquid-phase inorganic nanoparticle synthesis includes an extensive (but not exhaustive) collection of stabilizers, sorted into tables by donor atom. Some of the most common capping ligands include oleic acid, hexadecylamine, long chain ($-(CH_2)_n- > 8$) alkanethiols, trialkylphosphines and trioctylphosphine oxide. In cases where a well-studied metal like Pt [15] or Pd [14, 62] is used, specific growth facets can be expressed with use of ligands like cetyltetraamonium bromide (CTAB), where the bromide anion preferentially adsorbs to some crystal planes more strongly than others, encouraging different shapes to form while the long-chain ammonium ion provides steric particle separation. Polymers

such as poly(vinylpyrrolidone) and poly(vinylpyridine) work well for steric separation of Pt-group metals. All these techniques are capable of generating nanoparticles with narrow size distributions (often only ± 10% of the average diameter) and keeping them monodisperse, but selection of the correct particle-capping agent pair is highly empirical. Choosing the correct capping partner for a given material is non-trivial given the variety of reagents available and considering the end-use of the nanoparticle.

1.4 Fuel Cell Catalyst Research at the Energy Materials Center at Cornell (emc^2)

By looking at intermetallic compounds, the possibility exists for several improvements in electrocatalytic activity due to the ordered nature of those compounds. The order and disorder properties for bulk alloys and intermetallics that were discussed earlier manifest themselves in the crystal surfaces as well. In a random solid solution like PtRu, the surface is no more ordered than the bulk, and may promote elemental surface segregation, such as Pt-rich skins. These essentially behave like Pt, and can be just as susceptible to poisoning as the single element. In contrast, an intermetallic can be ordered even on the surface. In PtBi and PtPb, Pt atoms on many crystal faces are widely separated from each other, and the usual binding modes of CO and sulfur poisons are eliminated. We hypothesize that this may be the root of improved electrocatalytic performance. PtPb is a better electrocatalyst for formic acid oxidation than Pt, a comparison which also holds true against any other electrocatalyst [63]. The bulk form of PtPb has higher current density at all potentials, and the onset potential for formic acid oxidation is quite low, near 0 V vs. NHE.

When considering solution phase preparation of multi-component nanoparticles, the method must be able to reduce nearly all metal precursors

simultaneously to produce homogeneous intermetallic particles. If one metal is reduced at a faster rate than the other, it may nucleate a single-metal particle before the other metal is reduced. This results in either sequential formation of single element nanoparticles, or perhaps in the coating of one component by another (core-shell morphologies). Core-shell morphology is not the desired outcome in this research, though Adzic and coworkers have shown how to deposit a Pt shell on other metal particles for exciting electrocatalytic properties [32, 64-72]. To achieve the simultaneous co-reduction of two metal precursors (which likely have quite different reduction potentials), a strong reducing agent with fast electron transfer kinetics is needed. The reductant needs to have enough chemical potential to reduce each metal precursor on its own, and sufficiently rapid electron transfer to each precursor, so that whichever precursor collides with the reducing agent in solution becomes reduced, regardless of which precursor it is. This diffusion limited reaction should ensure simultaneous reduction of both metals and can lead to the nucleation of homogeneous intermetallic nanoparticles. The prospect of simultaneous co-reduction of the intermetallics' precursors used in past publications [57, 59] had not been verified experimentally, and research towards that end is presented in Chapter three of this dissertation.

After the brief discussion of nanoparticle capping ligands earlier, one will certainly notice their absence from the synthetic procedures in the upcoming chapters. Capping agents have been excluded due to their tendency to deactivate catalysts. By their very nature, capping ligands preferentially bind to particle surfaces; nanoparticles are kept segregated from one another, but their catalytic sites are blocked, and no fuel can reach the surface. Heat treatments (usually under vacuum) are often used to remove these ligands by decomposition and/or desorption. These methods have varying degrees of success in removing the ligands, but may result in excessive

particle sintering or coatings that stem from surfactant decomposition. Also, the interaction of traditional capping ligands with both noble and base metals in the same pot has not been extensively explored. The formation of intermetallic compounds as nanoparticles is quite complex due to the presence of many species in solution; research is not yet at the stage where we are willing to add even more. This is not to say that the intermetallics and alloys described in this dissertation are idealized nanoparticles. Since they do not have these capping agents, there is little to prevent the agglomeration of, for example, 5 nm particles into a 100 nm aggregate. This is accepted for the time being, so other factors than total particle size are used to assess nanoparticle composition, structure, and properties. Once the factors governing intermetallic crystallite formation are better understood (part of which is the goal of Chapter 2), future work in the group will undoubtedly include capping agents to impose better size control. Perhaps facet-directing ligand techniques will be able to preferentially expose crystal faces that are shown in related work to have enhanced activities.

As the study of single component, binary and ternary heterogeneous electrocatalysts has proceeded over time, it is apparent that improved electrocatalysis occurs with more and more complex materials. The synergistic effects of density of state variations through crystal strain, substitution, and surface composition are difficult to parse out *a priori*, so much of the success of catalyst development has been through empirical observation. Though the combinations of metals that researchers explore for fuel cell catalysts are not random, there are certainly limits to the Edisonian method of trying any possible combination of elements in hopes that a new fuel oxidation or oxygen reduction catalyst is discovered. If one considers the "convenient" (excluding noble gases and radioactive) elements in the periodic table, one is left with 80 or so elements in play. Even if one only considers 1:1 binaries of

these elements (indulging in the dubious prospect of being able to form actual binary alloys or compounds out of *all* combinations) that would generate 80 × 79 = 6320 combinations. When expanding the list to ternaries of fixed, equal composition, the list balloons to 80 × 79 × 78 = 492,960 combinations, and when allowing the metal ratios to vary by 1 at% at a time instead of fixing their ratios, the list grows into the millions of compositions which could conceivably be synthesized and tested. Clearly a high throughput method is needed to rapidly screen potential catalysts, and one such method is magnetron sputtering of metals as thin films.

The Bruce van Dover research group in Cornell's Materials Science and Engineering department specializes in such thin film methodologies, and has developed a way of depositing up to four metals simultaneously onto a three inch diameter silicon substrate, and then characterizing the continuous composition spread. The technique as applied to fuel cell catalyst discovery has been described by Prochaska [73], Jin [74], and Gregoire [75], and involves a high vacuum chamber with four metal target guns available for magnetron sputtering. They are able to control metal deposition rate as well as heating of the substrate to achieve annealing of the as-deposited film. Reactive gases like methane and ammonia can be introduced to the sputter chamber so that even carbon and nitrogen can be present in films. The spatial composition gradient of the films is approximately one atomic percent per millimeter. By optimizing the orientation of the guns when depositing the film, they are able to cover 60 - 80% of the ternary phase space. These films and their compositions are evaluated simultaneously as a single electrode, speeding the search for better catalysts in these ternary or quaternary systems. The compositions of active regions of the film are then verified through energy- and wavelength-dispersive X-ray spectroscopy [74], X-ray diffraction and fluorescence spectroscopy [76], and X-ray photoelectron

spectroscopy [74, 77]. Thousands of metal films have been deposited and evaluated through these methods (though many of those are duplicate compositions).

The truly high-throughput aspect of this method lies in the electrochemical screening process. The fastest technique available is to use a fluorescence indicator (quinine for fuel oxidation and unbelliferone for oxygen reduction) in neutral solution and applying a potential to the film in an electrochemical cell. When fuel is oxidized, the local hydronium ion concentration increases near the active catalyst area, which is detected optically with the fluorescent indicator in a method first reported by Reddington et al [78], and subsequently in the references listed earlier [73-75]. Onset of fuel oxidation can be determined by plotting fluorescence intensity versus applied potential, much like a normal electrochemical polarization curve. Once the fluorescence method determines the existence of a catalytically interesting phase, a smaller electrochemical cell (described by Gregoire et al. [75]) can also be rastered across the surface of the wafer in order to further probe the electrocatalytic properties of the 1 cm^2 area that the cell covers. This smaller cell allows for more realistic fuel cell conditions of pH = 1 to be used, rather than at near-neutral pH for the fluorescence assay.

The end goal of the continuous composition thin film method is to enable an efficient search for novel catalyst compositions which will then be recreated as nanoparticles. It must be acknowledged that the electrocatalytic properties of thin films may not directly translate to those of nanoparticles. Thin film strain and other factors can play a large role in electrocatalytic behavior, which may lead to false positives from combinatorial searches. A more unfortunate alternative to a false-positive would be a missed catalyst, which is a possibility if there is a phase which is inactive in thin film but would be active as nanoparticles. This possibility is recognized as a limitation of the thin film method. Nonetheless, if our collaborators

discover an exciting anode or cathode electrocatalyst, it will not be feasible to use in thin film form, and will need to be duplicated as nanoparticles. The nanoparticle synthesis techniques which have been discussed earlier are being developed as a toolbox of sorts, so that the synthetic methodologies necessary for making a homogeneous multimetallic nanoparticle are available when needed. This interplay between understanding the formation of complex nanomaterials and the goal of duplicating the results of combinatorial methods constitutes the majority of the present work.

1.5 Outline of the Dissertation

The dissertation will proceed into four chapters on research and one on conclusions. Chapters two and three deal with the efforts taken to understand the mechanism of the formation of PtPb under established synthetic parameters, and to see if our group's hypothesis of the model for the formation of intermetallic nanoparticles is feasible. Chapter two uses alterations of synthesis conditions and treatment with gases before work-up to gauge the effect that the conditions have on nanoparticle domain size, surface area, and electrocatalytic activity. Chapter three covers experiments used to determine the likelihood of co-reduction of metal precursors under electrochemical parameters as close to the synthesis conditions as possible. The goal there was to see if electroanalytical kinetic rate constants for precursor reduction were comparable with each other. If they were vastly different, the model of the reaction would need to be reconsidered. Chapter four moves away from PtPb intermetallic as an anode catalyst, and describes the synthesis of a ternary palladium alloy for oxygen reduction at the cathode. By taking inspiration from combinatorial thin film catalyst searches, the goal in Chapter four was to synthesize ternary

nanoparticles that have electrocatalytic activity that could not have been predicted without the thin film experiments. Chapter five finishes the research by covering preliminary attempts to synthesize transition metal carbides *via* sodium naphthalide reduction. Given the van Dover group's carbon "sputtering" capabilities and our group's interest in the inclusion of carbon in nanoparticle catalysts, the preliminary results from those experiments are included here. Chapter five also describes classic solid state synthesis techniques that were used in collaboration with research groups interested in exotic solid materials, but without the means to synthesize them. Chapter six finishes by offering the take-home messages from each chapter, and then giving suggestions for future work.

REFERENCES

1. O'Hayre, R.O., Suk-Won Cha, Whitney Colella, and Fritz B. Prinz, *Fuel Cell Fundamentals*. 1st ed. 2006, Hoboken, NJ: John Wiley & Sons, Inc.

2. Mathias, M., et al., *Two Fuel Cell Cars in Every Garage?* The Electrochemical Society Interface, 2005. **14**(3): p. 24-35.

3. Borup, R., et al., *Scientific aspects of polymer electrolyte fuel cell durability and degradation.* Chemical Reviews, 2007. **107**(10): p. 3904-3951.

4. Devanathan, R., *Recent developments in proton exchange membranes for fuel cells.* Energy & Environmental Science, 2008. **1**(1): p. 101-119.

5. Cheng, X., et al., *A review of PEM hydrogen fuel cell contamination: Impacts, mechanisms, and mitigation.* Journal of Power Sources, 2007. **165**(2): p. 739-756.

6. Liu, S.H., et al., *Fabrication and characterization of well-dispersed and highly stable PtRu nanoparticles on carbon mesoporous material for applications in direct methanol fuel cell.* Chemistry of Materials, 2008. **20**(4): p. 1622-1628.

7. Anderson, A.B. and E. Grantscharova, *Catalytic Effect of Ruthenium in Ruthenium-Platinum Alloys on the Electrooxidation of Methanol - Molecular-Orbital Theory.* Journal of Physical Chemistry, 1995. **99**(22): p. 9149-9154.

8. Liu, H.S., et al., *A review of anode catalysis in the direct methanol fuel cell.* Journal of Power Sources, 2006. **155**(2): p. 95-110.

9. Frelink, T., W. Visscher, and J.A.R. Vanveen, *On the Role of Ru and Sn as Promoters of Methanol Electrooxidation Over Pt.* Surface Science, 1995. **335**(1-3): p. 353-360.

10. Mathias, M., et al., *Can available membranes and catalysts meet automotive PEFC requirements?* Abstracts of Papers of the American Chemical Society, 2004. **228**: p. 002-FUEL.

11. Habas, S.E., et al., *Shaping binary metal nanocrystals through epitaxial seeded growth.* Nature Materials, 2007. **6**(9): p. 692-697.

12. Lee, H., et al., *Morphological control of catalytically active platinum nanocrystals.* Angewandte Chemie-International Edition, 2006. **45**(46): p. 7824-7828.

13. Mazumder, V., Y. Lee, and S.H. Sun, *Recent Development of Active Nanoparticle Catalysts for Fuel Cell Reactions.* Advanced Functional Materials. **20**(8): p. 1224-1231.

14. Semagina, N. and L. Kiwi-Minsker, *Recent Advances in the Liquid-Phase Synthesis of Metal Nanostructures with Controlled Shape and Size for Catalysis.* Catalysis Reviews: Science and Engineering, 2009. **51**(2): p. 147 - 217.

15. Chen, J., et al., *Shape-controlled synthesis of platinum nanocrystals for catalytic and electrocatalytic applications.* Nano Today, 2009. **4**(1): p. 81-95.

16. Lu, L.L. and G.P. Yin, *Shape-Controlled Synthesis and Applications of Platinum Nanocrystals.* Progress in Chemistry. **22**(2-3): p. 338-344.

17. Zhang, J. and J.Y. Fang, *A General Strategy for Preparation of Pt 3d-Transition Metal (Co, Fe, Ni) Nanocubes.* Journal of the American Chemical Society, 2009. **131**(51): p. 18543-18547.

18. Kalra, V., et al., *Controlling Nanoparticle Location via Confined Assembly in Electrospun Block Copolymer Nanofibers.* Small, 2008. **4**(11): p. 2067-2073.

19. Kamperman, M., et al., *Integrating Structure Control over Multiple Length Scales in Porous High Temperature Ceramics with Functional Platinum Nanoparticles.* Nano Letters, 2009. **9**(7): p. 2756-2762.

20. Orilall, M.C., et al., *One-Pot Synthesis of Platinum-Based Nanoparticles Incorporated into Mesoporous Niobium Oxide-Carbon Composites for Fuel Cell Electrodes.* Journal of the American Chemical Society, 2009. **131**(26): p. 9389-9395.

21. Li, Z.H., et al., *Metal Nanoparticle-Block Copolymer Composite Assembly and Disassembly.* Chemistry of Materials, 2009. **21**(23): p. 5578-5584.

22. Gasteiger, H.A., et al., *Activity benchmarks and requirements for Pt, Pt-alloy, and non-Pt oxygen reduction catalysts for PEMFCs.* Applied Catalysis B-Environmental, 2005. **56**(1-2): p. 9-35.

23. Wang, B., *Recent development of non-platinum catalysts for oxygen reduction reaction.* Journal of Power Sources, 2005. **152**(1): p. 1-15.

24. Fu, Y., et al., *Synthesis of Pd/TiO2 nanotubes/Ti for oxygen reduction reaction in acidic solution.* Journal of Power Sources, 2009. **189**(2): p. 982-987.

25. Jiang, C.M. and X.Q. Lin, *A novel nanocomposite of Pd nanocluster/poly(N-acetylaniline) nanorod modified electrode for the electrocatalytic reduction of oxygen.* Journal of Applied Electrochemistry, 2008. **38**(12): p. 1659-1664.

26. Salvador-Pascual, J.J., S. Citalan-Cigarroa, and O. Solorza-Feria, *Kinetics of oxygen reduction reaction on nanosized Pd electrocatalyst in acid media.* Journal of Power Sources, 2007. **172**(1): p. 229-234.

27. Shao, M.H., K. Sasaki, and R.R. Adzic, *Pd-Fe nanoparticles as electrocatalysts for oxygen reduction.* Journal of the American Chemical Society, 2006. **128**(11): p. 3526-3527.

28. Wang, W.M., et al., *Surface and structure characteristics of carbon-supported Pd3Pt1 bimetallic nanoparticles for methanol-tolerant oxygen reduction reaction.* Journal of Catalysis, 2009. **266**(1): p. 156-163.

29. Xiao, L., et al., *Activating Pd by Morphology Tailoring for Oxygen Reduction.* Journal of the American Chemical Society, 2009. **131**(2): p. 602-608.

30. Yang, J.H., et al., *Carbon-supported pseudo-core-shell Pd-Pt nanoparticles for ORR with and without methanol.* Journal of the Electrochemical Society, 2008. **155**(7): p. B776-B781.

31. Yeh, Y.C., et al., *Pd-C-Fe Nanoparticles Investigated by X-ray Absorption Spectroscopy as Electrocatalysts for Oxygen Reduction.* Chemistry of Materials, 2009. **21**(17): p. 4030-4036.

32. Zhang, J., et al., *Platinum monolayer electrocatalysts for O-2 reduction: Pt monolayer on Pd(111) and on carbon-supported Pd nanoparticles.* Journal of Physical Chemistry B, 2004. **108**(30): p. 10955-10964.

33. Zhang, Z.H., et al., *Pd nanoparticles supported on WO3/C hybrid material as catalyst for oxygen reduction reaction.* Journal of Power Sources, 2008. **185**(2): p. 941-945.

34. Boennemann, H. and G. Khelashvili, *Efficient fuel cell catalysts emerging from organometallic chemistry.* Applied Organometallic Chemistry, 2010. **24**(4): p. 257-268.

35. Cushing, B.L., V.L. Kolesnichenko, and C.J. O'Connor, *Recent advances in the liquid-phase syntheses of inorganic nanoparticles.* Chemical Reviews, 2004. **104**(9): p. 3893-3946.

36. Gubin, S.P., N.A. Kataeva, and G.B. Khomutov, *Promising avenues of research in nanoscience: chemistry of semiconductor nanoparticles.* Russian Chemical Bulletin, 2005. **54**(4): p. 827-852.

37. Roucoux, A., J. Schulz, and H. Patin, *Reduced transition metal colloids: A novel family of reusable catalysts?* Chemical Reviews, 2002. **102**(10): p. 3757-3778.

38. Schaak, R.E., et al., *Metallurgy in a beaker: Nanoparticle toolkit for the rapid low-temperature solution synthesis of functional multimetallic solid-state materials.* Journal of the American Chemical Society, 2005. **127**(10): p. 3506-3515.

39. Pechini, M.P., *Method of preparing lead and alkaline earth titanates and niobates and coating method using the same to form a capacitor*, U.S.P. Office, Editor. 1967, SPRAGUE ELECTRIC CO: United States. p. 7.

40. Yao, W.T., et al., *Synthesis of Early-Transition-Metal Carbide and Nitride Nanoparticles through the Urea Route and Their Use as Alkylation Catalysts.* Chemistry-a European Journal, 2009. **15**(44): p. 11999-12004.

41. Pauling, L., *The Nature of the Chemical Bond*. 3 ed. The George Fisher Baker Non-Resident Lectureship in Chemistry at Cornell University. 1960, Ithaca NY: Cornell University Press. 644.

42. Schaefer, Z.L., D.D. Vaughn, and R.E. Schaak, *Solution chemistry synthesis, morphology studies, and optical properties of five distinct nanocrystalline Au-Zn intermetallic compounds.* Journal of Alloys and Compounds. **490**(1-2): p. 98-102.

43. Henderson, N.L., et al., *Toward green metallurgy: low-temperature solution synthesis of bulk-scale intermetallic compounds in edible plant and seed oils.* Green Chemistry, 2009. **11**(7): p. 974-978.

44. Vasquez, Y., Z.P. Luo, and R.E. Schaak, *Low-temperature solution synthesis of the non-equilibrium ordered intermetallic compounds Au3Fe, Au3Co, and Au3Ni as nanocrystals.* Journal of the American Chemical Society, 2008. **130**(36): p. 11866-11867.

45. Vasquez, Y., et al., *Nanocrystal conversion chemistry: A unified and materials-general strategy for the template-based synthesis of nanocrystalline solids.* Journal of Solid State Chemistry, 2008. **181**(7): p. 1509-1523.

46. Henderson, N.L. and R.E. Schaak, *Low-temperature solution-mediated synthesis of polycrystalline intermetallic compounds from bulk metal powders.* Chemistry of Materials, 2008. **20**(9): p. 3212-3217.

47. Bauer, J.C., et al., *Converting nanocrystalline metals into alloys and intermetallic compounds for applications in catalysis.* Journal of Materials Chemistry, 2008. **18**(3): p. 275-282.

48. Cable, R.E. and R.E. Schaak, *Solution synthesis of nanocrystalline M-Zn (M = Pd, Au, Cu) intermetallic compounds via chemical conversion of metal nanoparticle precursors.* Chemistry of Materials, 2007. **19**(16): p. 4098-4104.

49. Chou, N.H. and R.E. Schaak, *Shape-controlled conversion of beta-Sn nanocrystals into intermetallic M-Sn (M = Fe, Co, Ni, Pd) nanocrystals.* Journal of the American Chemical Society, 2007. **129**(23): p. 7339-7345.

50. Leonard, B.M. and R.E. Schaak, *Multistep solution-mediated formation of AuCuSn2: Mechanistic insights for the guided design of intermetallic solid-state materials and complex multimetal nanocrystals.* Journal of the American Chemical Society, 2006. **128**(35): p. 11475-11482.

51. Cable, R.E. and R.E. Schaak, *Reacting the unreactive: A toolbox of low-temperature solution-mediated reactions for the facile interconversion of nanocrystalline intermetallic compounds.* Journal of the American Chemical Society, 2006. **128**(30): p. 9588-9589.

52. Cable, R.E. and R.E. Schaak, *Low-temperature solution synthesis of nanocrystalline binary intermetallic compounds using the polyol process.* Chemistry of Materials, 2005. **17**(26): p. 6835-6841.

53. Leonard, B.M., N.S.P. Bhuvanesh, and R.E. Schaak, *Low-temperature polyol synthesis of AuCuSn2 and AuNiSn2: Using solution chemistry to access ternary intermetallic compounds as nanocrystals.* Journal of the American Chemical Society, 2005. **127**(20): p. 7326-7327.

54. Sra, A.K. and R.E. Schaak, *Synthesis of atomically ordered AuCu and AuCU3 nanocrystals from bimetallic nanoparticle precursors.* Journal of the American Chemical Society, 2004. **126**(21): p. 6667-6672.

55. Leonard, B.M., et al., *Orthogonal Reactivity of Metal and Multimetal Nanostructures for Selective, Stepwise, and Spatially-Controlled Solid-State Modification.* Acs Nano, 2009. **3**(4): p. 940-948.

56. Roychowdhury, C., et al., *Synthesis, characterization, and electrocatalytic activity of PtBi nanoparticles prepared by the polyol process.* Chemistry of Materials, 2005. **17**(23): p. 5871-5876.

57. Alden, L.R., et al., *Intermetallic PtPb nanoparticles prepared by sodium naphthalide reduction of metal-organic precursors: Electrocatalytic oxidation of formic acid.* Chemistry of Materials, 2006. **18**(23): p. 5591-5596.

58. Abe, H., et al., *Electrocatalytic performance of fuel oxidation by Pt3Ti nanoparticles.* Journal of the American Chemical Society, 2008. **130**(16): p. 5452-5458.

59. Ghosh, T., et al., *PtPb nanoparticle electrocatalysts: control of activity through synthetic methods.* Journal of Nanoparticle Research, 2009. **11**(4): p. 965-980.

60. Ghosh, T., et al., *Pt Alloy and Intermetallic Phases with V, Cr, Mn, Ni, and Cu: Synthesis As Nanomaterials and Possible Applications As Fuel Cell Catalysts.* Chemistry of Materials, 2010. **22**(7): p. 2190-2202.

61. Miura, A., et al., *Synthesis of Intermetallic PtZn Nanoparticles by Reaction of Pt Nanoparticles with Zn Vapor and Their Application as Fuel Cell Catalysts.* Chemistry of Materials, 2009. **21**(13): p. 2661-2667.

62. Niu, W., L. Zhang, and G. Xu, *Shape-Controlled Synthesis of Single-Crystalline Palladium Nanocrystals.* ACS Nano. **4**(4): p. 1987-1996.

63. Matsumoto, F., et al., *Electrocatalytic activity of ordered intermetallic PtPb nanoparticles prepared by borohydride reduction toward formic acid oxidation.* Journal of the Electrochemical Society, 2008. **155**(2): p. B148-B154.

64. Lima, F.H.B., et al., *Pt monolayer electrocatalysts for O-2 reduction: PdCo/C substrate-induced activity in alkaline media.* Journal of Solid State Electrochemistry, 2008. **12**(4): p. 399-407.

65. Shao, M., et al., *Synthesis and characterization of platinum monolayer oxygen-reduction electrocatalysts with Co-Pd core-shell nanoparticle supports.* Electrochemistry Communications, 2007. **9**(12): p. 2848-2853.

66. Shao, M.H., et al., *Palladium monolayer and palladium alloy electrocatalysts for oxygen reduction.* Langmuir, 2006. **22**(25): p. 10409-10415.

67. Shao, M.H., et al., *Pd3Fe and pt monolayer-modified Pd3Fe electrocatalysts for oxygen reduction.* Zeitschrift Fur Physikalische Chemie-International

Journal of Research in Physical Chemistry & Chemical Physics, 2007. **221**: p. 1175-1190.

68. Zhang, J., et al., *Platinum monolayer on nonnoble metal-noble metal core-shell nanoparticle electrocatalysts for O-2 reduction.* Journal of Physical Chemistry B, 2005. **109**(48): p. 22701-22704.

69. Adzic, R.R., et al., *Platinum monolayer fuel cell electrocatalysts.* Topics in Catalysis, 2007. **46**(3-4): p. 249-262.

70. Ghosh, T., et al., *Intermetallics as Novel Supports for Pt Monolayer O-2 Reduction Electrocatalysts: Potential for Significantly Improving Properties.* Journal of the American Chemical Society, 2010. **132**(3): p. 906-+.

71. Inoue, H., et al., *Oxygen reduction on bare and Pt monolayer-modified Ru(0001), Ru(1010) and Ru nanostructured surfaces.* Electrochimica Acta, 2002. **47**(22-23): p. 3777-3785.

72. Zhou, W.P., et al., *Improving Electrocatalysts for O-2 Reduction by Fine-Tuning the Pt-Support Interaction: Pt Monolayer on the Surfaces of a Pd3Fe(111) Single-Crystal Alloy.* Journal of the American Chemical Society, 2009. **131**(35): p. 12755-12762.

73. Prochaska, M., et al., *High throughput screening of electrocatalysts for fuel cell applications.* Review of Scientific Instruments, 2006. **77**(5).

74. Jin, J., et al., *A high-throughput search for direct methanol fuel cell anode electrocatalysts of type PtxBiyPbz.* Applied Surface Science, 2007. **254**(3): p. 653-661.

75. Gregoire, J.M., et al., *High-Throughput Evaluation of Dealloyed Pt-Zn Composition-Spread Thin Film for Methanol-Oxidation Catalysis.* Journal of the Electrochemical Society, 2009. **156**(1): p. B160-B166.

76. Gregoire, J.M., et al., *High energy x-ray diffraction/x-ray fluorescence spectroscopy for high-throughput analysis of composition spread thin films.* Review of Scientific Instruments, 2009. **80**(12): p. 6.

77. Gregoire, J.M., et al., *Improved Fuel Cell Oxidation Catalysis in Pt1-xTax.* Chemistry of Materials. **22**(3): p. 1080-1087.

78. Reddington, E., et al., *Combinatorial electrochemistry: A highly parallel, optical screening method for discovery of better electrocatalysts.* Science, 1998. **280**(5370): p. 1735.

CHAPTER 2

PtPb *via* Sodium Naphthalide Reduction: Mechanistic Insights Through Synthesis Alterations

2.1 Introduction

As was briefly mentioned in Chapter 1, platinum lead (PtPb) has served the researchers at the Cornell Fuel Cell institute as a model system to explore new avenues of solid-state materials as fuel cell electrocatalysts [1-12]. Studies in the DiSalvo group by Dr. Laif Alden [1, 2, 13] and Dr. Chandrani Roy Chowdhury [2, 7, 9, 10] were excellent explorations of the compound's utility as a formic acid electrocatalyst, and also laid out the basis for future work in the group on how to prepare ordered intermetallic compounds as nanoparticles. Their work, particularly the reactions using sodium naphthalide (NaNp) as a reducing agent, was of great interest in CFCI, so the present work (and the dissertation work of Dr. Tanushree Ghosh [6]) began as a direct offshoot of that. Those authors established the baseline for formic acid oxidation on PtPb nanoparticles, and set benchmarks for producing particles that had consistent crystallite sizes, crystallinities, and electrocatalytic activities.

Dr. Roy Chowdhury's PtPb nanoparticles were synthesized by co-reduction of Pt and Pb precursors via sodium borohydride in methanol [10]. This system was found to be exceptionally "clean", in that the reaction not only formed the PtPb phase (at room temperature, no less) but also had very little surface contamination by side products, as inferred from the high electrocatalytic activity. We hypothesized that the oxidized form of the reducing agent and all precursor ligands remained soluble to the point where they were easily washed away, and allowed the desired phase to form at room temperature. When compared to samples reduced by sodium naphthalide but

with the same wash procedure, the borohydride samples had much higher current densities: 5.5 mA cm^{-2} at +0.2 V vs. Ag/AgCl, compared to 1.98 mA cm^{-2} for the naphthalide-reduced samples when both were normalized to particle BET surface area. At the time of that investigation [7], PtPb nanoparticles synthesized by borohydride reduction showed the highest known electrocatalytic activity for formic acid oxidation. Unfortunately, the borohydride reduction method is not universally applicable. The only elements that can be included in compounds made by this method are those whose precursors' reduction potentials fall above the value for BH_4^-, which in diglyme is around -0.6 V vs. NHE [14]. Of course standard reduction potentials will vary with solvent and metal precursor ligand, but generally only elements whose oxides can be reduced to neutral metal by heating under hydrogen gas will work. For example, WO_3 can be fully reduced to W metal when heating under flowing H_2, so tungsten and corresponding W^{VI} precursors are candidates for borohydride reduction (see Chapter 4 for research involving this reaction). For early transition metals to be included in intermetallic and alloy nanoparticles, a stronger reducing agent is needed.

The utility of sodium naphthalide as a reducing agent has been addressed elsewhere [14-17], but is worth reviewing here. By stirring clean pieces of sodium with an equimolar amount of naphthalene in an aprotic solvent (THF and glymes work well) naphthalene is reduced to form the naphthalide radical anion. Most other common solvents react with the Np anion [14]. In general, the reactants are best left stirring overnight under an inert gas to ensure complete reaction of the sodium metal, and fewer, larger pieces of sodium are preferred over finer dispersions. The naphthalide species is relatively stable in solution, but in the presence of oxidants is capable of a powerful one-electron reduction at approximately -2.3V vs. NHE [14]. Thus, alkali naphthalides are some of the few chemical reductants capable of fully reducing some of the more electropositive elements in the periodic table, particularly

early transition metals such as Ti [18, 19], Cr [20], Hf [21] and Zr [21], as well as main group elements like Ge [22, 23] and Si [24, 25]. Even though these metals are able to be reduced to their zero-valent state, the more electropositive metals are highly likely to re-oxidize when exposed to even the slightest amount of air or water, conditions which are found in a fuel cell. The only chance such elements have of remaining in a fuel cell electrocatalyst nanoparticle is by forming a thin (few nm thick) passivating oxide layer on the surface (which itself could be, or be part of, the catalytically active phase) or if the electropositive metal is stabilized in a matrix of a more noble metal. Such stability could be imparted in the intermetallic and alloy phases studied in this dissertation.

Single-element precursors were first studied to establish the efficacy using sodium naphthalide as a reducing agent for the elements of interest. Previous efforts were successful in synthesizing nanoparticles of Pt, Pb, Bi, and Sn by injecting respective precursor complexes into sodium naphthalide in diglyme under argon [13]. Dimethyl platinum cyclooctadiene and lead (II) 2-ethylhexanoate were then used as precursors for PtPb synthesis. When either the Pt (Eq. 2.1) or the Pb complex (Eq. 2.2) is injected into NaNp solution, there is an instant reaction, which by eye appears to be complete in less than a second.

$$Pt(COD)(CH_3)_2 + 2\ NaNp \rightarrow Pt_{(s)} + \text{organic side products} + 2Na^+ \quad (2.1)$$

$$Pb(\text{2-ethylhexanoate})_2 + 2\ NaNp \rightarrow Pb_{(s)} + \text{organic side products} + 2Na^+ \quad (2.2)$$

Work-up of the black precipitate in each case yields a black powder which indexes by powder X-ray diffraction to either Pt or Pb, respectively. These observations were repeated later, but not included in the present chapter. Since both reactants appear to react “instantaneously” (in less than a second), and the reaction of both in a heated

solution produces a 1:1 ordered intermetallic compound, the hypothesis of a simultaneous co-reduction of precursors was introduced. The viability of such a reaction timeframe, where both reduction rates are on the same order of magnitude from the observed minimum of ~1 s^{-1} to the diffusion-controlled maximum of ~10^9 s^{-1}, is tenuous at best, and is the subject of investigation in this and the next chapter.

A less demanding reaction rate is obtained by estimating the timeframe for a homogeneous solution of reduced metal centers to nucleate an arbitrary sized particle. For instance, for a 1 mM solution of a generic Pt precursor to nucleate a 5×5×5 nm^3 Pt particle (which would contain about 8000 atoms), the volume of solution which would contain the necessary number of atoms is approximately 10^{-14} cm^3. From such a volume, the farthest a reduced metal would have to travel in solution is about 10^{-5} cm, which given a usual diffusion constant for solvated species of 10^{-5} to 10^{-6} cm^2s^{-1}, would take about 10^{-5} seconds. So, for a homogeneous nanoparticle to form, all the metal precursors must be reduced faster than this nucleation timeframe; this rate is still too rapid to estimate by eye, but need not necessarily be as fast as the diffusion controlled reduction mentioned earlier. The fact that the two precursors' observed chemical reduction rates are not noticeably different (with one occurring in seconds, the other in ten minutes, for example) keeps the prospect of a co-reduction in place.

These past explorations of PtPb nanoparticle synthesis via sodium naphthalide reduction brought to light three key parameters in these syntheses: reaction temperature, time spent at that temperature, and reaction concentration. The first two parameters were explored in detail, while the third was inferred from some observations in later experiments. Varying the temperature was accomplished in several ways. One was to perform the reduction at room temperature, work up the product, and anneal in an evacuated tube without exposing to air. Another was to perform the reduction at room temperature, dry the product and expose directly to air;

the heat generated by rapid oxidation of the surfaces of the particles was found to be significant enough to induce intermetallic phase formation. The third way to alter the reaction temperature was to reduce at room temperature, then heat to a fixed temperature and stir for a specified time in the reaction solvent. Finally, the precursors could be injected into a solution that was already heated to a chosen temperature, and stirred there. Each method produced subtle differences in the products and in catalyst activity, but they all had a common theme: in order to be assured that the ordered intermetallic phase was being formed, some sort of thermal treatment had to be administered. None of Dr. Alden's sodium naphthalide reductions produced ordered PtPb at room temperature.

The simplest way of characterizing which syntheses produced ordered PtPb was by powder X-ray diffraction. Room temperature preparations yield black solids that show almost no Bragg peaks by XRD. Instead they show only a few broad humps that are roughly centered around 30 and 42 degrees 2θ, where the highest-intensity Bragg peaks in crystalline PtPb occur. These diffuse diffraction features are indicative of a product that either has nearly amorphous (or poorly ordered) crystal structure or is crystalline but with domains that are around 2-3 nm in size. Of course, in the limit of crystal domains becoming infinitely small, these two cases are actually one and the same. However, when sampling reactions carried out at increasing reaction temperature, there is often a temperature above which the as-formed products give sharp Bragg peaks without any post-synthesis annealing. There is only a 5°C difference in temperature between products with an amorphous diffraction pattern and products with sharp diffraction peaks [13], which is a very sudden increase in calculated domain size across a narrow range of temperatures. Clearly there is some thermally activated process that either induces growth of the intermetallic phase, or allows mobility of the reduced metal atoms and growth of the sub-nanometer as-

nucleated particles into particles that are large enough to give a coherent diffraction pattern.

In a way these explorations of ways to make ordered intermetallic nanoparticles are in competition with their use as a fuel cell anode electrocatalysts. Although the most straightforward way of identifying whether the reduced metal product is an intermetallic is by either X-ray or electron diffraction, the 3-5nm crystallites of interest for practical electrocatalysis [26], have broad Bragg peaks and low intensities. Thus, the degree of intermetallic ordering can be difficult to determine. This phenomenon is especially problematic when dealing with intermetallics whose crystal structures are closely related to their constituent metals. For example, gold, copper and intermetallic $AuCu_3$ all have face-centered cubic (FCC) structures. The strongest FCC reflections are common to all three diffraction patterns, but additional low-intensity ordering peaks arise in the ordered intermetallic. These peaks would be difficult or impossible to detect in 3 nm particles of $AuCu_3$. PtPb is less susceptible to this phenomenon, since the diffraction pattern from its hexagonal NiAs structure type is quite different from FCC Pt or Pb. Still, when the crystal domains are quite small, it becomes difficult to clearly quantify the degree of order. The irony of this discussion is that when crystal domains become large enough to easily determine when a nanoparticle is an ordered intermetallic, it is usually the case that the particles have grown too large to be practical fuel cell catalysts; too much of the metal (often costly platinum-group metals) is buried in the bulk of the particle and not available on the surface to perform catalysis. Therefore the studies of PtPb in this dissertation will focus on deconvoluting the factors that may impede the formation of crystalline PtPb, rather than focusing on preparing end-use ready nanoparticles.

The complex reaction of the formation of PtPb bears further consideration when trying to understand the mechanism of the formation of these bimetallic

particles, especially when the reaction could have implications for similar reactions in nanoparticle literature. This idea is the heart of the matter regarding the work presented in this chapter. It was relatively clear from the original PtPb work of Alden and Roy Chowdhury that the compound had certain limitations as far as a "game-changing" fuel cell catalyst. It showed good activity for formic acid oxidation, and its insensitivity to carbon monoxide poisoning is remarkable [7]. But while it was clear that the preparation methods could be altered to maximize the electrocatalytic activity, it was never a reasonable expectation to achieve anything greater than a 50-100% increase in current density at a lower overpotential (as opposed to a 1000% or more increase that would truly revolutionize fuel cell technology). The expectation was that by altering the synthesis conditions, one could obtain clues as to the mechanism of nanoparticle formation in this particular reaction. Due to the many beneficial aspects of sodium naphthalide that were noted earlier, that reducing agent and its corresponding chemistries would be of interest to both Cornell collaborators and the greater nanoparticle research community. The aim of the work presented in this chapter and the next is to provide a framework for understanding the formation of PtPb nanoparticles obtained by the co-reduction of Pt and Pb precursors by sodium naphthalide.

2.2 Variations in Solution Concentration and Excess Reducing Agent

Dr. Alden's findings using sodium naphthalide as a reducing agent [1] were some of the first that showed that NaNp could be used to make ordered intermetallic compounds as nanoparticles, and it is worthwhile to recall some of the questions left unanswered. One of those was what effects the initial concentrations of the reducing agent and the metal precursors had on the observed product. It was asserted that increasing the concentration of the precursors would lead to smaller crystallite sizes

[13], on the argument that performing the reaction at higher concentration meant more metal reduction per unit volume, and therefore more nucleation events per unit volume, leading to a greater number of smaller particles, as opposed to a smaller number of larger particles in a more dilute system [27]. However, that assertion was not explored in a systematic way, but rather relied on essentially two data points- one unpublished reaction performed at a relatively high concentration compared to many reactions at lower concentration. The first part of this section will cover more systematic experiments exploring the effects of concentration variation.

Another question was whether or not varying the excess reducing agent with respect to the metal precursors would produce a noticeable effect on the crystallite size as seen by X-ray diffraction. Most sodium naphthalide reactions done in the group had been performed with a 50% excess reducing agent. This is certainly a large excess, but previous observations had shown that, due to the highly reactive nature of the naphthalide radical anion and its propensity to react with any trace impurities of water or oxygen, such a large excess was necessary to ensure enough reducing agent would be available to fully reduce the metal precursors. While the impurities present in even modestly clean solvents, gloveboxes and Schlenk lines should not be enough to react with 1/3 of the amount of sodium naphthalide used in most reactions (1.5 mmol), this amount of excess was preserved as the starting point in these studies to keep the same reference point.

The main hypothesis when considering the effect of this considerable excess in reducing agent was that having so many molecular and ionic species in solution created a competition with the nucleation and growth of the reduced metal species. Single-crystal intermetallic nanoparticles can only be described as such if the neutral metal atoms are allowed to collide during nucleation and growth in such a manner so that metal-metal bonds can form. If unsaturated hydrocarbons such as naphthalene are

adsorbed to a metal surface or coordinated to atomic M^0 in a η^4- or η^6- mode [14], the rate of metal-metal bond formation could be significantly slowed. Similarly, the presence of sodium in such a large excess might promote the formation of $PtNa_x$ intermetallics or alloys. This possibility could not be ruled out *a priori*. By using less and less excess reducing agent, it was postulated that the PtPb phase might form with less aggressive heat treatments, thus avoiding excess particle sintering and improving its utility as an electrocatalyst.

2.2.1 Experimental

Dimethyl platinum (1,5) cyclooctadiene was purchased from Strem and used as-received. Neat lead (II) 2-ethylhexanoate was purchased from Aldrich and diluted in dry THF to approximately 0.05M for ease of handling the highly viscous precursor (a more precise concentration was calculated from the mass of the precursor used for each batch, and the per-reaction volume was adjusted accordingly). Sodium and naphthalene were purchased from Aldrich and used as-received. Tetrahydrofuran and diglyme were distilled over sodium-benzophenone before use. All manipulations were carried out in either an argon atmosphere glovebox, or on a Schlenk argon/vacuum line.

In a typical reaction, sodium (0.0345 g, 1.5 mmole) and naphthalene (0.1923 g, 1.5 mmole) were dissolved in 45 mL diglyme in a glovebox, transferred to a Schlenk line, and left to stir overnight to form sodium naphthalide. The resulting solution was the expected dark green color. Due to the solution's relatively high concentration and the large molar absorptivity coefficient of sodium naphthalide ($\varepsilon \approx 2500$ $mol^{-1}cm^{-1}$ at visible wavelengths [14]) the solution was nearly opaque. Once sodium naphthalide had formed, dimethyl platinum (1,5) cyclooctadiene (0.0833 g, 0.25 mmole) was dissolved in the lead (II) 2-ethylhexanoate THF solution (4.9 mL of a 0.05149 M

solution, 0.25 mmole), drawn into a syringe, brought out of the glovebox and immediately injected into the sodium naphthalide diglyme solution. The temperature of the reaction varied depending on the specific experiment, but for the purposes of this section, the precursors were injected into a solution that had already been heated to 135°C. After stirring for thirty minutes, the solution temperature was lowered to 40°C, and the solvent was distilled to a cold trap first by static, then dynamic vacuum until a dry black coating remained at the bottom of the flask. The solid was washed with degassed absolute ethanol, sonicated, and cannula transferred to a sealed centrifuge tube with an argon atmosphere. After centrifugation at 2000 rpm for 10 minutes, a black precipitate and a light amber supernatant were separated. The latter was removed with a syringe. The process of wash, sonicate, cannula, centrifuge, draw off supernatant was repeated with distilled hexanes, and the black powder in the sealed tube was dried for two hours under dynamic vacuum. The tube was backfilled with argon, and the septum was pierced with a needle to allow slow diffusion of air (and therefore a slow and controlled oxidation of the particle surfaces) overnight.

2.2.2 Characterization

Powder X-ray characterization was performed primarily on a Scintag XDS 2000 X-ray diffractometer, and later on a Rigaku Ultima IV, both with Cu K_α radiation. Microprobe analysis was done in a JEOL8900 EPMA microprobe at 20 kV accelerating voltage. Particle surface area measurements were performed on a Micromeritics ASAP 2020 surface area analyzer, with krypton as the adsorptive. Thermogravimetric analysis was done on a TA Instruments Q50 thermogravimetric analyzer. Electrocatalytic analysis was performed by Dr. Futoshi Matsumoto, and consisted of preparation of a nanoparticle-Nafion ink in ethanol, and depositing and drying the ink on a 3 mm diameter glassy carbon electrode at a loading of 70 μg

unsupported catalyst. Oxidation currents were measured while rotating the electrode at 2000 rpm and at a potential sweep rate of 10 mVs^{-1} from -0.2 V to +0.2 V vs. Ag^{+}/AgCl in a solution of 0.1 M H_2SO_4 and 0.5 M formic acid.

2.2.3 Results and Discussion

A series of reactions were performed where the concentration of the sodium naphthalide solution, the temperature of the reaction, and the time spent at that temperature were all kept constant, but the excess amount of reducing agent was varied from the 50% excess that had been the standard in past experiments. The formally platinum (II) and lead (II) precursors (0.25 mmol of each) need a total of 1.0 mmol of NaNp to be fully reduced to Pt^0 and Pb^0, so the reactions were performed with 100, 75, 50, 40, 30, 20, 10, and 0% excess reducing agent (2 mmol for 100% excess, down to 1 mmol for 0% excess). The effect of such drastic changes in the amount of sodium and naphthalene present do not appear to dramatically affect the full-width at half-max (FWHM) of X-ray diffraction peaks, contrary to what was expected. As seen in Figure 2.1, lowering the amount of excess reducing agent causes no appreciable or systematic change in domain sizes calculated by the Scherer equation, where the domain size $d = 0.9\times\lambda/(\cos\theta)(FWHM)$ for λ=1.54 Å and both the peak position (θ) and the full-width at half-max are in radians. The relative low intensity of the 10% excess pattern make the peaks look broader than they actually are. At the largest excess amounts of NaNp, there appears to be a slight difference between the powder patterns. At 100% excess the peaks appear to be of lower intensity when compared to the background than is the case in the 75% excess pattern, and the domain size is slightly smaller- 19 nm versus 22 nm for 75% excess. This is consistent with the prediction that high amounts of excess sodium and naphthalene would lessen the domain size, but the difference seen here is within the error

associated with domain size calculations (±10%) , and should not be given undue weight. No peaks were found which could be indexed to any sodium-platinum intermetallics, further excluding the possibility Na-Pt compound formation at these amounts of excess NaNp.

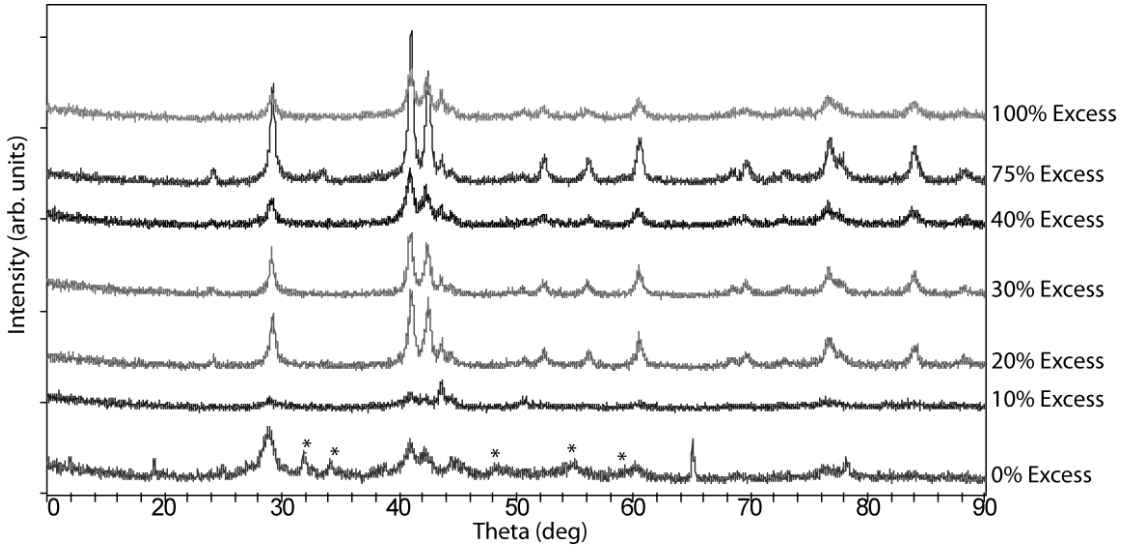

Figure 2.1 Powder X-ray diffraction patterns for PtPb samples reduced with 100% excess sodium naphthalide down to 0% excess. The domain sizes (top to bottom) are 19, 22, 20, 25, 23, 21 and 25 nm. The relative low intensities of the 10% excess pattern make the peaks look broader than they actually are. The starred peaks in the 0% excess pattern index to PbO.

The energy dispersive X-ray spectra (EDX) of the PtPb products measured by microprobe show a 1:1 Pt:Pb ratio, at least within the error associated with EDX (± 5%). Figure 2.2 shows a representative spectrum from the series of samples synthesized at 135° C with 100% down to 10% excess reducing agent at a concentration of 5.0 mM. Pt $M_{\alpha 1}$ and Pb $M_{\alpha 1}$ peaks are clearly seen, and no signal is attributed to other elements than trace copper from the sample mount. Carbon and oxygen are always plentiful, and presumably are contributed to by organic side

products and metal oxide, but quantification is not possible given the carbon conductive tape used to fix the samples to the mount. Sodium is sometimes detected at the one atomic percent level, showing the degree to which the washing procedures are successful in removing sodium ions left from the reducing agent. This is in agreement with the results of Ghosh et al. [6], who also saw approximately one atomic percent sodium in PtPb nanoparticles reduced by sodium naphthalide. Samples from the present study synthesized with zero percent excess reducing agent show lead-rich regions on micron-sized length scales (Figure 2.3), owing to lead oxide phase separation which is seen in the X-ray diffraction pattern in Figure 2.1 (starred peaks). The evidence from XRD and EDX suggests that if zero percent excess reducing agent is used, the precursor or precursors do not become fully reduced, as the highly reactive reducing agent is likely partly oxidized by adventitious oxygen or water. This would lead to insufficient molar equivalents to reduce either Pt or Pb, though it is likely that the more electropositive metal is more susceptible to this phenomenon.

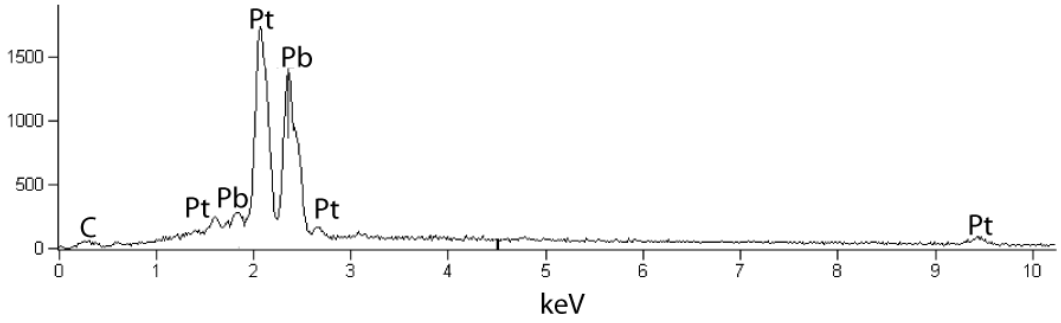

Figure 2.2 Energy-dispersive X-ray spectrum of PtPb. The Pt:Pb ratio is 52:48; the source of the shoulder in the Pb M_α peak at 2.34 keV is not known, but has been seen in other well-characerized PtPb samples [6].

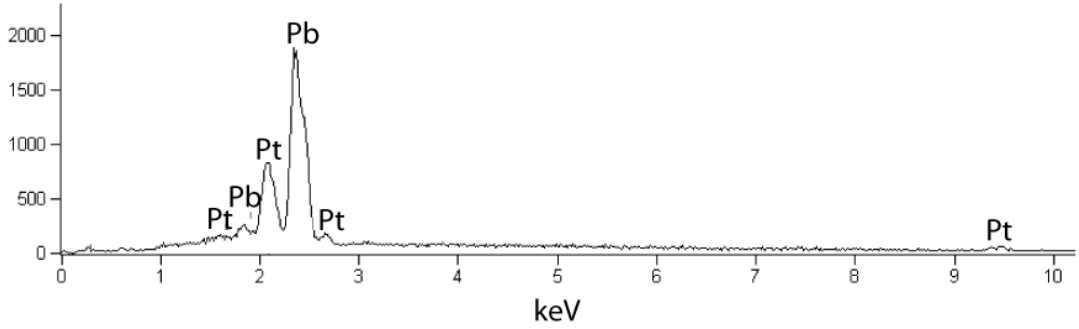

Figure 2.3 Energy-dispersive X-ray spectrum of PtPb where the Pt:Pb ratio was not 1:1. Here it was 30:69, presumably because PbO had phase separated from PtPb, and was the crystallite analyzed in this spectrum.

Varying the concentration of the solution also did not have the profound effect on the diffraction pattern as had been hypothesized in earlier work [13]. The patterns shown in Figure 2.4 show the end-points of a series of seven reactions that range from 3.3 mM to 16 mM with respect to metal precursors. They are nearly indistinguishable from each other, as are the ones in between these end points, and the calculated domain sizes for the patterns in Figure 2.4 are 24 ± 3nm for the high concentration sample and 25 ± 7nm for the low. Thermogravimetric analysis of each showed approximately the same percent weight loss (6.5% for the high-concentration sample, 8.5% for the low concentration one), so there is little evidence that the post-washing behavior of one sample contains more organic contaminants than the other. The concentrations studied here are not the highest or lowest achievable values, but they allow reasonable reaction volumes (10 to 100 mL, total) and masses of starting materials to be utilized.

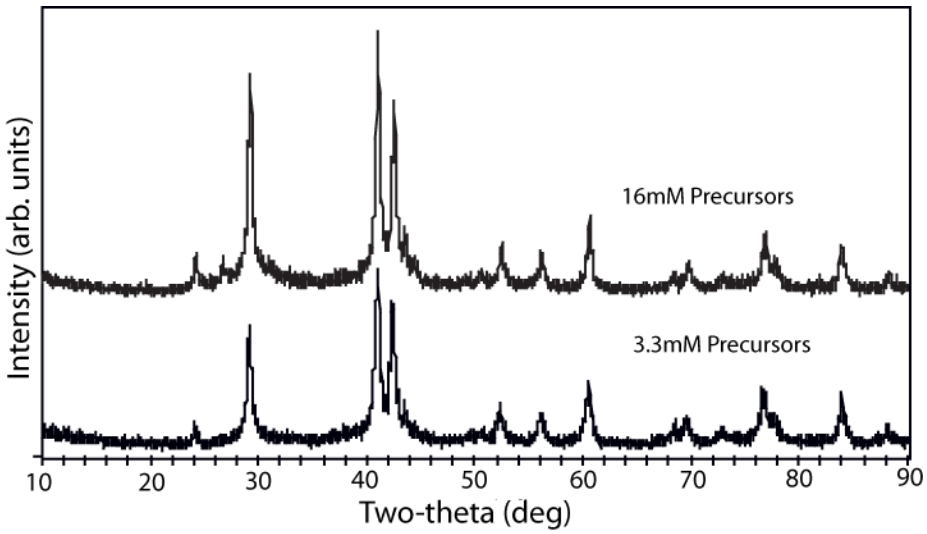

Figure 2.4 Powder X-ray diffraction pattern of two PtPb products synthesized at 135°C. The top pattern was 16mM with respect to each metal precursor after injection, and had a domain size of 24 nm, while the bottom was 3.3mM with 25 nm domains.

Since there were no drastic differences in XRD peak sharpness (the samples shown in Figure 2.4 were heated, so it should be of little surprise that sharp peaks appeared), the electrocatalytic activity would need to be sufficiently different for concentration-dependent behavior to be established. The BET-normalized formic acid oxidation current density at +0.2 V vs Ag/AgCl for the low-concentration preparation was 0.35 $mAcm^{-2}$ and was 0.56 $mAcm^{-2}$ for the high-concentration. These values are not too different from one another given the variability between synthesis parameters and possible errors in surface area measurements, and are at the low end of those reported for PtPb nanoparticles prepared by other methods [2, 7]. Those current densities for the concentration end points are about 2.5 times lower than those for samples injected in to 135°C diglyme at 5.0mM, the median concentration value, as had been reported earlier [2]. This conclusion calls into question the anecdotal

observations observed in past experiments; although some unpublished higher-concentration experiments in the past have shown enhanced electrocatalytic activity, it has not been reproducible in these systematic investigations. It would seem that the enhanced activity seen in one exciting sample was simply an example of the sample-to-sample variation found in preparing electrocatalyst nanoparticles.

2.3 In-Solution Hydrogen Treatments After Sodium Naphthalide Reduction

The aim of the next section of this chapter is to identify the source of the process that leads to the rapid change in crystallinity seen in X-ray diffraction pattern near a well-defined temperature. Does the extra thermal energy afforded by the higher-temperature reactions induce sufficient metal atom diffusion in the nucleated particle to make the intermetallic structure form? Or does the higher temperature give adsorbed species on the surface enough energy to be labile, thereby freeing surface sites to grow a larger crystallite of the intermetallic, rather than being blocked by the adsorbed molecular or anionic species?

A series of experiments were performed to test which one of these possibilities (metal mobility or ligand lability) was more likely influenced by temperature in this reaction. The reactions were performed at successively higher temperatures as before, but in these reactions, forming gas (6% hydrogen in nitrogen) was bubbled through the solution prior to heating. The original data of calculated domain size vs. preparation temperature from Alden et al. [1] were then compared to the new reactions. The hypothesis was that if unsaturated hydrocarbons were blocking surface sites and preventing crystallite growth, then treating with hydrogen should hydrogenate an appreciable amount of the alkenes, especially considering the abundant presence of colloidal platinum. In all likelihood it would only be (1,5) cyclooctadiene that will be hydrogenated at room temperature, not the aromatic naphthalene, due to relative

reaction rates for those processes under ambient conditions. Once (1,5) cyclooctadiene is reduced to cyclooctane, it would no longer have such a strong affinity for the neutral metal surface that the π-bonded alkene did, and would be more labile at considerably lower temperatures. There would then be a smaller proportion of blocked surface sites at room temperature, so the domain size should be larger at lower temperatures, and the diffraction pattern should undergo that relatively abrupt transition to larger domain sizes at lower temperatures [1].

2.3.1 Experimental

Dimethylplatinum (1,5) cyclooctadiene and lead (II) 2-ethylhexanoate were the metal precursors and were used as described in the previous section. To enable direct comparison to earlier experiments in the group, 50% excess reducing agent was used; as has already been shown, only the most extreme cases of varying the amount of excess seemed to matter, and 50% excess has been found to be a rather median amount (though in most chemistries it would be considered quite excessive). The reactions were carried out by injecting the precursors into the sodium naphthalide in diglyme solution at room temperature, stirring for ten minutes, then inserting a long needle attached to a 6% hydrogen supply line through the septum, the needle having already been purged with the gas. Forming gas (purchased from Airgas, and used instead of pure hydrogen for convenience and safety) was bubbled for thirty minutes while stirring the solution. An oil bath was heated to the desired reaction temperature during this time, and once the forming gas treatment ended, the needle was removed and the flask was immersed in the oil bath and stirred for ten minutes. The work-up of the product was identical to that described in the previous section, except that centrifugation was done at 7000 rpm for 10 min, which had been found to increase the amount of product collected.

2.3.2 Characterization

Powder X-ray characterization was performed primarily on a Scintag XDS 2000 X-ray diffractometer, and later on a Rigaku Ultima IV, both with Cu Kα radiation. Elemental analysis was done in a LEO-1550 field emission SEM (FESEM) at 20kV accelerating voltage. Transmission electron micrographs were taken on a Tecnai T12 transmission electron microscope with 200kV accelerating voltage. Particle surface area measurements were performed on a Micromeritics ASAP 2020 surface area analyzer, with krypton as the adsorptive. Thermogravimetric analysis was done on a TA Instruments Q50 thermogravimetric analyzer. Electrocatalytic analysis was performed by Dr. Futoshi Matsumoto, and consisted of preparation of a nanoparticle-Nafion ink in ethanol, and depositing and drying the ink on a 3mm diameter glassy carbon electrode at a loading of 70μg unsupported catalyst. Oxidation currents were measured while rotating the electrode at 2000rpm and at a potential sweep rate of $10mVs^{-1}$ from -0.2V to 0.2V vs. $Ag^{+}/AgCl$ in a solution of 0.1M H_2SO_4 and 0.5M formic acid.

2.3.3 Results and discussion

Ten reactions are compared in the powder X-ray diffraction patterns shown in Figure 2.5, and were performed at 25, 40, 80, 90, 95, 100, 105, 110, 130 and 162°C (diglyme reflux). The patterns can be separated into two regimes- ones that contain sharp diffraction peaks that are easily indexed to PtPb and those that have amorphous, featureless humps. As was the case in the reactions performed by Alden et al. [1], there is a sudden onset of crystalline diffraction peaks across a narrow (5°C) difference in temperature. However, where earlier results showed this transition to occur between 110°C and 115°C, these reactions with forming gas show the transition to occur between 95°C and 100°C (Figure 2.6). The reactions on both sides of the

transition temperature were performed in triplicate, and all consistently obey this observed phenomenon. This lowering of the temperature to achieve crystalline X-ray diffraction patterns follows the prediction which was outlined earlier, and is consistent with the view that adsorbed ligands are blocking the formation of the intermetallic at lower temperatures.

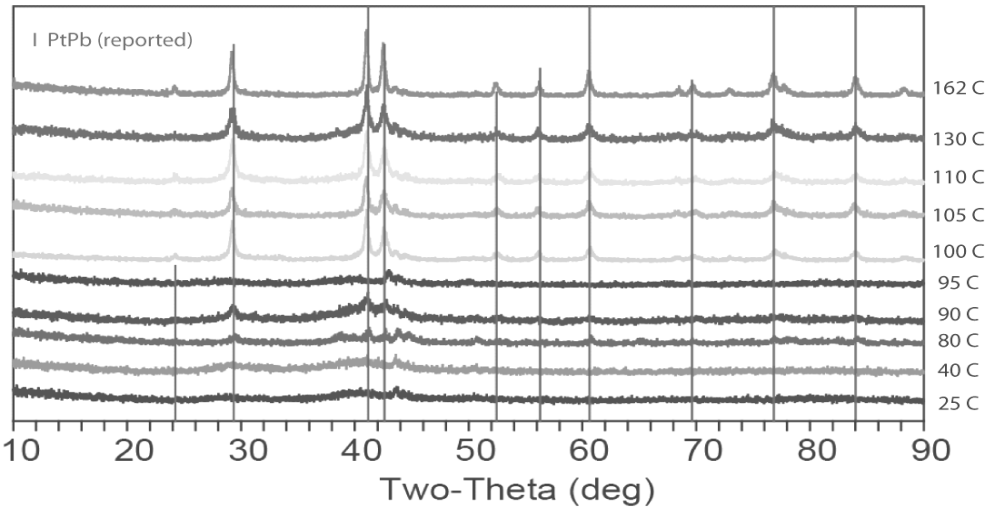

Figure 2.5 Powder X-ray diffraction patterns of PtPb nanoparticles treated with forming gas and heated in solution at the listed temperatures. Overlaid lines are the reported PtPb peaks.

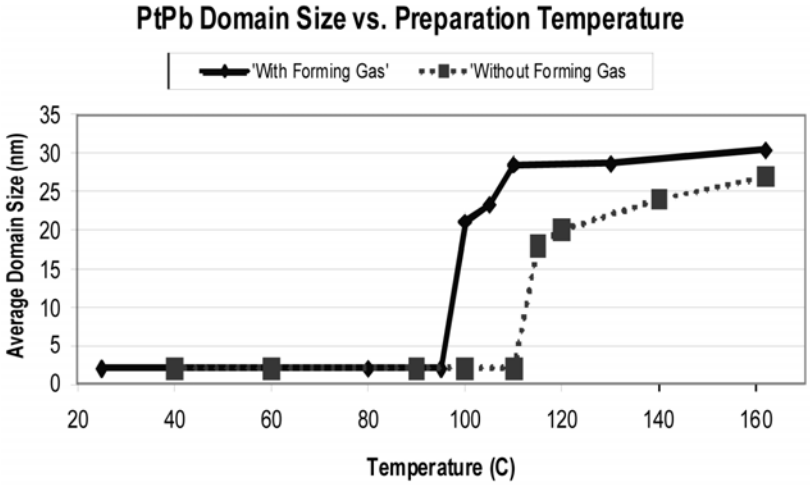

Figure 2.6 Crystallite domain sizes for the diffraction patterns shown in Figure 2.5 compared to similar products without forming gas treatment [1].

The chemisorption of unsaturated hydrocarbons onto Pt surfaces is a well-studied phenomenon, and although most of those studies were performed on single-crystal platinum, some analogies work here. Temperature programmed desorption experiments [28-30] show that most alkene molecules chemisorbed to a platinum surface will desorb at less than 300 K, as shown by a *ca.* 17 kcal·mol^{-1} activation energy [28] for desorption of butene from Pt(111). According to Campbell [31], The heat of adsorption scales roughly linearly with the number of sp^2 carbons per molecule, as each Pt-C σ bond perpendicular to the C-C σ bond of the adsorbed molecule contributes approximately 7 kcal mol^{-1}. This would imply 25-30 kcal·mol^{-1} for the heat of adsorption of (1,5)cyclooctadiene, and a very significant bond energy of around 70 kcal·mol^{-1} for adsorption of naphthalene [31], depending on coverage. The heats of adsorption tend to increase with metal defect density, but decrease in the presence of alloying metals such as Sn [28, 32] and in the presence of adatoms of alkali metals such as potassium [30]. All these factors contribute to the hypothesis that increasing the temperature of nanoparticle synthesis to approximately 375 K and above would be in the range for desorption of cyclooctadiene, but perhaps not for desorption of naphthalene.

It is conceivable that the mere act of forcing a gas through the reaction solution could affect the multitude of factors that govern nanoparticle formation in this system, so a control reaction was performed to test this hypothesis. The 100°C reaction was redone with bubbling argon instead of forming gas, which would eliminate the possibility of reacting with either the ligands or particles, yet would duplicate the physical agitation of bubbling forming gas. At 100° C, the forming gas-treated system showed sharp diffraction peaks; the absence of such peaks in the argon-treated reaction would further the claim that it is ligand hydrogenation that is responsible for the shift in transition temperature. As seen in the diffraction pattern in Figure 2.7, this

absence of sharp PtPb peaks is what was observed. Only broad X-ray scattering features are found, and the pattern cannot be indexed to PtPb. Another argon-treated sample heated at 115°C is also shown in Figure 2.7, and has sharp PtPb peaks as originally expected, showing that Ar acts as an unreactive gas and that it is the forming gas that causes the shift in the onset of crystallinity temperature. While these observations are not direct confirmation that the hydrogenation of (1,5) cyclooctadiene is occurring, all observations point to the likelihood of the proposed model. Studies by Miller, Lee, and Whitesides [33-38] show that under the conditions of these experiments (room temperature, ~0.1 atm hydrogen, aprotic solvent, and the presence of colloidal platinum) it is certainly possible to hydrogenate 1,5-cyclooctadiene to cyclooctane. Attempts were made to identify the side products of the reactions with GC/MS, but neither cyclooctane nor 1,5-cyclooctadiene were detected in solution, presumably due to the low concentration of these compounds.

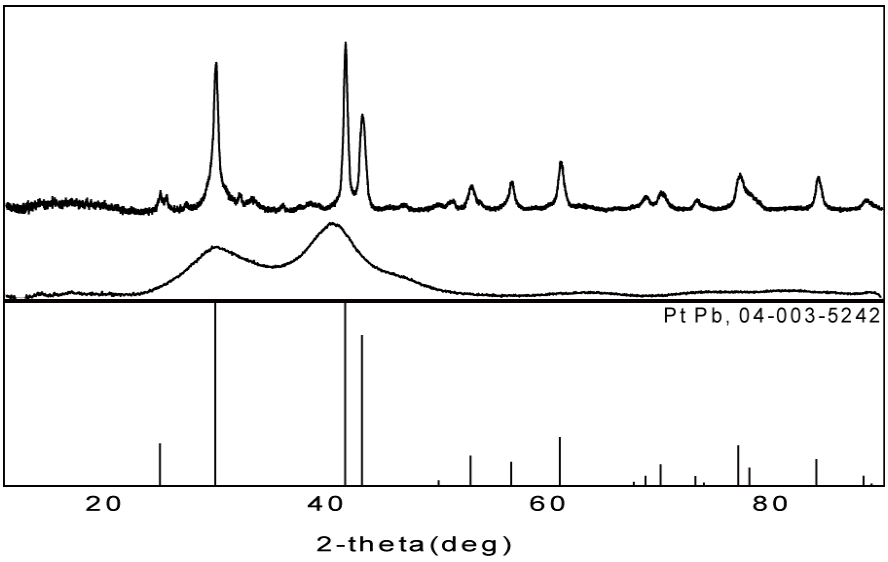

Figure 2.7 Powder X-ray diffraction patterns of PtPb products synthesized under identical conditions as Figures 2.5 and 2.6, but with argon treatment instead of forming gas. The top pattern was from a product heated to 115°C, while the bottom pattern was heated to 100°C.

Transmission electron micrographs of all nanoparticle samples show aggregated crystallites, and the crystallite sizes are consistently comparable to the domain size calculated from the powder X-ray diffraction patterns *via* the Debye-Scherrer equation. Figure 2.8 shows a large aggregation of 2-3nm particles. Since the sample shown was treated with forming gas but only heated to 80°C, its diffraction pattern showed only broad, diffuse peaks, corresponding to 2-3nm domain sizes and agreeing with TEM images.

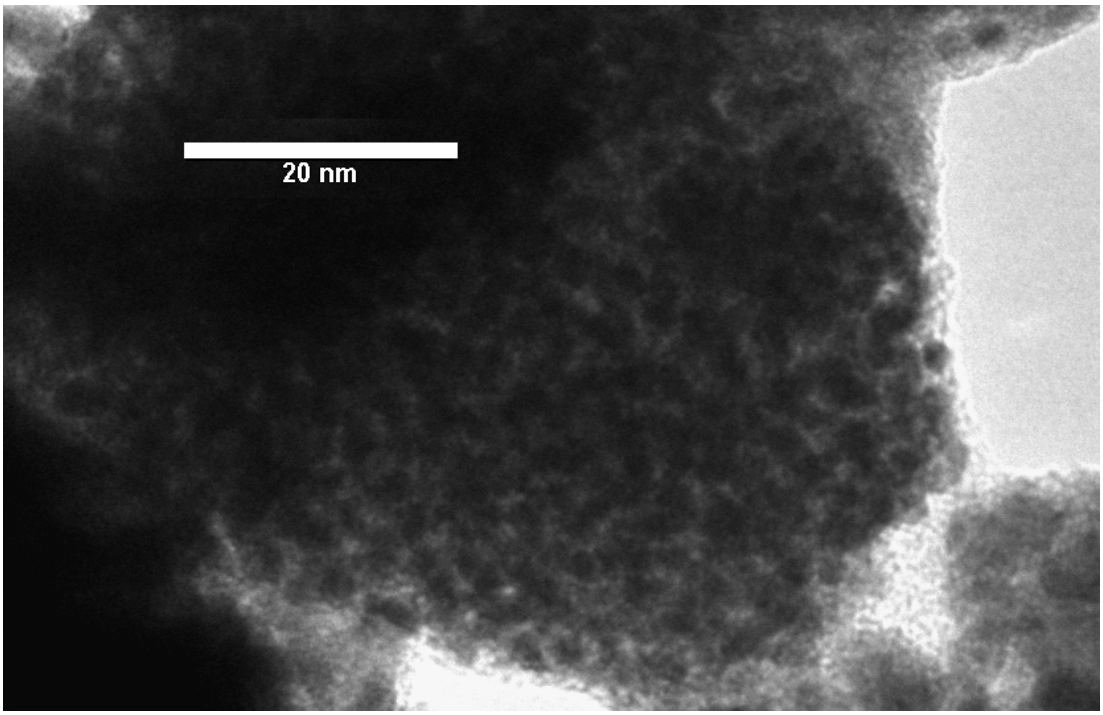

Figure 2.8 TEM of PtPb particles treated with forming gas and heated to 80°C during synthesis.

In contrast, Figure 2.9 shows a small collection of particles that are from a forming gas-treated sampled heated to 110° C; this was a sample that had passed that critical temperature threshold and had calculated domain sizes of 28.5 nm.

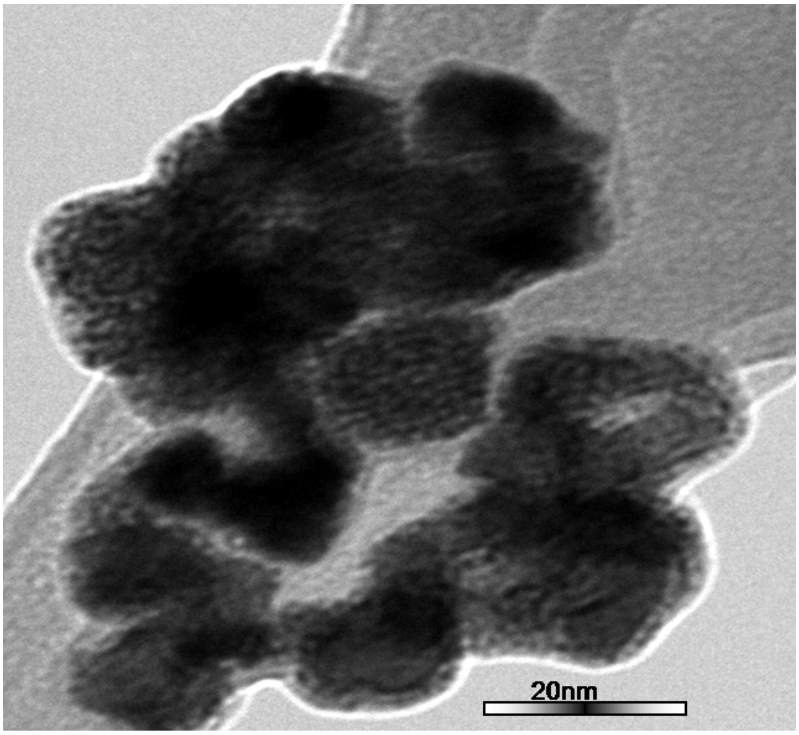

Figure 2.9 TEM of PtPb particles treated with forming gas and heated to 110°C during synthesis

The crystallite sizes shown through TEM are certainly on par with those calculated by the Scherrer equation. There are rarely any highly faceted crystals found in these nanoparticles, though it was relatively common to view lattice fringes in samples prepared at higher temperatures (Figure 2.10).

The elemental analysis for the forming-gas treated samples had mostly the same results as for the samples discussed earlier where concentration and excess reducing agent were altered. The Pt:Pb ratio was almost precisely 1:1 in all samples measured, and no other non-hydrocarbon (C or O) elements were detected other than sodium at around 1 at%. Since these analyses were performed on a plasma-cleaned GaAs wafer, the values for carbon content are more meaningful than for samples

measured on carbon tape. All samples measured for the forming gas-treated reactions showed high carbon content, usually in the vicinity of 30 at%. This indicates that organic ligands and spent reducing agent strongly adhere to the particles even after washing.

.

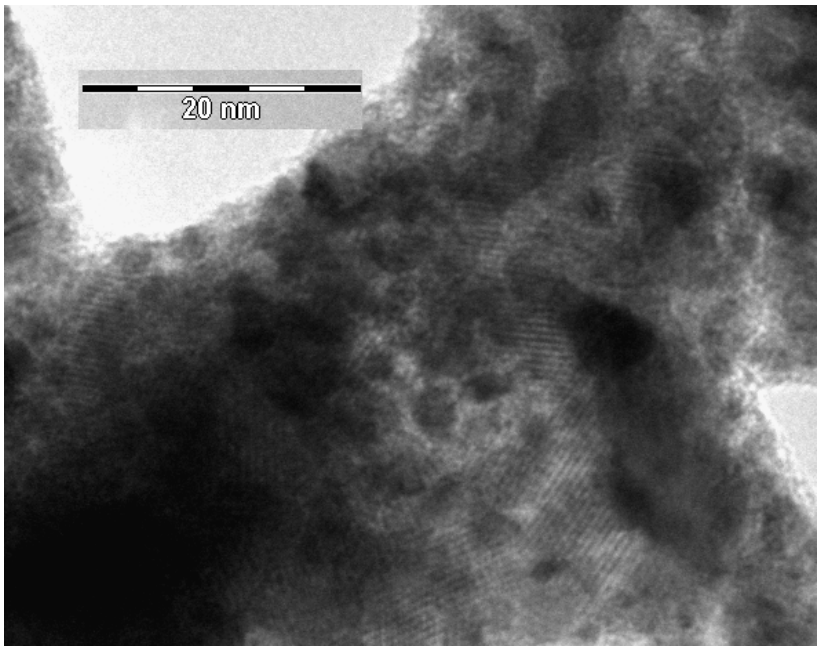

Figure 2.10 TEM of PtPb particles treated with forming gas and heated to 130°C during synthesis. Lattice fringes are visible in the particles aggregated near the center.

Thermogravimetric analysis (TGA) also confirms the high organic content of the PtPb particles. A representative TGA trace of the forming-gas treated samples is shown in Figure 2.11. Upon heating to 550°C under flowing argon, most samples undergo weight loss beginning at 150°C and achieve maximum weight loss around 350°C. All samples lost between 5-10% of their mass upon heating, which, assuming mass loss is all carbon, and an approximate average molar mass for PtPb of 200gmol^{-1}, would roughly correspond to one to two carbon atoms adhering to each "PtPb atom". This mass loss is consistent with that seen for other PtPb particles synthesized by

sodium naphthalide reduction [6], but is higher than the usual mass loss for particles synthesized through sodium borohydride reduction.

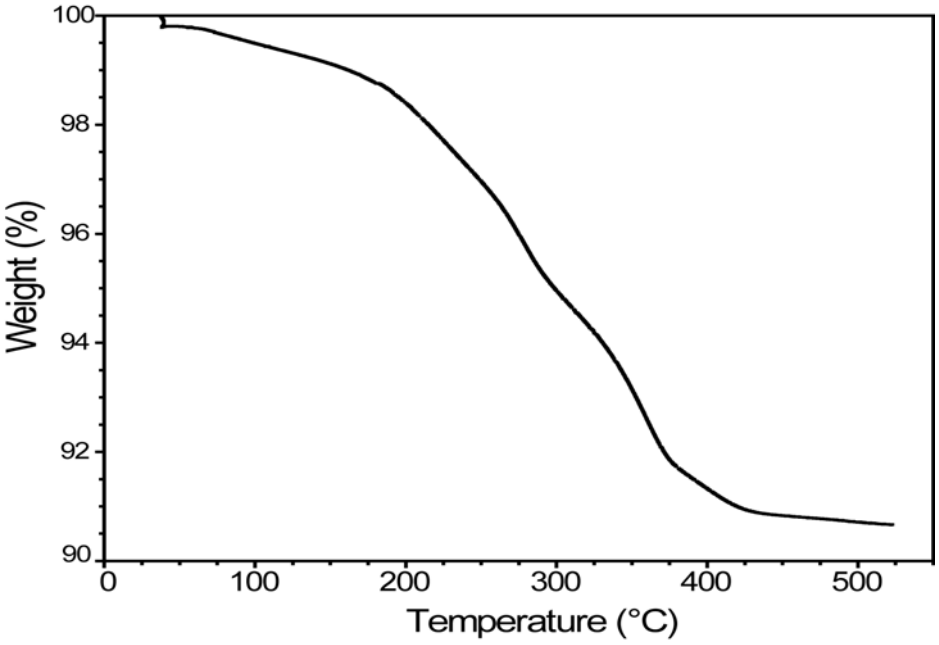

Figure 2.11 Representative weight loss of PtPb nanoparticles from forming gas samples upon heating under argon.

The BET surface area was measured for all samples treated with forming gas. These measurements allowed for conversion of all electrocatalysis assessments from mass activities (current per unit mass of catalyst) to current densities (current per unit catalyst surface area). Though BET physisorption values are inherently imprecise measurements, they roughly agree with the observation that high reaction temperatures (greater than approximately 100°C) lead to larger particles, in that lower specific surface areas are observed above the crystallinity transition temperature. A plot of those measurements is shown in Figure 2.12; note that any value above 15 m^2g^{-1} occurs below the transition temperature, and the experiments above the transition show reproducibly low specific surface areas (the forming-gas point at 130°C is

actually two data points directly on top of one another). If the products of reactions performed without forming gas are measured for specific surface area (triangular data points), they give higher values at higher temperatures. The average value of the BET coefficient, C, was 21.4 ± 2.1. Though this is not a tremendously high value for C (larger values, upwards of 100, indicate a stronger adsorptive-sample interaction, and more precise results), it is not so low as to cause concern over the validity of the measurements. If one assumes monodisperse spherical particles with a density of 15.69 g cm^{-3} for PtPb, 15 m^2g^{-1} specific surface area would correspond to 26 nm diameter particles, which is a reasonable value given TEM and X-ray diffraction analyses.

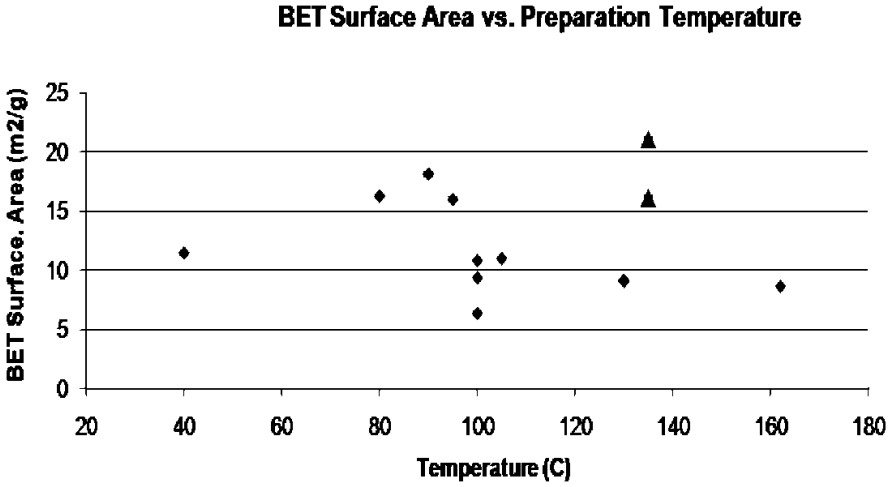

Figure 2.12 Brunauer-Emmett-Teller isotherm surface area of forming gas-treated and non-forming gas treated (two triangles) PtPb as a function of preparation temperature.

The forming gas-treated samples were tested for electrooxidation of formic acid; all samples showed catalytic activity, but not all to the same extent. The highest BET surface area-normalized current density at 0.2V vs. Ag/AgCl was 2.42 mA cm^{-2}, which corresponded to a sample refluxed in diglyme (162°C), and the lowest was 0.07 mA cm^{-2} for a sample heated at 40°C. Samples heated above the crystalline transition

temperature generally showed the highest current densities, though there were a few exceptions right around that temperature (95-100°C). The best electrocatalytic activity is found in samples heated well above 100°C, as all samples heated that high in this study and in previous work had current densities around 2 mA cm^{-2} [2].

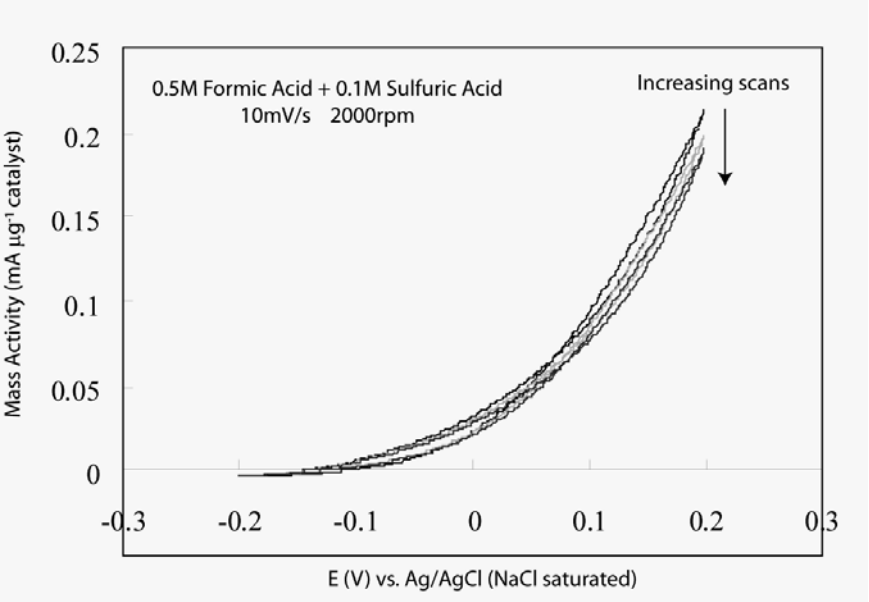

Figure 2.13 Formic acid polarization curves under experimental conditions listed.

As noted earlier in the chapter, these samples reduced by sodium naphthalide do not approach the activity of those made by sodium borohydride reduction of a platinum chloride precursor and Pb(2-[2-{2-methoxy}ethoxy]ethoxy) $acetate)_2$, which have been shown to have current densities of 5.5 $mAcm^{-2}$ at +0.2 V vs. Ag/AgCl [7]. This difference cannot just be attributed to use of sodium naphthalide as the reducing agent, as they also do not show as high a current density as samples prepared by NaNp reduction of $Pt(acac)_2$ instead of $Pt(COD)Me_2$ [6], which were shown to be as high as 5.95 $mAcm^{-2}$- the record for oxidation of formic acid on PtPb as of 2009. The high activity found by Ghosh et al. [6] also cannot be dismissed as merely a case of

unusually high surface area, as the mass activity (0.5 $mA\mu g^{-1}$) is also higher than for the PtPb particles shown here (0.2 $mA\mu g^{-1}$, Figure 2.13). The lower activities found in the current work indicate that the preparation methods used here do not yield the best end-product catalysts.

2.4 Other Mechanistic Clues: Attempted Characterization of Side Products

When considering the mechanism of the reduction of the lead and platinum precursors, a question of electron counting arises. It is easy to reconcile the 2-electron reduction of Pb(2-ethylhexanoate)$_2$ by two equivalents of sodium naphthalide: lead (II) is reduced to lead (0), the carboxylate groups dissociate and are charge-balanced by 2 Na^+, and naphthalide is oxidized to naphthalene. However, the electron counting conventions surrounding organometallic species like Pt(COD)Me_2 confuse the situation. This complex is formally Pt(II), with a neutral bidentate (1,5) cyclooctadiene ligand and two formally anionic CH_3^- methyl groups comprising its square planar coordination. The main unanswered question is the fate of the methyl groups. The very reactive CH_3^- species would not last long in solution, as 2-ethylhexanoate might when balanced by sodium, and although $NaCH_3$ is known to exist and has been characterized as a tetrahedral tetramer by single crystal X-ray diffraction [39], it is still unlikely that it would be a stable side product of the reduction of Pt(COD)Me_2.

A possible scenario which reconciles the dissociation of the two methyl groups would be the reductive elimination of ethane from the Pt center. This reaction from the current Pt complex would not be symmetry-allowed without first dissociating the cyclooctadiene [40], but since the exact mechanism of reduction by naphthalide is unknown in this case, elimination of ethane could still be a possible route. This would especially be true if the naphthalide ion acted as an inner-sphere electron transfer

agent, and actually associated to the complex in an associative-type ligand exchange reaction. Were that the case, the complex would go from PtL_2Me_2 to $PtL'Me_2$, and elimination of ethane could be allowed. Of course, the exact series of steps which would take Pt^{II} to Pt^0 is unknown.

An experiment was devised to determine whether or not ethane was being eliminated by the dimethyl platinum precursor. Since both room temperature reduction by sodium naphthalide in THF and straight injection into boiling diglyme each produce Pt nanoparticles from this precursor, both the classic thermal reductive elimination and the 2-electron chemical reduction route are possible. Instead of relying on clues inferred from different synthesis methods, an attempt was made to directly observe ethane being generated during the reaction.

2.4.1 Experimental

Dimethyl platinum (1,5) cyclooctadiene (0.1256 g, 0.37 mmol) and lead (II) 2-ethylhexanoate (7.4 mL of 0.0514 M solution in THF, 0.37mmol) were reduced by 1.5 equivalents sodium naphthalide at room temperature in a similar manner as described before. Note that the amount of precursors has been increased over those described earlier to provide a larger yield of ethane to sample, if that indeed is the by-product. A Hiden Analytical mass spectrometer with a flexible tube sampling arm ending in a needle was inserted through the septum of the flask to sample the headspace for volatile ethane. A mass spectrum was recorded for the reaction headspace before and shortly after injection of the precursors. In a second identical reaction, a program run was made to simultaneously detect the partial pressures of eight different m/z charged fragments as a function of time. The pressure range sampled was from 1×10^{-8} to 5×10^{-7} Torr, and the m/z fragment channels that were recorded were 15, 16, 29, 30, 31, 44, 58 and 59 amu. The background was established for the first 4min 41sec of

the experiment, and then the precursors were injected from 4:41-5:10. The experiment continued for another ten minutes, for an approximate detection time period of fifteen minutes. After concluding the volatile product detection experiment, the product was worked up as described earlier in this chapter.

2.4.2 Results and Discussion

The mass spectra for two spot-checks during the reaction are shown in Figure 2.14. The spectra show a multitude of peaks, both before and after the injection of the metal precursors, and due to the lack of chromatographic separation column found in conventional GC-MS, the peaks here correspond to all volatile species, not just one common analyte. It was therefore prudent to largely ignore the peaks that were present in both spectra, and rather focus either on peaks unique to the "after" spectrum, or on ones whose relative intensities had significantly changed. The most intense peaks in each spectrum were found at 40 and 20 amu; they corresponded to Ar^{+} and Ar^{2+}, and are of no interest. The areas of the spectrum that show the most change are 14-20, 25-35, 40-45, and 55-60 amu. The most compelling region for evidence of ethane generation is the 25-35amu region, where the literature spectrum [41] shows the 30, 29, and 28 amu peaks have relative intensities of 100, 76.2, and 388.5, respectively. The intensities of all three of those peaks increase in the spectrum in Figure 2.14, but the relative intensities to each other do not satisfactorily match the literature values. The observed peak for m/z = 29amu is the most intense of the three, where the literature shows it should be the least intense. As observed above, it is not known whether the peak intensities do not match those of ethane due to ethane not being a product, or due to other volatile species adding to the intensities of peaks which are partially due to ethane. Gas chromatography would easily handle this separation, but was not attempted due to the impractical nature of such an experiment.

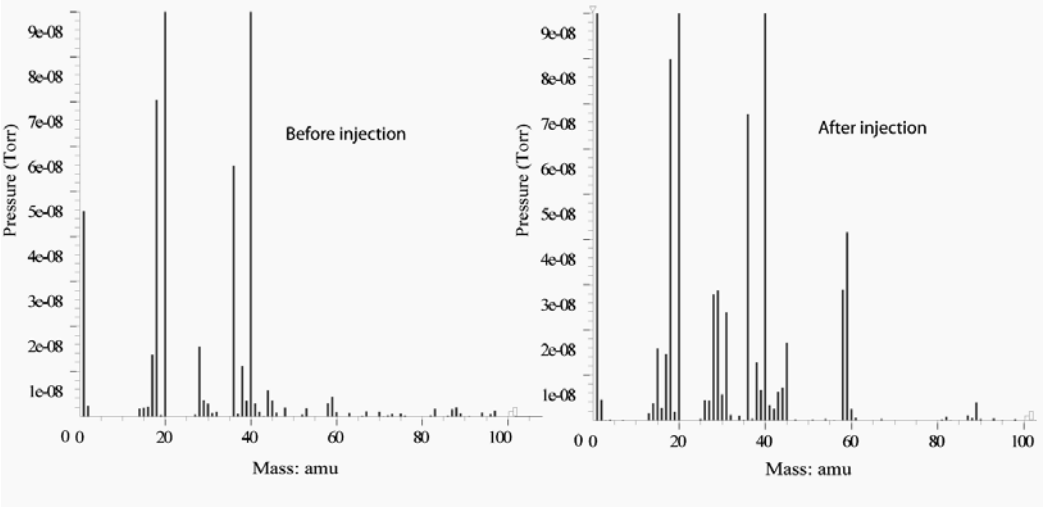

Figure 2.14 Mass spectrum of headspace gas of room temperature reaction of Pt(COD)Me_2 and Pb(ethex)2 with NaNp.

In order to obtain a qualitative view of the mass spectrum before and after injection, the timed MS experiment mentioned earlier was attempted, the results of which are shown in Figure 2.15. The recorded mass traces were chosen for their likelihood of being part of the mass spectrum for ethane. M/z = 30 would correspond to $C_2H_6^+$, 29 would be for $C_2H_5^+$, 15 would be for CH_3^+, and 44, 58, and 59 were chosen to track unidentified yet intense peaks from the mass spectrum in Figure 2.14. There is a simultaneous increase in the traces for 15, 16, and 29 amu shortly after the precursors are injected, and a very slight increase in the traces for 31 and 44 amu. The increase in fragments of m/z = 15 and 29 are possible indicators of ethane evolution, corresponding to the fragments noted before. However, there is a lack of evidence for the parent ion $C_2H_6^+$ at 30 amu, as this trace stays constant throughout the experiment. While the presence of increased intensities of m/z = 29 and 15 are evidence of ethane generation, the results are not conclusive enough to claim the mechanism proceeds by reductive elimination of ethane. Further study would be necessary to completely

characterize the complicated reduction mechanism of the Pt precursor in this chapter, and it is unclear what effect the results of those studies would have on future PtPb nanoparticle synthesis. Instead, it was decided that the validity of the co-reduction hypothesis and the timeframe of reduction would be a better avenue of study, as will be covered in Chapter 3.

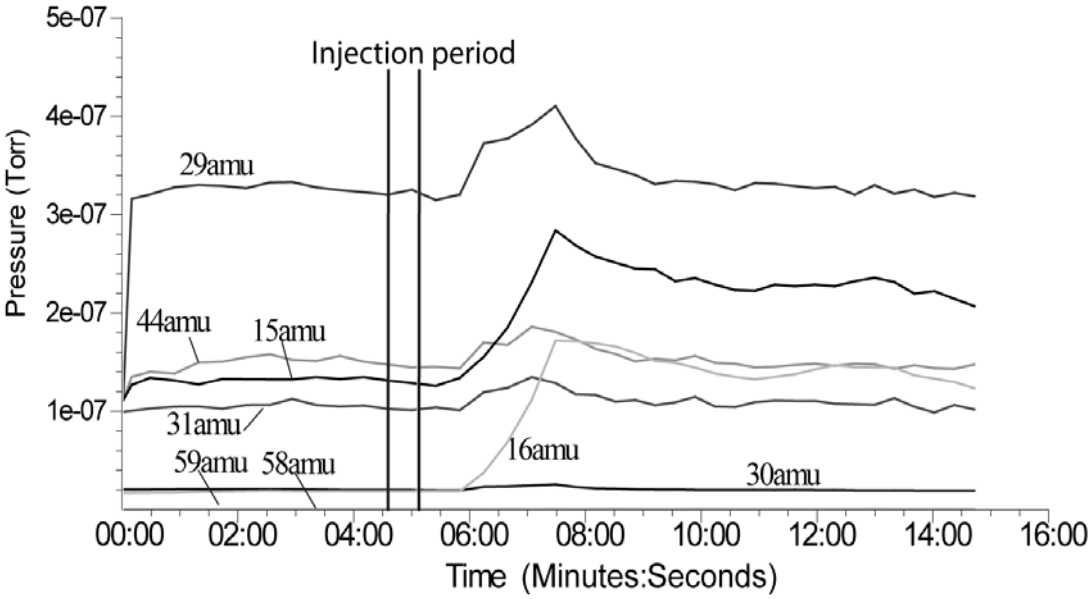

Figure 2.15 Timed mass spectrum traces of the headspace of a room temperature NaNp reduction of $Pt(COD)ME_2$ and $Pb(2\text{-ethylhexanoate})_2$ in THF. The traces for 58 and 59 amu remained at 0 Torr for the duration of the experiment.

At this point a tentative model of the composite mechanistic steps of the co-reduction of multiple metal precursors, and all the species in solution that might affect the reaction, is introduced. This model reflects only one possible mechanism of the most generalized form of the reaction, and there is no direct evidence of the intermediate steps between reactants and products. The only compelling evidence of a co-reduction of metal precursors is the fact that a homogeneous bi-metallic product is

formed; all other steps are pure conjecture, and any number of mechanisms can be described which would satisfy the data presented up to this point.

In a co-reduction mechanism such as in Figure 2.16, two metal precursors, written generically as M and M', are present in a chosen ratio (a to b) and bear a given collection of ligands (X if charged, L if neutral donor ligand). The precursors are treated with enough equivalents of sodium naphthalide to completely reduce the sum of the formal oxidation states in the precursors to zero, with some excess to account for side reactions with impurities that remove some of the reducing agent. After any reduction takes place, the reduced metal atoms would not be bare, but rather would still be coordinated by solvent, and likely by precursor ligands or anions. These complexes would have a negative charge in solution if anions are present, a charge that would lead to an electrostatic barrier that would slow the rate of metal-metal bond formation and the nucleation of a crystalline phase. If the ligands or anions are labile, then the reaction could proceed at some appreciable rate. The possible timeframe for those dissociations will be covered in Chapter 3 of this dissertation. Once ligand dissociation has occurred, the reduced metal centers would undergo a very rapid nucleation to form a metal particle, and due to the identity of those metals and their associated solid-state thermodynamics, they could form the alloy or intermetallic compound, hopefully in the ratio designated by the amount of reactants present in the beginning. At this time, one must certainly keep in mind the potential participation of all other species in solution- namely the oxidized reducing agent (naphthalene) and dissociated ligands (often unsaturated hydrocarbons- which will likely have an affinity for the reduced metal surfaces as mentioned in section 2.2.3). The last step would be the growth of the nucleated metal particles. The final two steps are the ones most likely to be influenced by the solvent temperature in the experiments mentioned

earlier, where either the nucleation or the growth of the particle is likely a thermally activated process.

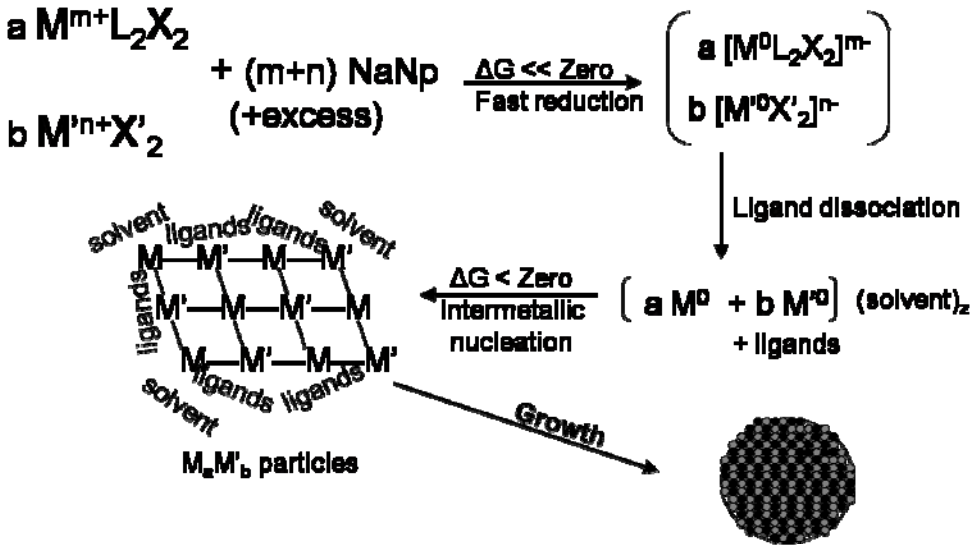

Figure 2.16 Idealized representation of the hypothetical order of reaction steps to form binary intermetallic nanoparticles.

If both metal precursors get reduced at the same rate, then this mechanism could be viable. However, the odds of that happening are miniscule. As pointed out earlier, the only metric at this point for the reaction rate is the visual cue of reduction, which appears to be over in about a second. All this says is that the overall rate constant is greater than 1 s^{-1}: hardly an indicator of a borderline-instantaneous reduction. To judge how close it may be to a diffusion-limited reduction (which would be a full eight orders of magnitude more rapid than can be observed by eye), electrochemical experiments were performed, and are presented in the next chapter.

A more complex and more chemically viable mechanism could even circumvent the proposed co-reduction altogether. Cyclic voltammetry (see Chapter 3) shows that the organoplatinum precursors of interest in this and other [6] work ($Pt(COD)Me_2$ and $Pt(acac)_2$, respectively) have extremely negative reduction

potentials in excess of -3V vs. NHE. This is beyond the reducing power of sodium naphthalide, which would preclude the possibility of a co-reduction. The naphthalide anion would have to decompose $Pt(COD)Me_2$ in a chemical reaction to form Pt nanoparticles, and would not be acting as an innocent outer-sphere electron transfer agent. In this case, the "reduction" of just $Pt(COD)Me_2$ would have to be an associative-type ligand substitution reaction, possibly coupled with an autocatalytic reduction of Pt^{II} by as-formed Pt^0 (the work of Finney and Finke [42-45] can be consulted for exampled of autocatalytic Pt nanoparticle formation mechanisms). Alternatively, cyclic voltammogram measurements of the lead precursor used in this chapter show that it should easily be reduced by sodium naphthalide to form colloidal lead and sodium 2-ethylhexanoate. This colloidal lead, in the presence of sodium naphthalide, could participate in an autocatalytic decomposition of the Pt precursor, which would reconcile the extreme negative reduction potential of the Pt precursor with the fact that 1:1 PtPb is formed in this reaction. These suggested mechanisms are just a sampling of what could actually be occurring during this reaction, and it is unlikely that further study would greatly affect the manner in which PtPb would be synthesized.

2.5 Commentary on the Aging of PtPb Nanoparticles in Air

There have been numerous occasions in the group where the long-term stability of PtPb nanoparticles has been a matter of interest. As some of the samples under study in this chapter were prepared as early as 2006, there was opportunity to study the effects of three years of air exposure. Of course, this section has no relation to the aging process the catalyst would undergo in a working fuel cell, where the deleterious effects of an acidic environment and possibly hundreds of voltage cycles would alter the composition of the nanocrystal. It merely serves as a reference for

researchers to estimate how the structure and electrocatalytic activity of PtPb might change over time.

Figure 2.17 shows the powder X-ray diffraction pattern for a sample discussed earlier in this chapter, where the total reactant concentration of the metal precursors was 16 mM. The original diffraction pattern (inset) was nearly phase pure PtPb, with only the small peak at 27° 2-theta and the sample holder peaks at 44° not corresponding to the PtPb structure. That is in striking contrast to the other, newer pattern shown in the main window of Figure 2.17, which barely resembles PtPb at all. It is best indexed to $Pb_{10}(CO_3)_6(OH)_6O$ (PDF # 00-019-0680), along with several unidentified low intensity peaks. It is suspected that the product has reacted with oxygen, water vapor, and carbon dioxide to form the oxide, hydroxide, and carbonate, respectively. Curiously enough, there is no clear platinum phase found in the pattern, even though it would be expected that Pt would be unreactive towards oxygen, water and carbon species. The platinum in the sample has likely phase separated into sub-nanometer domains that are too small to be detected by powder X-ray diffraction. Even without identifying all the phases present in the aged sample, it is clear that a high degree of oxidation has occurred over three years. The electrocatalytic activity of the same sample for formic acid oxidation did decrease, but actually did not deteriorate to zero. The mass activity at +0.2 V vs. Ag/AgCl only dropped about 25%, from 0.056 mA μg^{-1} to 0.041 mA μg^{-1}. The lead carbonate hydroxide oxide phase identified by XRD is not known to be a formic acid electrocatalyst, but since the fate of the platinum is unknown, there could be ~2 nm domains of PtPb remaining which are catalytically active yet unseen in the X-ray pattern. Elemental analysis would be needed to determine the scale of phase separation and the location of the platinum.

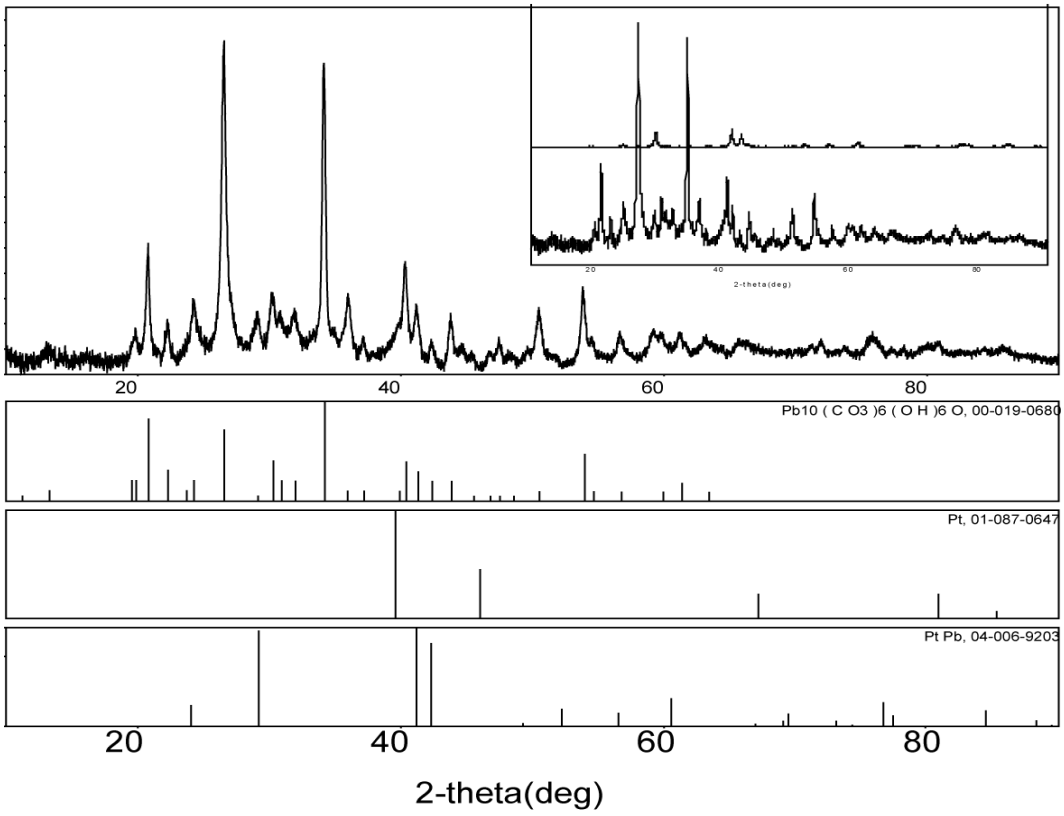

Figure 2.17 Powder X-ray diffraction pattern for PtPb sample which aged three years in air in a closed vial. Inset shows original (upper) pattern with PtPb structure, and lower pattern is duplicated in the main window. Peaks index mostly to $Pb_{10}(CO_3)_6(OH)_6O$. Pt and PtPb peaks are shown to provide reference.

While this comparison is only one example of what can occur when nanocatalysts are left exposed to air, it does bring to light the effects the ambient environment can have on samples left in lab. All characterization should be performed swiftly, instead of trusting in the relative stability of a mostly noble metal solid product like PtPb.

REFERENCES

1. Alden, L.R., et al., *Intermetallic PtPb nanoparticles prepared by sodium naphthalide reduction of metal-organic precursors: Electrocatalytic oxidation of formic acid.* Chemistry of Materials, 2006. **18**(23): p. 5591-5596.
2. Alden, L.R., et al., *Synthesis, characterization, and electrocatalytic activity of PtPb nanoparticles prepared by two synthetic approaches.* Langmuir, 2006. **22**(25): p. 10465-10471.
3. Blasini, D.R., et al., *Surface composition of ordered intermetallic compounds PtBi and PtPb.* Surface Science, 2006. **600**(13): p. 2670-2680.
4. Casado-Rivera, E., et al., *Electrocatalytic oxidation of formic acid at an ordered intermetallic PtBi surface.* Chemphyschem, 2003. **4**(2): p. 193-199.
5. Casado-Rivera, E., et al., *Electrocatalytic activity of ordered intermetallic phases for fuel cell applications.* Journal of the American Chemical Society, 2004. **126**(12): p. 4043-4049.
6. Ghosh, T., et al., *PtPb nanoparticle electrocatalysts: control of activity through synthetic methods.* Journal of Nanoparticle Research, 2009. **11**(4): p. 965-980.
7. Matsumoto, F., et al., *Electrocatalytic activity of ordered intermetallic PtPb nanoparticles prepared by borohydride reduction toward formic acid oxidation.* Journal of the Electrochemical Society, 2008. **155**(2): p. B148-B154.
8. Ranjan, C., et al., *Electronic effects in CO chemisorption on PtPb intermetallic surfaces: a theoretical study.* Journal of Physical Chemistry C, 2007. **111**(46): p. 17357-17369.

9. Roychowdhury, C., et al., *Synthesis, characterization, and electrocatalytic activity of PtBi nanoparticles prepared by the polyol process.* Chemistry of Materials, 2005. **17**(23): p. 5871-5876.

10. Roychowdhury, C., et al., *Synthesis, characterization, and electrocatalytic activity of PtBi and PtPb nanoparticles prepared by borohydride reduction in methanol.* Chemistry of Materials, 2006. **18**(14): p. 3365-3372.

11. Volpe, D., et al., *Surface treatment effects on the electrocatalytic activity and characterization of intermetallic phases.* Journal of the Electrochemical Society, 2004. **151**(7): p. A971-A977.

12. Wang, H.S., et al., *Electrocatalytic mechanism and kinetics of SOMs oxidation on ordered PtPb and PtBi intermetallic compounds: DEMS and FTIRS study.* Physical Chemistry Chemical Physics, 2008. **10**(25): p. 3739-3751.

13. Alden, L.R., *Synthesis of Platinum Intermetallic Compounds for Fuel Cell Anode Catalysts*, in *Department of Chemistry and Chemical Biology*. 2006, Cornell University: Ithaca NY. p. 169.

14. Connelly, N.G. and W.E. Geiger, *Chemical redox agents for organometallic chemistry.* Chemical Reviews, 1996. **96**(2): p. 877-910.

15. Scott, N.D., J.F. Walker, and V.L. Hansley, *Sodium naphthalene I A new method for the preparation of addition compounds of alkali metals and polycyclic aromatic hydrocarbons.* Journal of the American Chemical Society, 1936. **58**: p. 2442-2444.

16. Zandstra, P.J. and S.I. Weissman, *Effects of Ion Association on Rates of Oxidation-Reduction Transfer Reactions in Naphthalene-Naphthalenide Systems.* Journal of the American Chemical Society, 1962. **84**(23): p. 4408-&.

17. Closson, W.D., P. Wriede, and S. Bank, *Reductive Cleavage of Toluenesulfonates with Sodium Naphthalene1.* Journal of the American Chemical Society, 1966. **88**(7): p. 1581-1583.

18. Abe, H., et al., *Electrocatalytic performance of fuel oxidation by Pt3Ti nanoparticles.* Journal of the American Chemical Society, 2008. **130**(16): p. 5452-5458.

19. Chi, K.M., et al., *Highly Reduced Organometallics .20. The 1st General Synthetic Route to Zerovalent Titanium Carbonyls - Synthesis and Properties of TI(CO)5(ME2PCH2CH2PME2).* Journal of the American Chemical Society, 1988. **110**(1): p. 163-171.

20. Chu, T.L. and J.V. Friel, *Reducing Action of Sodium Naphthalide in Tetrahydrofuran Solution .1. the Reduction of Cobalt(Ii) Chloride.* Journal of the American Chemical Society, 1955. **77**(22): p. 5838-5840.

21. Blackburn, D.W., et al., *[TI(CO)4(CH3C(CH2PME2)3)], [ZR(CO)4[CH3C(CH2PME2)3]], [HF(CO)4[C43C(CH2PME2)3]] Complexes of Zerovalent Titanium, Zirconium, and Hafnium. 1st Structural Characterization of a Zr0-Carbonyl Complex.* Angewandte Chemie-International Edition in English, 1988. **27**(3): p. 437-438.

22. Chiu, H.W., C.N. Chervin, and S.M. Kauzlarich, *Phase changes in Ge nanoparticles.* Chemistry of Materials, 2005. **17**(19): p. 4858-4864.

23. Chiu, H.W. and S.M. Kauzlarich, *Investigation of reaction conditions for optimal germanium nanoparticle production by a simple reduction route.* Chemistry of Materials, 2006. **18**(4): p. 1023-1028.

24. Baldwin, R.K., et al., *Solution reduction synthesis of surface stabilized silicon nanoparticles.* Chemical Communications, 2002(17): p. 1822-1823.

25. Zou, J., et al., *Size and spectroscopy of silicon nanoparticles prepared via reduction of SiCl4.* Journal of Cluster Science, 2006. **17**(4): p. 565-578.

26. Mathias, M., et al., *Can available membranes and catalysts meet automotive PEFC requirements?* Abstracts of Papers of the American Chemical Society, 2004. **228**: p. 002-FUEL.

27. Shevchenko, E.V., et al., *Study of nucleation and growth in the organometallic synthesis of magnetic alloy nanocrystals: The role of nucleation rate in size control of CoPt3 nanocrystals.* Journal of the American Chemical Society, 2003. **125**(30): p. 9090-9101.

28. Tsai, Y.L. and B.E. Koel, *Temperature-programmed desorption investigation of the adsorption and reaction of butene isomers on Pt(111) and ordered Pt-Sn surface alloys.* Journal of Physical Chemistry B, 1997. **101**(15): p. 2895-2906.

29. Salmeron, M. and G.A. Somorjai, *Desorption, decomposition, and deuterium exchange reactions of unsaturated hydrocarbons (ethylene, acetylene, propylene, and butenes) on the platinum(111) crystal face.* The Journal of Physical Chemistry, 1982. **86**(3): p. 341-350.

30. Windham, R.G. and B.E. Koel, *Coadsorption of Ethylene and Potassium on Pt(111). 2. Influence of Potassium on the Decomposition of Ethylene.* Journal of Physical Chemistry, 1990. **94**(4): p. 1489-1496.

31. Gottfried, J.M., et al., *Heat of adsorption of naphthalene on Pt(111) measured by adsorption calorimetry.* Journal of Physical Chemistry B, 2006. **110**(35): p. 17539-17545.

32. Tsai, Y.L., C. Xu, and B.E. Koel, *Chemisorption of ethylene, propylene and isobutylene on ordered Sn/Pt(111) surface alloys.* Surface Science, 1997. **385**(1): p. 37-59.

33. Lee, T.R. and G.M. Whitesides, *Heterogeneous Reductions of (Diolefin)Dialkylplatinum(II) Complexes on Platinum Black in Ethyl-Alcohol - Kinetics, Isotopic Interchange of Hydrogen Between Coadsorbed Surface Alkyls, and Comparison of Surface Alkyls Generated from the Platinum Complexes and from Olefins.* Journal of the American Chemical Society, 1991. **113**(7): p. 2576-2585.

34. Lee, T.R. and G.M. Whitesides, *The Extent of Incorporation of Excess Deuterium in the Platinum-Catalyzed Reduction of Unsubstituted Cycloolefins by H-2 in D2O/THF Increases with the Strain-Energy of the Product of Cycloalkanes.* Journal of the American Chemical Society, 1991. **113**(1): p. 369-370.

35. Lee, T.R. and G.M. Whitesides, *Heterogeneous, Platinum-Catalyzed Hydrogenations of (Diolefin)Dialkylplatinum(II) Complexes.* Accounts of Chemical Research, 1992. **25**(6): p. 266-272.

36. Miller, T.M., et al., *Heterogeneous, Platinum-Catalyzed Hydrogenation of (Diolefin)Dialkylplatinum(II) Complexes - Kinetics.* Journal of the American Chemical Society, 1988. **110**(10): p. 3146-3156.

37. Miller, T.M., T.J. McCarthy, and G.M. Whitesides, *Deuterium-Labeling Experiments Relevant to the Mechanism of Platinum-Catalyzed Hydrogenation of (Diolefin)Dialkylplatinum(II) Complexes - Evidence for Isotopic Exchange via Platinum Surface Hydrogen - The Sterochemistry of Reduction.* Journal of the American Chemical Society, 1988. **110**(10): p. 3156-3163.

38. Miller, T.M. and G.M. Whitesides, *Isotopic Exchange-Reactions Occurring in the Hydrogenation of (1,5-Cyclooctadiene)Dialkylplatinum(II) Complexes Over Platinum Black.* Journal of the American Chemical Society, 1988. **110**(10): p. 3164-3170.

39. Cotton, F.A., Geoffrey Wilkinson, Carlos Murillo, and Manfred Bochmann, *Advanced Inorganic Chemistry*. 6th ed. 1999: Wiley. 1376.

40. Kazuyuki Tatsumi, R.H., Akio Yamamoto, and John K. Stille, *Reductive Elimination of d^8-Organotransition Metal Complexes.* Bulletin of the Chemical Society of Japan, 1981. **54**: p. 1857-1867.

41. Amenomiy.Y and R.F. Pottie, *Mass Spectra of Some Deuterated Ethanes .I. Effect of Ionizing Voltage.* Canadian Journal of Chemistry, 1968. **46**(10): p. 1735-&.

42. Watzky, M.A., E.E. Finney, and R.G. Finke, *Transition-metal nanocluster size vs formation time and the catalytically effective nucleus number: A mechanism-based treatment.* Journal of the American Chemical Society, 2008. **130**(36): p. 11959-11969.

43. Finney, E.E. and R.G. Finke, *The four-step, double-autocatalytic mechanism for transition-metal nanocluster nucleation, growth, and then agglomeration: Metal, ligand, concentration, temperature, and solvent dependency studies.* Chemistry of Materials, 2008. **20**(5): p. 1956-1970.

44. Finney, E.E. and R.G. Finke, *Nanocluster nucleation and growth kinetic and mechanistic studies: A review emphasizing transition-metal nanoclusters.* Journal of Colloid and Interface Science, 2008. **317**(2): p. 351-374.

45. Finney, E.E. and R.G. Finke, *Is it homogeneous Pt(II) or heterogeneous Pt(0)(n) catalysis? Evidence that Pt(1,5-COD)Cl-2 and Pt(1.5-COD)(CH3)(2) plus H-2 form heterogeneous, nanocluster plus bulk-metal Pt(0) hydrogenation catalysts.* Inorganica Chimica Acta, 2006. **359**(9): p. 2879-2887.

CHAPTER 3

Electroanalytical Studies of Metal Precursor Reduction

3.1 Introduction

In the previous chapter, the rationale for the selection of precursors, reducing agent and solvent was discussed. It was hypothesized that a strong reducing agent is needed to simultaneously co-reduce two different metal precursors. Under those conditions, it is expected that any precursor thermodynamically capable of being reduced by that agent will be reduced as soon as it encounters it in solution, independent of particular precursor features, such as the identity of ligands. Agents such as sodium naphthalide, n-butyllithium and even sodium borohydrides (including trialkylborohydrides) all have standard reduction potentials in excess of -0.6 Vvs. NHE, and have been shown to successfully reduce multiple metal precursors during the synthesis of nanoparticles. Since synthetic methods outlined in this dissertation depend on the validity of this hypothesis, it is desirable to elucidate some of the kinetic and thermodynamic factors governing the reduction of a metal precursor to a neutral metal atom by a strong reducing agent. Well-known electrochemical methods exist for measuring electron transfer and ligand dissociation rates, but these have rarely been utilized in non-aqueous media, and certainly not for the solvents and precursors of interest in these syntheses. To get a better understanding of the reduction potentials and the rates of reduction or decomposition of relevant precursors in THF, cyclic voltammograms and electroanalytical kinetic experiments were performed.

Well-established single- and double-potential step chronoamperometry techniques were used to derive kinetic information regarding the reduction process of metal-organic platinum and lead precursors, and the dissociations of their respective

ligands. While it is shown that under these conditions the two precursors undergo ligand dissociation and deposition on the electrode at similar rates (but nowhere near diffusion-limited rates), the aim is to begin a dialogue on a more complete understanding of the reduction processes of technologically relevant precursors. Rather than performing an exhaustive evaluation of all possible interesting metal precursors, the use of two related electrochemical techniques and their subsequent analyses is highlighted to provide a contrast of methods when their uses are appropriate. Each section will provide a small introduction to the technique, followed by the results and discussions for each.

3.2 Single Potential Step Chronoamperometry

One electroanalytical method of measuring the reduction of a metal complex is single-step chronoamperometry (SSCA), where a potential is applied and held and the current recorded as a function of time. Depending on the metal precursor, the applied potential and the electrode, it is common for the metal to reduce from M^{x+} to M^0, shed its ligands, and nucleate an adatom on the electrode surface. The applied potential is a parameter that influences and/or controls rates, and a compelling reason to use electrochemical methods over, for example, gas-phase spectroscopies [1]. Single potential step chronoamperometry was used because of the obvious parallels electrochemical nucleation under a constant potential has with the chemical reduction of a metal precursor to form a neutral metal atom or nanoparticle. These experiments would operate in the regime of overpotential deposition, so as to most closely resemble the highly negative potential of the strong reducing agents we use experimentally.

It must be noted that the differences between chemical and electrochemical reduction and nucleation are significant, and should not be dismissed lightly. One of

the more obvious points of difference is that chemical reduction takes place between two species in solution, where both oxidant and reductant are free to move and collide with each other, while electroreduction occurs between a solvated species and an electrode surface. Marcus points out [2-4] that the analogous values for chemical and electrochemical rate constants are related on a collision frequency basis, where the homogeneous and heterogeneous collision frequencies are 10^{11} $M^{-1}s^{-1}$ (Z_{soln}) and 10^{4}cm s^{-1}(Z_{el}), respectively[3]. When work terms for each process are negligible, chemical electron transfer rates (k_{ex}) and electrochemical transfer rates (k_{el}) are comparable through the relation $(k_{ex}/Z_{soln})^{1/2} \approx (k_{el}/Z_{el})$. Reviews comparing electrochemically derived rate constants to their known homogeneous electron transfer counterparts usually follow the above behavior, but discrepancies of several orders of magnitude are not uncommon [2, 3]. Electrode techniques also differ from chemical reduction as applied to nanoparticle synthesis in that there are inescapable electrode-particle interactions with the nucleated metal that do not exist in homogeneous chemical synthesis. These interactions- particularly specific interactions where there is an extra enthalpic contribution in nucleating a particle rather than simply lowering the surface energy of the particle by adsorption- will often skew the comparison to show higher electroreduction rates. Even given these qualifications, SSCA does have utility for estimation of the timescale of reduction processes.

The theory of electrodeposition has been described by several models, most notably by Scharifker and Hills [1, 5, 6], Scharifker and Mostany [7-9], and by Sluyters-Rehbach [10]. Though they each differ in a few ways (some more subtle than others), all theories must account for diffusion of the oxidized species (Ox) to the electrode, electron transfer to Ox, nucleation of the reduced species on the surface, and growth of those nuclei until they overlap and form a continuous layer. The experiments in this section will be analyzed according to Heerman and Tarallo [11-

14], who attempted to reconcile the theories of Scharifker and Hills and Sluyters-Rehbach. Their assumptions include: 1.) the electrode is a homogeneous surface, 2.) there is a finite number of specific sites which are highly active for electrodeposition, and 3.) electron transfer to the metal precursor is facile, and the electrodeposition is limited by diffusion only. The expected chronoamperometric wave shape is shown in Figure 3.1, which depicts an exponential decay in current at short times after the applied potential step (corresponding to double layer charging on the electrode) followed by a rise and then fall in current as time increases. The rising portion of the wave corresponds to the events of interest (namely diffusion-limited nucleation and growth) while the falling portion of the current-time profile is a confluence of overlapping deposition islands and Cottrell-type diffusion current. It is in the best interest of the analysis to only use numerical fits on the rising portion of the wave and before Cottrell current takes over, where the most data corresponding to metal nucleation is obtained.

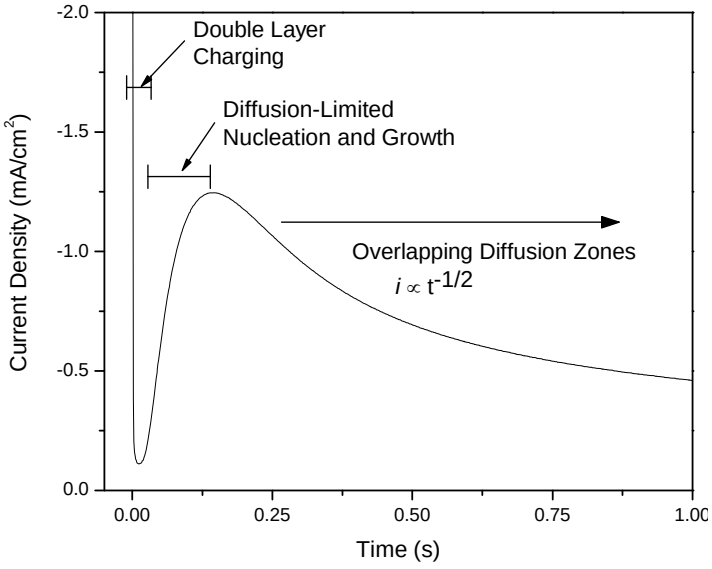

Figure 3.1 Diagram of the expected shape of the chronoamperogram for classical electrodeposition

The most complete understanding of nucleation mechanisms can only be attained when using well-characterized, single crystal electrodes, where the assumption of a homogeneous surface is valid. In this study, such rigorous electrode characterization was deemed unnecessary, as the kinetic parameter of greatest interest- nucleation rate constant- is able to be extracted from even a polycrystalline electrode surface. The mechanism of deposition *per se* was not desired as much as the rate at which it occurs. Therefore, the single step chronoamperometry measurements shown here cannot be analyzed beyond certain limits, and all attempts to determine the mechanism of deposition (such as "instantaneous" or "progressive" nucleation according to Scharifker and Hills) must be measured carefully against the underlying assumptions of the model. However, the data will be sufficient for obtaining the parameters of interest. The single-step chronoamperometry experiments shown in the first section of this chapter will produce a nucleation rate constant, which serves as the analogue to chemical reduction.

3.2.1 Experimental

Tetrahydrofuran (Fisher, HPLC grade) was dried over molecular sieves in a stainless steel solvent dispensing system, and lead (II) 2-ethylhexanoate (Strem Chemicals, Inc.) was first dissolved to 0.050 M in THF (due to its high viscosity) before diluting in THF to 5 mM. Platinum (II) acetylacetonate (Aldrich) and dimethyl platinum (1,5) cyclooctadiene (Strem Chemicals, Inc.) were used as received. Tetra-n-butylammonium perchlorate (Aldrich, electrochemical grade) was recrystallized from ethyl acetate before use. All solution preparation was performed in an argon atmosphere glovebox, and measurements were done under flowing nitrogen. All solutions were nominally prepared as 0.1M tetra-n-butylammonium perchlorate and 0.005 M metal precursor. Voltammograms and chronoamperograms were recorded on

a Hokuto Denko HSV-100 potentiostat and a BAS Epsilon potentiostat. The measurements were done in a three-chamber electrochemical cell with glass frit joints and a platinum wire counter electrode. The reference electrode consisted of a glass tube containing 0.05 M $AgNO_3$ in acetonitrile and all potentials are versus Ag/Ag^+ without regard to junction potential. Due to wide variances in junction potentials when measuring non-aqueous reference electrodes versus the popular aqueous ones like NHE, SCE, and Ag/AgCl, there is no one value for converting Ag/Ag^+ to NHE. In this dissertation, the conversion of +0.550 V vs. NHE will be used [15]. Lead (II) 2-ethylhexanoate depositions were studied using a 1mm diameter gold working electrode, dimethyl platinum cyclooctadiene on a 1mm gold working electrode, and platinum (II) acetylacetonate on a 1mm platinum working electrode. The electrodes were polished after each deposition experiment to remove the deposited layer and renew the electrode surface. It was necessary to purge the solutions with nitrogen upon polishing the electrode; this agitation inevitably leads to an evaporation of THF and a slight increase in solution concentration.

3.2.2 Results and Discussion

3.2.2.1 Lead (II) 2-ethylhexanoate

A clear way to distinguish a system that exhibits electrodeposition rather than simple diffusive-behavior reduction is to examine the cyclic voltammogram[1]. While a straightforward reversible reduction will contain two defined, separated peaks in the current potential profile (one for reduction, one for oxidation), a reduction and deposition case will show a large separation between peaks, a shift in cathodic peak position upon multiple sweeps, and- most tellingly- a crossover in the cathodic current [1]. As seen in Figure 3.2, the linear sweep voltammogram for lead (II) 2-ethylhexanoate in THF exhibits all these features.

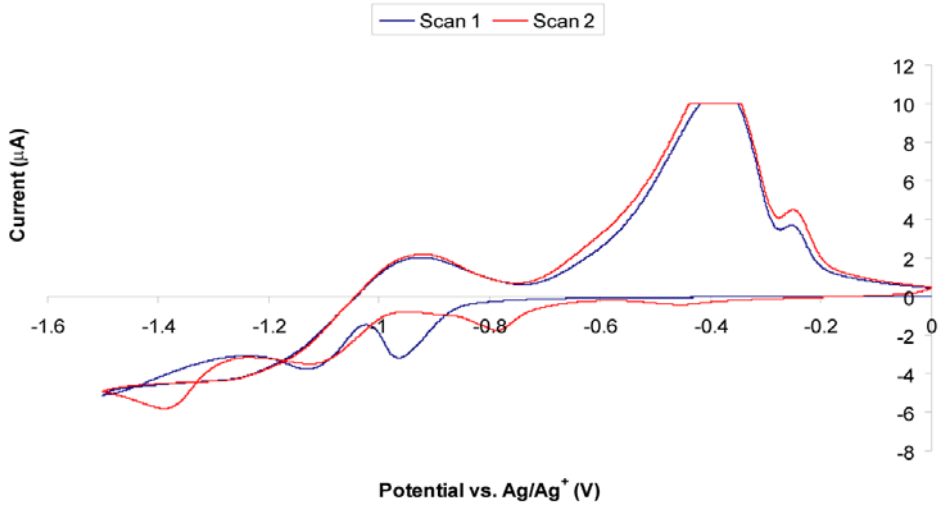

Figure 3.2 Cyclic voltammogram of approximately 7.5 mM lead (II) 2-ethylhexanoate in THF with 0.1 M TBAP. Scan rate = 100 mV s^{-1}. Note the change in reduction potential on the second cathodic scan.

Clearly the i-V behavior of this precursor in an electrochemical system is not simple; there are no fewer than three cathodic and three anodic peaks present, and all show significant E_{peak} separation (at least 400 mV each). Despite this complexity, the features of interest are distinguishable. The cathodic current crossover is easily seen at the most negative potentials, and the two cycles shown in the figure demonstrate the shifting of a peak due to lead deposition. On the first cycle, Pb^{II} is reduced to Pb^{0} at approximately -0.97 V vs. Ag/Ag^{+}, and deposits on the gold electrode. But on the second sweep, Pb^{II} is no longer depositing on a gold electrode, but on a lead-modified gold electrode. Due to higher affinity of Pb^{0} for a lead surface than a gold surface, the process occurs at a less negative potential than the original lead-on-gold deposition by about 200 mV. The large oxidative peaks near -0.4 and -0.25 V vs. Ag/Ag^{+} presumably correspond to oxidative stripping of the deposited lead layer. Subsequent sweeps (Figure 3.3) show that the lead-on-lead deposition peak continues at the less-

negative potential. This potential corresponds to approximately -1.5 V vs. NHE, compared to the standard 2-electron reduction potential of $Pb^{II}_{(aq)}$ at -0.1251 V vs. NHE. This ~1.4 V shift in reduction potential is illustrative of the large shifts due to ligand coordination and the use of non-aqueous solvents. It is once again noted that this conversion is approximate, and could be off by as much as a few hundred millivolts. Such conversions to NHE will be made here sparingly, and for estimating purposes only. Comparisons of reduction potentials are best left to ones measured on the same electrode.

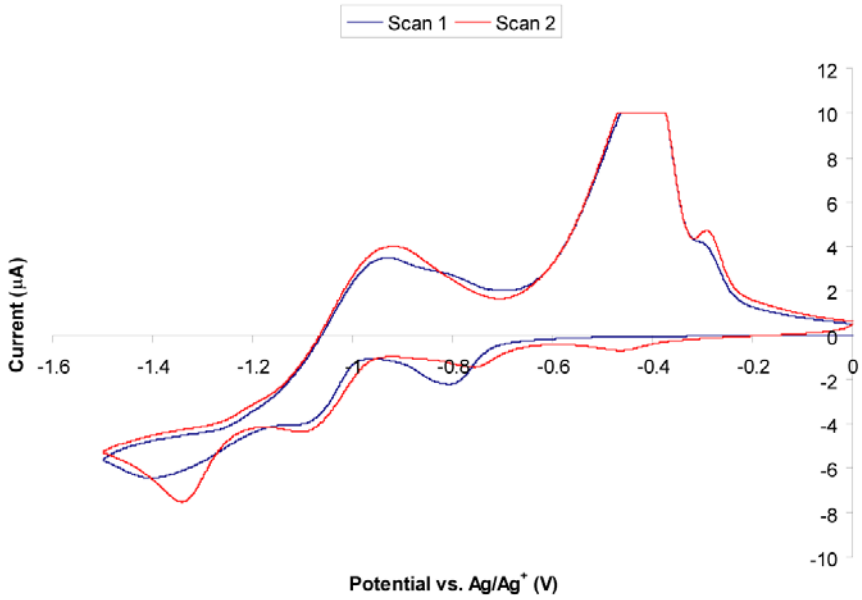

Figure 3.3 Cyclic voltammogram s at 100 mV s^{-1} for the same solution as in Figure 3.2, but after the sweeps in that figure. The cathodic peak at -0.8 vs. Ag/Ag^{+} remains.

Since the CV of this lead precursor indicated the desired electrodeposition phenomenon, chronoamperograms were recorded at potentials near that of the lead deposition potential. The chronoamperometric curves are shown in Figure 3.4, and

were performed at -750, -800, -825, -850, -875, and -900mV (all vs. Ag/Ag^+). They exhibit the classic wave shape for electrodeposition as depicted earlier; first a double layer decay at short times, followed by a broad "hump" with a temporal width on the order of several (i.e. less than 10) seconds. This rising then falling wave shape corresponds to electron transfer to molecular lead precursors, which are reduced to lead adatoms at nucleation sites. These sites quickly become saturated on the electrode surface, leading to increased lead coverage, diminished deposition from solution and a decrease in current to nearly zero. Even though the CV shows lead deposition at around -0.9 V vs Ag/Ag^+, all the chronoamperograms in Figure 3.4 show clear electrodeposition at potentials less negative than -0.9 V.

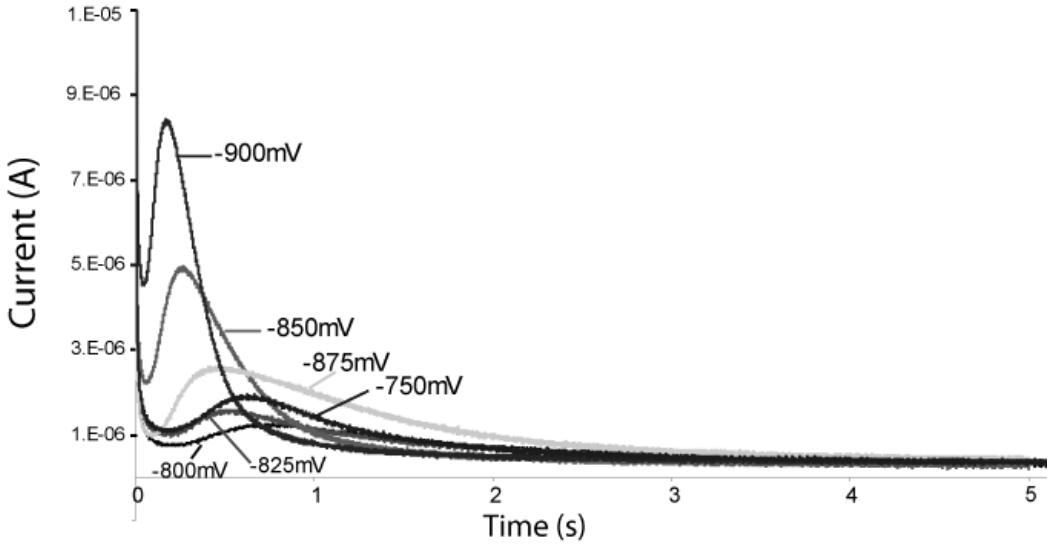

Figure 3.4 Single potential step **c**hronoamperograms of 7.5 mM lead (II) 2-ethylhexanoate in THF with 0.1 M TBAP. at – 750, -800, -825, -850, -875, and -900mV vs. Ag/Ag^+.

Kinetic analysis was performed on the i-t trace at each potential. The current-time profile was fit for the time interval beginning where the curve starts to rise again

after the initial decay and ending after the peak at i_{max}, t_{max} (Figure 3.5), according to Equation 3.1:

$$-I(t) = nFA_{electrode}c\frac{\Phi}{\Theta t^{1/2}}\left\{1-\exp\left[-(8\pi^3 V_m c)^{1/2} DN_0\Theta t\right]\right\} \qquad (3.1)$$

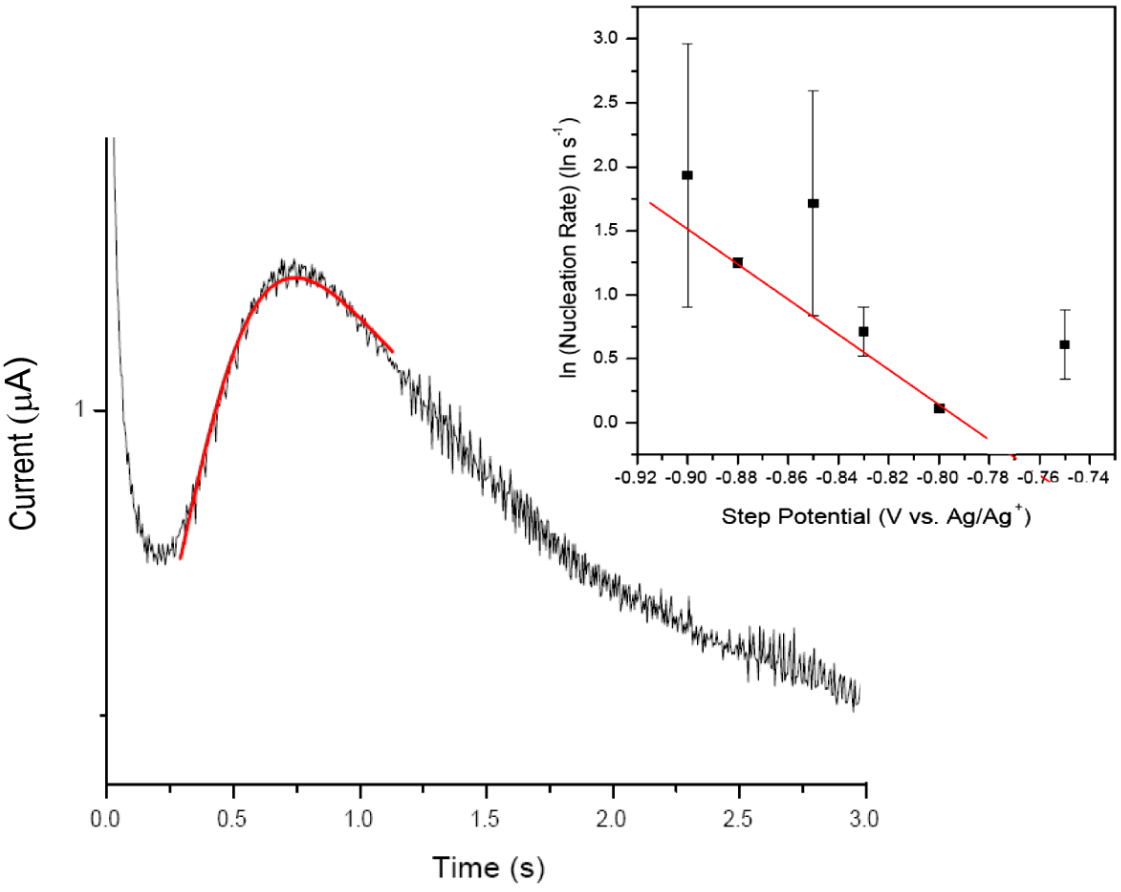

Figure 3.5 Fit of sample chronoamperometric trace to Equation 3.1. Inset shows the ln(nucleation rate) as a function of applied potential, and the slope which gives the critical nucleus size. Error bars reflect the goodness of fit for the chronoamperograms at each potential; absent error bars are implied as being smaller than the data point.

Equation 3.1 shows current as a function of time, where n is the molar number of electrons transferred (nominally the oxidation state of the metal), F is the Faraday

constant, $A_{electrode}$ is the electrode area, c is the concentration of the analyte ($mol \cdot cm^{-3}$), V_m is the metal's molar volume ($cm^3 mol^{-1}$), D is the diffusion coefficient ($cm^2 s^{-1}$), and N_0 is the available site density on the surface (cm^{-2}). Θ and Φ are functions that describe the nucleation rate constant, A (s^{-1}), and are described by Equations 3.2 and 3.3, respectively.

$$\Theta = 1 - \frac{1 - \exp(-At)}{At} \tag{3.2}$$

$$\Phi = 1 - \frac{\exp(-At)}{(At)^{1/2}} \int_0^{(At)^{1/2}} \exp(\lambda^2) d\lambda \tag{3.3}$$

The λ term is a variable to allow for experimental deviations from the theory. Fortunately for computational simplicity, it is not necessary to fit for λ as a fourth parameter, since Φ only appears in Equation 3.1 in the ratio $\Phi \cdot \Theta^{-1} t^{-1/2}$, and that ratio can be approximated to 0.6% accuracy according to Heerman and Tarallo [12] by the polynomial:

$$\frac{\Phi}{\Theta t^{1/2}} \approx \frac{0.520893\ At^{1/2} - 1.206814\ A^{3/2}t + 1.185724\ A^2 t^{3/2} - 0.051314\ A^{1/2}}{\left[At - 1 + \exp(-At)\right](1 - 1.206814\ A^{1/2}t^{1/2} + 1.185724\ At)} \tag{3.4}$$

By fitting the data to these equations, three parameters are extracted: the diffusion coefficient D, the site density N_0, and the nucleation rate constant A.

Table 3.1. Kinetic parameters obtained from fits of curves in Figure 3.4.

Potential (mV vs. Ag/Ag$^+$)	**D (10^{-8} $cm^2 s^{-1}$)**	**N_0 ($10^8 cm^{-2}$)**	**A(s^{-1})**
-750	4.2 ± 0.13	11.1 ± 2.1	1.8 ± 0.27
-800	2.2 ± 0.011	25.0 ± 0.50	1.1 ± 0.029
-825	2.5 ± 0.039	22.7 ± 2.6	2.0 ± 0.19
-850	11.6 ± 0.57	8.0 ± 1.8	5.6 ±0.88
-875	7.5 ± 0.032	5.2 ± 0.080	3.5 ± 0.039
-900	22.9 ± 0.79	7.2 ± 1.4	6.9 ± 1.0

These values are known to be potential-dependent, and the data in Table 3.1 reflects this, as D, N_0 and A all show about a factor of five difference from the smallest value to the largest values. Most values are on the correct order of magnitudes when comparing to expected estimates for known quantities with physical meaning. The diffusion constants ($\sim 10^{-8} cm^2 s^{-1}$) are very low compared to those usually found for liquids ($\sim 10^{-5}$ to $10^{-6} cm^2 s^{-1}$); this might be due to oligomerization of the lead carboxylate in solution, as four unit oligomers have been detected by FTIR in films of lead (II) 2-ethylhexanoate after solvent evaporation [16]. Such a large solvated unit of the electroactive species would be expected to diffuse slowly, so it may not be such a surprise that it has a much smaller diffusion constant in THF than, for example, hexaquo copper (II) in water ($1.94 \times 10^{-5} cm^2 s^{-1}$) [13]. The available site density (N_0) is a miniscule fraction of the electrode surface atomic density: 10^8 active sites per cm^2, compared to around 10^{15} gold surface atoms per cm^2. Though at first this might seem to be a low value, it is common for analyses of this type to give N_0 values between 10^4 and 10^{10} cm^{-2}, and never approach the density of surface metal atoms [13]. The nucleation rate constants, A, are all between 1 and 7 s^{-1}, which corresponds to the nucleation occurring in less than a second; this not only is a realistic value, but also does not conflict with observations of nanoparticle synthesis in strong reducing agents, where metal precursors usually are reduced and begin to precipitate in less than a second. These values on the order of 1 to 10 s^{-1} are the best estimate for the reduction and nucleation of lead under the electrochemical conditions of the experiment, and shall be compared to reduction rate constants found for Pt precursors to determine whether the co-reduction hypothesis is valid or must be reconsidered.

The potential dependence of A is shown in the inset of Figure 3.5, where lnA vs. the applied potential data is fit to a straight line. The atomistic theory of electrochemical nucleation, covered extensively in the work of Milchev et al. [17-21],

shows that the size of the critical nucleus (n_c), the minimum number of atoms needed to establish a stable deposited adatom on the surface, is found by the relation $n_c = (RT/nF)(-d\ln A/dE)$. By fitting to at straight line, the slope $d\ln A/dE$ is found to be -13.7 $\ln(s^{-1})/V$, and by filling in appropriate values for the gas constant (R), absolute temperature (T), number electrons transferred (n), and the Faraday (F), one obtains a critical nucleus size of 0.18 atoms, which is understood as zero atoms. When such a result appears, the interpretation is that there is no thermodynamic barrier to Pb nucleation when the lead precursor under consideration is reduced in THF. Therefore it can be concluded that lead freely deposits on the gold electrode, and is only limited by kinetic factors. In the Sharifker and Hill terminology, this would be in the instantaneous deposition regime, rather than progressive. Such a claim is rather dubious, and its importance should not be overstated; as the working electrode is polycrystalline, it is of no surprise to find instantaneous nucleation. Progressive nucleation mechanisms are usually only distinguishable on single crystal electrodes.

3.2.2.2 Dimethyl Platinum Cyclooctadiene and Platinum (II) Acetylacetonate SSCA

Once it was seen that the reduction of lead (II) 2-ethylhexanoate could be analyzed by potential step chronoamperometry, it was desirable to repeat the experiments with the platinum precursor used in Chapter 2 ($Pt(COD)Me_2$) and $Pt(acac)_2$, another common Pt precursor in nanoparticle syntheses. But as will be shown throughout this chapter, a given metal complex is not necessarily compatible with a given electroanalytical technique. A chronoamperogram for the single-step reduction of $Pt(acac)_2$ at -2.9 V vs. Ag/Ag^+ is shown in Figure 3.6. The expected waveshape that was so clearly demonstrated for the lead precursor is not found, even over the course of sixty seconds. The cyclic voltammogram for $Pt(acac)_2$ which is shown later in the chapter exhibits compelling evidence of an electrodeposition

system, and -2.9 V should be negative enough to reduce the Pt^{II} precursor to Pt^0 (see Figure 3.8). The absence of the characteristic current-time profile indicates that reduction and deposition of $Pt(acac)_2$ does not follow the classic theory of diffusion-limited reduction and overlapping deposition zones. It goes without saying that this precursor is not amenable to analysis in the manner of Heerman and Tarallo (Figure 3.5).

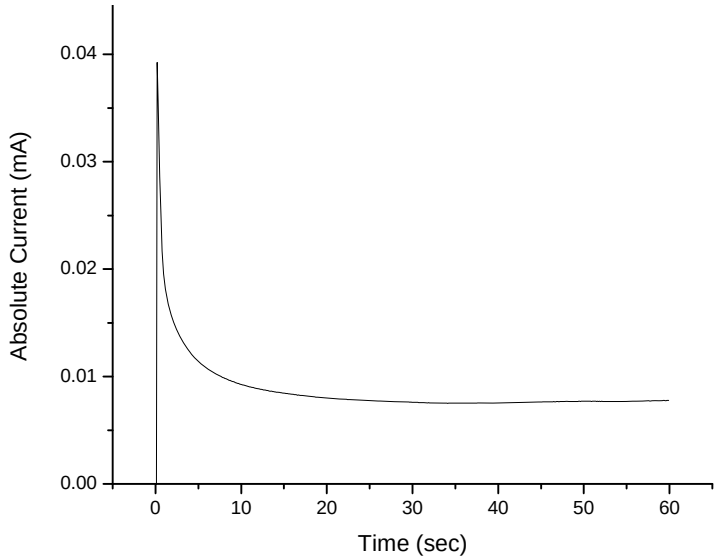

Figure 3.6 Single potential step **c**hronoamperogram of 5.0 mM $Pt(acac)_2$ in THF with 0.1 M TBAP at -2.9 V vs. Ag/Ag^+. Faradaic electron transfer is occurring, as the current does not decay to zero, but the expected hump from electrodeposition is not present.

The appropriateness of SSCA for analysis of $Pt(COD)Me_2$ is less well-known. At the point of the initial investigation into $Pt(COD)Me_2$, the reduction potential of the precursor in THF with TBAP was severely underestimated. SSCA experiments were conducted, but only at potentials as negative as -0.7 V vs. Ag/Ag^+. Using the standard reduction potential of 1.18 V vs. NHE for $Pt^{2+}_{(aq)}$ as a starting point, it was assumed that the organometallic Pt precursor would certainly be reduced at that potential step,

which would correspond to approximately -1.25 V vs. NHE. At a step potential of -0.7 V vs. Ag/Ag^+, the waveshape looked identical to Figure 3.6 for $Pt(acac)_2$, where no distinct electrodeposition could be found. However, cyclic voltammetry (Figure 3.7) shows reduction onset occurring near -1.7 V vs. Ag/Ag^+, and further irreversible reduction past -2.7 V.

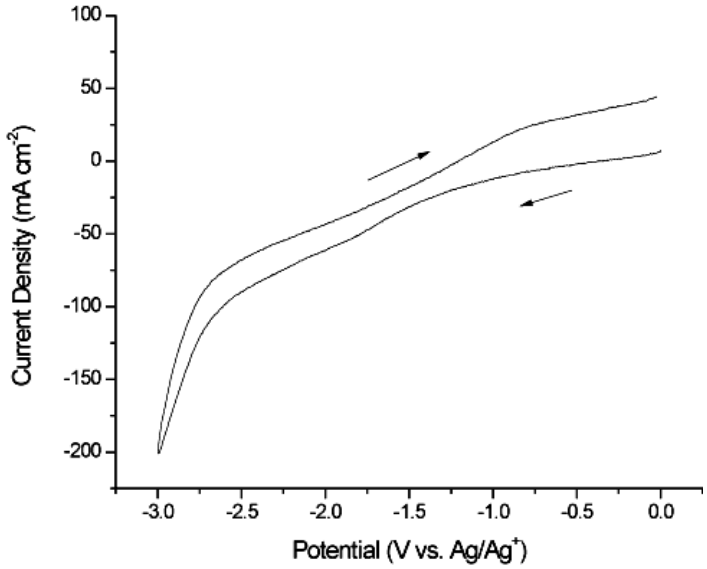

Figure 3.7 Cyclic voltammogram of 5.0 mM $Pt(COD)Me_2$ in THF with 0.1 M TBAP. Sweep rate = 500 mVs^{-1}. 240μm diameter Pt working electrode, Pt wire counter.

This was dismissed at the time; -2.75 V seemed too negative for an electronegative element such as platinum, no matter what its ligand sphere was. That assessment has since been changed, as non-aqueous electrochemical measurements have shown that the reduction of organoplatinum complexes occurs at quite negative potentials indeed. Also, at that time we had begun to investigate double potential step chronoamperometry as the preferred method, since it is more generalized and does not rely on the common- but by no means ubiquitous- electrodeposition phenomenon. It

is possible that revisiting SSCA for $Pt(COD)Me_2$ could yield meaningful data amenable to Heerman and Tarallo's analysis if the potential is stepped to sufficiently negative values. However, experiments from later in this chapter do not bode well for kinetic analysis of any sort for $Pt(COD)Me_2$. The only meaningful data which could be extracted and applied to the mechanistic considerations in Chapter 2 is the reduction potential; the interpretation of this data in light of the chemical reduction will be addressed in section 3.4 of this chapter.

3.3 Double Potential Step Chronoamperometry

The other class of electrochemical experiments used to estimate the timeframe of ligand dissociation is double step chronoamperometry (DSCA). This method is a potential reversal technique that has been utilized for decades and is applicable to a multitude of electrochemical systems, but has usually been used for more electrochemically reversible systems and has been mostly limited to aqueous media. DSCA has several benefits over single-step chronoamperometry, foremost being that the nature of the electrode plays a less important role. It was mentioned earlier that the most rigorous SSCA measurements are used to determine the deposition mechanism, and therefore the electrode surface is of paramount importance. A single-crystal, atomically flat electrode is preferred, and a well characterized electrode is desired for any in-depth discussion of the mechanism beyond what was shown earlier. That description is in contrast to DSCA. As will be shown in the Results and Discussion section, a popular and convenient DSCA analysis employs a ratio of the anodic current to the cathodic current; such expressions naturally cause many of the factors governing the magnitudes of current (geometric area, surface roughness, solution concentration, etc.) to mathematically cancel each other. Therefore, it is conceivable (though never advisable) for one to perform these potential reversal

techniques without knowing the electrochemical surface area of the electrode or the solution concentration. Another benefit of DSCA over SSCA is that the analysis of DSCA (in the manner described by Schwarz and Shain [22]) is inherently more robust that the numerical fits of the SSCA from earlier in this chapter. Rather than fitting the direct current-time response (and all possible instrumental and chemical complications associated with it) single current-time data points are plotted as ratios versus reversal time and evaluated against established working curves, leading to a sturdier analysis of the current. Finally, another reason for switching to a current reversal technique is that for some systems *single potential step experiments do not work.* As shown in the previous section, the systems of $Pt(COD)Me_2$ and $Pt(acac)_2$ were not amenable to the same electrodeposition analysis that the lead precursor was (though the finality of that statement for dimethyl platinum (1,5)cyclooctadiene is debatable). Some flexibility must be employed so one can apply the correct experiment and analysis to a given metal precursor.

3.3.1 Experimental

Platinum (II) acetylacetonate, iron (III) acetylacetonate (Aldrich) and dimethyl platinum (1,5)cyclooctadiene (Strem Chemicals, Inc.) were used as received, and tetra-n-butylammonium perchlorate (Aldrich, electrochemical grade) was recrystallized from ethyl acetate before use. Tetrahydrofuran (Fisher, HPLC grade) was dried over molecular sieves in a stainless steel solvent dispensing system, and lead (II) 2-ethylhexanoate (Strem Chemicals, Inc.) was dissolved to 0.050 M in THF (due to its high viscosity) before diluting further in THF to 5 mM. All solution preparation and electrochemical measurements were performed in an argon atmosphere glovebox. Cyclic voltammograms and chronoamperograms were recorded on a Hokuto Denko HSV-100 potentiostat, and verified on a BAS Epsilon potentiostat.

Solutions were analyzed in a three-chamber electrochemical cell with glass frit joints and a platinum wire counter electrode. The reference electrode consisted of a glass tube containing 0.05 M $AgNO_3$ in acetonitrile, and all potentials are versus Ag/Ag^+ (*ca.* +550 mV vs. NHE) without regard to junction potential. Platinum electrodes were used, and their sizes are noted in the text.

3.3.2 Results and Discussion

At first approximation, the reduction of $Pt(acac)_2$ can be modeled after an E_rC_i coupled electrochemical-chemical reaction in the parlance of Testa and Reinmuth [23], where a reversible electron transfer step (E_r) is followed by an irreversible chemical reaction (C_i) to an electrochemically silent species. As a general mechanism, the two-step reaction can be written as Ox↔Red→C, where Ox is the metal precursor in its native solvated state, Red is that species in a reduced state, and C is the product of a chemical transformation of Red, and is not detectable by the electrode in the potential range under analysis. In the specific case of $Pt(acac)_2$, Ox and Red would be $Pt(acac)_2$ and $Pt(acac)_2^{2-}$, respectively, and C is Pt adsorbed to the electrode surface with acetylacetonate ligands dissociated in solution. Though no literature could be found that explicitly demonstrated this electrochemical reduction mechanism for $Pt(acac)_2$, $M(acac)_2$ species of nickel and copper are known to reduce through this mechanism [24, 25]. It is reasonable that a similar d^8 transition metal acetylacetonate complex would have similar electrochemical reactivity, and it would be expected that a noble metal such as platinum would have even more a propensity to be reduced to (and remain) M^0 than would nickel (though it should be noted that the fully reduced Ni in reference [15] was imparted stability by amalgamation in a mercury electrode).

The assertion that the precursor is reduced *via* an E_rC_i mechanism is corroborated by cyclic voltammetry of the molecule in solution. The voltammogram

in Figure 3.7 shows the i-V behavior of $Pt(acac)_2$ in tetrahydrofuran with dissolved tetra-n-butylammonium perchlorate as supporting electrolyte, as well as a background sweep of TBAP in THF. The background demonstrates the large potential window accessible with the TBAP/THF system, as the non-double layer current is negligible from 0 V to -2.25 V; over that potential range, the solvent and supporting electrolyte are clearly stable, and the solvent contains no detectable levels of redox-active impurities. From -2.25 V to -3 V, it is clear that some irreversible reduction process is occurring, and can most likely be ascribed to partial electroreduction of the tetraalkyl cation. When $Pt(acac)_2$ is added, a clear reduction wave is seen at similar negative potentials, but the current values are much larger than those seen in the background. The large cathodic peak centered at $E_{1/2}$ = -2.75 V cannot be ascribed only to that same background process, and is expected to be due to reduction of the platinum precursor. Since this cathodic peak's corresponding oxidation wave is absent, the reaction is highly indicative of an irreversible reduction process, specifically that Pt is deposited on the surface of the Pt electrode and no longer electrochemically active. It must be noted, however, that at this point the innocence of the supporting electrolyte with regard to the reduction of the Pt precursor is not assured.

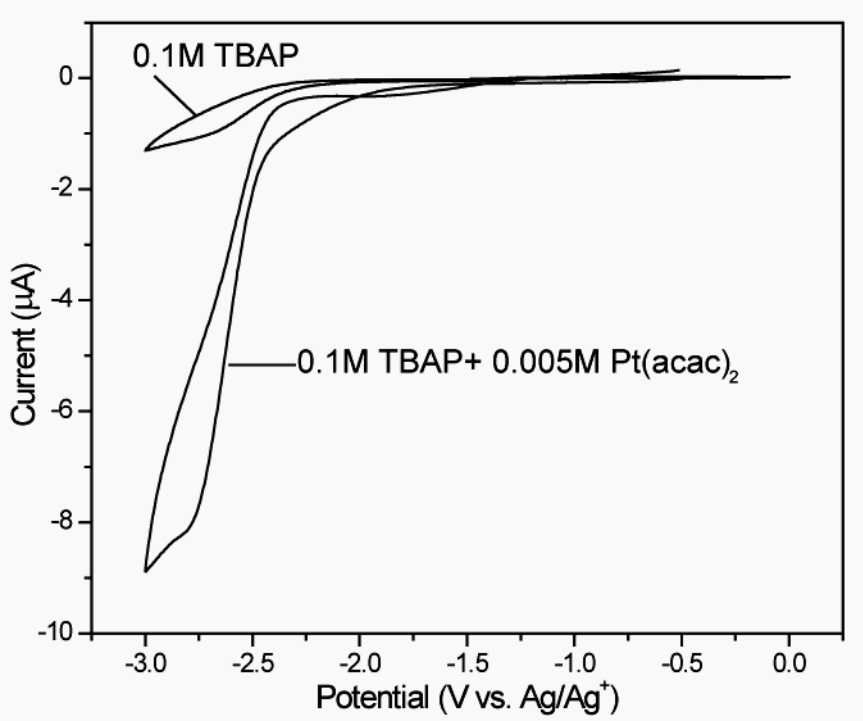

Figure 3.8 Cyclic voltammograms of 0.1 M TBAP in THF, and 0.1 M TBAP and 5.0 mM $Pt(acac)_2$ in THF, both at 50 mV s^{-1}.

The behavior of DSCA for an E_rC_i mechanism was solved explicitly by Schwarz and Shain in 1965 [22], and the use of DSCA is convenient for a suspected E_rC_i reaction like the precursor under investigation [26]. The experiment proceeds by starting with the applied potential at a value where no Faradaic current is being drawn. Then, at an arbitrary start time, the potential is stepped to a negative value large enough to access mass-transport limited reduction of O, held there for a varying switching time τ, and then stepped back to the starting value. The resulting current-time profile is recorded, and values for the anodic current (i_a) and cathodic current (i_c) at are plotted as a dimensionless ratio vs. the product of a rate constant times the switching time period τ (also dimensionless). A graphical representation of the

measured values is shown in Figure 3.9, which simultaneously depicts the applied potential and the expected current response versus time.

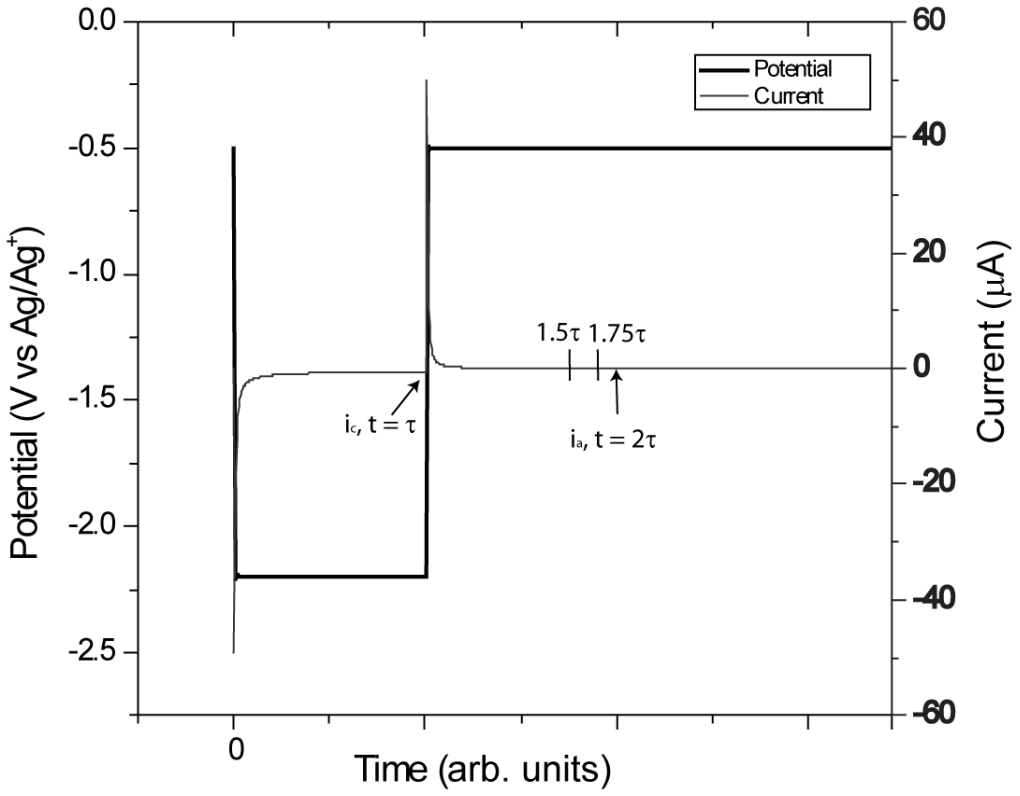

Figure 3.9 Diagram of a double step chronoamperometry experiment. The dark line is the applied potential, and the light line is the current response. Conventions for current and time values are labeled.

Schwarz and Shain were able to derive the relationship between the currents ratio and the switching time by beginning with Fick's planar diffusion laws and three potential conditions (one initial and two boundary) - before the oxidative step, during the reductive potential step, and after the applied potential has been removed. LaPlace transforms were employed to obtain anodic and cathodic current terms that contained

complicated function found in Equation 3.5, which at its core lies a confluent hypergeometric series.

$$\Phi = e^{-\frac{k\tau}{2}} I_0\left(\frac{k\tau}{2}\right) + 2e^{-k\tau_r/2} e^{-k(t-\tau)} \sum_{n=1}^{\infty} I_n\left(\frac{k\tau}{2}\right) \frac{\int_0^{k(t-\tau)} \cdots \int_0^{\lambda_2} \lambda_1^n e^{\lambda_1} d\lambda_1 \cdots d\lambda_n}{[k(t-\tau)]^n} \tag{3.5}$$

Here, k and τ are defined as before, $I_n(k\tau/2)$ is a modified Bessel function, and λ terms are hypergeometric variables with no direct chemical meaning. Substituting Equation 3.5 into the terms for the cathodic and anodic currents allowed for expression of those currents for any value of time, but the authors noted the desirable aspects of dividing i_a by i_c and eliminating the currents' dependence on electrode area, concentration, and even diffusion constant (benefits that were noted earlier in this chapter). The ratio of those terms is found in the final working equation shown in Equation 3.6:

$$-\frac{i_a}{i_c} = \Phi\left[k\tau_r \frac{(t-\tau)}{\tau}\right] - \sqrt{\frac{(t-\tau)/\tau}{1+(t-\tau)/\tau}} \tag{3.6}$$

Schwarz and Shain then allow for working curves to be plotted from Equation 3.6 that plot i_a/i_c versus the switching time τ for several values of the reduced time constant $(t-\tau)/\tau$. Part of the simplification found in using the working curves is by restricting the times in the experiment at which the current values are measured. If the cathodic current is measured at $t = \tau$ (or rather at a value called $t_{cathodic}$) and the anodic current measured only at $t = 2\tau$ (which is to say at $t_{anodic} = t_{cathodic} + \tau$), then the coupling of the current values at a single time value separation simplifies the treatment. The rate constant for the first order chemical reaction (the "C" portion of the E_rC_i mechanism) is then determined by fitting the data to the Schwarz and Shain curves. A numerical analysis is appropriate, but a simpler method is to only measure the current ratios at convenient $(t-\tau)/\tau$ values (i.e. the ones for which Schwarz and Shain calculated a curve), then plot $k(2\tau)$ vs τ. The slope of such a plot directly gives k. Even though all values of τ used in these experiments lay on one of the curves, making it simple to

assign a kτ value for each ratio, numerical fits were employed to find the rate constants in this section. Analysis of the i_a/i_c ratio was first found for i_c at $t = \tau$ and i_a at $t = 2\tau$ (this convention is labeled "2τ"); 2τ is convenient, but not mathematically sacred, so current ratios were also analyzed for other times, such as when i_a at $t = 1.5\tau$ and 1.75τ, or simply "1.5τ" and "1.75τ", for example. Measuring the anodic current at earlier time values has the advantage of sampling higher current values which are more likely to be non-zero for long τ's where the current has had ample time to decay. Agreement among ratios taken at multiple time constants is desired and expected. For an E_rC_i mechanism, the behavior of the current ratio i_a/i_c vs. kτ should decrease with increasing τ, because the longer the duration of τ, the longer R has to react to C. Less and less R is then available to be re-oxidized to O (and thus detectable during the oxidative step), so the anodic current decreases with respect to constant cathodic current at longer switching times. The current-time profile for five DSCA experiments on a 240μm Pt electrode is shown in Figure 3.10, where the potential begins at -0.5 V, is stepped to -2.9V and is held for 10, 20, 40, 60, and 80 ms, and then stepped back to -0.5 V. The expected waveshape is easily seen, and cathodic and anodic current values were extracted at times τ and 2τ, respectively (i.e. for the experiment where the applied potential is held for 40 ms, i_c is measured at 40 ms and i_a is measured at 80 ms). When plotting the current ratio i_a/i_c vs τ, it was found that the behavior of $Pt(acac)_2$ agrees with that predicted by theory, as seen in Figure 3.11. The ratio decays in the manner predicted by Schwarz and Shain. By fitting the data to theoretical curves at different time constants, rate constants on the order of 11-13 s^{-1} are found for $Pt(acac)_2$ in THF at -2.9 V vs Ag/Ag^+ (Table 3.2).

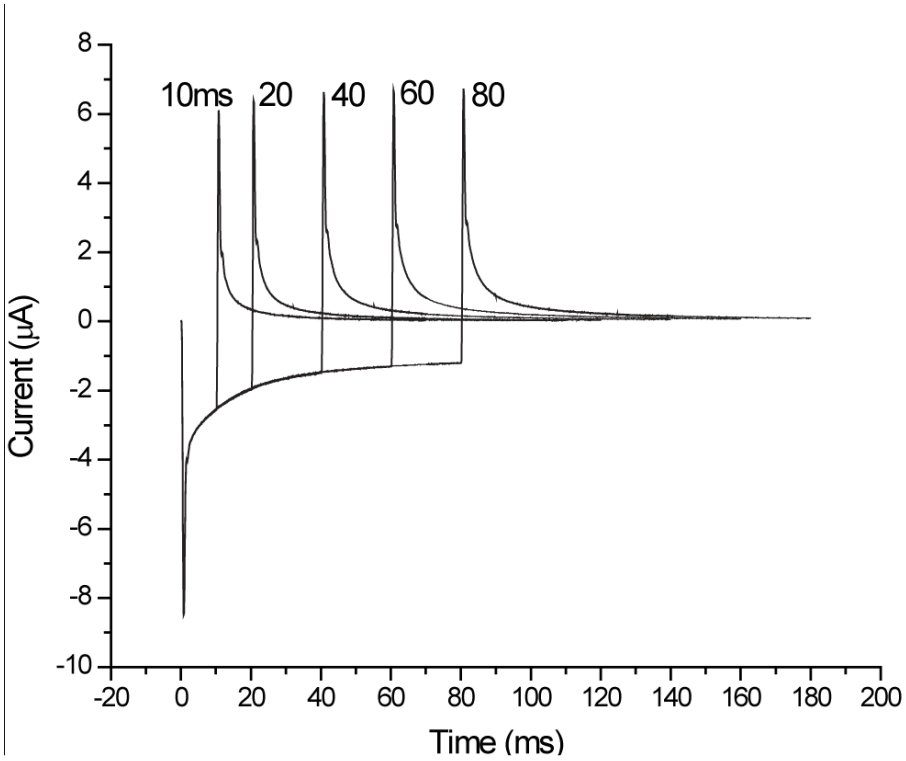

Figure 3.10 DSCA traces for $Pt(acac)_2$ at different values of τ. The applied potential steps from -0.5 V to -2.9 V and back.

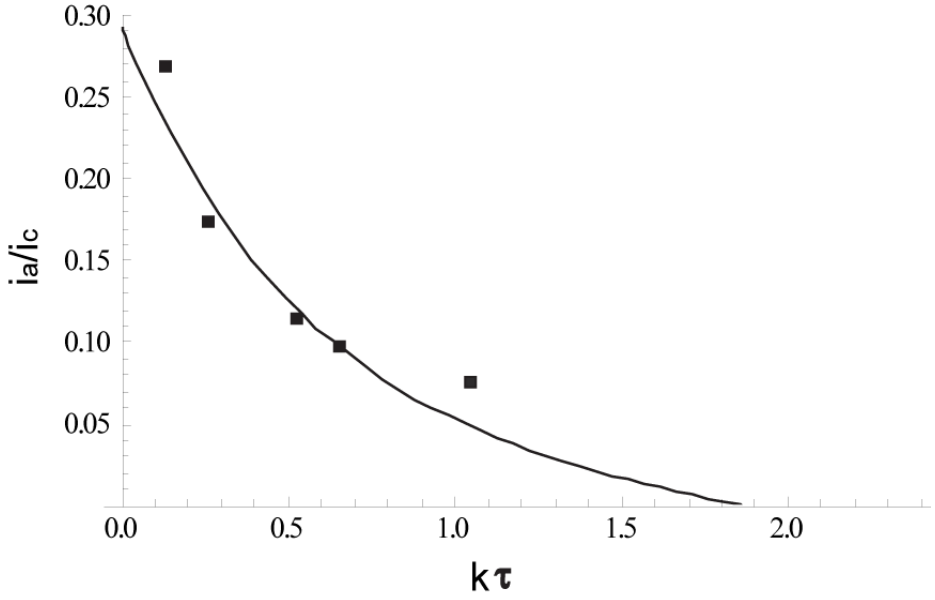

Figure 3.11. i_a/i_c ratios vs. τ for the traces in Figure 3.9, with fit to Equation 3.6.

Table 3.2. Results for values calculated at different time constants from Figure 3.11

"xτ"	Reduced Time [(t-τ)/τ]	k (s^{-1})	Error(s^{-1})
1.5τ	0.5	11	3
1.75τ	0.75	13	2
2τ	1	11	4

Table 3.2 shows the first order rate constants k calculated for the irreversible chemical dissociation of $Pt(acac)_2$. The values all show good agreement at different time constants, and the errors are on the order of 20%, which are usually acceptable for electroanalytical measurements. If the limiting step in the reduction of this Pt precursor to form nanoparticles is ligand dissociation, and if this electroanalytical measurement reflects that ligand dissociation, then that step happens in less than a second; like the nucleation rates found in the Pb SSCA section, this timeframe does not disagree with what is observed in the actual synthesis.

In order to determine the influence of reduction of supporting electrolyte which was alluded to earlier, $Pt(acac)_2$ was also analyzed at a concentration of 10mM, or twice that described above. Increasing the concentration would also have the effect of increasing the Faradaic current due to redox processes involving $Pt(acac)_2$, especially allowing for enhanced signal at large values of 2τ where anodic currents are smallest. Another strategy to increase signal to noise was to use two different electrodes- one with a diameter of 240 μm and one of 1 mm. The larger area electrode naturally gives larger currents, so it was used for experiments with longer switching times. Figure 3.12 shows the current ratios vs. τ at -2.75 V for 10mM $Pt(acac)_2$ for the 240 μm electrode. The stepped potential is slightly lower than the -2.9 V used in the 5 mM experiments since it was found to generate the desired Schwarz and Shain response but had less overpotential to drive the suspected side reaction with the supporting

electrolyte. The data points roughly follow the decaying trend that is expected. Analysis of the current ratio for the 240 μm electrode found rate constants which were higher than the results shown in Table 3.2, which were for the same electrode but half the $Pt(acac)_2$ concentration. The rate constants for the 10mM [Pt] solution at the 240 μm electrode were $28 \pm 11\ s^{-1}$ at 2τ and $20 \pm 5\ s^{-1}$ at 1.5τ

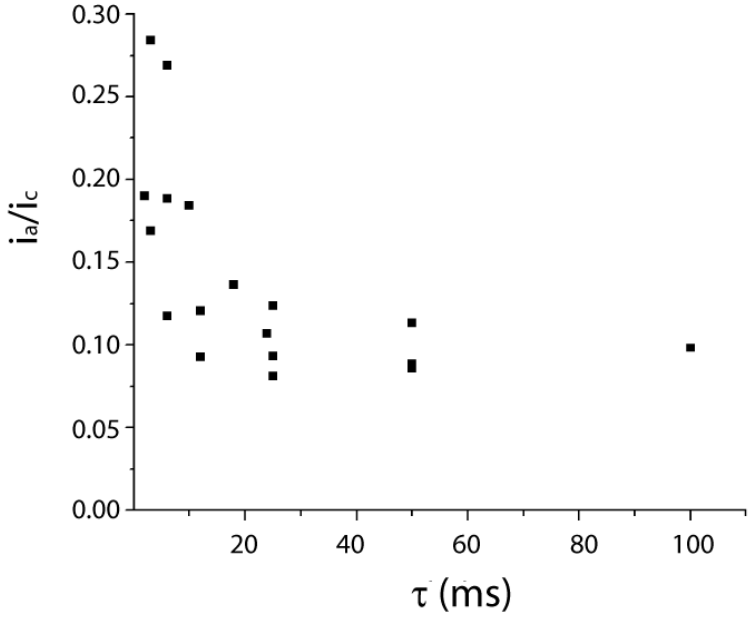

Figure 3.12. i_a/i_c ratios vs. τ for DSCA traces of 10 mM $Pt(acac)_2$ at 240 μm Pt electrode. The analysis curve is not shown, and the time constants are shown in milliseconds instead of the dimensionless kτ.

Though theory predicts that the electrode area should not play a role in the current ratio, deviations from theory are seen for the 1 mm electrode that are not seen for the 240 μm electrode. This deviation is not attributed to the larger electrode *per se*, but rather to the longer switching times investigated at that electrode. Figure 3.13 shows that there is more deviation from the Schwarz and Shain curve at longer τ values on the larger electrode, implying that a second reaction pathway is taking over

at long reaction times, and the E_rC_i mechanism is likely no longer the only one at work.

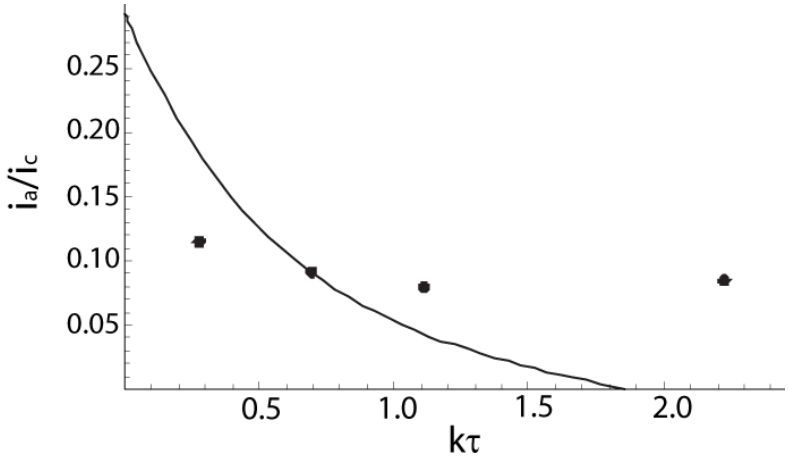

Figure 3.13. i_a/i_c ratios vs. τ for 10 mM $Pt(acac)_2$ at 1 mm diameter electrode. Switching times in milliseconds are 20, 50, 80 and 160 ms, with a step potential of 0 V to -2.75 V and back to 0 V, all vs. Ag/Ag^+. Line represents prediction by theory.

The rate constants for the 10 mM $Pt(acac)_2$ solution were approximately twice the values obtained for the 5 mM solution (~10 s^{-1}). This discrepancy in and of itself is not unexpected; the variance of electroanalytical measurements in organic solution is high, and since the rate constants are on the same order of magnitude for each concentration, it shows acceptable agreement. But as was shown earlier in the chapter, the i_a/i_c current ratio is not a function of depolarizer concentration, and the doubling of the first order rate constant with the doubling of [Pt] concentration is troublesome. It is now inferred that the supporting electrolyte is not completely innocent. The measured values are not necessarily only describing the behavior of acetylacetonate ligand dissociation, but also may be influenced by the reduction of the tetra-n-butylammonium ion at such low negative potentials.

Given the relative success of DSCA measurements for measuring what is presumed to be the ligand dissociation rate for $Pt(acac)_2$, the technique was then used

to study lead (II) 2-ethylhexanoate and $Pt(COD)Me_2$. Unfortunately, similar difficulties that prevented applying SSCA to all metal precursors of interest also prevented DSCA from being universally applied. The current ratio vs. switching time plot for 5mM lead (II) 2-ethylhexanoate at a step potential of -1.0 V vs. Ag/Ag^+ is shown in Figure 3.14. It is clear that it does not follow the trend for E_rC_i mechanisms, even though at first approximation that mechanism seems just as valid for this precursor as it did for $Pt(acac_2)$. The ratio increases at larger τ values rather than decreasing according to Schwarz and Shain's working curves. Not only does the trend deviate from theory for the E_rC_i mechanism, but also the ratio values are much higher than theory predicts for any mechanism. The ratios measured at 1.5τ, 1.75τ, and 2τ on a 240 μm Pt electrode are all above the predicted maximum value of 0.293, which should not be possible for a stable electrode and depolarizer.

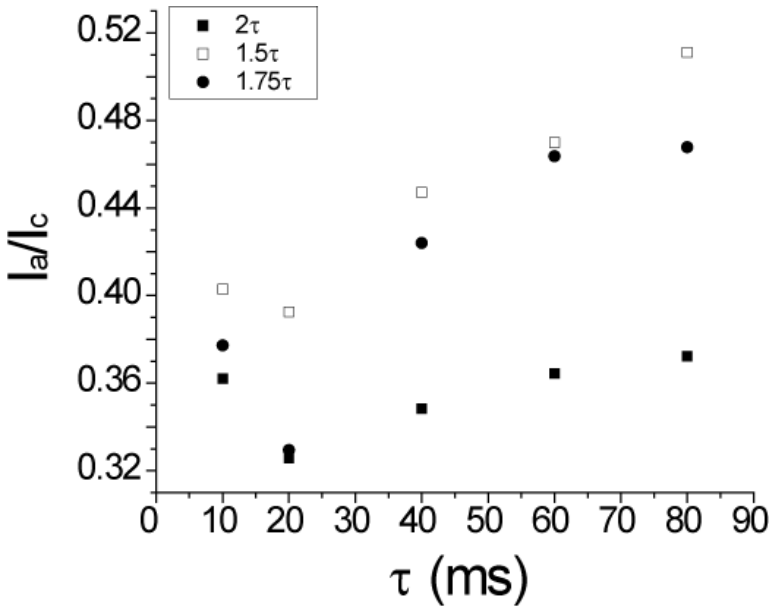

Figure 3.14 i_a/i_c ratio vs. switching time plot for 5.0 mM lead (II) 2-ethylhexanoate and 0.1 M TBAP at a step potential of 0 V to -1.0 V and back to 0 V, all vs. Ag/Ag^+.

A possible explanation of this effect is that the deposited species on the electrode (whether or not it is metallic lead) increases the capacitance of the electrode surface, equally increasing the measured current on both the cathodic and anodic steps. Since the anodic current will decrease with respect to the cathodic current in the E_rC_i mechanism, it would be disproportionately amplified by the increase in capacitance; the anodic current value would instead increase with respect to the constant cathodic current, and the ratio would increase. That explanation could account for a side process masking an E_rC_i mechanism, but an equally plausible description for the i-t behavior is that the lead precursor has a different reduction mechanism than predicted, and should not be expected to follow Schwarz and Shain's working curves at all. Dimethyl platinum (1,5) cyclooctadiene was equally unsuccessful. For the DSCA's attempted for this precursor, there was essentially no current on the anodic step when the potential was stepped from -0.5 V to -2.2 V and back. This could indicate an intermediate ("Red" in the E_rC_i mechanism shown earlier in the chapter) that is too short-lived to be detected by the potentiostat's resolution, which was 0.1msec. It could also be indicative of electropolymerization of (1,5) cyclooctadiene on the electrode surface, which would passivate and irrevocably alter the double layer during the course of the experiment. Either way, kinetic analysis was not feasible for $Pt(COD)Me_2$.

3.3.2.1 Iron (III) acetylacetonate DSCA

The behavior of Pb (II) 2-ethylhexanoate and both platinum precursors towards DSCA had enough idiosyncrasies to warrant examination of another molecular metal species. To ensure that the DSCA analysis was drawing correct conclusions, a metal precursor with a simple, known electrochemical response in THF was desired. The simplicity of that response was meant to entail a reversible, diffusion-controlled

reduction with clear oxidation/reduction peaks and no other electrochemical processes. For direct analogy to $Pt(acac)_2$, a complex with acetylacetonate ligands would be preferred to, for example, the ferrocene/ferrocenium couple. Literature searches found relatively few results dealing with THF as a solvent in general, none of which were for metal acetylacetonates. But it was found that iron (III) acetylacetonate has the desired simple redox behavior in acetonitrile and dimethylformamide with tetraethylammonium perchlorate as the supporting electrolyte [27]. Figure 3.15 shows that this uncomplicated redox behavior more or less extends to THF/TBAP as well. The CV shows that there is a redox peak at -1.25 V vs. Ag/Ag^+, with well-defined reduction and oxidation peaks indicating a reversible reduction. There are vestiges of other minor processes past -1.5 V, but the iron precursor seems to satisfy the requirements for the desired metal analyte.

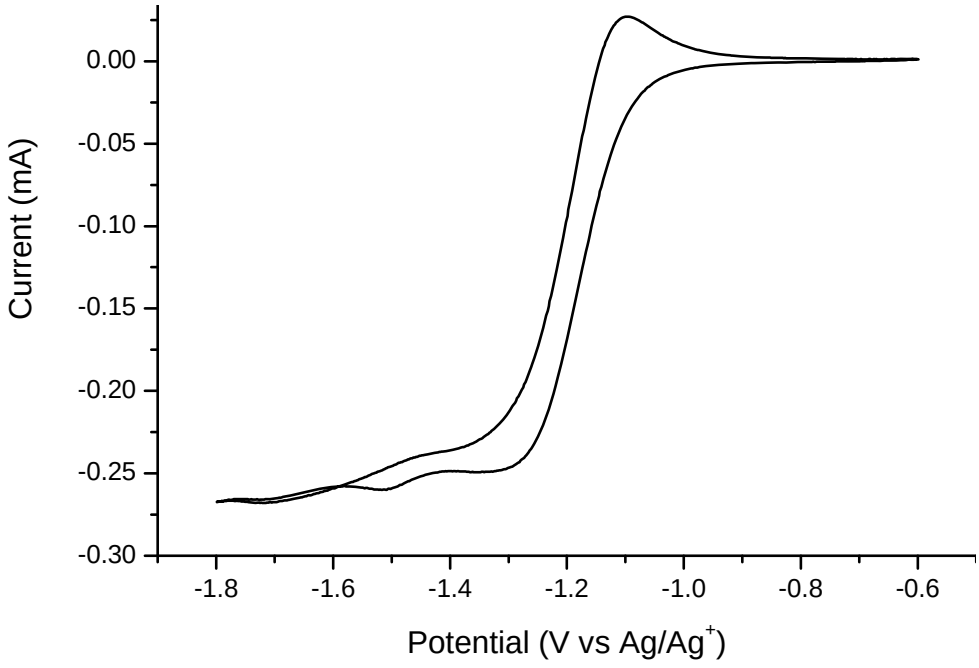

Figure 3.15 Cyclic voltammogram of 5.0 mM $Fe(acac)_3$ and 0.1 M TBAP in THF at 20 mV s^{-1}.

If $Fe(acac)_3$ does exhibit a reversible electron transfer step and no other coupled chemical reactions, it can be thought of simply as an "E_r" mechanism, rather than the E_rC_i suspected for $Pt(acac)_2$. Such a mechanism would manifest itself in DSCA analysis in a different manner than covered earlier. Since the reduced species Red is no longer reacting to form an electrochemically silent species like in the E_rC_i mechanism, the i_a/i_c ratio would not be expected to decrease like before. The reduced species would simply remain in solution for the duration of the potential step, and be oxidized back to Ox when the potential is switched back. In essence, all Red generated would be converted back to Ox (less the number of species which have diffused away from the electrode during that time period), and the current ratio would remain constant over any value of τ [28]. That behavior is precisely what is seen in Figure 3.16

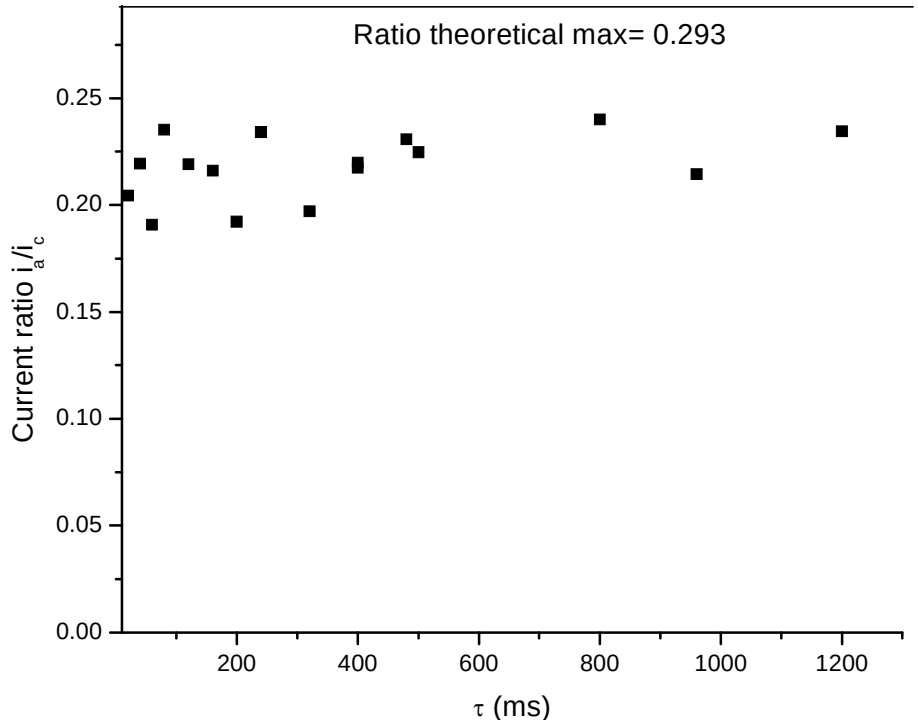

Figure 3.16 i_a/i_c vs τ for $Fe(acac)_3$. Applied potential was -0.6V at the beginning, then stepped to -1.65V and back to -0.6V, all vs. Ag/Ag+.

Sixteen different measurements are plotted from τ = 20 ms to 1200 ms, and the values average to $i_a/i_c = 0.218 \pm 0.015$ (7%). The agreement with the decaying trend in Schwarz and Shain's working curves is nowhere to be found, as is expected for processes without coupled chemical reaction complications. The theoretical value for the constant current ratio as a function of τ when measured at τ and 2τ is 0.2928, a result that is calculated from an idealized system (no coupled chemical reactions, a completely reversible redox couple, and idealized diffusion behavior for both Ox and Red). The average value found for this ratio for $Fe(acac)_3$ is smaller than that ideal number by 25%; this deviation from the theoretical value could be due to unequal diffusion coefficients for the oxidized and reduced forms of the iron complex.

3.4 Comparison of the Two PtPb Precursors Measured by Different Techniques

It is lamentable that the precursors under study in this chapter were not amenable to analysis by the same type of experiments. The analogy of electroreduction to chemical reduction is already strained at best, so comparison of reduction rates would have been stronger if they were able to be compared by the same electroanalytical methods. Though $Pt(acac)_2$ was not the platinum precursor used in Chapter 1, it is used extensively in the nanoparticle literature, and has been used to synthesize PtPb nanoparticles, so its comparison to lead (II) 2-ethylhexanoate is desirable. The rate constants at overpotential reduction conditions that were obtained in this chapter were $A \approx 10\ s^{-1}$ for single-step deposition of lead, and $k \approx 10\text{-}30\ s^{-1}$ for ligand dissociation from $Pt(acac)_2$. Given the host of assumptions taken in each set of experiments, there is compelling agreement between the two values, but the reader is once again reminded of the chasm separating electrode processes and homogeneous chemical reduction. It was never expected to find reduction rate constants which were exactly the same for each precursor, thus "proving" the

assumption of co-reduction asserted in the reaction model in Chapter 2. The goal was instead to see whether or not such analyses would yield reduction rate constants which were along the same order of magnitude as one another, thereby *not disproving* the assumption. However, the notion of a diffusion-limited reduction can most likely be eliminated. Even under the strong reductive driving forces employed in these experiments, the "reaction rates" which were obtained (~10 s^{-1}) are orders of magnitude lower than the 10^9 s^{-1} needed to assume a diffusion-limited reaction.

Besides the kinetic information garnered from these experiments, reduction potentials were estimated for all precursors in THF. They all differed greatly from their respective aqueous standard reduction potentials, and are shown in Table 3.3.

Table 3.3. Reduction potentials measured for the metal precursors in this chapter

Compound	Standard Reduction Potential of $M^{2+}_{(aq)}$ (V vs. NHE) [26]	Reduction Potential in THF (Approximate V vs. NHE, measured vs. Ag/Ag^+)	Reversible ?
$Pb(ethex)_2$	$Pb^{2+}_{(aq)}$: -0.1251	-1.5	Yes
Pt(acac)2	$PtCl_4^{2-}$: +0.758 V	< -3.3	No
$Pt(COD)Me_2$	$PtCl_4^{2-}$: +0.758 V	< -3.3	No

Obviously the two platinum precursors measured in this work had the largest shifts, which were on the order of 4 V more negative than the accepted value for the two-electron reduction of $PtCl_4^{2-}{}_{(aq)}$ to Pt^0 and $4Cl^-$ (+0.758 V vs. NHE). By comparison, Pb(2-ethylhexanoate)$_2$, only shifted approximately 1.4 V more negative than its accepted value for $Pb^{2+}_{(aq)}$ to Pb^0 (which is still a large deviation). It is assumed that the lead precursor's M-ligand interactions are more ionic in nature (like the $PtCl_4^{2-}$ complex), and the Pt-C and Pt-O interactions are more covalent [29]. The large ligand field splittings imparted to the Pt molecules (especially for the alkyl/olefin complex)

raise the Pt-L σ-bond HOMO to a much higher energy than would be present in the chloride complex. Populating the LUMO at an even higher energy level during reduction is even more difficult. The original hypothesis about the co-reduction of Pt and Pb precursors used to make PtPb nanoparticles was that the two would have very different reduction potentials, and that [Pt] would be easier to reduce than [Pb]. These experiments show the opposite is true, which would indicate that the redox potentials in organometallic species should not be expected to be close to the standard tabulated values, and that those standard values themselves should be invoked cautiously. These experimental reduction potentials indicate that, as discussed in Chapter 2, the "reduction" of $Pt(COD)Me_2$ by sodium naphthalide is more likely a chemical decomposition than a simple redox process. It also lends more credence to the possibility of an autocatalytic decomposition of $Pt(COD)Me_2$ by Pb^0 (or Pt^0). This hypothesis of a specific chemical reaction (as opposed to a diffusion-limited chemical reduction) which yields a 1:1 intermetallic certainly would be serendipitous, and could be the reason for PtPb being one of the more reproducible intermetallic nanoparticle syntheses our group has encountered.

One of the goals in undertaking this project which was so outside direct nanoparticle synthesis was to develop the capability of screening metal complexes before use as nanoparticle precursors. If a table of relative reduction or ligand dissociation rates could be generated, it might be possible to rule out certain combinations of precursors *a priori* as unfeasible for co-reduction. Unfortunately, it would seem each metal precursor necessitates its own dedicated study. Only systems which undergo straightforward reduction processes would be viable for kinetic analysis, which even in the best case would require copious time and effort to realize those results. The more common scenario for the metal complexes of interest is that seen for $Pt(COD)Me_2$, and two tin precursors whose results are shown in Appendix 1

(tin (IV) t-butoxide and tin (IV) isopropoxide) where no meaningful kinetic analyses could be applied. For metal complexes with organic ligands, it is quite common for other reaction pathways to convolute the current-potential and current-time behavior and render the reduction mechanism intractable.

If long-term research were to be continued along these lines, it would have to include complimentary techniques which could also give evidence of the timescale of reduction for nanoparticle precursors. The original treatment published by Schwarz and Shain for DSCA was as meaningful as it was because the chemical reaction they were measuring electrochemically (the reduction of azobenzene to hydrazobenzene, and subsequent benzidine rearrangement) had already been well established by several other techniques, most of which were not electrochemical. By having a known rate constant for the benzidine rearrangement, they could compare the results found through DSCA and find that they agreed with the literature values. It would be prudent to find methods other than chronoamperometry to determine the validity of the rate constants discussed in this chapter.

A different electrochemical technique which could be used is electrochemical quartz crystal microbalance, where deposition would occur on the quartz microbalance and the amount of metal deposited could be measured with time. This technique is extensively used [30], and has been demonstrated for single metal [31] as well as alloy [32] depositions. The drawback to this technique would be the relatively large size of these electrodes limiting the sweep rate and therefore the timescale able to be measured, but for slower electrode processes such as those measured in this chapter, ECQM could be a viable complimentary technique. Another possible category of experiments is flow-reaction techniques, where microchannel reactors could be used to monitor the mixing and reaction of reducing agent and metal precursor on short timescales. The method of tracking the reaction could be as simple as measuring the

decay of optical absorption due to sodium naphthalide and the increase in absorption due to colloidal metal particles, or could be as complex as using synchrotron radiation to perform XAFS analysis and monitor the appearance of metal-metal nearest-neighbor interactions in nucleated nanoparticles. Flow techniques have the drawback of requiring even more expertise from specialized researchers than electrochemical methods do, but that shortcoming is compensated by the satisfaction that there is better comparison to what occurs in an actual synthesis. The process being monitored would be genuine chemical reduction, and no analogy to synthesis would be required as in electrochemical methods.

REFERENCES

1. Gunawardena, G., et al., *Electrochemical Nucleation .1. General-Considerations.* Journal of Electroanalytical Chemistry, 1982. **138**(2): p. 225-239.
2. Marcus, R.A., *On the Theory of Oxidation-Reduction Reactions Involving Electron Transfer. V.Comparison and Properities of Electrochemicaland Chemical Rate Constants.* The Journal of Physical Chemistry, 1963. **67**(4): p. 853-857.
3. Marcus, R.A., *Chemical and Electrochemical Electron-Transfer Theory.* 1964. **15**(1): p. 155-196.
4. Marcus, R.A., *On the Theory of Electron-Transfer Reactions. VI. Unified Treatment for Homogeneous and Electrode Reactions.* The Journal of Chemical Physics, 1965. **43**(2): p. 679-701.
5. Gunawardena, G., et al., *Electrochemical Nucleation .3. the Electrodeposition of Mercury on Vitreous Carbon.* Journal of Electroanalytical Chemistry, 1982. **138**(2): p. 255-271.
6. Gunawardena, G., G. Hills, and B. Scharifker, *Induction Times for the Formation of Single Mercury Nuclei on a Platinum Microelectrode.* Journal of Electroanalytical Chemistry, 1981. **130**(1-3): p. 99-112.
7. Scharifker, B.R. and J. Mostany, *3-Dimensional Nucleation with Diffusion-Controlled Growth .1. Number Density of Active-Sites and Nucleation Rates Per Site.* Journal of Electroanalytical Chemistry, 1984. **177**(1-2): p. 13-23.

8. Mostany, J., J. Mozota, and B.R. Scharifker, *3-Dimensional Nucleation with Diffusion-Controlled Growth. 2. The Nucleation of Lead on Vitreous Carbon.* Journal of Electroanalytical Chemistry, 1984. **177**(1-2): p. 25-37.

9. Mostany, J., J. Parra, and B.R. Scharifker, *The Nucleation of Lead from Halide-Containing Solutions.* Journal of Applied Electrochemistry, 1986. **16**(3): p. 333-338.

10. Sluyters-Rehbach, M., et al., *The Theory of Chronoamperometry for the Investigation of Electrocrystallization - Mathematical Description and Analysis in the Case of Diffusion-Controlled Growth.* Journal of Electroanalytical Chemistry, 1987. **236**(1-2): p. 1-20.

11. Heerman, L. and A. Tarallo, *Digital simulation of the growth of a hemispherical nucleus by diffusion limited aggregation.* Journal of Electroanalytical Chemistry, 1998. **455**(1-2): p. 265-269.

12. Heerman, L. and A. Tarallo, *Electrochemical nucleation on microelectrodes. Theory and experiment for diffusion-controlled growth.* Journal of Electroanalytical Chemistry, 1998. **451**(1-2): p. 101-109.

13. Heerman, L. and A. Tarallo, *Theory of the chronoamperometric transient for electrochemical nucleation with diffusion-controlled growth.* Journal of Electroanalytical Chemistry, 1999. **470**(1): p. 70-76.

14. Heerman, L. and A. Tarallo, *Electrochemical nucleation with diffusion-limited growth. Properties and analysis of transients.* Electrochemistry Communications, 2000. **2**(2): p. 85-89.

15. Butler, J.N., *Reference Electrodes*, in *Advances in Electrochemistry and Electrochemical Engineering*, P. Delahay, C. Tobias, Editor. 1970, John Wiley and Sons: New York. p. 77-175.

16. Andronic, L.S. and R.H. Hill, *The mechanism of the photochemical metal organic deposition of lead oxide films from thin films of lead (II) 2-ethylhexanoate.* Journal of Photochemistry and Photobiology a-Chemistry, 2002. **152**(1-3): p. 259-265.

17. Kashchiev, D. and A. Milchev, *Kinetics of Initial-Stage of Electrolytic Deposition of Metals .1. General Theory.* Thin Solid Films, 1975. **28**(2): p. 189-200.

18. Kashchiev, D. and A. Milchev, *Kinetics of Initial-Stage of Electrolytic Deposition of Metals .2. Potentiostatic Conditions.* Thin Solid Films, 1975. **28**(2): p. 201-211.

19. Milchev, A., E. Michailova, and T. Zapryanova, *Initial stages of electrochemical alloy formation: size and composition of critical nuclei.* Electrochemistry Communications, 2004. **6**(7): p. 713-718.

20. Milchev, A. and S. Stoyanov, *Classical and Atomistic Models of Electrolytic Nucleation: Comparison with Experimental Data.* Journal of Electroanalytical Chemistry, 1976. **72**(1): p. 33-43.

21. Milchev, A., et al., *Electrocrystallisation of metal catalysts: nucleation and growth of platinum on a titanium electrode.* Journal of Crystal Growth, 2001. **226**(1): p. 138-147.

22. Schwarz, W.M. and I. Shain, *Investigation of First-Order Chemical Reactions Following Charge Transfer by a Step-Functional Controlled Potential Method. The Benzidine Rearrangement.* 1965. **69**(1): p. 30-40.

23. Testa, A.C. and W.H. Reinmuth, *Stepwise Reactions in Chronopotentiometry.* Analytical Chemistry, 1961. **33**(10): p. 1320-&.

24. Anderson, C.W., K.R. Lung, and T.A. Nile, *Electrochemistry of Homogeneous Catalysts - Correlation of the Electrochemistry and the Ziegler-Natta Catalytic*

Activity of Metal Acetylacetonate Complexes. Inorganica Chimica Acta-Articles and Letters, 1984. **85**(1): p. 33-36.

25. Sock, O., P. Lemoine, and M. Gross, *Mechanisms of Electrochemical Reduction of Acetylacetonate Complexes of Transition-Metals.* Electrochimica Acta, 1981. **26**(1): p. 99-109.
26. Bard, A.J., Faulkner, Larry R. , *Electrochemical Methods: Fundamentals and Applications*. 2nd ed. 2001, Hoboken NJ: John Wiley and Sons, Inc. 833.
27. Richert, S.A., P.K.S. Tsang, and D.T. Sawyer, *Ligand-Centered Redox Processes for Mnl3, Fel3, and Col3 Complexes (L = Acetylacetonate, 8-Quinolinate, Picolinate, 2,2'-Bipyridyl, 1,10-Phenanthroline) and for Their Tetrakis(2,6-Dichlorophenyl)Porphinato Complexes [M(Por)].* Inorganic Chemistry, 1989. **28**(12): p. 2471-2475.
28. Childs, W.V., et al., *Voltammetric and Coulometric Studies of Mechanism of Electrohydrodimerization of Diethyl Fumarate in Dimethylformamide Solutions.* Journal of the Electrochemical Society, 1971. **118**(6): p. 874-&.
29. Lever, A.B.P., *Electrochemical Parametrization of Metal-Complex Redox Potentials, Using the Ruthenium(Iii) Ruthenium(Ii) Couple to Generate a Ligand Electrochemical Series.* Inorganic Chemistry, 1990. **29**(6): p. 1271-1285.
30. Eickes, C., et al., *The electrochemical quartz crystal microbalance (EQCM) in the studies of complex electrochemical reactions.* Electrochimica Acta, 2000. **45**(22-23): p. 3623-3628.
31. Smith, E.L., et al., *Time Resolved in Situ Liquid Atomic Force Microscopy and Simultaneous Acoustic Impedance Electrochemical Quartz Crystal Microbalance Measurements: A Study of Zn Deposition.* Analytical Chemistry, 2009. **81**(20): p. 8466-8471.

32. Martin, A.J., A.M. Chaparro, and L. Daza, *Electrochemical quartz crystal microbalance study of the electrodeposition of Co, Pt and Pt-Co alloy.* Journal of Power Sources, 2007. **169**(1): p. 65-70.

CHAPTER 4

Thin-Film Inspired Palladium Alloy Nanoparticle Electrocatalysts for Oxygen Reduction

4.1 Introduction

This chapter focuses on the exploration of a potential catalyst system for the oxygen reduction reaction (ORR). This reaction, as mentioned in the introduction chapter, is difficult to catalyze, owing to the demanding requirements of the relatively complex reaction where nine species (four electrons, four protons, and one O_2 molecule) must participate. The slow rate of this reaction is the single largest contributor to loss of potential in a working fuel cell. Also covered in that discussion was that one of the tools used in the Energy Materials Center at Cornell to tackle the search for new catalysts for fuel oxidation and oxygen reduction is the thin film sputtering capabilities found in the Bruce van Dover group [1]. They use magnetron sputtering to deposit continuous composition spreads of any three or four metals on a three inch silicon substrate. The result is a metal film that varies in atomic composition across the wafer at approximately one atomic percent per millimeter [1]. By precisely controlling the deposition rates of the three metals, the composition spread encompasses over 60% of the phase space of a ternary phase diagram. The electrocatalytic evaluation of the film with a spatially sensitive assay (either a fluorescence technique, or a movable electrochemical cell) is able to rapidly screen the film for areas of increased activity, and post-analysis characterization gives the metal ratio and crystal structure of that active area [1-8]. It is then the goal of the current research to reproduce any active thin film areas as nanoparticles.

Palladium has been a material of interest for oxygen reduction for some time, and has ample precedent in the literature [9-14], though not as much as Pt [12]. Fuel cell researchers have modified palladium for electrocatalytic purposes [10, 11, 13, 15-28], and this line of research was pursued further in the van Dover group. One system that was investigated for ORR activity by Jonathan Petrie (Ph.D. 2010 [29]) is a ternary alloy of palladium, tungsten and X, where X is a first-row transition metal. By using a novel 1cm^2 electrochemical cell to spatially probe the three inch substrate [3], the most active areas of the film could be determined. When the current densities for oxygen reduction at +0.85V vs. RHE for Pd-W-X are plotted versus element X (Figure 4.1), it is apparent that the most active area from the film where X is vanadium gives a higher current density than the most active areas of the films from the other eight first row transition metals (scandium was not studied due to its impractical use as a sputtering target). Post-analysis using an X-ray diffraction area detector (GADDS), microprobe elemental analysis and X-ray photoelectron spectroscopy (XPS) found the most active area to be an FCC phase that indexed to Pd crystal structure, and showed a metal ratio of 88 at% Pd, 6 at% W, and 6 at% V. This ternary composition is a departure from the dogmas given earlier about intermetallic compounds being a chief interest for electrocatalysis, as the compositions shown in this chapter are alloys. The activities of the Pd-W-V thin film were also plotted versus the lattice constant determined by GADDS (Figure 4.2), and showed a sharp peak in current density at a=3.887 Å (slightly off the accepted unit cell constant of 3.889 Å for Pd) and lower current densities for lower and higher cell constants. The plot in Figure 4.2 shows a trend established for the addition of base metals to the Pd thin film; the current density at 0.85 V vs. RHE is the highest for $Pd_{0.88}W_{0.06}V_{0.06}$, but $Pd_{0.90}W_{0.10}$ (middle dashed line, "Pd-W") also has a higher activity than just palladium (lowest dashed line). It would be a consistent observation if the nanoparticle catalysts also exhibited this

increasing activity when metals are added to palladium. Reproduction of thin film activity by nanoparticles has not consistently yielded the same electrocatalytic results, so successfully attaining this activity would make a compelling case for the use of thin film combinatorial methods in the development of new fuel cell electrocatalysts.

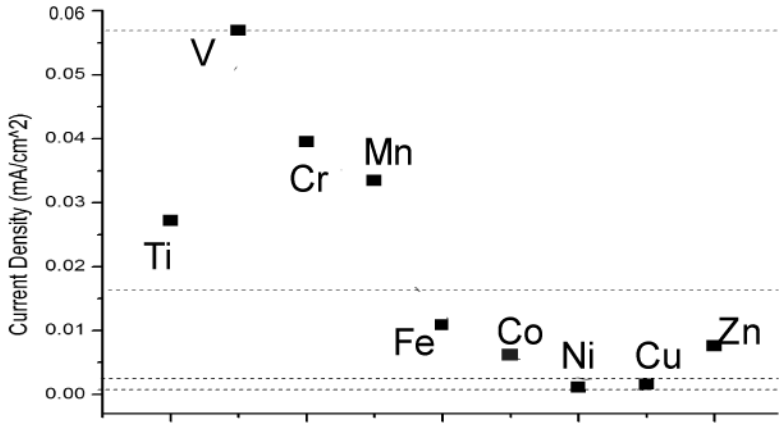

Figure 4.1 Current density at 0.85V vs. RHE of an air-saturated 0.1M sulfuric acid solution in a 1 cm^2 scanning cell over sputtered thin film electrodes. Each element listed represents a thin film continuous composition spread co-sputtered with Pd and W, and each point corresponds to the current density at the most active area on those films.

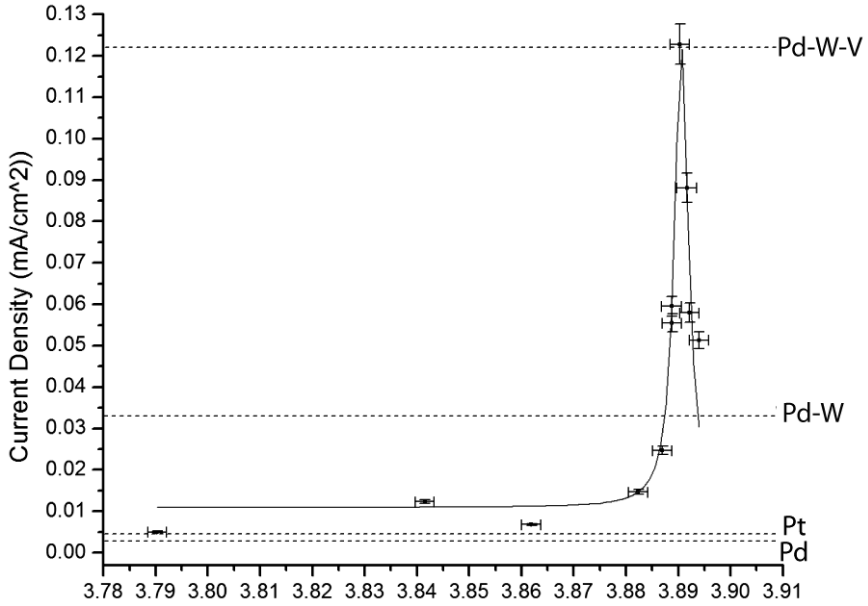

Figure 4.2 Current density at 0.85V vs. RHE of an air-saturated 0.1M sulfuric acid solution in a 1 cm^2 scanning cell over a thin film electrode of co-sputtered Pd, W and V, versus the Pd lattice constant of different spots on the film. Dashed lines mark the current density benchmarks for thin film Pd, thin film Pt, and alloys of Pd-W and Pd-W-V with the approximate compositions $Pd_{0.90}W_{0.10}$ and $Pd_{0.88}W_{0.06}V_{0.06}$.

The binary phase diagrams of Pd-W and Pd-V [30] show that the solid-solution solubility limits from room temperature up to 1552°C of both W (22%) and V (approximately 21%) in Pd are well above the composition of the target phases, where the total alloying metal concentration never exceeds 20%. It is unknown whether or not the Pd-W-V ternary phase diagram allows for more than 22% alloying metal (W + V), but need not be known for the purposes of this study. Long-term stability of the alloy at the high operating potentials (greater than +0.8 V vs. RHE) and the acidic pH (~1) of a fuel cell cathode is recognized as an issue right away. In the Pourbaix diagrams [31] of electrochemical equilibria, both tungsten and vanadium are expected under these conditions to be oxidized to WO_3 and water-soluble VO^{2+}, respectively,

and certainly the metals themselves would not be stable. Palladium is also relatively unstable under those conditions compared to platinum or gold, for example, and could be prone to dissolution at the highest potentials of fuel cell operation, but it is possible that the proper conditions could be used where Pd remains in its neutral metal form. Given palladium's relative stability, a low-concentration metal alloy such as the ~12 at% compositions under consideration could be trapped in the Pd particle or thin film, protecting the electropositive metal or metals from electrochemical leaching and retaining the properties of the alloy. Testing of long-term stability would be necessary if the composition shows electrocatalytic activity that compares favorably to platinum.

4.2 Pd and W Nanoparticles Synthesized by Different Reducing Agents

It was mentioned in Chapter two that using sodium borohydride as a reducing agent has the advantage of rinsing cleanly away after synthesis of PtPb nanoparticles, and that cleanliness is hypothesized to explain higher electrocatalytic activity when comparing to nanoparticles prepared by sodium naphthalide reductions. While sodium borohydride (-0.6 V vs. NHE) is not a strong enough reducing agent to reduce a V^{n+} precursor where n= 2, 3 or 4 to V^0 (-1.13 V vs. NHE for V^{II}, and more negative for higher oxidation states), it is capable of reducing Pd^{II} (+0.915 V, and even more positive than that for Pd^{IV}) and W^{VI} (-0.09V), at least according to their standard reduction potentials. Sodium naphthalide (-2.3V) should be able to reduce all three, though ligand-induced potential shifts and relative reduction rates are still a concern as was discussed in Chapters 2 and 3. Both sodium naphthalide and sodium borohydride were used to synthesize palladium nanoparticles, and attempts were made to synthesize tungsten nanoparticles with each reducing agent. Single component nanoparticles are the simplest to prepare and characterize, and they serve as baselines for the binary and ternary targets discussed later.

4.2.1 Experimental

Sodium hexachloropalladate tetrahydrate ($Na_2PdCl_6 \cdot 4H_2O$), tungsten hexachloride, sodium, naphthalene and sodium borohydride were purchased from Aldrich and used as-received. Absolute methanol was deaerated with bubbling argon for one hour before use, while tetrahydrofuran and diglyme were dried over molecular sieves in a stainless steel solvent system and dispensed under positive pressure of argon. All manipulations were carried out in either an argon atmosphere glovebox, or on a Schlenk argon/vacuum line.

For sodium naphthalide reductions, sodium (0.0442 g, 1.9 mmole) and naphthalene (0.2458 g, 1.9 mmole) were left to stir overnight as described in Chapter two. Once sodium naphthalide had formed, sodium hexachloropalladate tetrahydrate (0.0700 g, 0.16 mmole) was placed in a flask, then evacuated and purged with argon three times. The large molar excess of reducing agent in each case was used to account for side reactions involving adventitious water and oxygen, as well as the waters of hydration from the palladium precursor. After dissolving in diglyme, the clear orange Pd precursor solution was cannlulaed to the room-temperature NaNp solution and stirred for fifteen minutes. The reactants were then heated to 150° C and stirred for sixty minutes. Sixty minutes is an arbitrary reaction time; it has given ample time for particle precipitation in past experiments such as in Chapter two, but the conditions have not been optimized for this system. After heating and stirring were stopped, there was a black precipitate in a dark suspension. The suspension was transferred by cannula to a sealed Ar-atmosphere centrifuge tube, and centrifuged at 7000 rpm for twenty minutes. Methanol and hexanes wash steps followed in the same manner as in Chapter two, and lead to a black solid product and a clear, tea-colored supernatants. After drying the black solid under vacuum, the tube was backfilled with argon, and the septum was pierced with a needle to allow slow in-diffusion of air

overnight. This same procedure was followed in attempts to make W nanoparticles from WCl_6 (0.1079 g, 0.272 mmol), except methanol wash was avoided due to the propensity for methanol to oxidize W powder to some soluble tungsten methoxide, $W(OMe)_x$. The same reaction observations from Pd held true for W, except that the clear metal precursor solution that was cannulaed to the reducing agent was blue instead of orange.

When sodium borohydride was the reducing agent for Pd reduction, sodium borohydride (0.1532 g, 4.0 mmole) and sodium hexachloropalladate tetrahydrate (0.0700 g, 0.16 mmole) were each placed in separate flasks, evacuated and purged with argon, and each dissolved in 20mL methanol. Mild effervescence occurred during the first few minutes after dissolving sodium borohydride. One-hundred percent excess $NaBH_4$ past the stoichiometric amount was used to account for the side reaction of BH_4^- with methanol and still have enough borohydride to reduce the metal precursor. The Pd precursor was cannulaed to the $NaBH_4$ solution and stirred at room temperature for sixty minutes. At that time there was a black precipitate in a clear colorless solution. The product work-up was the same as described for Pd via NaNp reduction.

Alternate borohydride reducing agents were explored for W nanoparticle synthesis. Lithium triethyl borohydride and potassium triethyl borohydride were purchased from Aldrich as 1.0 M solutions in THF, and directly used. 1.6 mL (1.6 mmole each) were injected directly to the tungsten hexachloride precursor (0.1079g, 0.272mmol) dissolved in THF while in the glovebox. Both reducing agents yielded an instant color change to black solutions. The potassium triethylborohydride product precipitated after only ten minutes, so after the precipitate settled, the supernatant THF was decanted, then the product was washed with THF, poured in a centrifuge tube, sealed with a septum, removed from the glovebox, and centrifuged at 9000 rpm for 20

minutes. The clear tea-colored supernatant was removed and the sample was pumped back into the glovebox without air exposure. The dark brown-to-black powder was transferred to a fused silica tube, sealed under vacuum and annealed at 650°C for 24 hours. The lithium triethylborohydride product did not precipitate on its own, so it was precipitated by addition of hexanes to the THF suspension, and then centrifuged at 4000 rpm for five minutes. The clear colorless supernatant was removed, and the tube was also pumped back into the glovebox without air exposure. In this case, the black powder was not annealed.

4.2.2 Characterization

Powder X-ray characterization was performed on a Rigaku Ultima IV X-ray diffractometer with Cu Kα radiation. Microprobe analysis was done in a JEOL8900 EPMA microprobe at 20 kV accelerating voltage. Thermogravimetric analysis was done on a TA Instruments Q50 thermogravimetric analyzer. Electrocatalytic analysis was performed by Dr. Qin Zhou, and consisted of preparation of a nanoparticle-Nafion ink in isopropanol, and depositing and drying the ink on a 4 mm diameter glassy carbon electrode at a loading of 20 μg unsupported catalyst. Reduction currents were measured while rotating the electrode at 1600 rpm and at a potential sweep rate of 5 mVs^{-1} from 1.0 V to 0 V vs. Ag/AgCl in O_2-saturated 0.1 M $HClO_4$. Potentials were then converted to RHE for all figures. To prevent false-positive ORR current due to trace platinum left over from analysis of Pt-containing catalysts, all electrochemical cells and glassware was kept separate from those used for Pt-containing systems. A carbon fiber counter electrode was used rather than a Pt wire, as trace Pt can dissolve from the counter electrode at fuel cell cathode potentials and re-deposit elsewhere. Any reference to “electrochemical cycling” or “electrochemical cleaning” in this

chapter refers to cycling the potential between 0 and 1.2 V vs. NHE at 50 mV s^{-1} for 20 minutes.

4.2.3 Results and discussion

Powder X-ray diffraction showed that the NaNp reduction of the Pd precursor yielded nanoparticles that matched the literature diffraction pattern of palladium (PDF# 00-046-1043) (Figure 4.3). Whole pattern profile fitting determined the average Pd crystallite sizes to be between 2-3 nanometers for all samples.

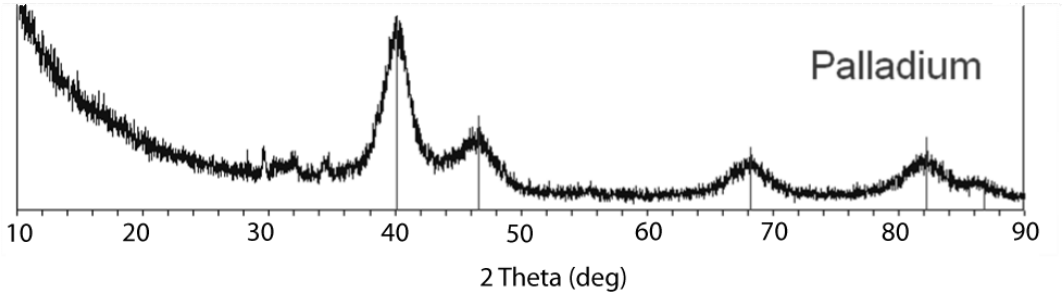

Figure 4.3 Powder X-ray diffraction pattern of palladium nanoparticles synthesized by injection into sodium naphthalide in diglyme at room temperature, then stirring at 150°C.

Most elements like palladium have several reported diffraction patterns due to different preparation methods of the standards they were measured from, and the deviations among those patterns can match a given Pd nanoparticle product better than others. Since departures from the literature values indicate structural changes due to a variety of reasons (i.e. alloying, crystal strain, etc.), it is important to consistently use the same International Centre for Diffraction Data (ICDD) powder diffraction file (PDF) card as the reference pattern when making sample-to-sample nanoparticle

comparisons. For borohydride-reduced samples, the powder X-ray diffraction patterns are shifted to lower angles from those literature values as seen in Figure 4.4.

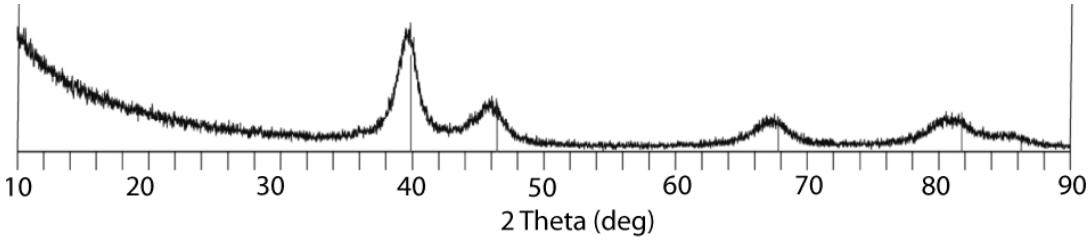

Figure 4.4 Powder X-ray diffraction pattern of palladium nanoparticles synthesized by sodium borohydride reduction in methanol at 25°C.

This shift and corresponding Pd lattice expansion is attributed to hydrogen absorption into the Pd particles. Sodium borohydride reacts with methanol to form sodium tetramethoxyborate and hydrogen, (Equation 4.1) [32], and is the source of the H_2 in solution.

$$NaBH_4 + 4\,CH_3OH \rightarrow NaB(OCH_3)_4 + 4\,H_2 \qquad (4.1)$$

The diffraction pattern in Figure 4.4 matches a palladium PDF card (#01-087-0643) which has a lattice constant of 3.91Å instead of 3.89Å, but no titration was performed to confirm the degree of hydrogen incorporation. The domain sizes for these borohydride-reduced samples were between 2 and 3 nm, just like the naphthalide products. Many of the patterns from naphthalide reactions showed inclusion of sodium chloride, the main expected secondary phase, indicating that several methanol or even water wash steps were often necessary to fully remove the salt byproduct. The borohydride products showed no salt by XRD.

Tungsten nanoparticles are highly susceptible to oxidation upon exposure to air. Attempts to exclude oxygen and water vapor yielded black products, some of

which eventually turned white before air-free X-ray diffraction patterns could be taken. In the case where NaNp was the reducing agent, the white product corresponds to a mixture of sodium tungstate (Na_2WO_4) and sodium chloride by XRD (not shown). Microprobe analysis for these samples shows only Na, W and Cl, and O (also not shown). As was discussed in Chapter 2, all microprobe results shown here are semiquantitative, and will not include carbon or oxygen in their analyses; both those elements are assuredly present in the products, but their quantification will not be attempted. The presence of sodium tungstate is hypothesized to have occurred by reaction with water vapor, oxygen, and sodium, possibly in a manner as shown in Equations 4.2 - 4.3.

$$W_{nano} + 3/2\ O_{2(g)} + H_2O_{(g)} \rightarrow H_2WO_4 \quad (4.2)$$

$$H_2WO_4 + 2NaCl \rightarrow Na_2WO_4 + 2HCl \quad (4.3)$$

Equations 4.2 and 4.3 have not been verified for this system, but they account for the presence of sodium tungstate from possible reactants.

As a few side experiments, alternative reducing agents (agents which were largely not used in this dissertation) were used to reduce WCl_6 in THF. The lithium and potassium triethyl borohydrides ($LiB(Et)_3H$ and $KB(Et)_3H$) are slightly stronger reducing agents than $NaBH_4$, but are soluble in THF, so they could be used to synthesize W nanoparticles without use of methanol, which can dissolve W precipitates. Neither of the triethylborohydrides was able to conclusively produce pure W nanoparticles, even upon annealing. Potassium triethyl borohydride yielded a black powder that was a mixture of KCl and WO_2 by XRD (Figure 4.5), and lithium triethyl borohydride gave a mixture of LiCl and $Li_2WO_2Cl_2$ (not shown). The usual visual cues for metal oxidation (dark powder turning white) explain the occurrence of Na_2WO_4, since in that case the tungsten is W^{VI}, and therefore fully oxidized. But since tungsten is W^{IV} in both WO_2 and $Li_2WO_2Cl_2$, dark colors are expected due to the

metallic conductivity of W^{IV} in WO_2, for instance. The presence of W cannot be entirely ruled out by XRD in either case, as both KCl and $Li_2WO_2Cl_2$ contain peaks which overlap with tungsten's strongest reflection (as shown for KCl in Figure 4.5). The rest of the tungsten reflections in each case are either absent because tungsten did not form, or are too weak with respect to the more crystalline oxide phases.

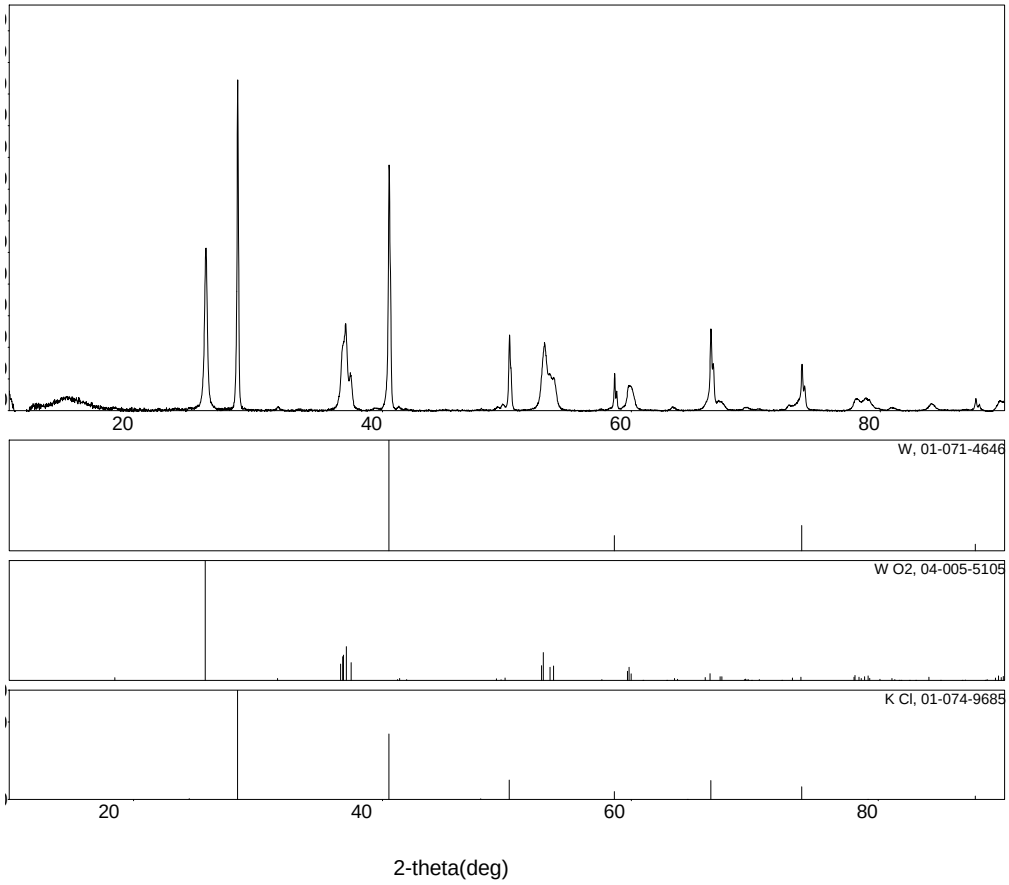

Figure 4.5 Powder X-ray diffraction pattern of annealed product of $KB(Et)_3H$ reduction of WCl_6. The powder is composed of KCl (lowest window containing reported peaks) and WO_2 (middle), but may or may not contain W metal (upper window).

As was the case for PtPb nanoparticles discussed in Chapter 2, transmission electron microscopy confirmed the similarities between particle size and the crystallite sizes calculated by XRD peak broadening. Figure 4.6 shows a micrograph of a Pd nanoparticle sample synthesized by sodium naphthalide reduction, while Figure 4.7 shows a sodium borohydride product. Each shows the expected highly agglomerated particles, and that the crystallites are between 4-6 nm. The calculated domain sizes for the same samples were 3.5 nm and 3.0 nm, which are in rough agreement with the visual particle sizes. Since no capping agents were used, we expect X-ray domain sizes to always be less than (or at best, equal to) the TEM particles size. No TEM characterization was performed for the W nanoparticle products, as they would have oxidized upon deliberate air exposure before analysis, and would more accurately be described at that point as WO_x particles.

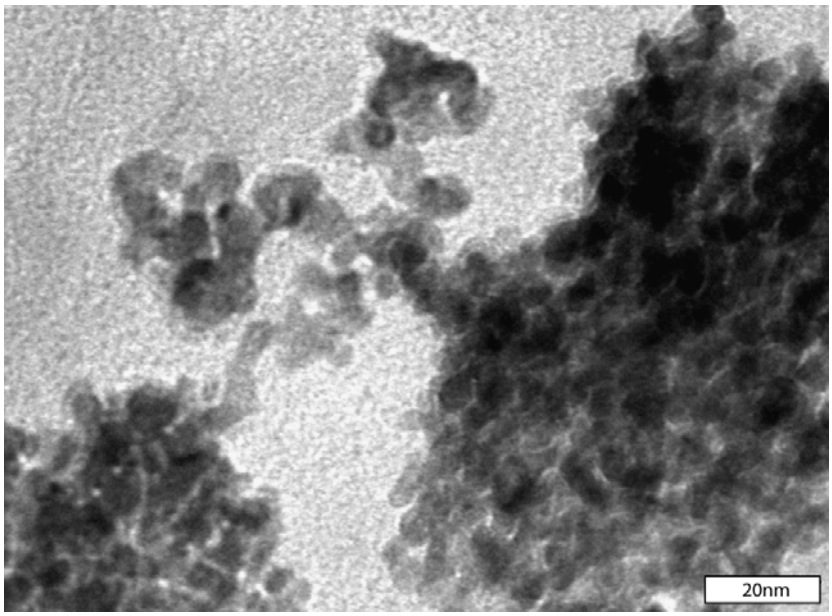

Figure 4.6 Transmission electron micrograph of palladium nanoparticles synthesized by sodium naphthalide reduction in diglyme at 150°C.

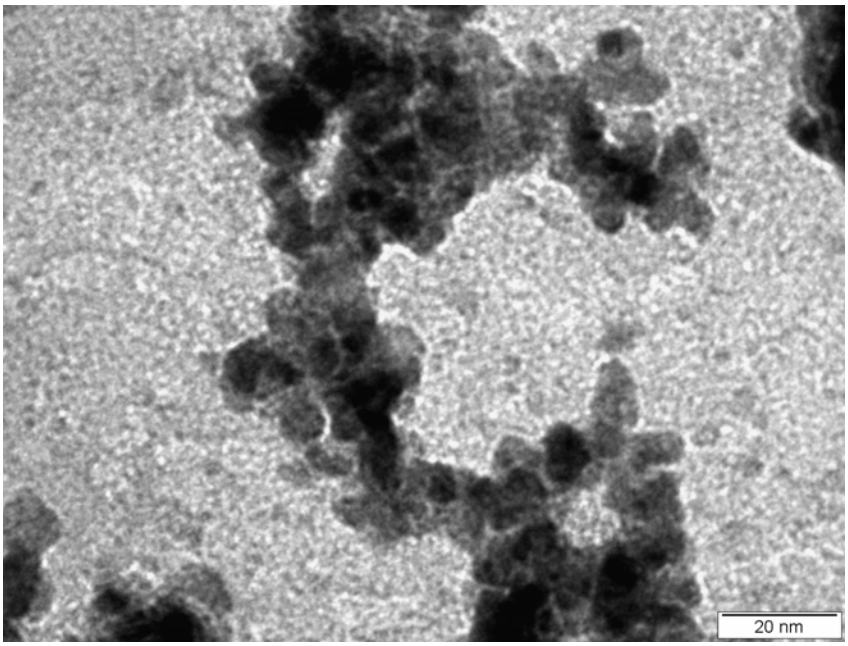

Figure 4.7 Transmission electron micrograph of palladium nanoparticles synthesized by sodium borohydride reduction in methanol at 25°C.

Elemental analysis of NaNp-reduced palladium showed what has been consistently found for metal nanoparticles from sodium naphthalide reductions- there is almost always left over sodium that does not wash away. Figure 4.8 shows a representative EDX spectrum from palladium particles which have been reduced by sodium naphthalide and heated in solution to 150°C. Though palladium is the major non-oxygen element detected, there is approximately the same amount of sodium as palladium present in all the spectra (the large silicon peak is from the sample's substrate). When excluding silicon and oxygen from quantification, sodium accounted for between 20 and 60 at% of the sample. Curiously, there is very little (<1 at%) chlorine detected. Quantification of chloride in the presence of excess palladium is problematic due to the Cl $K_{\beta 1}$ (2.82keV) and Pd $L_{\alpha 1}$ (2.84keV) lines overlapping (this is especially apparent in Figure 4.13), so it is presumed that the Na:Cl ratio is closer to

1:1 than the quantification results would suggest. However, the Cl $K_{\alpha 1}$ peak's intensity is indeed quite small compared to the relative intensity of the Pd and Na peaks, and there appears to be a genuine dearth of chlorine. The sodium ions must be counter-balanced by some negatively charged species, which is likely oxygen-containing. Microprobe analysis for the Pd nanoparticles reduced by sodium borohydride (Figure 4.9) showed palladium and a small amount (<1at%) of sulfur of unknown origin. Sodium and chlorine were nearly undetectable, presumably because the greater solubility of NaCl in methanol than in diglyme prevents the salt side product from precipitating along with the palladium. This phase purity agrees with what was seen in XRD, and illustrates the benefits of using borohydride over naphthalide as the reducing agent, even though the precursors are identical to those used in comparable naphthalide reductions.

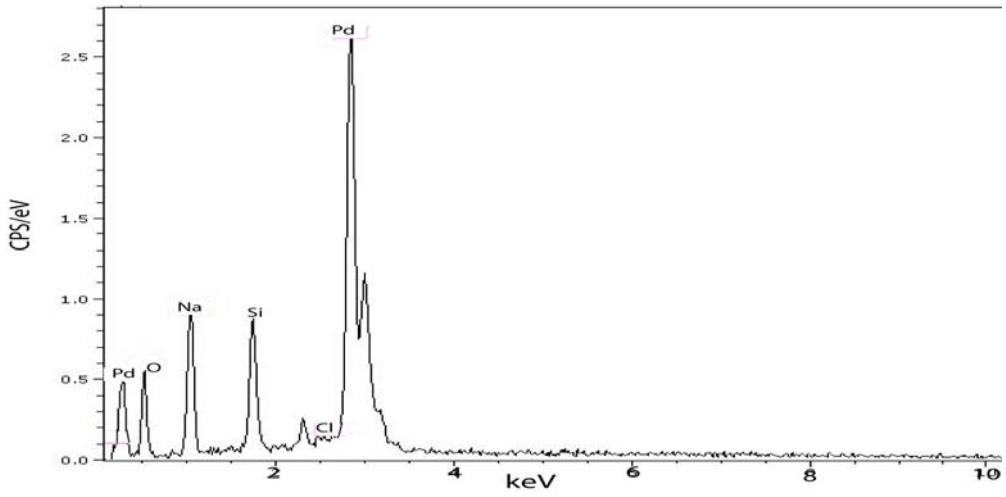

Figure 4.8 Energy-dispersive X-ray spectrum of palladium nanoparticles synthesized by sodium naphthalide reduction in diglyme at 150°C.

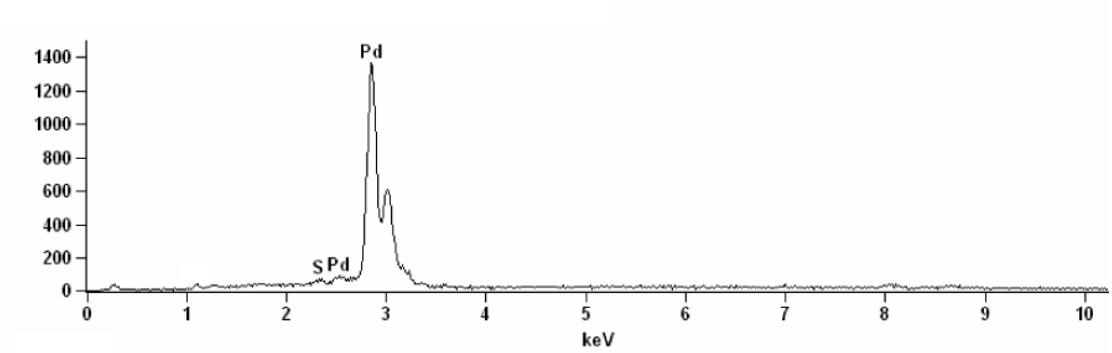

Figure 4.9 Energy-dispersive X-ray spectrum of palladium nanoparticles synthesized by sodium borohydride reduction in methanol at 25°C.

Thermogravimetric analysis of the products corroborated the observations that sodium borohydride reductions leave less organic side products than sodium naphthalide. Figure 4.10 shows two TGA traces for Pd nanoparticles: one for NaNp reduction, and one for $NaBH_4$. The sample prepared through sodium borohydride reduction shows mass loss of only 6% when heated in argon to 550°C, while the sodium naphthalide-reduced sample loses 16% of its mass. That high a mass loss is ascribed to pyrolysis and sublimation of organic residues, and when accounting for the large mass difference between Pd and C, would correspond to a large carbon to metal atom ratio in the as-formed product, since a 1:1 C:Pd ratio would be 11 wt% carbon. The presence of at least one carbon atom for every palladium atom is presumed to affect the electrocatalytic activity, so at first glance we expect that the borohydride-reduced samples will have better ORR activity than the naphthalide-reduced ones.

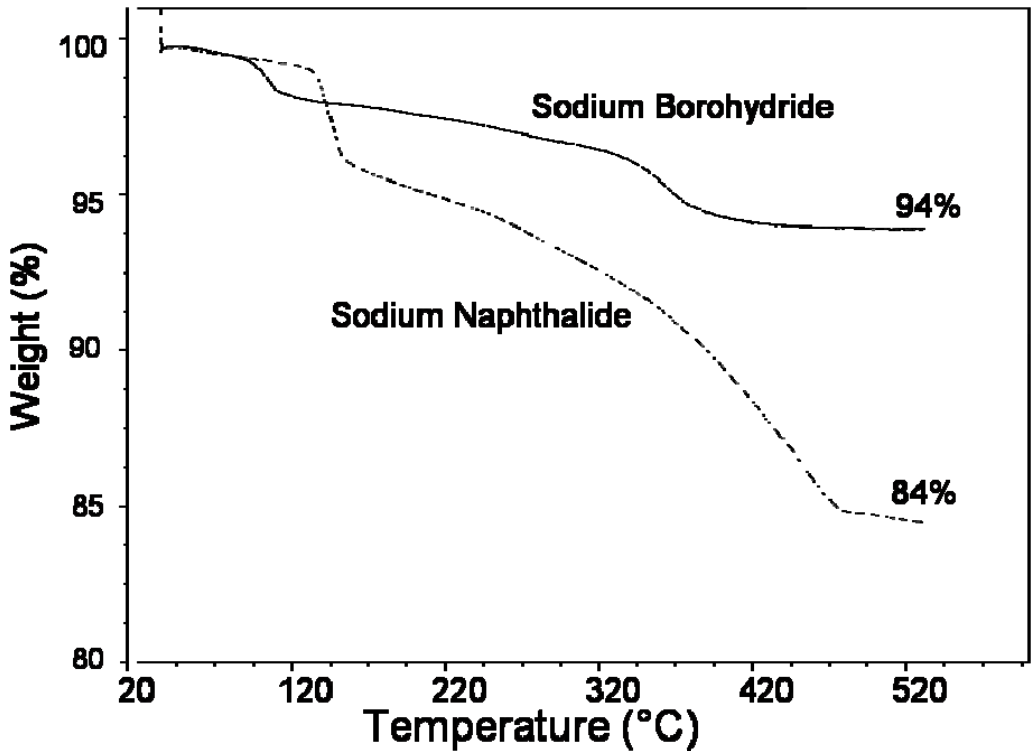

Figure 4.10 Thermogravimetric analysis of palladium nanoparticles synthesized by sodium naphthalide reduction in diglyme at 150°C and by sodium borohydride reduction in methanol at 25°C.

Oxygen reduction polarization curves were recorded for both types of Pd nanoparticles, and are shown in Figure 4.11. Both show onset of oxygen reduction current at approximately 0.85 V vs. RHE, but the Pd particles reduced by sodium borohydride has a steeper slope and higher current density on the first sweep down to 0.23 V vs. RHE, showing that it is a better electrocatalyst than Pd prepared by sodium naphthalide, at least on the first sweep. However, the distinct hump in the rotating disk voltammogram is indicative of the electrocatalyst itself reacting, and should not be inferred to be a sign of ORR activity enhancement over the NaNp sample. After multiple potential cycles to achieve electrochemical steady state, each has suffered a considerable loss of electrocatalytic activity. The current density of the NaNp-

palladium sample at 0.23 V vs. RHE has decreased by one quarter its original value, and the onset potential of the $NaBH_4$ catalyst is lowered by approximately 70 mV. The positive observation of the $NaBH_4$-derived Pd catalyst is that it regains some of the activity after electrochemical cycling. Though the post-cycling ORR curve does not rebound to the same level as the first scan, it shows enhanced activity over the second scan, whereas the activity of the NaNp sample only degrades.

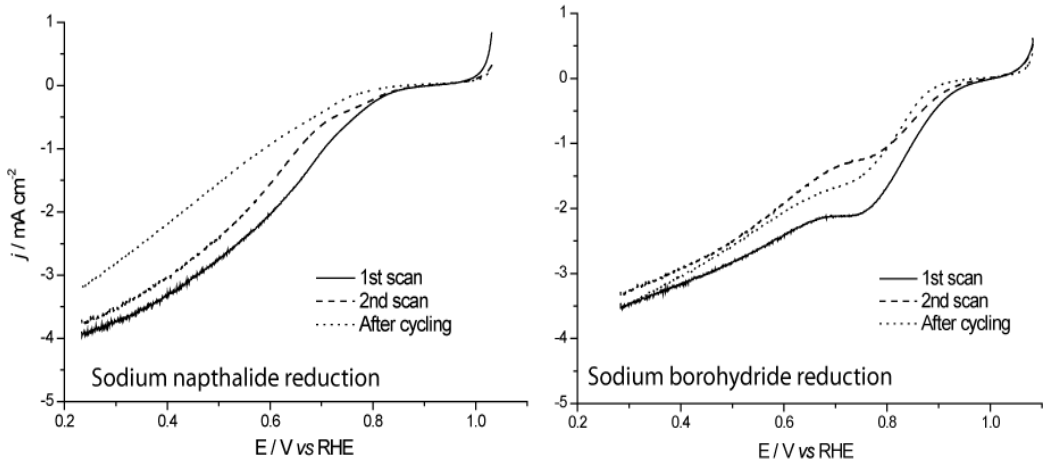

Figure 4.11 Oxygen polarization curves of palladium nanoparticles synthesized by sodium naphthalide reduction in diglyme at 150°C and by sodium borohydride reduction in methanol at 25°C. Conditions were oxygen-saturated aqueous 0.1 M $HClO_4$, 1600 rpm rotation, and a sweep rate of 5 mVs^{-1}.

Of course, the onset of reduction for both Pd samples is below the thermodynamically possible potential of 1.23V vs. RHE, but they are near the reported values for Pd nanoparticles [12, 27, 33]. The relative activity of the borohydride-reduced sample after multiple sweeps when compared to sodium naphthalide-reduced catalysts is consistent with past observations of the utility of using borohydride reduction

whenever possible. These polarization curves serve as the baseline for comparisons to the binary and ternary compounds.

4.3 Pd-W Nanoparticles Synthesized by Different Reducing Agents

Though it would be desirable to include all three elements from the ternary alloy study in the comparison of sodium naphthalide to sodium borohydride reduction, the fact that a $Pd_{0.90}W_{0.10}$ thin film alloy showed enhanced activity over Pd thin film allows for meaningful investigation of the binary Pd-W. Petrie showed that optimal W composition in a binary Pd-W film was 10 at% tungsten, which he correlated to shifting the Pd d-band center to lower energies as measured by XPS, and that alloying tungsten appears to weaken the binding of OH to palladium [29]. Synthesis of a Pd-W binary is part of the progression towards the goal of exploring ternary compositions, and serves as an intermediate step between the single and ternary component electrocatalysts. Showing that the enhanced activity of the binary is retained in nanoparticle form allows us not only to explore the synthesis of specific target compositions, but also allows for electrocatalytic assessment of those with respect to palladium. This section describes the synthesis and characterization of $Pd_{1-x}W_x$ nanoparticles via NaNp and $NaBH_4$ reduction as an analogue to the previous section which detailed similar syntheses of Pd particles.

4.3.1 Experimental

Sodium hexachloropalladate tetrahydrate, tungsten hexachloride, sodium, naphthalene and sodium borohydride were purchased from Aldrich and used as-received. Diglyme was dried over molecular sieves under argon in a solvent dispensing system, and absolute methanol was degassed for one hour before use. All manipulations were carried out on a Schlenk argon/vacuum line. Preparation of the reducing agents and palladium precursors was accomplished in the same manner as

the previous section. Tungsten hexachloride (0.0064 g, 0.016 mmole) was dissolved in approximately 5 mL solvent (diglyme for NaNp, methanol for $NaBH_4$) in a flask, capped, and brought out of the glovebox to the Schlenck line. Dissolution in methanol was performed outside of the box. The same large excesses of reducing agent that were used in the previous section were calculated to be sufficient to reduce the small amount of tungsten (VI) precursor. The W precursor solution was cannulaed to the Pd precursor flask, and the $Na_2PdCl_6 \cdot 4H_2O$ was dissolved by ultrasonication. The clear orange solution containing both metal precursors was cannlulaed to the room-temperature NaNp or $NaBH_4$ solution and stirred for two hours, at which time there was a black precipitate in each case. The products were cannulaed to a purged centrifuge tube, centrifuged at 7000 rpm for 20 minutes, and the supernatant was removed. The product was then re-suspended in methanol to remove any remaining NaCl, and centrifuged at 8000 rpm for ten minutes. A hexane wash followed in the same manner as was described earlier, and lead to a black solid product and clear supernatant, which was removed with a syringe, and the product was dried under vacuum. The tube was then backfilled with argon, and the septum was pierced with a needle to allow slow in-diffusion of air overnight. Characterization was performed by the same instruments and methods as described in the previous section on palladium and tungsten nanoparticles.

4.3.2 Results and Discussion

Alloying tungsten with palladium should not shift the Pd lattice constant by an amount detectable by powder XRD. Since the Pauling atomic radii of tungsten (1.394 Å) and palladium (1.373 Å) [34] are so similar (though it is understood that the BCC and FCC packing for W and Pd would subtly affect the calculated Pauling radii), the lattice constant is expected to resemble that of palladium.

This is what is seen for the diffraction pattern shown in Figure 4.12, where the center peak positions for sodium naphthalide reduction products line up with the literature peaks. Ten atomic percent tungsten is not sufficient to cause an appreciable shift in Pd lattice constant, since even at $Pd_{0.78}W_{0.22}$ (the solid-solution solubility limit for W in Pd) the ICDD PDF card shows only a 0.003 Å difference from palladium's lattice constant. This miniscule lattice expansion is the *maximum* achieved by alloying W into Pd, and the corresponding shift is almost imperceptible to conventional XRD. On top of that, the broad nature of these diffraction peaks and the difficulty of determining the exact center position make assessing Pd-W nanoparticle alloy composition by powder XRD impossible. The patterns in Figure 4.12 are from the same sample, and illustrate the efficacy of washing NaCl from the as-prepared product. The diffraction pattern for sodium borohydride Pd-W samples (not shown) has the same peak shift attributed to hydrogen absorption, and resembles the pattern shown in Figure 4.4.

The microprobe analysis of the Pd-W NaNp samples (Figure 4.13) showed a Pd:W ratio of 90:10 when averaged over four spectra, which was the same as the ratio of reactants. Homogeneity is not assured, as one of the spots in the sample had tungsten content as high as 20%. Given that the ~1 μm^3 volume excited by the electron beam in all EDX experiments could mask a large distribution of W content per particle, it cannot be claimed that each individual particle has a 90:10 Pd:W ratio. However, the fact that tungsten is not only present in palladium, but also at the desired concentration on the micron scale is encouraging. Sodium was still present in large amounts in the as-made NaNp product (66 at% on average), and chlorine was also seen (6 at% on average). Post-synthesis water washes remove the sodium chloride found in XRD as mentioned above, but the effects of such washes on the W content

before electrocatalytic evaluation have not been systematically studied for these syntheses.

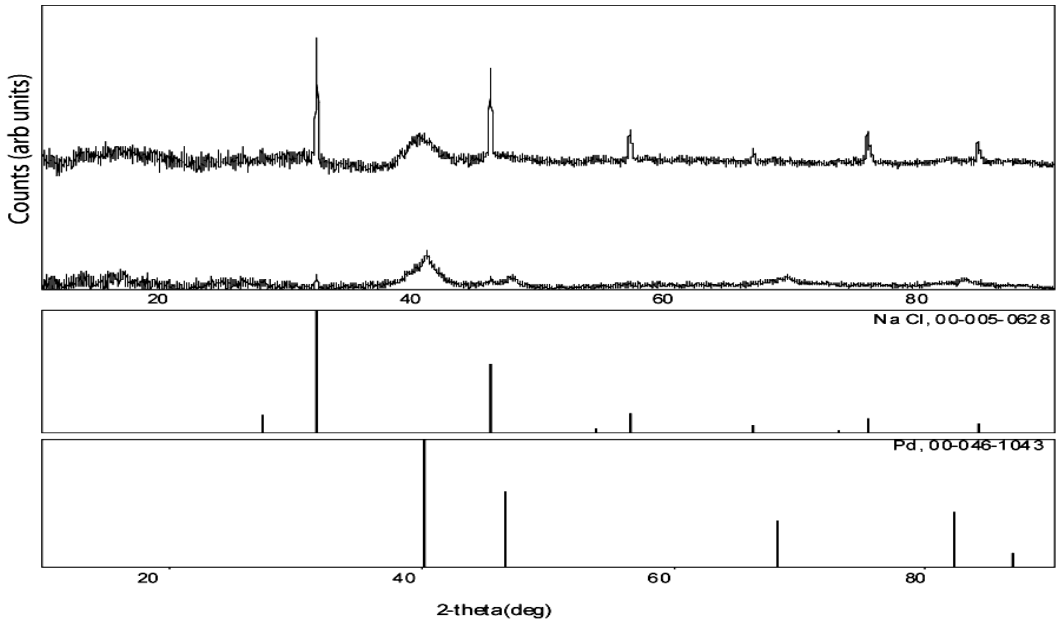

Figure 4.12 Powder X-ray diffraction pattern of nominally $Pd_{0.90}W_{0.10}$ nanoparticles synthesized by sodium naphthalide reduction in diglyme at 150°C. The top pattern is the as-made product, and the bottom is after washing with distilled water, where most of the salt is removed.

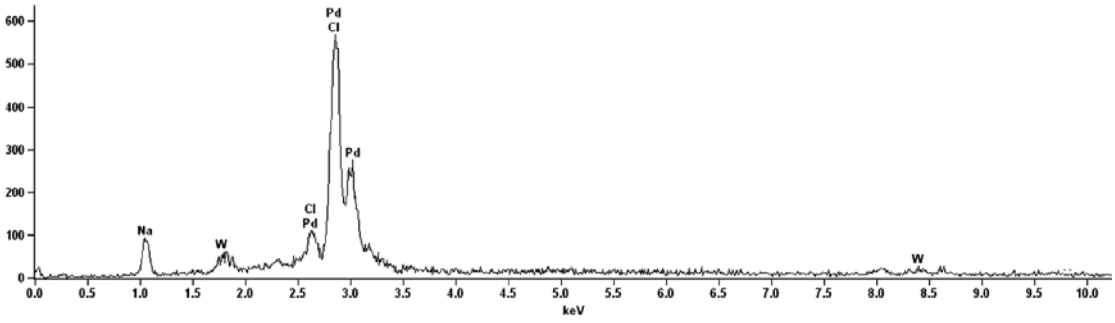

Figure 4.13 Energy-dispersive X-ray spectrum of nominally $Pd_{0.90}W_{0.10}$ nanoparticles synthesized by sodium naphthalide reduction in diglyme at 150°C. The small peaks on either side of the 8.4 keV W peak are from the brass sample holder.

Elemental analysis for $Pd_{0.90}W_{0.10}$ target compound made by borohydride reduction was also encouraging. Sodium and chlorine from NaCl were barely detected, presumably for the same reasons given for the Pd-only particles. Figure 4.14 shows a representative EDX spectrum for a spot on the $Pd_{0.90}W_{0.10}$ nanoparticle product, which, when averaged over all spectra, corresponds to a composition of 5 at% tungsten in Pd. Though the usual error of ±5 at% for microprobe could still put the results within the 10 at% W range, the average amount is a smaller concentration of tungsten than was originally desired, and seems to be a genuine deficiency. The reason for the loss of tungsten from reactants to dried nanoparticle products might be due to synthesis in and washing with methanol, though if that is the case, it is not known why the methanol did not simply dissolve all the tungsten.

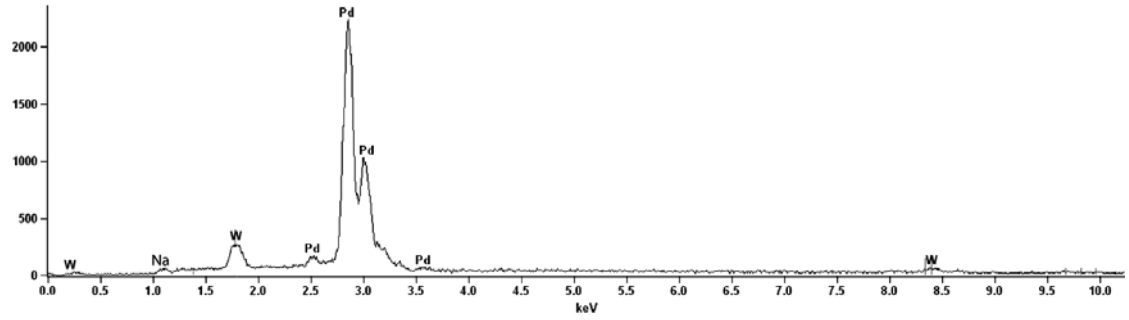

Figure 4.14 Energy-dispersive X-ray spectrum of nominally $Pd_{0.90}W_{0.10}$ nanoparticles synthesized by sodium borohydride reduction in methanol at 25°C. Note the decrease in Na intensity with respect to the sample made by sodium naphthalide reduction (Figure 4.13).

The Pd-W particles from each reducing agent had similar appearances in TEM. Figure 4.15 shows two transmission electron micrographs of Pd-W particles synthesized by sodium naphthalide reduction at 150°C, while Figure 4.16 shows

micrographs of Pd-W particles reduced by sodium borohydride at room temperature. Both Figure 4.15 and Figure 4.16 depict agglomerated particles, with aggregates on the order of 100 nm. All the samples' X-ray domain sizes were around 3 nm, which again is corroborated by the visual particle sizes, especially in the micrographs with 20 nm scale bars, but statistically exhaustive particle size analyses were not performed. The reducing agent does not appear to impact particle morphology or size, and no low-contrast coating due to low-Z element coverage could be found. Thus, the large carbon content expected from TGA studies (shown next) could not be visually confirmed.

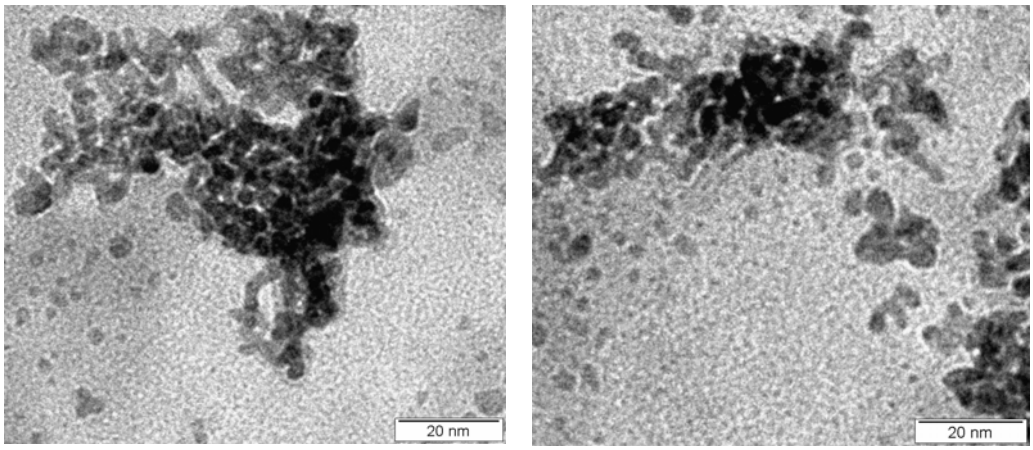

Figure 4.15 Transmission electron micrographs of Pd-W nanoparticles synthesized by sodium naphthalide reduction in diglyme at 150°C.

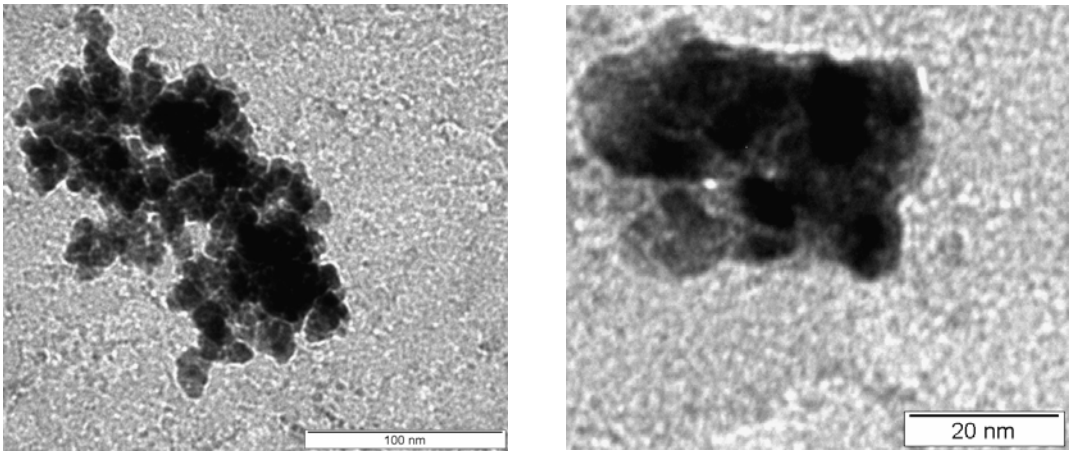

Figure 4.16 Transmission electron micrographs of Pd-W nanoparticles synthesized by sodium borohydride reduction in methanol at 25°C.

Thermogravimetric analysis of the products showed results similar to those for Pd alone. Figure 4.17 shows two Pd-W TGA traces corresponding to synthesis by each reducing agent, and once again samples prepared through sodium borohydride reduction show less mass loss (~2%) than sodium naphthalide-reduced samples (~20%). The uptake in mass past 275°C in Figure is due to oxidation of Pd in the TGA from trace oxygen or water vapor in the argon flow, since the rust-colored post-TGA powder indexes to PdO by XRD. The weight loss for the borohydride sample is quite low, and is the lowest of the nanoparticle electrocatalysts produced by chemical reduction in this dissertation (even when discounting any oxidative weight gain).

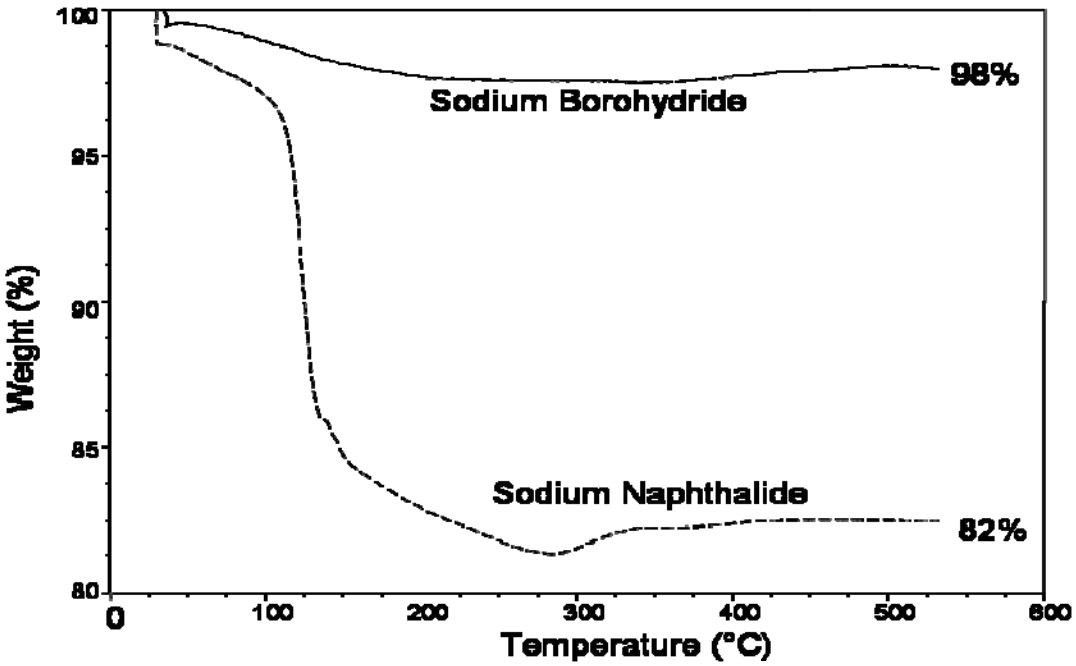

Figure 4.17 Thermogravimetric analysis of nominally $Pd_{0.90}W_{0.10}$ nanoparticles synthesized by sodium naphthalide reduction in diglyme at 150°C and by sodium borohydride reduction in methanol at 25°C.

The oxygen reduction polarization curves for the Pd-W nanoparticles prepared by each reducing agent are shown in Figure 4.18. On the first scan, the $NaBH_4$ sample has oxygen reduction onset around 0.87 V vs. RHE, which is a slight improvement over those seen for sodium naphthalide reduction samples at 0.85 V. Subsequent sweeps show the NaNp catalysts are unstable, as the second scan has a less positive onset potential, and a scan taken after electrochemical cycling shows an even less positive onset potential (0.7 V vs. RHE). As was the case for the palladium-only oxygen reduction curves, the borohydride Pd-W products do regain some of their oxygen reduction activity after electrochemical cleaning, and more closely resemble the first sweeps.

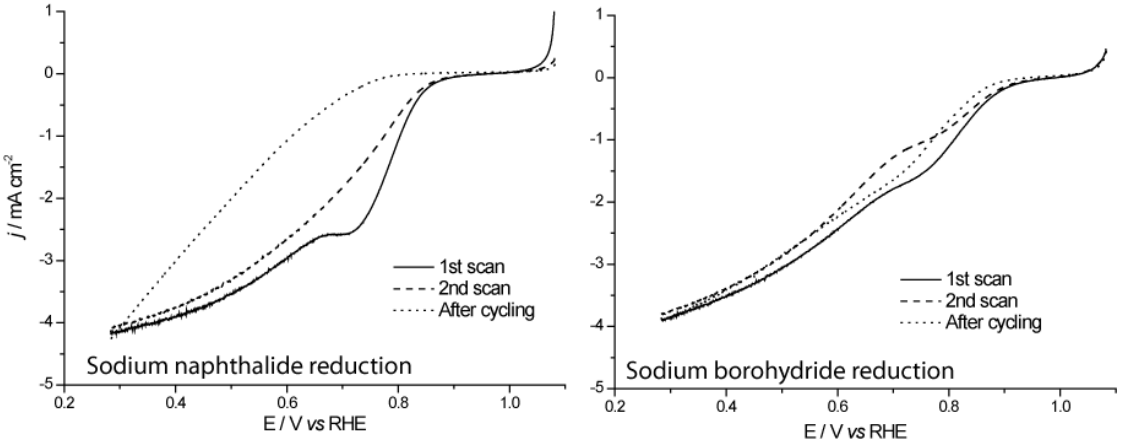

Figure 4.18 Oxygen polarization curves of nominally $Pd_{0.90}W_{0.10}$ nanoparticles synthesized by sodium naphthalide reduction in diglyme at 150°C and by sodium borohydride reduction in methanol at 25°C. Conditions were oxygen-saturated aqueous 0.1M $HClO_4$, 1600 rpm, 5 mVs^{-1}. The sodium naphthalide-reduced catalyst was approximately the target composition, while the sodium-borohydride-reduced catalyst was closer to $Pd_{0.95}W_{0.05}$.

The retention of the original activity speaks to the relative stability of the borohydride samples compared to the naphthalide ones. The final shape of the curves after electrochemical cleaning illustrates the largest difference between the two synthesis methods. For each curve (1^{st}, 2^{nd}, and last), the borohydride samples have higher current densities at more positive potentials- especially on the last sweep, which is the most meaningful statement of the immediate stability. It is concluded that the ORR activity for the products of $NaBH_4$ reduction are superior ORR electrocatalysts than the NaNp samples for the reasons given in the introduction to Chapter 2. Since elemental analysis of the $NaBH_4$ binary showed a tungsten deficiency compared to the desired 10 at% composition, it is not clear whether a true 10 at% tungsten palladium binary would have improved even more upon the

approximate 5 at% W catalyst which appears in Figure 4.18. Either way, it appears that when no naphthalene is present to adhere to the surface of the as-made nanoparticles, the electrocatalytic reaction is enhanced.

4.4 Pd-W-V Nanoparticles via Sodium Naphthalide Reduction

The final section of this chapter covers attempts to synthesize homogeneous nanoparticles with the ternary composition that showed the highest activity in the thin film- $Pd_{0.88}W_{0.06}V_{0.06}$. It should be noted that in this section, only sodium naphthalide reductions were employed, since no borohydride is capable of reducing a V^{n+} precursor where $n \geq 2$. The challenges inherent in this synthesis are considerable; precursors must be chosen that are all soluble so that a homogeneous solution is obtained, and those three precursors must reduce at the same rates for the reasons discussed in earlier chapters. Then those nanoparticles must precipitate in the presence of a host of side products and oxidized reducing agents, and keep the small level of alloyed metals not only through wash steps and exposure to air, but also under the potential and pH of a fuel cell. Adherence to all these criteria is non-trivial for a single element, challenging for a binary target composition, and exceedingly difficult for a ternary composition, especially when the target ternary has such a small fraction of alloyed elements. The nanoparticles described in this section show evidence of phase separation, inconsistent ORR activity, and are difficult to characterize as far as their composition. Still, they represent a step in the transition from thin film composition spreads to ternary nanoparticle electrocatalysts.

4.4.1 Experimental

Sodium hexachloropalladate tetrahydrate, tungsten hexachloride, dichlorovanadocene (bis-cyclopentadienyl vanadium dichloride), sodium and naphthalene were purchased from Aldrich and used as-received. Diglyme was dried

over molecular sieves in a stainless steel solvent system and dispensed under positive pressure of argon. All manipulations were carried out in either an argon atmosphere glovebox, or on a Schlenk argon/vacuum line.

Sodium (0.0442 g, 1.9 mmole) and naphthalene (0.2458 g, 1.9 mmole) were dissolved in 40 mL diglyme in a glovebox, transferred to a Schlenk line, and left to stir overnight to form sodium naphthalide. Once sodium naphthalide had formed, sodium hexachloropalladate tetrahydrate (0.0700 g, 0.16 mmole) was placed in a flask and purged with argon. Tungsten hexachloride (0.0038 g, 0.0096 mmole) and dichlorovanadocene (0.0024 g, 0.0096 mmole) were dissolved in approximately 10 mL diglyme in a flask, capped, and brought out of the glovebox to the Schlenk line. The mixed W and V precursor solution was cannulaed to the Pd precursor flask, and the $Na_2PdCl_6 \cdot 4H_2O$ was dissolved by ultrasonication. The clear orange solution containing the three metals was cannlulaed to the room-temperature NaNp solution and stirred for fifteen minutes. The reactants were then heated to 150°C and stirred for sixty minutes, at which time a black precipitate was apparent. The suspended product was transferred by cannula to a sealed Ar-atmosphere centrifuge tube, and centrifuged at 7000 rpm for twenty minutes. Methanol and hexanes wash steps followed in the same manner as described in previous sections, and lead to black solid product and clear supernatants. After drying under vacuum, the tube was backfilled with argon, and pierced for controlled oxidation overnight. Characterization was performed with the same instruments and methods as in the previous two sections.

4.4.2 Results and discussion

Attempts were made to synthesize nanoparticles that match the composition of the active catalyst area in the original sputtered thin film. Some samples had a starting nominal reactant metal ratio of $Pd_{0.88}W_{0.06}V_{0.06}$, while others were deliberately left off-stoichiometry to see if the behavior seen in the thin film (where the small area with

that specific composition gave marked improvements over its off-composition neighbors) could be duplicated in nanoparticles. The reactant ratios of W and V with respect to Pd were from three to nine percent W, and four to eleven percent V. The powder X-ray diffraction patterns (such as a representative pattern shown in Figure 4.19) all match that of palladium, with no observable peak shifts due to alloying or to use of hydrogen-producing borohydrides. A 12% total alloy of W and V in Pd does not appreciably alter the Pd lattice constant, so the absence of peak shifts was not surprising. The crystallite size determined by whole pattern profile fitting was found to be between 1 and 4nm in all cases but one, where it was an anomalous 5.8nm. Sodium chloride is often found in most patterns, but to preclude pre-analysis metal dissolution, the analyses were performed without washing beyond that described in the Experimental section.

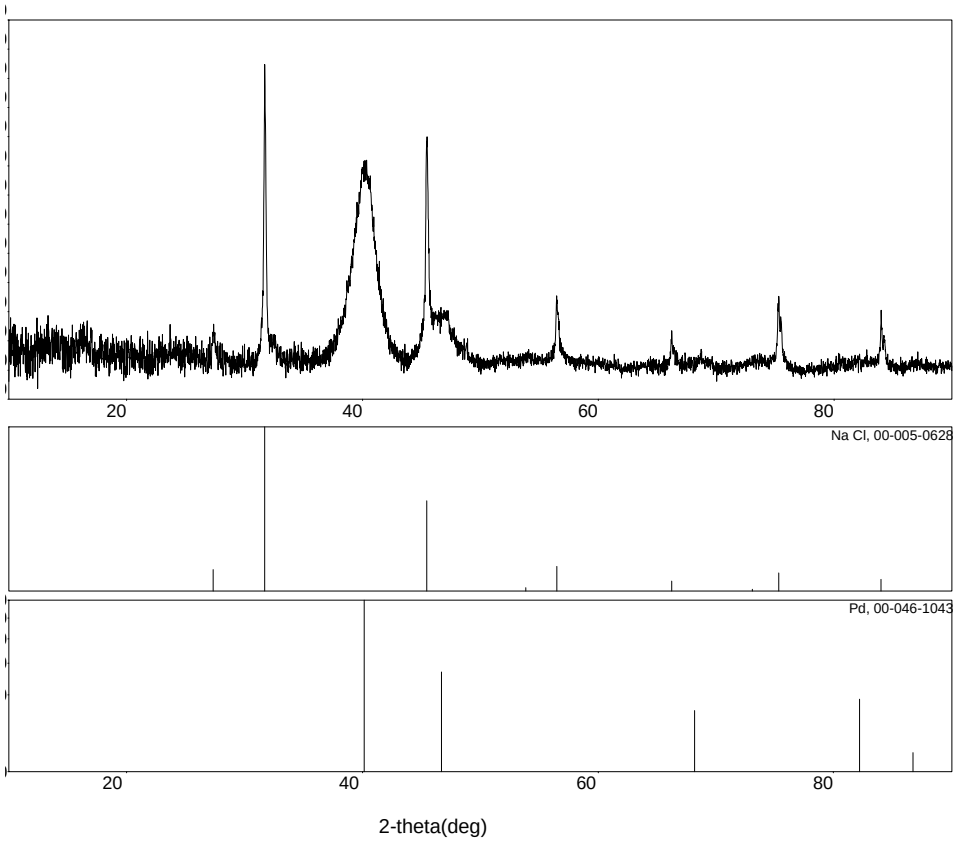

Figure 4.19 Powder X-ray diffraction pattern of nominally $Pd_{0.9}W_{0.04}V_{0.06}$ nanoparticles synthesized by sodium naphthalide reduction in diglyme at 150°C.

Microprobe analysis of the ternary compounds showed a large scatter in composition, indicating irreproducibility in obtaining ternary metal nanoparticles by standard solution phase chemical reduction. Palladium was always found in the final product just like the single-component syntheses, but there was a high degree of variability of the tungsten and vanadium content. In the best cases, both were present in the final product (averaged over the micron scale). Figure 4.20 shows the microprobe EDX spectrum from a ternary sample with the nominal composition which was similar to that for the thin film active area: $Pd_{0.90}W_{0.04}V_{0.06}$. Peaks are labeled for Pd, W, and V, and correspond to a ratio of 90 at% Pd, and 5 at% each for W and V.

Sodium and chlorine are also present, with sodium at around 10 at%, and chlorine at approximately 6%, though the Cl/Pd overlap once again obscures direct quantification of Cl. Such close agreement of the metals ratio with the desired composition is remarkable, but does not occur in every sample.

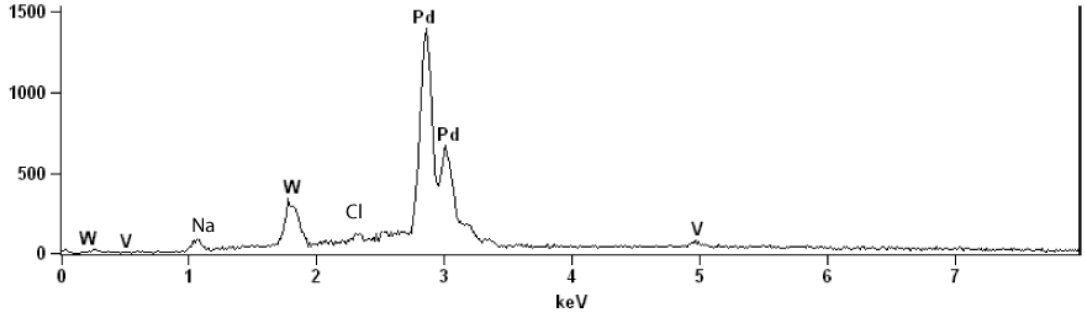

Figure 4.20 Energy-dispersive X-ray spectrum of nominally $Pd_{0.88}W_{0.06}V_{0.06}$ nanoparticles synthesized by sodium naphthalide reduction in diglyme at 150°C. The composition from this spectrum was 90 at% Pd, 5 at% W, and 5 at% V.

Often V is not found at all, as seen in Figure 4.21, which corresponds to a Pd:W:V ratio of 77:23:0. The lack of vanadium in approximately half of recorded EDX spectra could be due to a.) The vanadium precursor was not reduced in the first place and remained in solution, b.) Vanadium reduced and then co-precipitated with Pd and W, only to leach out during methanol washes, or c.) There is significant phase separation of the V with respect to Pd and W, making the vanadium difficult to find in a given microprobe experiment. Leaching during wash steps has proven to be a problem for NaNp syntheses of nanoparticles containing base metals. Previous studies of the synthesis of Pt_xTi by sodium naphthalide reduction [35] were unsuccessful in making the 1:1 ratio due to the inability to keep Ti in the final product. Those studies never yielded PtTi in the 1:1 intermetallic phase, but rather formed the Pt_3Ti

intermetallic. This was due to either leaching of Ti from the as-formed 1:1-phase nanoparticles during washing steps, or incomplete Ti reduction, or possibly phase separation and then Ti reaction with washing solvents. The target compositions in the current work contain so little electropositive metals that leaching is not as extensive as it would be for a 1:1 ratio, but it was never a certainty that vanadium would be found by EDX in the final product. The fact that it does appear in some of the samples is encouraging.

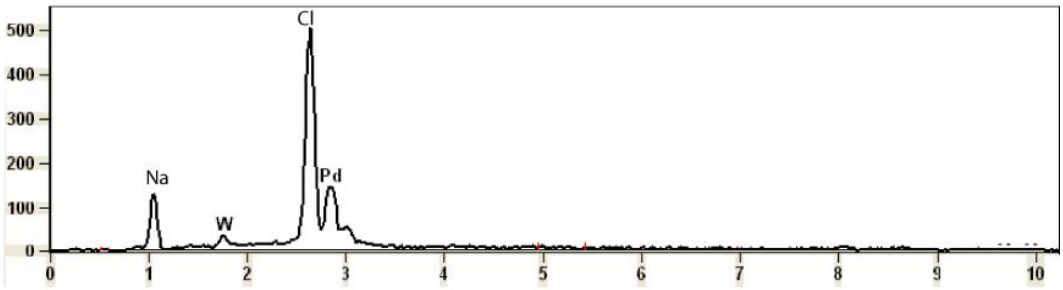

Figure 4.21 Energy-dispersive X-ray spectrum of nominally $Pd_{0.9}W_{0.04}V_{0.06}$ nanoparticles synthesized by sodium naphthalide reduction in diglyme at 150°C. The 5 keV vanadium peak is not seen, as the composition from this spectrum was 7 at% Pd, and 2 at% W (for a 77:23 Pd:W ratio) with 57% sodium and 33% chlorine.

There is also evidence for vanadium being found in the final product, but being segregated on the micron scale. Figure 4.22 shows a scanning electron micrograph of an aggregated nanoparticle powder that has discrete morphological features which stick out in comparison to its neighbors. One is the aggregate labeled as "Point 2". Its spectrum, shown in the bottom portion of Figure 4.23, is mostly composed of vanadium, as V peaks are seen in much larger proportion than in other spectra. The crystal adjacent to it, "Point 1", is sodium chloride, with signal from the surrounding sample contributing some Pd content. The exact form of the vanadium at

Point 2 is not known, beyond a general expectation that it is not metallic vanadium after air exposure. It is likely a vanadium oxide of some sort (the surface at least will be oxidized), or could be some left over molecular byproduct of VCp_2Cl_2 which was not fully reduced yet still precipitated with the products. The irreproducibility of the nanoparticle composition prevents a more thorough analysis of the effect of the precise variations of metal precursor ratios on the electrocatalytic activity. For simplicity's sake, the following characterizations which refer to specific samples will be labeled with nominal ratios, as if all target compositions were achieved. Interpretation of the electrochemistry observed in ternary samples must be tempered with the realization that the composition of each is usually not the same as the nominal stoichiometry.

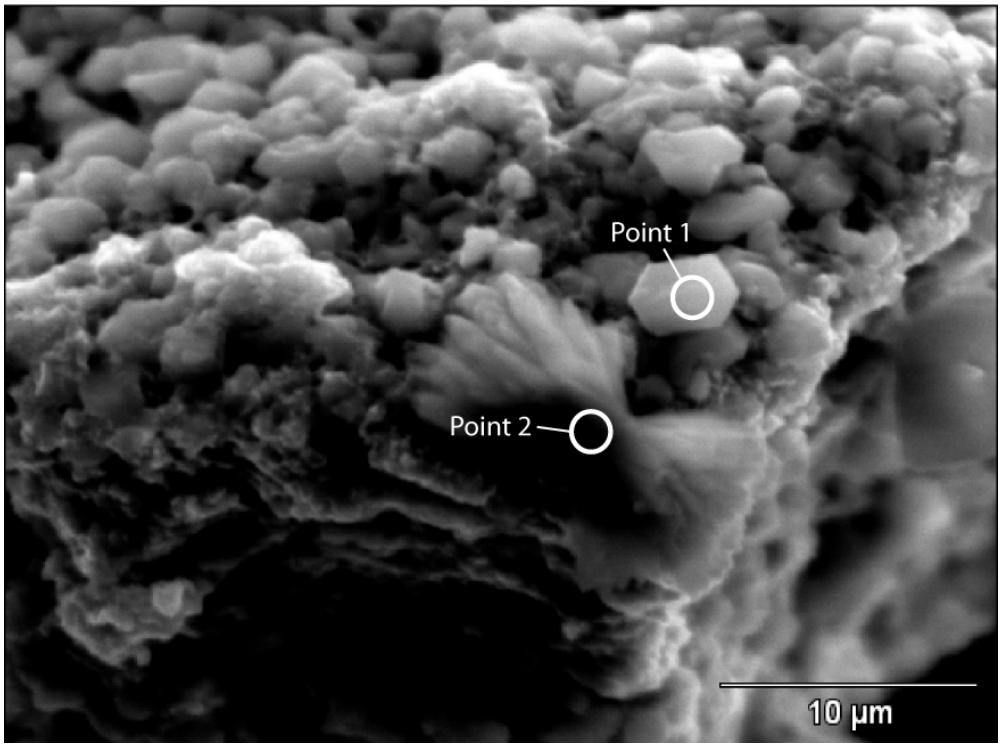

Figure 4.22 Scanning electron micrograph of an aggregate of nominally $Pd_{0.90}W_{0.04}V_{0.06}$ nanoparticles. EDX spectra for Points 1 and 2 are shown in Figure 4.23.

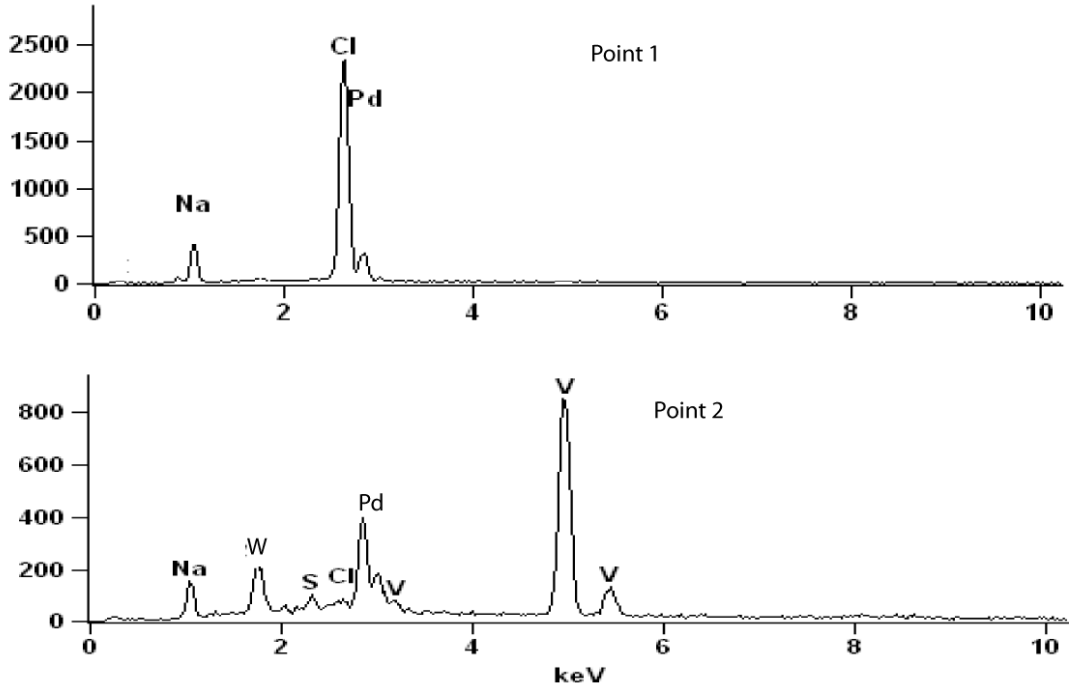

Figure 4.23 Energy-dispersive X-ray spectra from the two points in Figure 4.22. Point one is clearly a sodium chloride crystal, while point two is rich in vanadium, showing the micron-level phase separation.

Transmission electron microscopy studies for the Pd-W-V alloy nanoparticles yielded results quite similar to those for Pd and Pd-W binary alloys as discussed earlier. The solid found in the micrographs (Figure 4.24) was composed of aggregates that were tens to hundreds of nanometers across, and made up of small particles on the order of the size of the calculated domain size, which was 2-3 nm. The particle morphology was unremarkable, as little faceting was seen. It is known that particle morphology could play a larger role than composition, since, for example, the Pd (110) crystal facets are known to have enhanced ORR activity [12]. This does not appear to be the case here, as no crystallite facets are apparent. Since no capping agents such as CTAB were employed to encourage Pd faceting, this is not surprising.

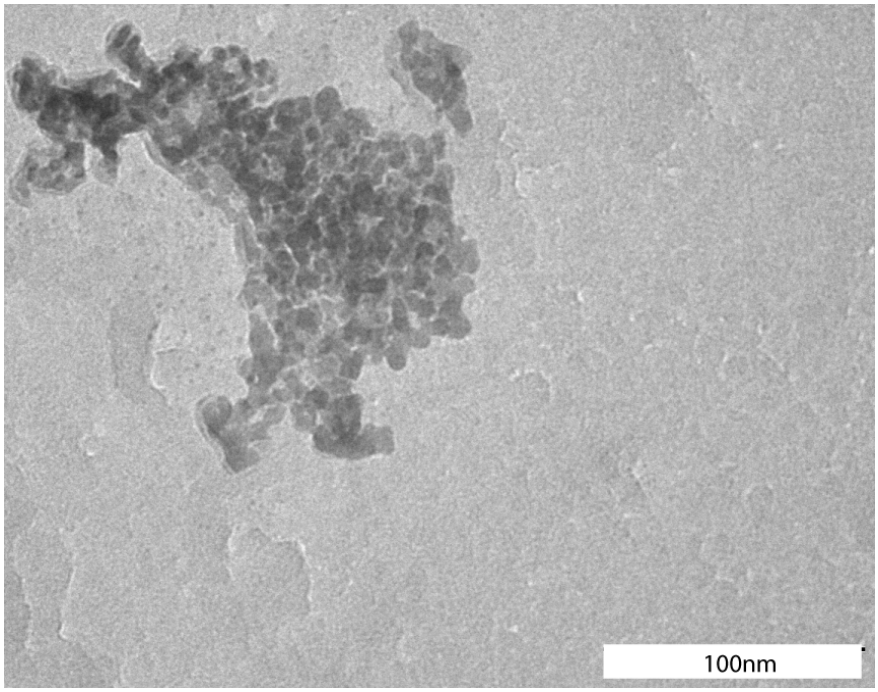

Figure 4.24 Transmission electron micrograph of nominally $Pd_{0.9}W_{0.04}V_{0.06}$ nanoparticles agglomerated into a ~100nm aggregate.

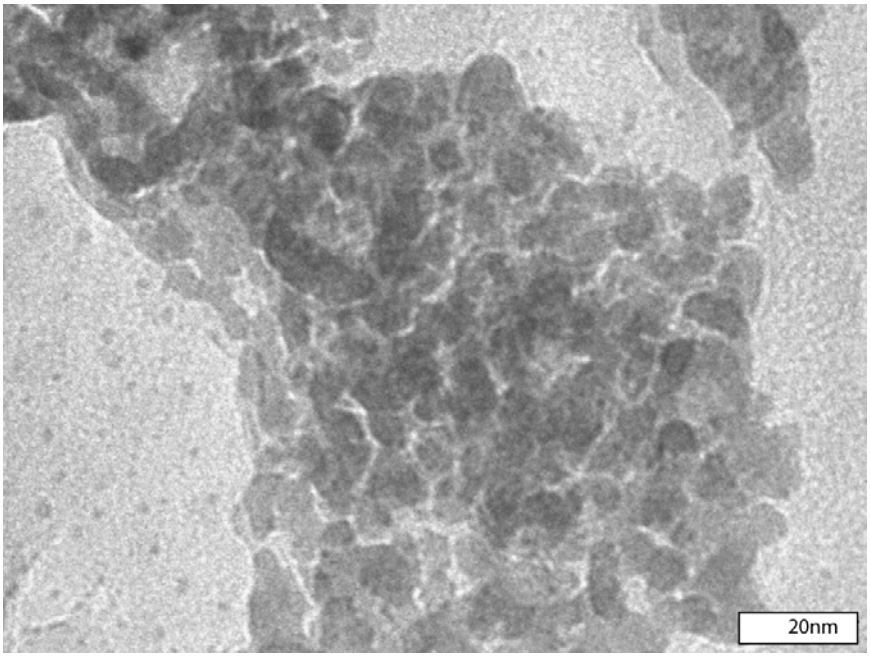

Figure 4.25 Zoomed in transmission electron micrograph of Figure 4.24

Since vanadium (IV) precursors can only be chemically reduced by a reducing agent as strong as sodium naphthalide, the products had the high carbon content usually associated with those syntheses, as attested by TGA. The traces for seven Pd-W-V products are shown in Figure 4.26. The main observation garnered from this figure is that all the samples lose a large portion of their weight when heated. Some lose it gradually at a somewhat constant slope, some in a monotonic stepwise fashion that clearly involves water desorption starting at 100°C (as well as other processes). The ones which increase in weight are being oxidized in the manner described in the previous section, and their final weight should be recognized as being artificially high. Regardless of the mechanism of weight loss, the products all lose on the order of 20% of their weight through loss of water and carbon-containing molecules. This is entirely too high for nanoparticles intended to be used as electrocatalysts, and steps must be taken in future similar reactions to enhance particle surface cleanliness. Eliminating the naphthalide reducing agent in favor of an agent without coordinating π bonds would be a good start, and further exploration of the possible combinations of reducing agent and precursor are needed.

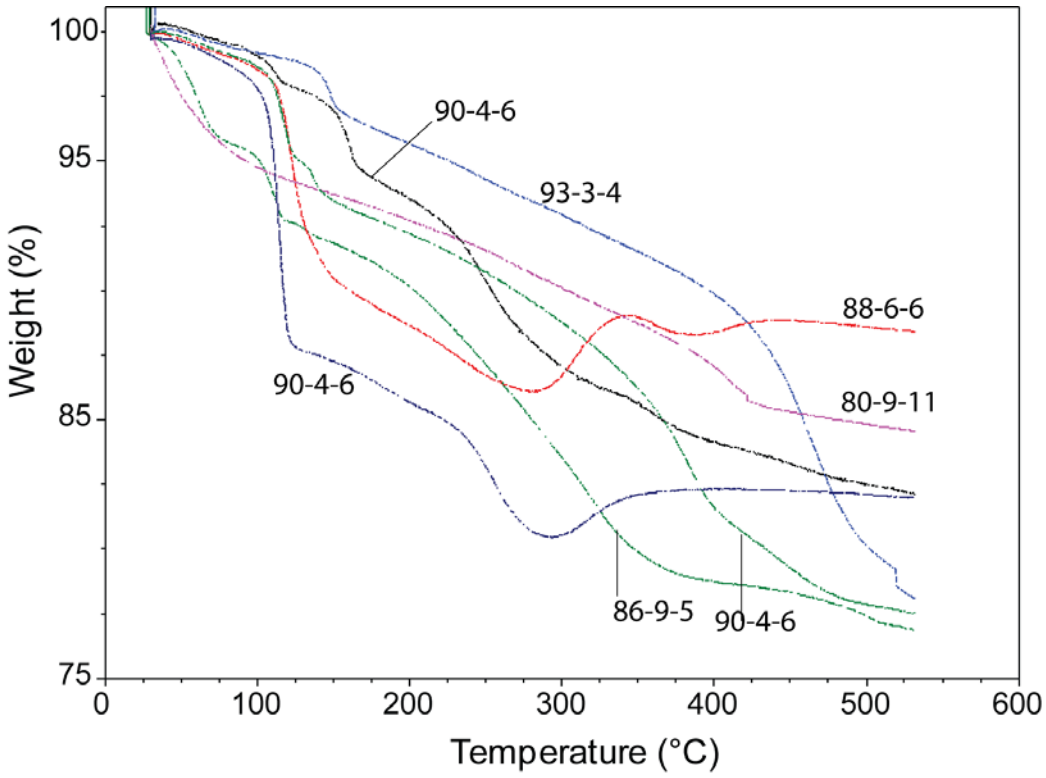

Figure 4.26 Thermogravimetric analysis of several Pd ternary alloys nanoparticles. Nominal ternary compositions are labeled in the form "Pd-W-V".

The electrocatalysis results for Pd ternary alloys did show activity for oxygen reduction. The sample which showed the highest first-sweep ORR activity had a nominal composition of $Pd_{0.90}W_{0.04}V_{0.06}$. While a rotating electrode polarization curve (Figure 4.27) of those particles in argon-saturated perchloric acid solution shows an essentially flat current response over a potential range of +1.1 V to +0.2 V vs. RHE, the same electrode in an oxygen-saturated solution shows the expected cathodic current, starting at an onset of +0.85 V. The onset potential is not as positive as that for Pt black (also shown in Figure 4.27), and is therefore neither an equal nor improvement on the current technology. The distinct peak in the first-scan ORR current density at 0.72V is indicative of some sort of surface process, and should not

be implicated as part of the catalysts' ORR activity. Indeed, the peak is not seen in the second sweep, indicating that the high current density of the first sweep was likely due to surface modification. The second sweep compares even less favorably to platinum than the first.

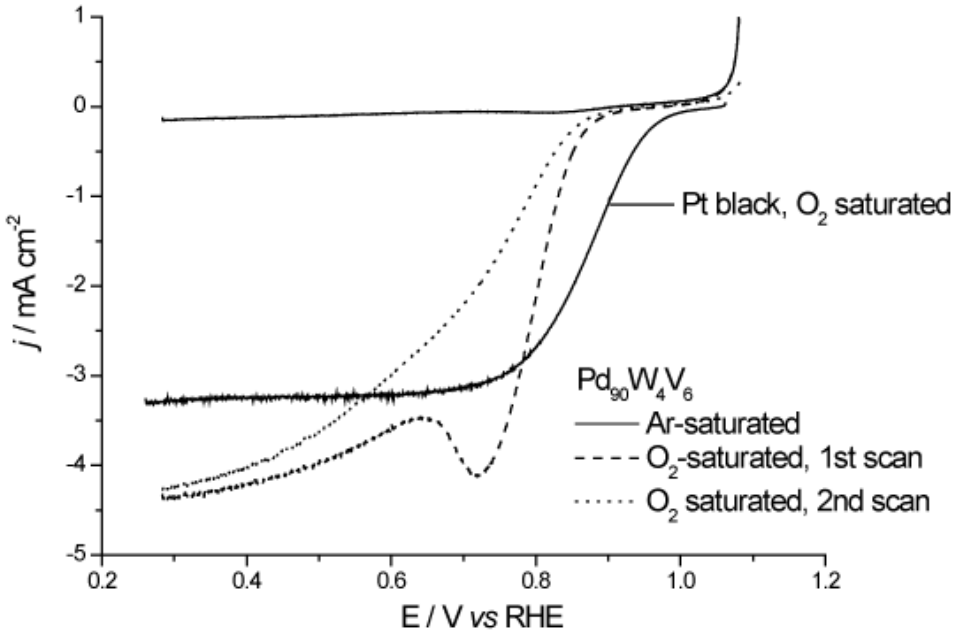

Figure 4.27 ORR polarization curves of nominally $Pd_{0.90}W_{0.04}V_{0.06}$ nanoparticles synthesized by sodium naphthalide reduction in diglyme at 150°C. First and second ORR scans are shown, along with the curve for an analogous commercial platinum nanoparticle sample, and a sweep in Ar-saturated perchloric acid. Conditions were oxygen-saturated aqueous 0.1 M $HClO_4$, 1600 rpm, 5 mVs^{-1}.

Despite the variability in the ternary compositions' electrocatalytic activities, the activity of the Pd-W-V nanoparticles do often follow the trends seen in the thin films- namely, that a 9:1 Pd:W ratio is better than just Pd, and a roughly 18:1:1 Pd:W:V ratio is better still. Figure 4.28 shows the ORR activities of the progression towards ternary nanoparticles from just palladium, where all samples were synthesized

by sodium naphthalide reduction. Both the first and second sweeps illustrate the improvements gained by adding tungsten and then vanadium to palladium. Since the first sweep has already been shown to include surface reduction processes, the second sweeps are also plotted in Figure 4.28, where there is a striking drop-off in apparent activity compared to the first sweeps. While the improvement in electrocatalytic activity in the second sweeps upon adding W and V is not as dramatic, it is more representative of the actual oxygen electrocatalysis. Here the same trend remains as was originally seen in the thin film experiments. The ternary nanoparticles outperform the binary and elemental Pd, which suggests that the combinatorial method used to find this ternary composition is an effective guide for nanoparticle synthesis.

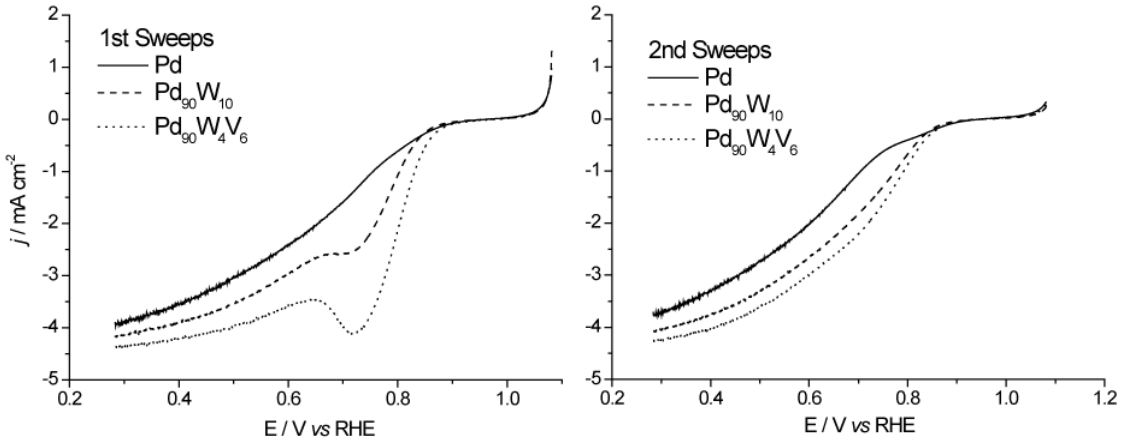

Figure 4.28 ORR polarization curves progressing from Pd only, to nominally $Pd_{0.90}W_{0.10}$, to nominally $Pd_{0.90}W_{0.04}V_{0.06}$, all synthesized by sodium naphthalide reduction. Conditions were oxygen-saturated aqueous 0.1 M $HClO_4$, 1600 rpm, 5 mVs^{-1}. The first sweeps for all three are plotted on the left while the second sweeps are on the right. In both cases, the materials follow the trend expected from thin film results.

Unfortunately, the nanoparticle synthesis itself and the resulting electrochemical behavior is irreproducible, as the wide variations in composition seen in the microprobe results might have indicated. Figure 4.29 shows a sampling of ORR reduction curves, each corresponding to different attempts at synthesizing the same active composition as was shown above: $Pd_{90}W_4V_6$. The curves (which all correspond to samples with the same nominal starting reactant composition) show significant deviation from one another, suggesting the importance of several uncontrolled factors which apparently govern the catalytic performance of ternary nanoparticles. As for the source of the wide range of activities, it is unknown whether metal composition or surface contamination plays more of a role. Certainly better reproducibility is essential for determining the exact influence of synthetic parameters.

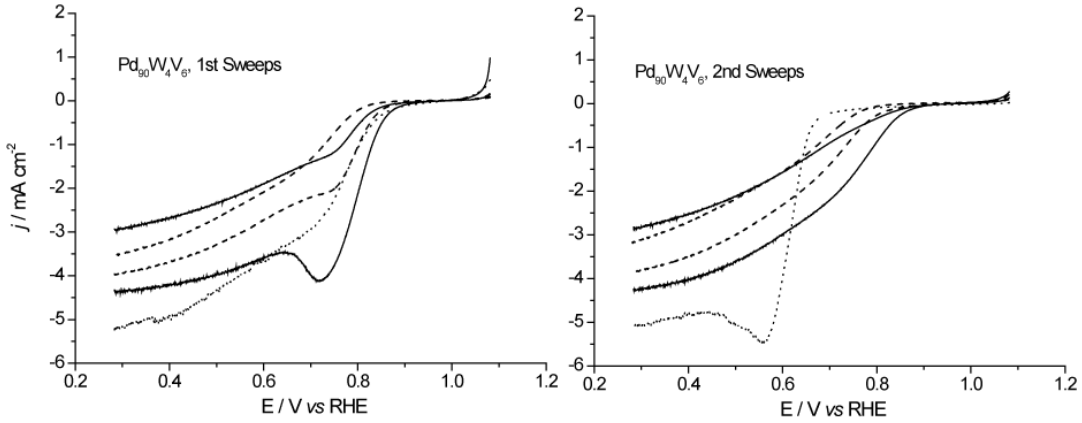

Figure 4.29. ORR polarization curves of five different samples of nominally $Pd_{0.90}W_{0.04}V_{0.06}$ nanoparticles synthesized by sodium naphthalide reduction in diglyme at 150°C. The first sweeps for all five are plotted on the left while the second sweeps are on the right. Conditions were oxygen-saturated aqueous 0.1M $HClO_4$, 1600 rpm, 5 mVs^{-1}.

4.5 Arc-Melt Synthesis of a Bulk Pd-W-V Slug

At this point, it is certainly clear that the chemical co-reduction of three metal precursors to reproducibly achieve homogeneous ternary nanoparticles is anything but trivial. The confluence of reducing agent, ligand side products, particle size, compositional heterogeneity and stoichiometric variations from the nominal composition all confuse the issue of what, if anything, could be significant about the thin film composition which originally inspired this work. It is even quite possible that thin film strain plays an important role, with the alloyed metals playing more of a physical role in the solid state than a chemical one. In order to exclude most of these factors, it was decided to use more traditional solid state chemical techniques to create a bulk sample with the $Pd_{0.88}W_{0.06}V_{0.06}$ composition. Due to the high melting points (and subsequent low solid-solid diffusion constants) of Pd and especially W and V, arc-melting was necessary to achieve a solid solution. By synthesizing a bulk slug and machining it to cast a disk electrode, the electrocatalytic properties of the alloy itself could be assessed. Hopefully this would help in understanding if the ORR activity was due to the ternary composition or to nanoparticle or thin film effects.

4.5.1 Experimental

Palladium wire (2.0330 g), tungsten wire (0.0582 g), and vanadium wire (0.2107 g) were weighed and cut to the desired ratio: 88 at% Pd, 6 at% W, and 6 at% V. Sandpaper was used to attempt to remove as much surface oxide as possible before weighing. Arc-melting was performed in a Centorr Model 5SA single-arc furnace with a Miller power supply. Water-cooled copper hearths were in place, the chamber had been evacuated and purged with argon three times, and trace oxygen was removed from the flowing argon stream by a Ti-getter in a furnace at 500°C. The arc-melted bead was melted, cooled, turned over, and re-melted four times, all with Ar

purging in between. Mass loss after melting was less than 0.5%. The bead was then mounted on a lathe and was turned down to a cylinder of 3.5 mm diameter and 5 mm length. Elemental analysis was performed on a JEOL8900 EPMA microprobe at 20 kV accelerating voltage before the slug was fashioned into an electrode by Dr. Qin Zhou. This mounting was accomplished by boring a 2 mm hole through the center of a Teflon cylinder, then heating the cylinder to 400°C for five minutes. The Pd alloy cylinder was pressed into the softened Teflon, which was tamped on a flat surface, and was left to cool and re-solidify. Back contact was made by filling the void immediately behind the slug with carbon fiber, then making contact to the fiber wad with a steel post. The post was sealed in the Teflon with epoxy, and the electrode surface was polished first with a Buehler 1200 grit abrasive disc followed by 1μm diamond paste. Rotating disk electrocatalytic measurements were made in an oxygen-saturated 0.1 M perchloric acid solution at a potential sweep rate of 5 mVs^{-1} and a rotation rate of 1600 rpm. Once again, "electrochemical cycling" or "electrochemical cleaning" refers to cycling the potential between 0 and 1.2 V vs. NHE at 50 mV s^{-1} for 20 minutes.

4.5.2 Results and Discussion

Microprobe elemental analysis of the slug showed that the metal composition was close to the desired ratio, but slightly vanadium deficient. All EDX spectra such as the representative one in Figure 4.30 showed nothing but the ternary metal mixture, and occasionally trace copper (< 1 at%) from the sample mount. The Pd:W:V ratio averaged over all spectra was 84:11:5, with the usual EDX error bar of ± 5% for any given metal. While all three metals are within error of the nominal composition, the spectra too often indicated vanadium deficiency for it to be ignored. The slug did, however, appear homogeneous. Figure 4.31 shows a scanning electron micrograph

overlaid with the results of a line scan spectrum. The line scan comprised of fifty spectra taken across a 1mm length of the cylinder before polishing. The metal signals stay approximately constant with regard to one another, and deviate mostly through random noise and from surface roughness. The starting spectrum for the scan was at the center where the Pd:W:V ratio was 85:11:4 at that point, and the vertical units of "counts" show little spatial deviation.

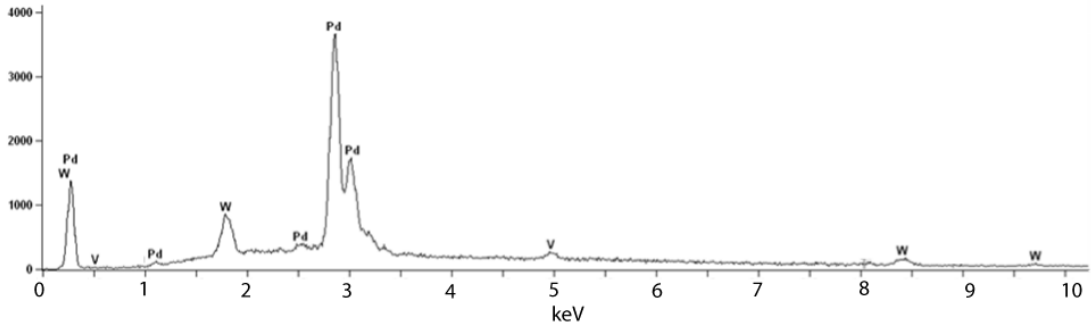

Figure 4.30 Representative EDX spectrum of Pd-W-V alloy slug, after machining but before embedding in Teflon and polishing.

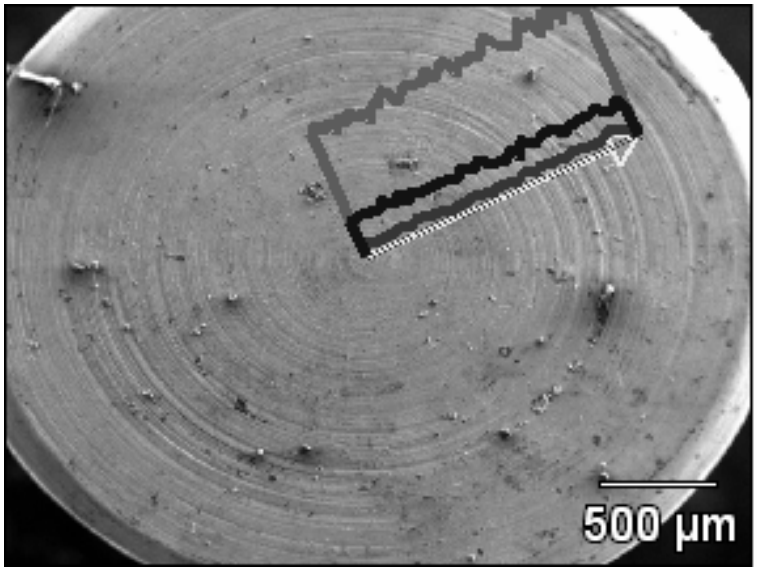

Figure 4.31 Scanning electron micrograph overlaid with the relative results of an EDX line scan. The metal counts in the line scan correspond to 85% Pd (top signal), 11% W (middle signal), and 4% V (bottom signal).

The ORR polarization curve for the bulk electrode is shown in Figure 4.32. Onset of oxygen reduction occurs below 0.7 V vs. RHE, a much less positive value than even the worst nanoparticle samples prepared by any of the methods discussed earlier. The slope as the current reaches its maximum cathodic value at 0.27 V is quite shallow, indicating a sluggish onset. The noteworthy characteristic of the curve is that electrochemical cleaning restores the electrocatalytic activity to resemble the first sweep, indicating that surface oxides or carbonaceous coatings have been reduced and desorbed, and that the electrocatalytic response is more robust than in most nanoparticle samples. However, it appears that the main contributor to ORR activity in the nanoparticles and thin films may be the nanocrystalline nature of those materials. Bulk polycrystalline slugs such as the one shown here do not appear to possess the same activity. It is also possible that the hypothesis that strain, not electronic or co-catalytic effects, plays more of a role in making the thin film ternary catalytically active.

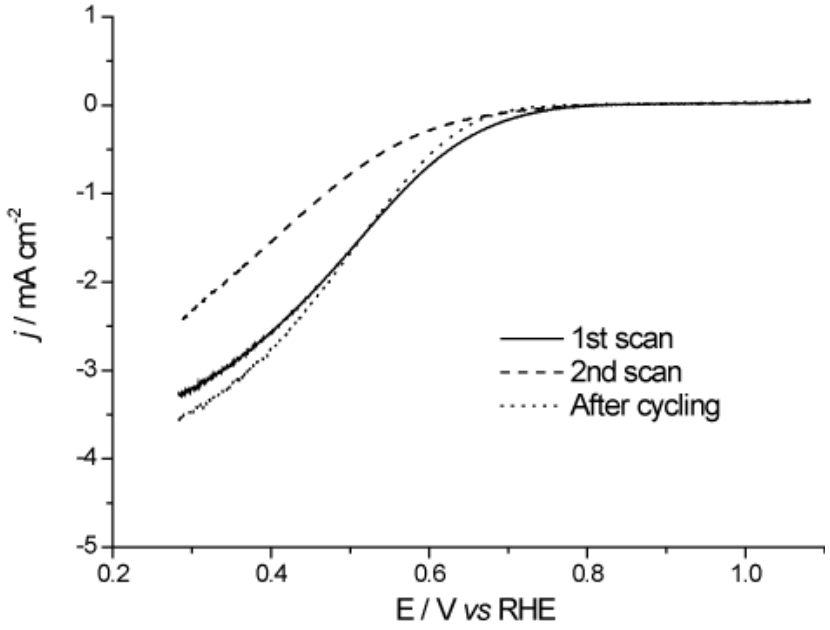

Figure 4.32 Oxygen polarization curves of Pd-W-V alloy slug, after embedding in Teflon and polishing.

This series of experiments in this chapter may not have delivered a remarkable oxygen reduction catalyst which will revolutionize fuel cell technology, but it has demonstrated an experimental transition from thin film combinatorial searches to viable nanoparticle catalysts. For all the efforts in CFCI to develop methods to deliver novel composition nanoparticles based on combinatorial findings, this system is one of the first to successfully demonstrate that transition.

REFERENCES

1. Prochaska, M., et al., *High throughput screening of electrocatalysts for fuel cell applications.* Review of Scientific Instruments, 2006. **77**(5).
2. Gregoire, J.M., et al., *High energy x-ray diffraction/x-ray fluorescence spectroscopy for high-throughput analysis of composition spread thin films.* Review of Scientific Instruments, 2009. **80**(12): p. 6.
3. Gregoire, J.M., et al., *High-Throughput Evaluation of Dealloyed Pt-Zn Composition-Spread Thin Film for Methanol-Oxidation Catalysis.* Journal of the Electrochemical Society, 2009. **156**(1): p. B160-B166.
4. Gregoire, J.M., et al., *Improved Fuel Cell Oxidation Catalysis in Pt1-xTax.* Chemistry of Materials. **22**(3): p. 1080-1087.
5. Jin, J., et al., *A high-throughput search for direct methanol fuel cell anode electrocatalysts of type PtxBiyPbz.* Applied Surface Science, 2007. **254**(3): p. 653-661.
6. van Dover, R.B. and L.F. Schneemeyer, *The codeposited composition spread approach to high-throughput discovery/exploration of inorganic materials.* Macromolecular Rapid Communications, 2004. **25**(1): p. 150-157.
7. Gurau, B., et al., *Structural and electrochemical characterization of binary, ternary, and quaternary platinum alloy catalysts for methanol electro-oxidation.* Journal of Physical Chemistry B, 1998. **102**(49): p. 9997-10003.
8. Reddington, E., et al., *Combinatorial electrochemistry: A highly parallel, optical screening method for discovery of better electrocatalysts.* Science, 1998. **280**(5370): p. 1735.

9. Jiang, C.M. and X.Q. Lin, *A novel nanocomposite of Pd nanocluster/poly(N-acetylaniline) nanorod modified electrode for the electrocatalytic reduction of oxygen.* Journal of Applied Electrochemistry, 2008. **38**(12): p. 1659-1664.
10. Jiang, L., et al., *Size-Dependent Activity of Palladium Nanoparticles for Oxygen Electroreduction in Alkaline Solutions.* Journal of the Electrochemical Society, 2009. **156**(5): p. B643-B649.
11. Salvador-Pascual, J.J., S. Citalan-Cigarroa, and O. Solorza-Feria, *Kinetics of oxygen reduction reaction on nanosized Pd electrocatalyst in acid media.* Journal of Power Sources, 2007. **172**(1): p. 229-234.
12. Xiao, L., et al., *Activating Pd by Morphology Tailoring for Oxygen Reduction.* Journal of the American Chemical Society, 2009. **131**(2): p. 602-608.
13. Zhang, Z.H., et al., *Pd nanoparticles supported on WO3/C hybrid material as catalyst for oxygen reduction reaction.* Journal of Power Sources, 2008. **185**(2): p. 941-945.
14. Wang, B., *Recent development of non-platinum catalysts for oxygen reduction reaction.* Journal of Power Sources, 2005. **152**(1): p. 1-15.
15. Wang, R.F., et al., *Pt decorating of PdNi/C as electrocatalysts for oxygen reduction.* Electrochimica Acta. **55**(5): p. 1519-1522.
16. Wang, W.M., et al., *Surface and structure characteristics of carbon-supported Pd3Pt1 bimetallic nanoparticles for methanol-tolerant oxygen reduction reaction.* Journal of Catalysis, 2009. **266**(1): p. 156-163.
17. Wang, W.M., et al., *Carbon-supported Pd-Co bimetallic nanoparticles as electrocatalysts for the oxygen reduction reaction.* Journal of Power Sources, 2007. **167**(2): p. 243-249.

18. Zhang, L., K. Lee, and J.J. Zhang, *The effect of heat treatment on nanoparticle size and ORR activity for carbon-supported Pd-Co alloy electrocatalysts.* Electrochimica Acta, 2007. **52**(9): p. 3088-3094.

19. Zhang, L., K.C. Lee, and J.J. Zhang, *Effect of synthetic reducing agents on morphology and ORR activity of carbon-supported nano-Pd-Co alloy electrocatalysts.* Electrochimica Acta, 2007. **52**(28): p. 7964-7971.

20. Li, H.Q., et al., *Design and preparation of highly active Pt-Pd/C catalyst for the oxygen reduction reaction.* Journal of Physical Chemistry C, 2007. **111**(15): p. 5605-5617.

21. Li, X.W., et al., *Simple Complexing-Reduction Synthesis of Pd-Pt/C Alloy Electrocatalysts for the Oxygen Reduction Reaction.* Journal of the Electrochemical Society, 2009. **156**(10): p. B1107-B1111.

22. Sarkar, A., A.V. Murugan, and A. Manthiram, *Pt-Encapsulated Pd-Co Nanoalloy Electrocatalysts for Oxygen Reduction Reaction in Fuel Cells.* Langmuir. **26**(4): p. 2894-2903.

23. Sarkar, A., A.V. Murugan, and A. Manthiram, *Synthesis and characterization of nanostructured Pd-Mo electrocatalysts for oxygen reduction reaction in fuel cells.* Journal of Physical Chemistry C, 2008. **112**(31): p. 12037-12043.

24. Shao, M., et al., *Synthesis and characterization of platinum monolayer oxygen-reduction electrocatalysts with Co-Pd core-shell nanoparticle supports.* Electrochemistry Communications, 2007. **9**(12): p. 2848-2853.

25. Shao, M.H., et al., *Palladium monolayer and palladium alloy electrocatalysts for oxygen reduction.* Langmuir, 2006. **22**(25): p. 10409-10415.

26. Shao, M.H., et al., *Origin of enhanced activity in palladium alloy electrocatalysts for oxygen reduction reaction.* Journal of Physical Chemistry B, 2007. **111**(24): p. 6772-6775.

27. Shao, M.H., K. Sasaki, and R.R. Adzic, *Pd-Fe nanoparticles as electrocatalysts for oxygen reduction.* Journal of the American Chemical Society, 2006. **128**(11): p. 3526-3527.

28. Shao, M.H., et al., *Pd3Fe and pt monolayer-modified Pd3Fe electrocatalysts for oxygen reduction.* Zeitschrift Fur Physikalische Chemie-International Journal of Research in Physical Chemistry & Chemical Physics, 2007. **221**(9-10): p. 1175-1190.

29. Petrie, J., *Combinatorial Exploration of the Non-Pt ORR Catalysts for Fuel Cell Cathodes*, in *Materials Science and Engineering*. 2010, Cornell University: Ithaca.

30. Moffatt, W.G., ed. *The Handbook of Binary Phase Diagrams*. ed. W.G. Moffatt. Vol. V, Genium Publishing Corporation.

31. Pourbaix, M., *Atlas of Electrochemical Equilibria in Aqueous Solutions*. Second ed, ed. M. Pourbaix. 1974, Houston: National Association of Corrosion Engineers. 644.

32. Lo, C.-t.F., Karan, Kunal, and Davis, Boyd R., *Kinetic Studies of Reaction between Sodium Borohydride and Methanol, Water, and Their Mixtures.* Industrial and Engineering Chemistry Research, 2007. **46**: p. 5478-5484.

33. Nilekar, A.U., et al., *Bimetallic and ternary alloys for improved oxygen reduction catalysis.* Topics in Catalysis, 2007. **46**(3-4): p. 276-284.

34. Pauling, L., *The Nature of the Chemical Bond*. 3 ed. The George Fisher Baker Non-Resident Lectureship in Chemistry at Cornell University. 1960, Ithaca NY: Cornell University Press. 644.

35. Abe, H., et al., *Electrocatalytic performance of fuel oxidation by Pt3Ti nanoparticles.* Journal of the American Chemical Society, 2008. **130**(16): p. 5452-5458.

CHAPTER 5

Projects Outside the Sphere of Fuel Cell Research

5.1 Transition Metal Carbide Synthesis by Sodium Naphthalide Reduction

After completing much of the research performed in Chapter 2, it was of interest to test the limits of sodium naphthalide reduction and the ability of the reducing agent to co-reduce both electropositive elements (especially early transition metals) and main-group nonmetals. One possibility for nonmetals was to explore whether or not NaNp could reduce a carbon precursor to make nanoscale diamond- or even more technologically interesting, boron-doped diamond. However, a group of compounds that could showcase both of the target element groups was transition metal carbides. Carbides are hard, refractory materials that are widely utilized in technology, from abrasives, cutting tools, and high-temperature materials to chemical and electrochemical catalysts [1]. Unfortunately, their high melting points require elevated temperature, energy-intensive syntheses which result in relatively coarse powders with low specific surface areas. A low-temperature solution phase synthesis is an attractive alternative to producing transition metal carbides with high specific surface areas (> ~20 m^2/g), which would be perfect for ceramic composites and catalytic processes [1]. Finding a suitable carbon precursor is also relevant for cases where combinatorial thin film methods may find an active catalyst where carbon is one of the components. Having these synthetic tools at the group's disposal will be of great advantage if such a catalyst is discovered.

Liquid-phase synthesis of transition metal carbides by co-reduction is not without precedent. Nelson and Wagner showed in 2002 [2, 3] that high surface area carbides could be synthesized in THF by co-reducing metal chlorides and carbon tetrabromide with an alkalide reducing agent at subambient temperatures. The

crystalline alkalide $K^+(15\text{-crown-}5)_2Na^-$ is soluble in THF [4], and since the reducing agent in solution is Na^- , a powerful two electron reduction occurs with any reducible species in solution. While sodium naphthalide is not as powerful a reducing agent as sodium anion (which has nearly the reducing power of a solvated electron [2]), it is still quite strong, as discussed in Chapter two. Attempting to recreate the phases formed by Nelson and Wagner [2] would serve as a test of the extent of sodium naphthalide's reducing abilities. So the synthesis of the phases Fe_3C, VC and TaC was attempted.

A general form for the balanced chemical equation of these reactions appears in Equation 5.1:

$$a\ MCl_x + b\ CBr_4 + (a{\cdot}x + b{\cdot}4)\ NaNp \rightarrow M_aC_b + (a{\cdot}x + b{\cdot}4)\ Np + a{\cdot}x\ NaCl + b{\cdot}4NaBr \quad (5.1)$$

Here the metal chloride and carbon tetrabromide are mixed in the ratio a to b, which was usually one to one, and is the desired final composition. As in all other sodium naphthalide reductions in this dissertation, enough NaNp is added so that there are enough one-electron reduction equivalents to fully reduce all moles of precursor to oxidation state zero. Since CBr_4 was the carbon precursor in all reactions, four equivalents were needed even before considering the metal precursor. Once the metal precursor was considered, the equivalents increased in the following manner: for VC (a 1:1 carbide), seven equivalents were needed to reduce V^{III} and C^{4+} to V^0 and C^0. For TaC from Ta^V, nine equivalents would be necessary. Fe_3C is a 3:1 carbide, so thirteen equivalents (3 times Fe^{III} plus four for C^{4+}) were necessary. It becomes apparent when performing the redox bookkeeping for these reactions that the molar equivalents of salt side products and oxidized reducing agent will be plentiful in comparison to the desired carbide products. Even the reaction with the smallest number of moles of side product (VC) will yield seven equivalents of mixed-anion

sodium salt and seven equivalents of naphthalene for every mole of metal carbide, an inescapable result when using CBr_4 and high oxidation state metal chlorides as precursors. The presence of these species in solution is a matter of concern, since they compete with the particle-particle interactions among both reduced metal species and reduced carbon. Nelson and Wagner utilized the rather onerous procedure of washing their as-made products in liquid ammonia to remove the potassium and sodium halides. While this method is effective, the philosophy in the current work was to wash in the manner described in earlier chapters; sodium halide side-products may still remain, but the carbide product could be initially characterized in their presence. The high melting points of these refractory materials necessitate post synthesis annealing at temperatures in excess of 1000°C, so particle sintering could also be a concern.

5.1.1 Experimental

Iron (III) chloride (Riedel-de Haën), vanadium (III) chloride (Aldrich), tantalum (V) chloride (Aldrich) and carbon tetrabromide (Acros) were purchased from the listed manufacturers and used as received. THF and hexanes were distilled over sodium/benzophenone before use, and all manipulations were carried out either in an Ar-atmosphere glovebox or on a Schlenk line. Sodium naphthalide was prepared in the same manner as in Chapters two and four, where it was allowed to form by stirring overnight under argon. The metal chloride and carbon tetrabromide were weighed out in the appropriate molar ratio for the desired product, dissolved in THF, drawn into a syringe (all in the glovebox) and then injected into the NaNp solution on the Schlenk line. Due to the exothermic formation of NaCl and NaBr byproducts, the reducing agent solution was cooled to -76°C in dry ice/acetone slush. After stirring for 90 minutes, the products were collected by distilling off the THF and then washed with

degassed absolute methanol and distilled hexanes. Centrifugation at 9000 rpm for 20 minutes collected the precipitates between washings, and the products were dried under vacuum while in the septum-sealed centrifuge tube. Exposure to air was made slowly by back-filling the tube with argon and piercing the septum with a needle (as was described in Chapters two and four), but only when specified.

All the products were annealed in silica tubes *in vacuo:* at 950°C for Fe_3C, 1100°C for VC and 1200°C for TaC following Nelson and Wagner's procedure. Since the products still had some salt mixed in them, the molten NaCl/Br attacked the silica tubing, causing tube failure. As an alternative to silica, tantalum and niobium tubes were used to encase the as-formed products while in the glovebox. After sealing these metal tubes in an arc furnace, they were sealed inside fused silica tubes. The tubes were heated to their target temperature over the span of 8 hours, and then held for one hour (again, following the procedure of Nelson and Wagner). After cooling in air, the tubes were opened to ambient conditions and the products were characterized. Powder X-ray diffraction patterns were taken with a Scintag XDS 2000, and later by a Rigaku Ultima IV, both with Cu Kα radiation. Energy-dispersive X-ray spectroscopy was performed on a LEO 1550 FESEM with an accelerating voltage of 20 kV.

5.1.2 Results and Discussion

The reduction of carbon tetrabromide yielded a black powder that turned light orange/brown after drying and slow air exposure without annealing. X-ray diffraction pattern showed crystalline NaBr in the as-formed product, but after washing with distilled water and filtering, a beige product remained. Powder X-ray diffraction (Figure 5.1) then revealed that the product contained very little (if any) sodium bromide, and was best indexed to the carbon allotropes "octacarbon" (a body-centered cubic C_8 phase, PDF# 01-072-2091) and diamond (a calculated orthorhombic phase,

PDF# 01-089-8494). Energy-dispersive X-ray spectroscopy (EDX) showed Ga and As from the sample holder plus an average of 5 at% oxygen, with the remainder as carbon, and detected no sodium or bromine. Combustion analysis or ^{1}H NMR spectroscopy would be needed to determine the hydrogen amount, and the extent of hydrocarbon character. Raman spectroscopy under 488nm excitation (Figure 5.2) showed the characteristic D and G bands (found at 1350 to 1380 cm^{-1} and 1580 to 1600 cm^{-1}, respectively [5]) associated with carbon materials at 1389.0 cm^{-1} and 1580.3 cm^{-1}, giving evidence which corroborates some of the carbon phases observed in X-ray diffraction. The commonly reported intensity ratio [I(D)/I(G)] of the D peak to G peak is 0.780, indicating a low amount of sp^3 carbon. The [I(D)/I(G)] ratio for amorphous carbon typically decreases from around 1.2 for 10% sp^3 to zero for higher than 30% sp^3 [5], so as a first approximation, this carbon can be thought to be between 10-30% diamond-like. Sodium naphthalide, it seems, is capable of reducing CBr_4 to carbon at subambient temperatures, and without post-annealing.

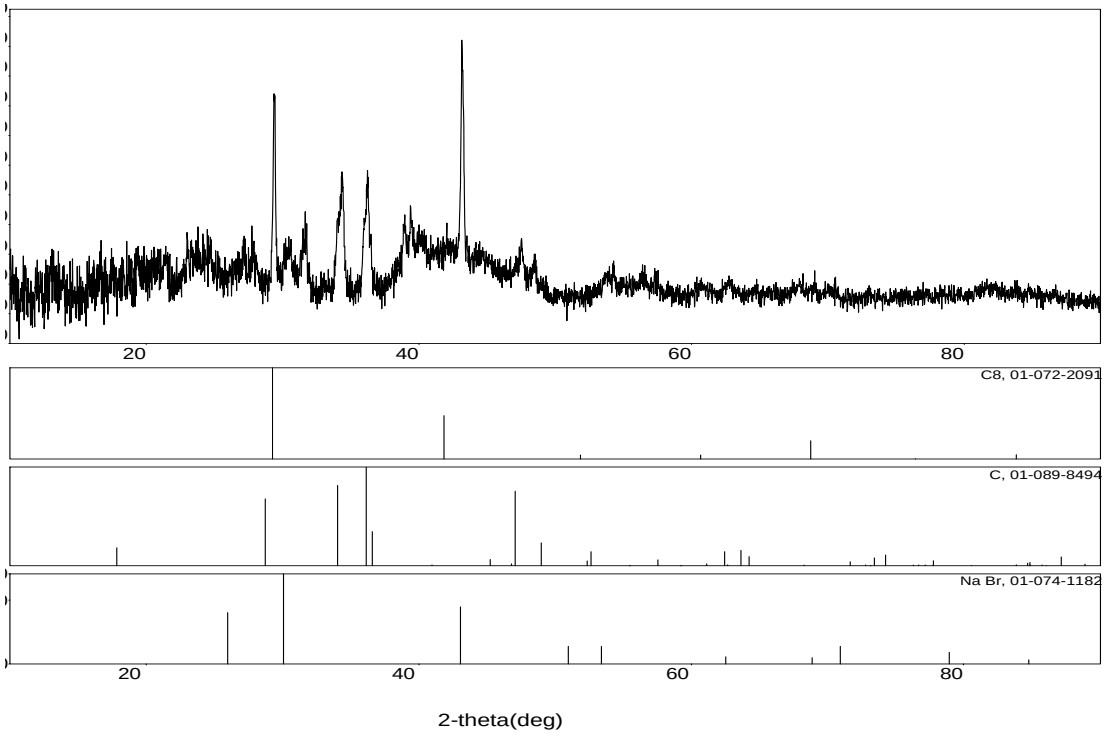

Figure 5.1. Powder X-ray diffraction pattern of carbon product of CBr_4 reduced by sodium naphthalide. Peaks index to octacarbon (top reported pattern) and diamond (middle), as well as a small amount of sodium bromide (bottom).

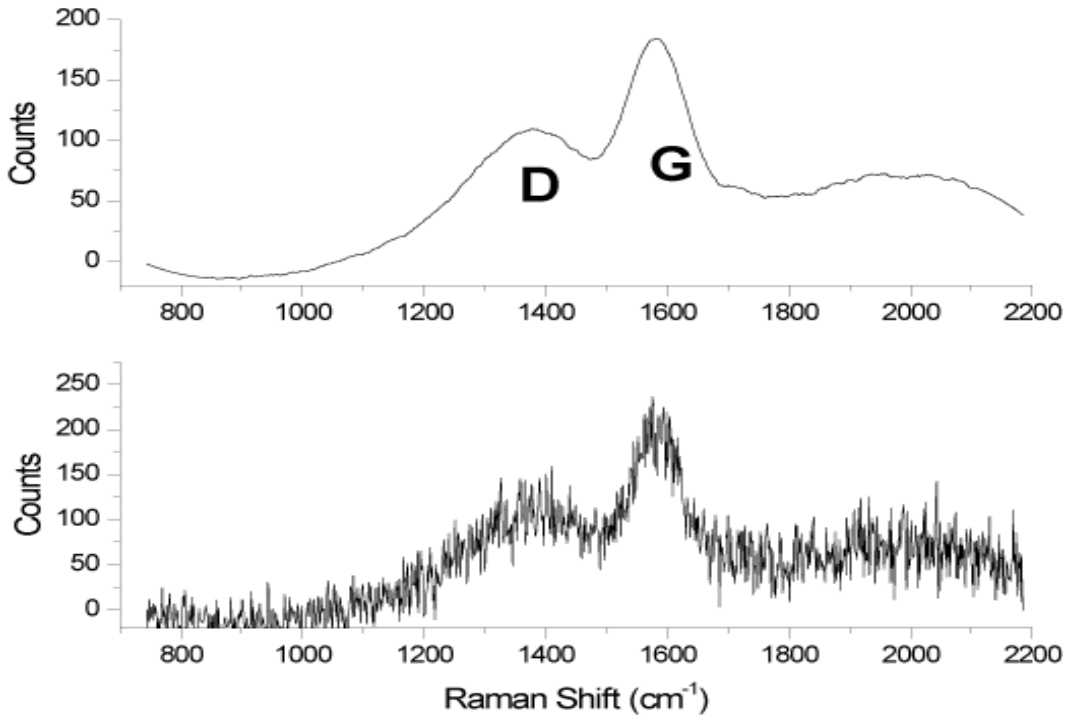

Figure 5.2. Raman spectrum under 488 nm excitation. Raw data (bottom) is shown with the smoothed curve (top), where the D and G peaks are in approximately a 1:1 ratio.

VC and Fe_3C were not successfully synthesized. Annealing the vanadium products gave a forest-green powder that indexed to a mixture of vanadium oxides by XRD, even though the samples were nominally not exposed to air. As-formed iron carbide attempts indexed to Fe_2O_3 and NaCl by XRD (Figure 5.3), and the annealed iron products gave a hard black powder with hints of dark-red, but indexed to a mixture of NaBr/Cl and magnetite (Figure 5.4). The powder is attracted by a magnet, which would support the presence of Fe_3O_4. The carbon in the material seems to have formed its own phase, as Raman spectroscopy shows the characteristic carbon peaks at 1358.4cm^{-1} and 1589.6cm^{-1} as seen in Figure 5.5. The I(D)/(G) ratio for that spectrum is 1.04.

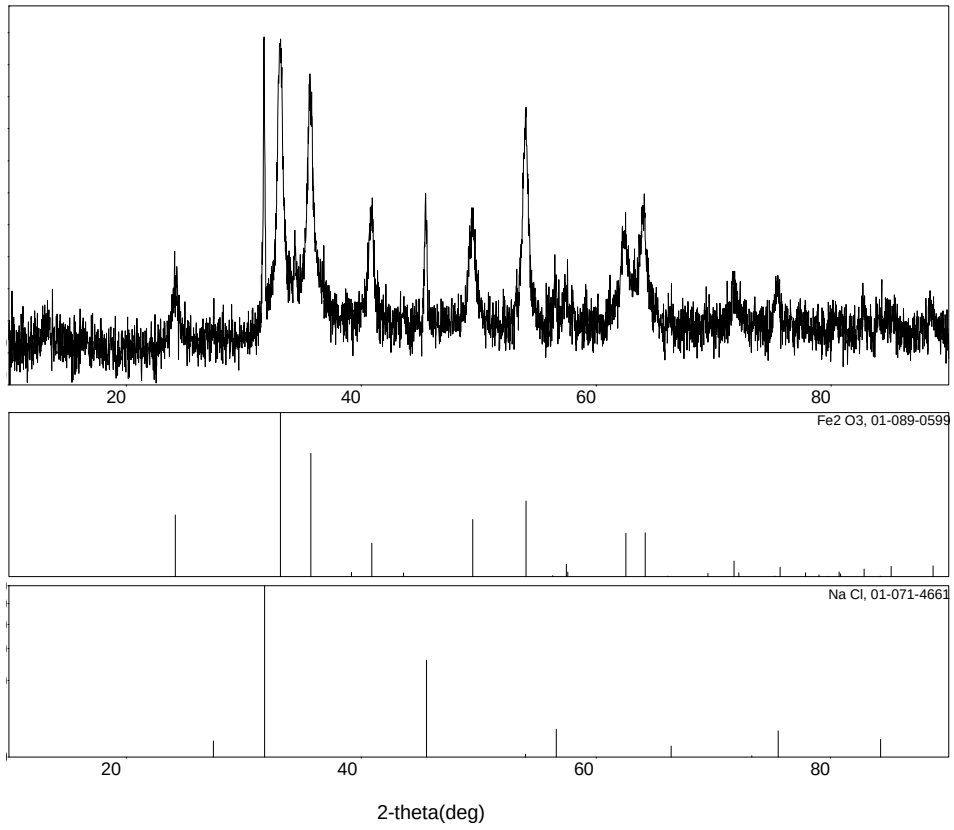

Figure 5.3. Powder X-ray diffraction pattern of as-formed product of $FeCl_3$ and CBr_4 reduced by sodium naphthalide. Peaks index to Fe_2O_3 and NaCl; even though there should be a mixed NaCl/Br salt of approximately 25% Br, the peaks have not shifted from NaCl.

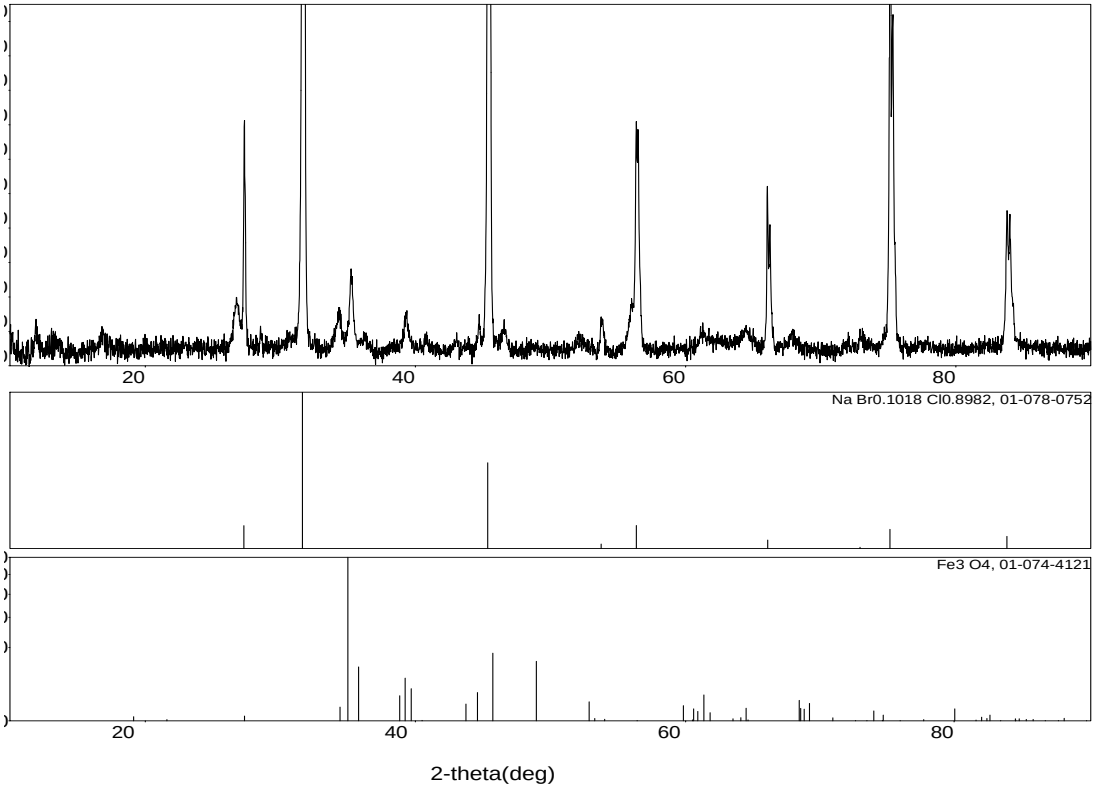

Figure 5.4. Powder X-ray diffraction pattern of annealed product of $FeCl_3$ and CBr_4 reduced by sodium naphthalide. In contrast to Figure 5.3, the peaks now index to a chloride-rich NaCl/NaBr solid solution and magnetite.

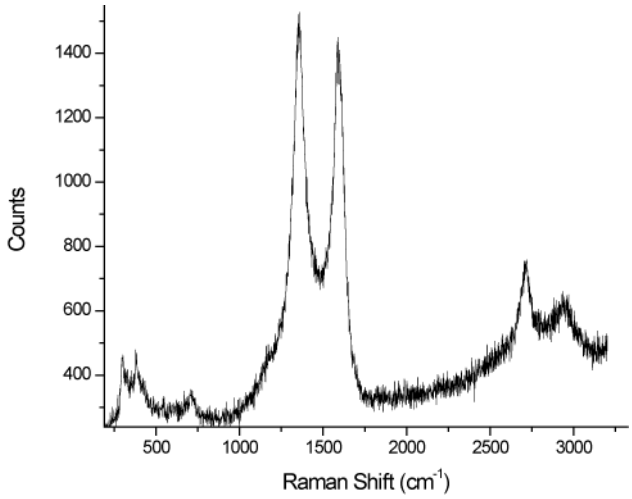

Figure 5.5. Raman spectrum of Fe-C product under 488nm excitation. Peaks attributed to carbon are found at 1358.4cm^{-1} and 1589.6cm^{-1}. The I(D)/(G) ratio is 1.0.

The one metal carbide product which seems to have formed successfully was tantalum carbide. Figure 5.6 shows the powder X-ray diffraction pattern for a sample annealed at 1200°C for one hour. Not all the peaks in Figure 5.6 were identified, but the most intense peaks correspond to TaC (PDF# 00-019-1292), and most of the other peaks index to a crystalline carbon phase (PDF# 00-046-0943). There is Raman evidence to confirm the existence of that carbon, as Figure 5.7 shows Raman peaks at 1363.3 cm^{-1} and 1583.1cm^{-1}, which are in the same D and G peak range as the carbon from Figure 5.2. Their intensity ratio was 0.863, indicating lower amounts of sp^3 carbon (less than about 30%). Since the TaC samples were annealed in a niobium tube, it is conceivable that the tube reacted with the carbon inside to form NbC, since the tube was brittle after annealing. The cubic lattice constants for TaC and NbC only differ by 0.013 Å, so it would be easy to incorrectly assign NbC Bragg peaks as TaC. However, EDX showed no trace of niobium, indicating that the material is indeed TaC. The product is black and very hard (it is difficult to crush in a mortar and

pestle), which qualitatively agrees with the expected properties. Unfortunately, the material is not a finely dispersed powder. The XRD domain size is 43 nm, and the product is comprised of macroscopic aggregates estimated at several hundred microns across. Presumably, annealing at lower temperatures would result in smaller domain sizes and finer powders, but this was not systematically explored. Since TaC was able to be synthesized, it is assumed that further attempts to synthesize VC, Fe_3C, and even TiC and NbC could successfully yield those products. These experiments instead serve as proof of principle for the wide range of molecular precursors which can be reduced to zero-valent elements by sodium naphthalide.

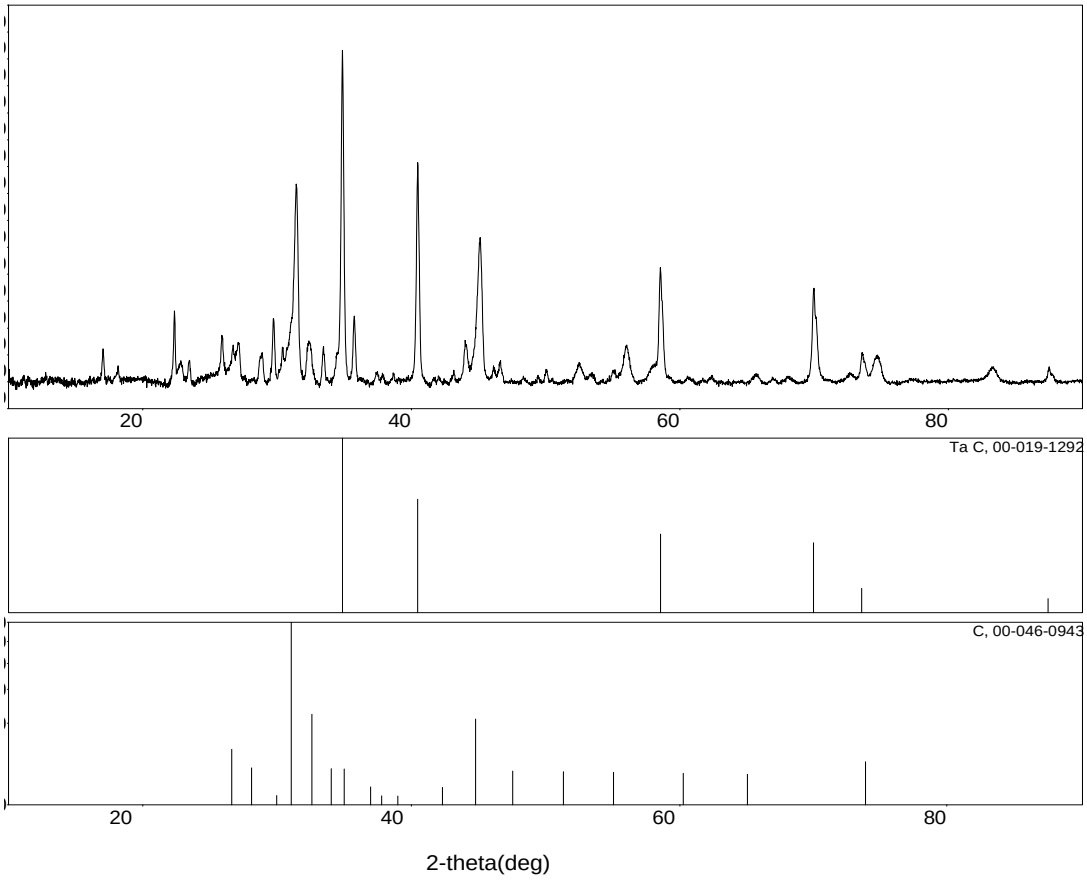

Figure 5.6. Powder X-ray diffraction pattern of mixture of tantalum carbide and carbon from annealed TaC product.

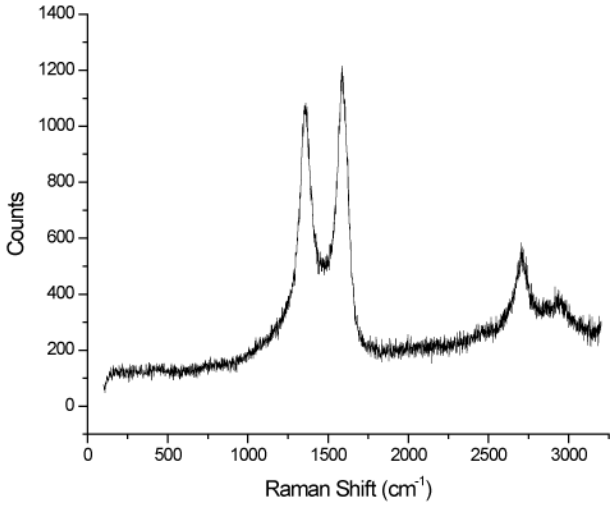

Figure 5.7. Raman spectrum of TaC sample under 488nm excitation, with peaks at 1363.3cm^{-1} and 1583.1cm^{-1} and a I(D)/(G) ratio of 0.863. This spectrum is attributed to carbon content also seen by XRD. Note the similarity with the spectrum from the Fe-C product in Figure 5.5.

5.2 Synthesis of High-T_c Superconductor Host Lattices: LaFePO and LaFeAsO

This side project began as a collaboration with the J. Seamus Davis group in Applied and Engineering Physics, who wished to conduct studies on a class of high-T_c superconductors that have come into the spotlight in the past few years: the rare-earth iron oxypnictides. The tetragonal layer structure compounds LaFePO and LaFeAsO (P4/nmm, Z=2, ZrCuSiAs structure type) were first synthesized by Wolfgang Jeitschko and co-workers in 1995 [6] and 2000 [7], respectively, but in 2008 it was discovered by Kamihara et al. [8] that doping fluorine into these compounds raised the superconducting critical temperature to 5K for the phosphide and as high as 26K for the arsenide. This was a considerable increase from their normal T_c's, and opened a new wave of interest in the field of high-T_c superconductivity. These layered

compounds exhibited high-T_c superconductivity in a manner never seen before, and in a compound largely unrelated to the yttrium barium cuprates from high-T_c superconductivity's heyday in the early 1980's. A plethora of publications followed, where the highest T_c attained for these groups of compounds was reported as 55 K for $Sm[O_{1-x}F_x]FeAs$ [9]. The Davis group wanted to study a large (~100 μm × 100 μm ×10 μm) crystal of the undoped host lattice in scanning tunneling microscope experiments that would reveal the low-temperature density of states in the compound, and hopefully shed light on the nature of the superconductivity.

5.2.1 Experimental

LaFePO and LaFeAsO were prepared according to Quebe et al. [7] from lanthanum filings, iron (III) oxide, iron powder, and red phosphorus and arsenic powder, respectively, in a 3:1:1:3 ratio. The solids were ground together in a mortar and pestle for ten minutes, and then ground ten minutes more in either 2 g of a 1:1 NaCl:KCl mixture, or 0.44 g tin (75 at% tin with respect to the reactants). Both the salt mixture [7] and tin [6] are known mineralizers for synthesis of these compounds from these reactants. The mixtures were sealed in fused silica tubing and heated slowly from room temperature to 400°C over 48 hours, held at 400°C for 72 hours, then heated to 950°C over 24 hours, held there for two weeks, and then cooled back to room temperature over the course of 48 hours. The slow heating followed by soaking at 400°C was to allow ample time for the red phosphorus to react with the other components (most notably iron), rather than convert to high vapor pressure white phosphorus (P_4), which could cause the tube to explode and the powder to ignite when exposed to air. The long reaction time at 950°C was to allow for adequate diffusion of the reactants in the molten tin or salt. Though tin and the salt appear to be used as fluxes and would therefore be expected to impart high diffusion rates to the reactants,

they are technically classified only as mineralizers, since the reactants are just moderately soluble in each. Only a small percentage of the reactants would be dissolved at a given time, so long annealing times were required. After reaching room temperature, the products were relieved of their salt or tin mineralizers by washing with water or slightly dilute cold HCl, respectively. The acid wash was limited to thirty minutes, as the target compound is also attacked by hydrochloric acid, albeit at a slower rate than tin. The acid-rinsed solids were rinsed with water several times, and both types of product were filtered and dried overnight yielding gray powders. Powder X-ray diffraction patterns were taken with a Scintag XDS 2000, and later by a Rigaku Ultima IV, both with Cu Kα radiation. Scanning electron microscopy was performed on a LEO 1550 FESEM with an accelerating voltage of 5 kV for imaging and 20 kV for energy-dispersive X-ray spectroscopy.

5.2.2 Results and Discussion

LaFePO was successfully formed, as determined by powder X-ray diffraction (Figure 5.8), which shows the pattern for LaFePO when tin was used as the mineralizer. The peaks belonging to the target phase were found, and match to the literature PDF card 00-50-0971. The product is not phase pure, and contains some secondary phase of Fe_2P (Baringerite, 04-006-6443). The presence of this iron phosphide means that some unreacted starting materials (Fe_xO_y or some form of lanthanum) must also still be present, but those were not detected by XRD. The mineralizer was also not detected by XRD after dissolution with HCl and rinsing.

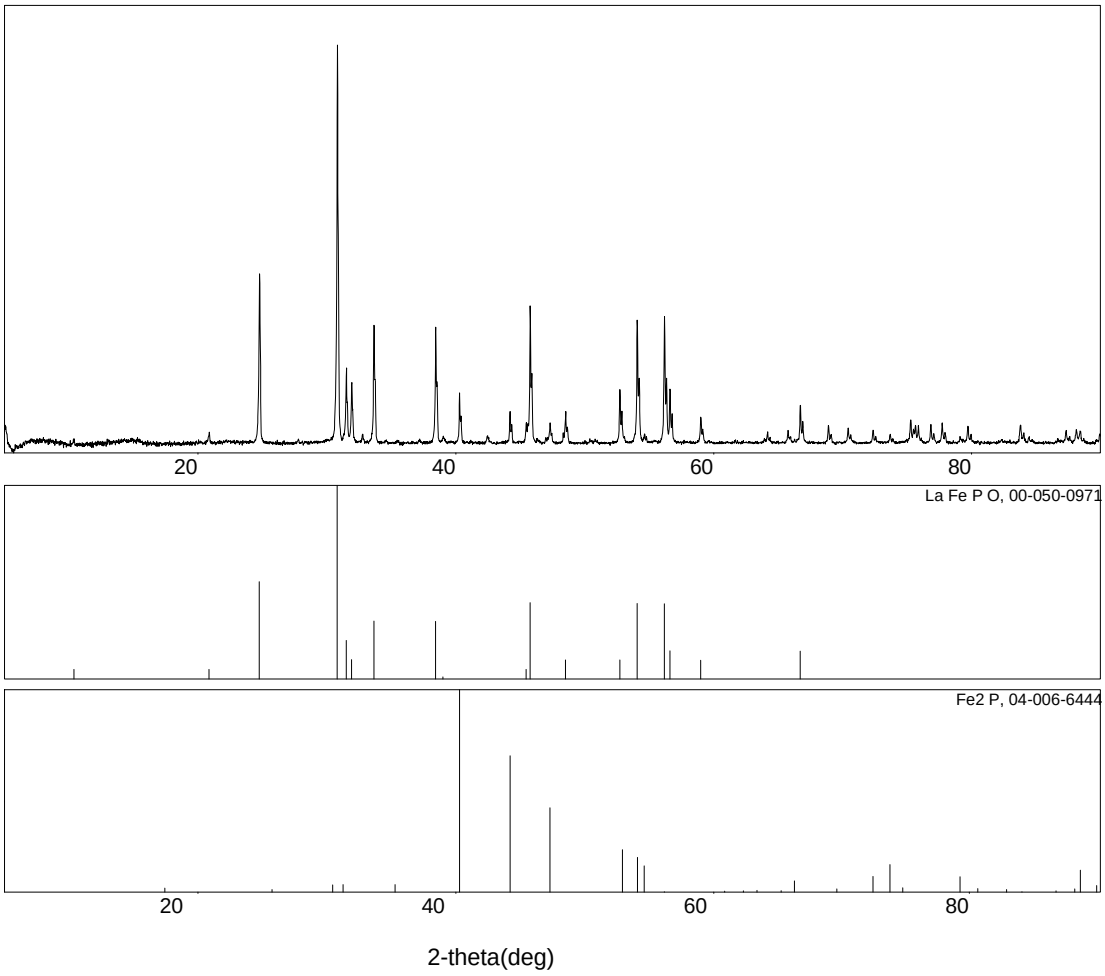

Figure 5.8. Powder X-ray diffraction pattern of LaFePO. Fe_2P (Baringerite, bottom reported pattern) is also present.

Scanning electron microscopy showed tetragonal crystals like the one seen in Figure 5.9. Energy-dispersive X-ray spectroscopy (Figure 5.10) shows almost perfect agreements with the expected composition of LaFePO, where all elements are in equal proportion to one another (Table 5.1). Several other spectra were recorded for other crystals, and show an average composition of 34.3 ± 1.9% La, 32.6 ± 2.0% Fe, and 33.0 ± 2.6% P when excluding oxygen. Quantification of oxygen is problematic due to its presence as an oxide in the substrate and any possible SnO_x present from

undissolved mineralizer, so it is the only element that deviates from the expected composition. Oxygen was always found between 25 and 43 atomic percent, so it did not deviate enough from the desired ratio to indicate an excess amount in the target crystals. Tin was detected at an average of 2 at% in the final product.

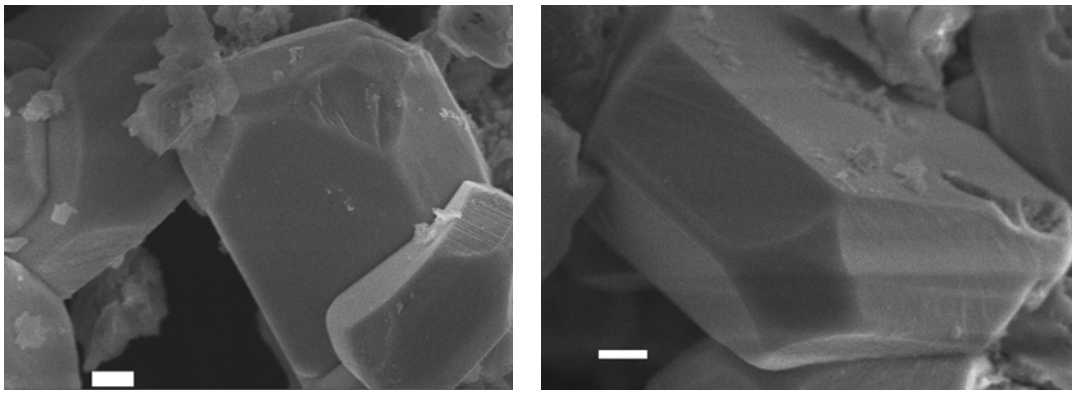

Figure 5.9. Scanning electron micrographs of LaFePO crystals. The tetragonal platelets have been etched at the corners by HCl during the removal of the Sn mineralizer. Scale bars = 1 μm.

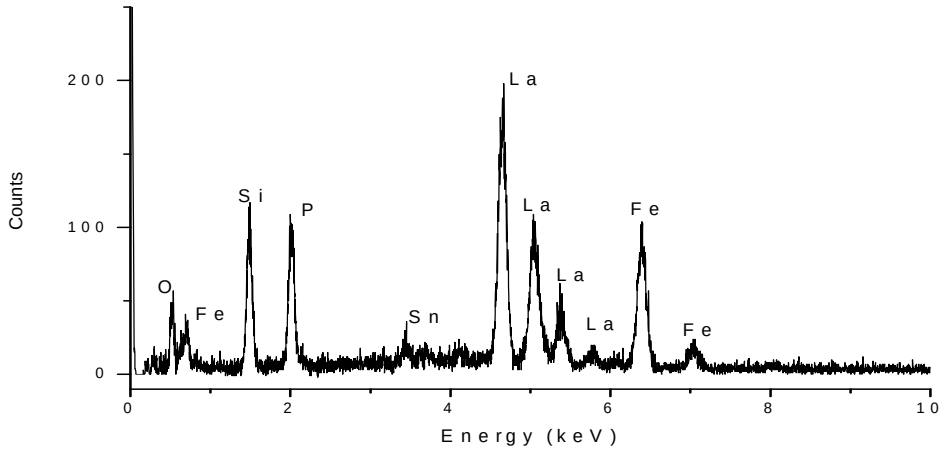

Figure 5.10. EDX spectrum of LaFePO. The Si peak is from the mounting substrate and the Sn peak is from undissolved mineralizer. The stoichiometric ratio was precisely the desired composition (Table 5.1).

Table 5.1 Results of EDX quantification from Figure 5.10

Element	La	Fe	P	O
Atomic Percent	25.5	24.1	25.8	24.6

It is clear that the product was not phase-pure, even though the desired phase formed. Large crystals with approximate 120° facets are also occasionally seen; the one in Figure 5.11 is an iron phosphide phase, given that Fe_2P is hexagonal. The crystal in Figure 5.11 could also be a truncated crystal of the orthorhombic FeP. Although XRD shows the overall presence of Fe_2P, the EDX ratio for the crystal in Figure 5.11 (EDX spectrum shown in Figure 5.12) shows a composition of FeP, a phase which was not found by XRD. It is possible that Fe_2P was the main secondary phase, but FeP still formed in a small amount, and stood out during EDX analysis. However, crystals with EDX ratios of Fe_2P were not found under SEM. The crystals of LaFePO found by SEM were all tens of microns across. This is quite large compared to the crystallites examined in other chapters of this thesis, but smaller than the original goal of approximately 100μm across. It is unclear whether or not the crystals shown here are of appropriate dimensions for STM analysis.

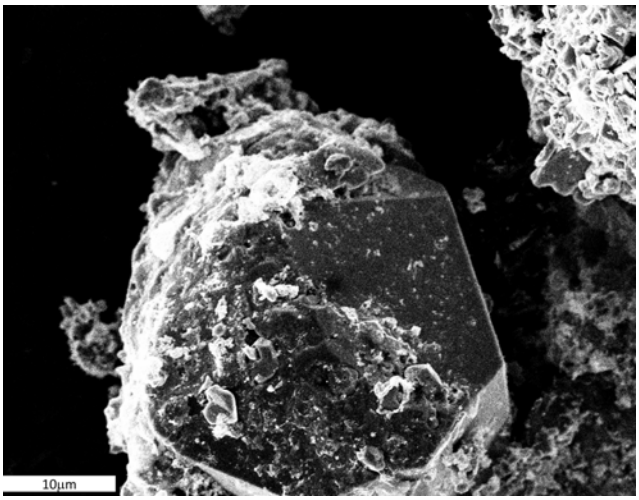

Figure 5.11. Scanning electron micrograph of an FeP crystal found in a LaFePO synthesis. Scale bar = 10µm.

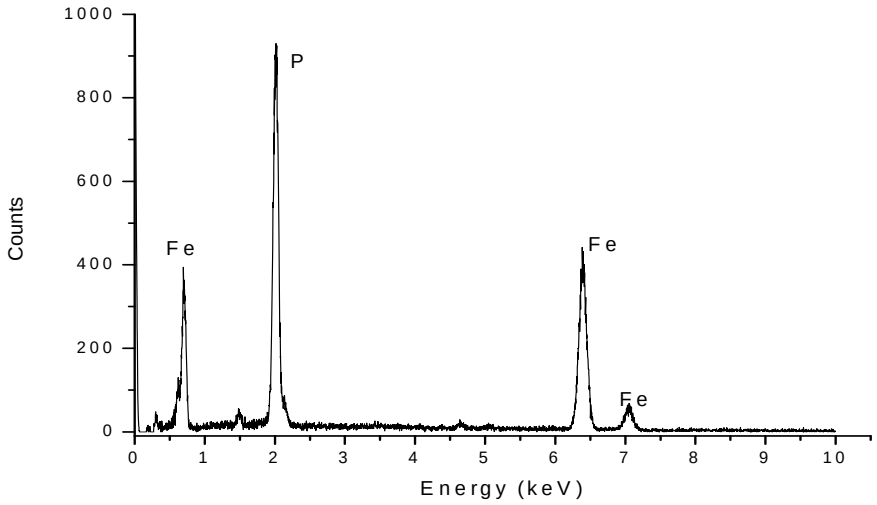

Figure 5.12. EDX spectrum of FeP in Figure 5.11. A peak from the aluminum sample holder is visible at 1.487keV. The elemental ratio was precisely 1:1 Fe:P within the limits of the detector.

Table 5.2 Results from quantification of Figure 5.12

Element	Fe	P
Atomic Percent	50.0	50.0

The formation of LaFeAsO was not as successful. Figure 5.13 shows the powder X-ray diffraction pattern for a LaFeAsO product where Na/KCl was the mineralizer. Despite several washings, the mixed-alkali salt was not completely removed. The powder pattern also shows some magnetite (Fe_3O_4), possibly from partial reduction of unreacted Fe_2O_3 starting material. Portions of the gray powder are attracted to a rare-earth iron boride magnet, which also indicates the presence of magnetite. There is at least one more phase present, as not all XRD peaks are accounted for in Figure 5.13.

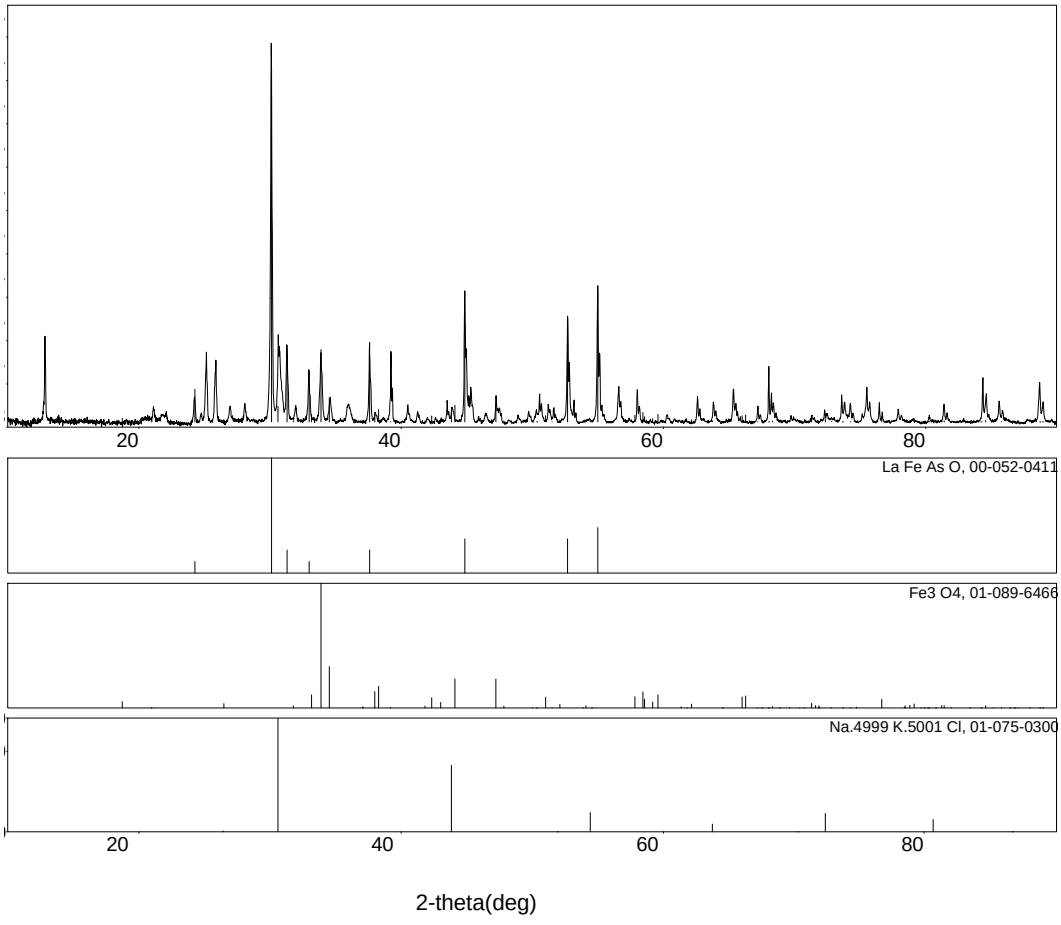

Figure 5.13. Powder X-ray diffraction pattern of LaFeAsO. Fe_3O_4 and Na/KCl are also present.

The SEM image in Figure 5.14 shows a collection of platelet crystals which are around 10 μm across. The platelets' morphologies are largely octagonal, though some hexagons are also seen. The octagons could correspond to truncations of tetragonal platelets of the target phase. Overall composition by EDX (Figure 5.15) approximately shows the desired 1:1:1 La:Fe:As ratio, with a (not-surprising) excess of oxygen. If this product is to be used in an STEM study, the LaFeAsO crystals could be separated from the product, but like the phosphide oxide above, the small size of the crystals could preclude their inclusion in such experiments. More practice with the exact heating profile could improve the annealing conditions and lead to larger crystals, and more current flux techniques [10-12] could be explored.

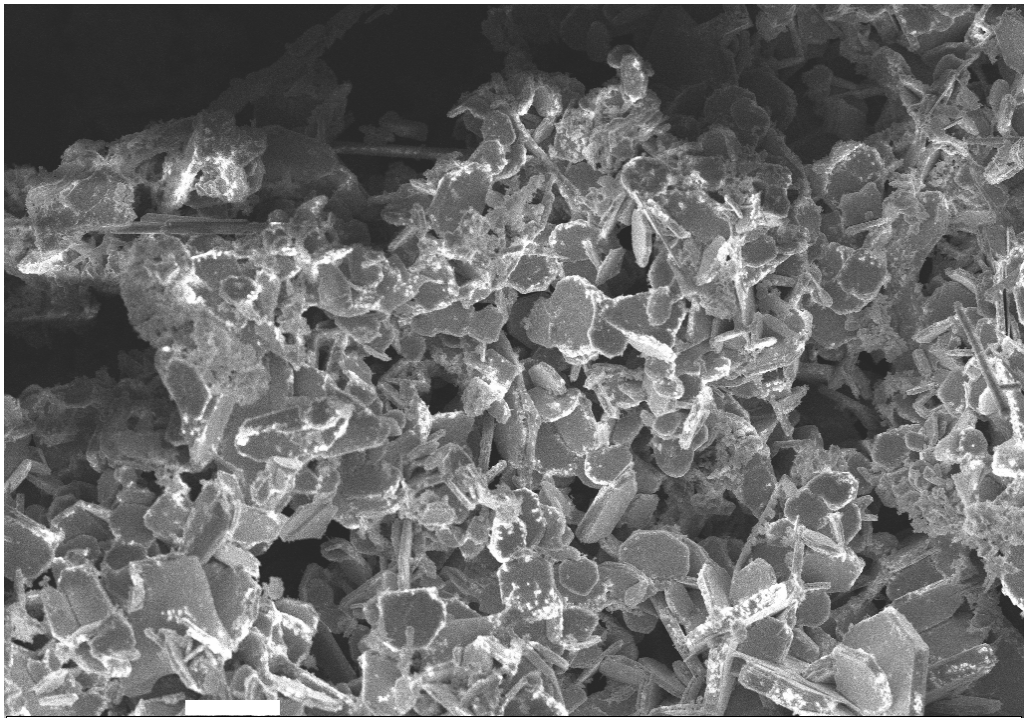

Figure 5.14. Scanning electron micrographs of LaFeAsO crystals. Both hexagonal and octagonal crystals are seen. Scale bar = 10 μm

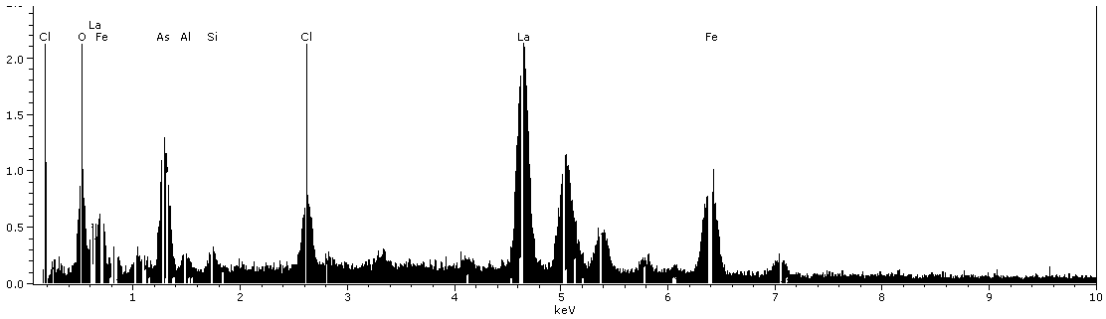

Figure 5.15. Broad-range EDX spectrum of Figure 5.14. The composition in atomic percent was 18% La, 14% As, 14% Fe, 43% O, 6%Cl, and 3% each Si (from tube fragments) and Al (from sample mount).

5.3 Synthesis of Rare Earth-Doped Gallium as a GaN Precursor

A collaboration with Tiju Thomas in the Michael Spencer group in Electrical Engineering was inherited from Dr. Jesse Reiherzer, and involved the preparation of gallium alloy samples that the Spencer group would convert to GaN in an ammonothermal reaction. The aim was to prepare rare earth-doped gallium nitride, which would serve as a red emission phosphor in a ceramic laser-gain material. This section expands on the synthesis of the starting material alloy which was only alluded to elsewhere [13], and describes alterations to the synthesis that are not written anywhere else, but improved the optical characteristics of the final products. Should our group continue this collaboration, this will hopefully save future group members unnecessary frustration.

All manipulations were carried out in an Ar-atmosphere glovebox. An alloy of 95.75at% Ga, 3at% Bi and 1.25at% Eu was obtained by breaking high purity gallium

(Alfa Aesar, 99.9999% purity) and placing it in fused silica tubes with the appropriate amount of bismuth turnings (99% purity) and freshly filed europium (Alfa Aesar, 99% purity). The tubes were then sealed with parafilm, and rapidly taken from the glovebox to a vacuum line where they were evacuated and sealed. The tubes were then wrapped in NiChrome brand thermocouple wire (leaving a long tail which served as a "leash" in high-temperature manipulations), and placed in a tube furnace. After annealing (time and temperature to be discussed below), the tubes were quenched in water, making use of the wire leash for ease of handling. Then the tubes were towel dried, quenched further in liquid nitrogen for ten to fifteen seconds, and pumped back into the glovebox. Once they were brought inside the box, the tubes were broken, and the glass removed from each alloy slug by gently tapping with a tack hammer. The ease with which the glass is removed in this manner stems from the liquid nitrogen quench, ostensibly from a difference in thermal contraction between the Ga alloy and silica under the extreme cold of the nitrogen. Failure to shock the tubes in liquid nitrogen results in glass sticking to the Ga slug. While the low-melting Ga alloy could be removed by gentle heating, one is reminded that re-melting the gallium could cause phase separation of the alloyed components, negating the entire synthesis up to this point. The slugs were then individually bottled in Nalgene containers inside the glovebox and transferred to the Spencer group in a plastic bag with an icepack for transport.

As mentioned earlier, the temperature and duration of heating were of paramount importance, and were altered with respect to past experiments. All previous samples were prepared in 25g batches and heated at 1100°C for three days. This method had been used in the past for its ease of quickly preparing 100g of starting material in only four batches, and the high temperature was employed to achieve rapid diffusion of the reactants. But repeated observations of poor red

luminescence and enhancement of undesired yellow luminescence brought doubts as to the efficacy of the preparation method. As yellow luminescence is a sign of oxygen or carbon-containing impurities, it was suspected that the electropositive rare earth element was attacking the silica tubing. Especially at such high temperatures, reaction with oxygen is not surprising, and such oxidation was inferred to be the cause of the inferior quality material. These difficulties were coupled with semi-frequent failures in the Spencer group's ammonia reaction chamber. Leaks were a regular occurrence, and entire 25 g batches were lost to oxidation. To combat these problems, two synthesis alterations were employed. First was that sample sizes were decreased from 25 g of gallium per tube to only five grams. This drop in sample size does introduce a certain tedium in that preparation of an equal mass of alloy requires sealing five times the number of tubes, but has the advantage that if a sample is lost during any step of the process (such as quenching or ammonolysis), only five grams of the expensive high purity gallium is lost instead of twenty-five. The other alteration was that instead of always heating at 1100°C as in past experiments, the binary phase diagrams of Ga-Bi and Ga-Eu were consulted to suggest a lower preparation temperature. High temperatures should be avoided if possible when working with rare-earth elements, as they are highly prone to reacting with silica. Since Eu has a melting point (822°C) that is considerably higher than that of Bi (271°C), one only needs to heat beyond the melting point of europium to achieve a fully molten sample and the enhanced diffusion rates that come with it. Gallium, of course, is molten at only 29°C, and both Bi and Eu are fully soluble in Ga at the compositions involved here. The lower annealing temperature (and subsequent decrease in diffusion rates) when compared to the former method of synthesis is tempered by the fact that the samples are only 1/5 of the previous volume. Less heating time is needed for diffusion to take its course in making a homogeneous product than for a 25 g sample. It was found that heating

samples at 850°C for 24 hours was sufficient to achieve the desired characteristics. The end-use properties of these precursors were published by Thomas et al.[13]

REFERENCES

1. Chorley, R.W. and P.W. Lednor, *Synthetic Routes to High Surface-Area Nonoxide Materials.* Advanced Materials, 1991. **3**(10): p. 474-485.
2. Nelson, J.A. and M.J. Wagner, *High surface area nanoparticulate transition metal carbides prepared by alkalide reduction.* Chemistry of Materials, 2002. **14**(10): p. 4460-4463.
3. Nelson, J.A. and M.J. Wagner, *High surface area Mo2C and WC prepared by alkalide reduction.* Chemistry of Materials, 2002. **14**(4): p. 1639-1642.
4. Dye, J.L. and K.L. Tsai, *Small Alloy Particles Formed by Coreduction of Soluble Precursors with Alkalides or Electrides in Aprotic Solvents.* Faraday Discussions, 1991. **92**: p. 45-55.
5. Ferrari, A.C. and J. Robertson, *Interpretation of Raman spectra of disordered and amorphous carbon.* Physical Review B, 2000. **61**(20): p. 14095-14107.
6. Zimmer, B.I., et al., *The rate earth transition metal phosphide oxides LnFePO, LnRuPO and LnCoPO with ZrCuSiAs type structure.* Journal of Alloys and Compounds, 1995. **229**(2): p. 238-242.
7. Quebe, P., L.J. Terbüchte, and W. Jeitschko, *Quaternary rare earth transition metal arsenide oxides RTAsO (T=Fe, Ru, Co) with ZrCuSiAs type structure.* Journal of Alloys and Compounds, 2000. **302**(1-2): p. 70-74.
8. Kamihara, Y.W., Takumi; Hirano, Masahiro; Hosono, Hideo, *Iron-Based Layered Superconductor La[O1-xFx]FeAs (x= 0.05-0.12) with Tc =26K.* Journal of the Americal Chemical Society, 2008. **130**: p. 3296-3297.

9. Ren, Z.-A. and et al., *Superconductivity at 55 K in Iron-Based F-Doped Layered Quaternary Compound Sm[O 1- x F x] FeAs.* Chinese Physics Letters, 2008. **25**(6): p. 2215.
10. Baumbach, R.E., et al., *Superconductivity in LnFePO (Ln = La, Pr and Nd) single crystals.* New Journal of Physics, 2009. **11**: p. 14.
11. Hamlin, J.J., et al., *Superconductivity in single crystals of LaFePO.* Journal of Physics-Condensed Matter, 2008. **20**(36): p. 6.
12. Yan, J.Q., et al., *Flux growth at ambient pressure of millimeter-sized single crystals of LaFeAsO, LaFeAsO1-xFx, and LaFe1-xCoxAsO.* Applied Physics Letters, 2009. **95**(22): p. 3.
13. Thomas, T., Xiamonei Guo, MVSChandrashekhar, Carl B. Poitras, William Shaff, Mark Dreibelbis, Jesse Reiherzer, Kewen Li, Francis J. DiSalvo, Michal Lipson, and M. G. Spencer *Purification and Mechanical Nanosizing of Eu-Doped GaN.* Journal of Crystal Growth, 2009. **311**: p. 4402-4407.

CHAPTER 6

Conclusions and Suggestions for Future Work

6.1 PtPb via Sodium Naphthalide Reduction

Chapter two showed that some parts of the complicated process of the formation of nanoparticles of a known intermetallic can be understood by systematic variations to the synthesis procedure. Though it had been suspected that slight differences in reaction solution volume or excess of reducing agent could drastically affect the end properties of the nanoparticles, that was shown not to be the case. The reverse was actually what was observed: drastic changes in those variable resulted in only slight differences in the products. Also, the puzzle of the products' behavior with different stirring temperatures has a new piece in place. It was previously unknown whether higher reaction temperatures induced metal diffusion or hydrocarbon desorption to explain the sudden onset of enlarged crystallite sizes. The experiments with hypothesized ligand hydrogenation indicate that the crystalline transition is more due to hydrocarbon desorption.

Further exploration of the PtPb system is unlikely to lead to truly exciting results. Plenty of research has been carried out both before and after the work described in Chapter 2, and it seems PtPb by sodium naphthalide reduction has reached most of its potential as an electrocatalyst. The most important trait that this system has to offer future research is its status as the best-understood intermetallic nanoparticle electrocatalyst in the DiSalvo group and EMC^2. It has been extensively explored in thin films and bulk crystals, and is the most reproducible as nanoparticles. If it was decided to begin using capping ligands for intermetallic nanoparticles as in most nanoparticle syntheses, PtPb should be the first product attempted. As for specific unanswered questions from the present work, the most straightforward would

be direct characterization of the side-products from the reaction in Chapter 2. Direct detection of ethane during chemical reduction, and detection of cyclooctane or cyclooctadiene after hydrogen treatment should be able to be accomplished. However, this avenue should only be pursued if similar organometallic precursor complexes are used in the future, where the fate of methyl or diolefin ligands would be of interest. Understanding this specific reduction behavior is unlikely to assist in understanding the co-reduction of two metal chloride species, for example. Alternate techniques of gaining mechanistic insight to nanoparticle formation have been published; if chemical kinetics and Arrhenius-type analyses such as those employed by Xie et al. [1] and Watzky et al. [2] are of interest, they could be explored with minimal investment in specialized apparatus.

6.2 Kinetic Electroanalysis of Metal Precursors

The results of Chapter three demonstrate that, given the assumptions of the techniques which were used, platinum (II) acetylacetonate and lead (II) (2-ethylhexanoate) undergo heterogeneous reduction and ligand dissociation at approximately the same rates. This result would indicate that the model of the reaction in Chapter two is viable. Chapter three also shows that if desired, we have a tool for estimating the reduction rates of molecular metal precursors. Unfortunately, it is apparent that these techniques are not universally applicable, and depend on the nature of the specific molecular precursors of interest. Future work to determine precursor reduction rates could be more universal if electrode techniques were traded for microchannel flow techniques [3-5], as was mentioned in Chapter three.

6.3 Thin-Film Inspired Pd Ternary Alloy Nanoparticles

Chapter four showed that the reproducible synthesis of nanoparticles with specific small amounts of base metals alloyed into them is anything but trivial. The

co-reduction of three metal precursors did result in nanoparticles which, when analyzed in aggregated form, had all three metals present, and often within reasonable relation to the desired composition. The electrocatalytic activity of those nanoparticles for the oxygen reduction reaction was not better than on platinum, but was better than palladium alone when synthesized under the same conditions. This observation is what was shown in "combinatorial" thin film experiments, and the retention of that electrocatalytic behavior bodes well for future thin-film inspired nanoparticle compositions.

The largest hurdles towards successful demonstration of homogeneous ternary alloy nanoparticles are reproducibility of metal composition, and determination of the distribution of alloyed metals. Even if conventional microprobe analysis like that used in Chapter four showed excellent agreement with the target composition every time, determining the composition for each particle is difficult. Analytical methods would have to show that vanadium or tungsten, for example, are alloyed into each nanoparticle on average. High energy X-ray methods could accomplish this through techniques such as XAFS or using Pair Distribution Function combined with reverse Monte Carlo simulations [6, 7], though each of these techniques require special expertise that may not be cultivated in the group. Outside collaboration would be needed, which Petkov [6, 7] has offered. Electron energy loss spectroscopy which specialists like the David Mueller group use would also be a fine tool for more rigorous characterization of complex alloy nanoparticles. Of course, only the most active catalysts would need to undergo such meticulous analysis.

Further experiments which are more specific to those in Chapter three would be annealing the products before exposure to air, to see if better homogeneity could be obtained. Also, different metal precursors could be used. While the three precursors seemed to fit the bill for what the precursors need to do, they were by no means

sacred. Tungsten (VI) ethoxide was used several times (but not reported here), and appeared to reduce easily in sodium naphthalide. Alternate vanadium precursors could also be explored.

6.4 Transition Metal Carbides via Sodium Naphthalide

Chapter five described some straightforward syntheses of solid state compounds and alloys. The LaFePO and LaFeAsO crystals, and Ga-Bi-Eu alloys were prepared according to practiced solid state methodologies, and require little expansion here, except to say that the layered superconductor compounds have had more extensive preparation techniques published since the experiments in Chapter five, especially when it comes to more effective flux methods. Should those syntheses be continued, more recent synthesis procedures should be consulted [8-10].

The more novel transition metal carbides *via* sodium naphthalide reduction successfully demonstrated synthesis of TaC from $TaCl_5$ and CBr_4. It is likely that more practiced attempts at other phases like Fe_3C, VC, TiC, and NbC would be successful, though it is possible that better precursors could be chosen. Should the thin film "combi" group be successful in finding an active fuel cell catalyst which contains carbon in the sputtered film, these techniques will be quite relevant. Work is recommended in working with alternate carbon precursors and alternate reducing agents, especially since the trialkylborohydrides have already been shown to make transition metal carbides [11].

REFERENCES

1. Xie, R.G., Z. Li, and X.G. Peng, *Nucleation Kinetics vs Chemical Kinetics in the Initial Formation of Semiconductor Nanocrystals.* Journal of the American Chemical Society, 2009. **131**(42): p. 15457-15466.
2. Watzky, M.A., E.E. Finney, and R.G. Finke, *Transition-metal nanocluster size vs formation time and the catalytically effective nucleus number: A mechanism-based treatment.* Journal of the American Chemical Society, 2008. **130**(36): p. 11959-11969.
3. Bokenkamp, D., et al., *Microfabricated silicon mixers for submillisecond quench-flow analysis.* Analytical Chemistry, 1998. **70**(2): p. 232-236.
4. Knight, J.B., et al., *Hydrodynamic focusing on a silicon chip: Mixing nanoliters in microseconds.* Physical Review Letters, 1998. **80**(17): p. 3863-3866.
5. Regenfuss, P., et al., *Mixing Liquids in Microseconds.* Review of Scientific Instruments, 1985. **56**(2): p. 283-290.
6. Petkov, V., *Nanostructure by high-energy X-ray diffraction.* Materials Today, 2008. **11**(11): p. 28-38.
7. Petkov, V., et al., *Periodicity and atomic ordering in nanosized particles of crystals.* Journal of Physical Chemistry C, 2008. **112**(24): p. 8907-8911.
8. Baumbach, R.E., et al., *Superconductivity in LnFePO (Ln = La, Pr and Nd) single crystals.* New Journal of Physics, 2009. **11**: p. 14.
9. Hamlin, J.J., et al., *Superconductivity in single crystals of LaFePO.* Journal of Physics-Condensed Matter, 2008. **20**(36): p. 6.

10. Yan, J.Q., et al., *Flux growth at ambient pressure of millimeter-sized single crystals of LaFeAsO, LaFeAsO1-xFx, and LaFe1-xCoxAsO.* Applied Physics Letters, 2009. **95**(22): p. 3.

11. Zeng, D. and M.J. Hampdensmith, *Synthesis and Characterization of Nanophase Group-6 Metal (M) and Metal Carbide (M(2)C) Powders by Chemical-Reduction Methods.* Chemistry of Materials, 1993. **5**(5): p. 681-689.

Appendix 1

Chemical and Electrochemical Reduction of Tin Alkoxides

Background

This appendix summarizes attempts to reconcile some anecdotal observations made by Chandrani Roy Chowdhury in 2006 when searching for tin precursors for PtSn synthesis by sodium borohydride reduction. Two convenient ones were tin (IV) isopropoxide and tin (IV) t-butoxide; both were easy-to-handle solids, soluble in methanol, and contained tin in its highest oxidation state to prevent internal redox reactions with Pt^{II} precursors. Neither was deemed suitable for co-reduction with platinum, since both of their chemical reduction rates were too slow compared to the instantaneous (by eye) reduction of H_2PtCl_6. The isopropoxide methanol solution turned dark only after several seconds when mixed with a sodium borohydride solution, violating the requirement of simultaneous reduction of each precursor to achieve homogeneous nanoparticles. However, this reduction and precipitation was rapid when compared with an identical reaction with tin tetra-t-butoxide, which did precipitate in solution, but only after ten minutes or more. This striking discrepancy in chemical reduction rate for two seemingly similar precursors was curious, and could not be satisfactorily reconciled. But experiments such as those in Chapter 3 were instituted for this very reason. If single or double potential step chronoamperometric experiments also found that there was an order of magnitude difference or more in reduction rate, it would both show that something fundamental was to blame for the sluggish homogeneous reduction and justify the inclusion of SSCA or DSCA in fuel cell nanocatalyst research. These measurements, as were shown in Chapter 3, are only possible if the metal complex is amenable to the particular analysis.

Experimental

Tin (IV) isopropoxide ($Sn(^{i}PrO)_4$) and tin (IV) (t-butoxide) ($Sn(^{t}BuO)_4$) were purchased from Gelest, Inc. and used as-received. Potassium and lithium triethylborohydride were each purchased as 1.0 M THF solutions and used as received. Tetra-n-butyammonium perchlorate (TBAP) was purchased from Sigma Aldrich and recrystallized from ethyl acetate before use. Absolute anhydrous methanol was degassed with bubbling argon, and tetrahydrofuran was purified over molecular sieves in a stainless steel solvent dispensing system before use. Solutions were made as 0.1 M TBAP and 0.005 M tin precursor; two tin precursors were each prepared in two different solvents, for a total of four solutions. All solution preparation and electrochemical measurements were performed in argon atmosphere gloveboxes. Methanol (usually forbidden in glvoebox use) was handled as quickly as possible in the glovebox while all chemicals in the box were sealed in jars. After all he methanol was taken back out, a tank of argon was forced through the box to purge methanol vapors, and the box was regenerated twice before normal use resumed. Cyclic voltammetric measurements were recorded on a BAS Epsilon potentiostat with a platinum wire counter electrode. All measurements are versus Ag/Ag^{+} as in Chapter three. For CV's taken in methanol, working electrodes were made from 30 μm diameter carbon fiber, and CV's taken in THF were done on a collection of 1mm, 125μm and 250μm diameter Pt electrodes (each electrode diameter is identified in the text or figure, and currents are normalized to area).

Results and Discussion

The cyclic voltammetric behavior of the tin precursors in methanol is shown in Figure A1.1. Like the organic metal complexes studied in Chapter 3, the potential range for reduction was quite negative, much more negative than the standard reduction potential of *ca.* -0.2 V for Sn(IV) to Sn(0). It is apparent that methanol,

even though it was the solvent actually used in the original chemical reduction, is not an appropriate solvent for working at such low potentials, as is expected. The current scales set as the limiting values for each tin precursor of the known concentration are overwhelmed by current due to solvent decomposition. It is also possible that the carbon fiber electrodes' epoxy seals are dissolved by methanol, effectively increasing the electrodes' areas. Either way, it is obvious that no meaningful chronoamperometry can be done in an electrode-solvent pairing which is so unstable at the potentials of interest. .

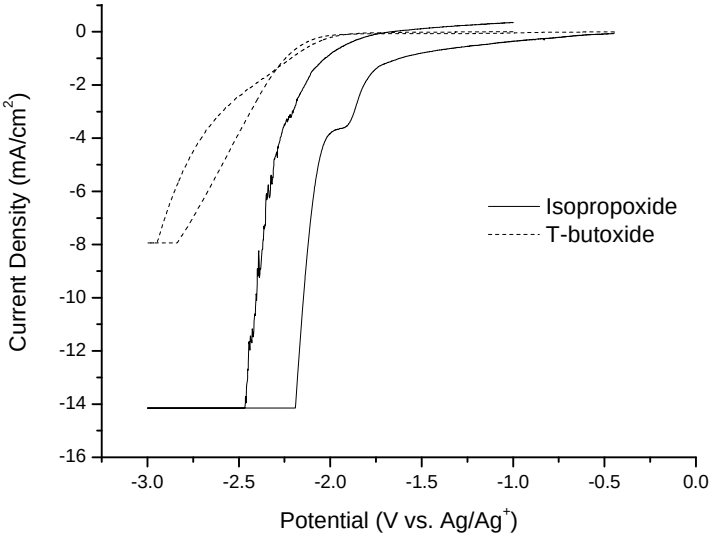

Figure A1.1 Cyclic voltammograms of 0.005 M $Sn(iPrO)_4$ and Sn(tBuO)4 in methanol with 0.1 M TBAP. Sweep rate was 50 mV s^{-1} on an electrode made from a carbon fiber with a 30 μm diameter.

The only consequential data which can be obtained from these experiments are the approximate reduction potentials of the precursors. These values are -1.8 V vs. Ag/Ag^+ for $Sn(^iPrO)_4$ and -2.4 V for $Sn(^tBuO)_4$, and due to the irreversible and irregular waveshape correspond only to the onset of reduction. The potentials may be neither the true values if the precursors had well-defined mass transport-limited redox

peaks, nor even the half-wave potentials, but their values relative to each other correspond to the chemical reduction observation, where the isopropoxide was easier to reduce than the t-butoxide. This surprising 600 mV difference in reduction potential is attributed to inductive effects. t-Butoxide is a better Lewis base than isopropoxide, so it would contribute more electron density to the tin center and make $Sn(^tBuO)_4$ harder to reduce.

While methanol proved to be an unsuitable solvent, THF is known to be stable up to -3.0 V vs. Ag/Ag^+. For this reason, the Roy Chowdhury chemical reductions were repeated in THF. Both tin precursors dissolved in THF, but sodium borohydride is insoluble in that solvent, so trialkylborohydrides with slightly more negative (but comparable to $NaBH_4$) reduction potentials were used. Potassium triethylborohydride reduced tin (IV) isopropoxide at presumably the same rate as sodium borohydride: the solution turned dark within three seconds, but the change was not instantaneous as would be desired for co-reduction with platinum. No color change was observed for $KB(Et)_3H$ reduction of tin(IV) t-butoxide, even after one hour. This is in agreement with the t-butoxide having a more negative reduction potential, as was seen in the methanol CV. Both tin compounds were then treated with lithium triethylborohydride, which has a more negative reduction potential than its potassium analogue. $Sn(^iPrO)_4$ reduced at the same rate as before, and this time $Sn(^tBuO)_4$ did precipitate, but only after twenty seconds. The relative reduction rates are consistent across a whole group of solvents and reducing agents, and the difference in reduction potentials between the two is substantiated by both chemical and electrochemical evidence. Incidentally, the reduction of $Sn(^iPrO)_4$ by $LiB(Et)_3H$ yields a metallic gray powder which by X-ray diffraction perfectly matches the literature pattern for tin, is phase pure, and has 70nm domains (Figure A1.2). The phase purity without washing is attributed to the high solubility of the alkoxide ligands with the alkali metal cations from the reducing agent,

and the low melting point of tin would lead to high bulk and particle surface diffusion rates, and explain the large domain size.

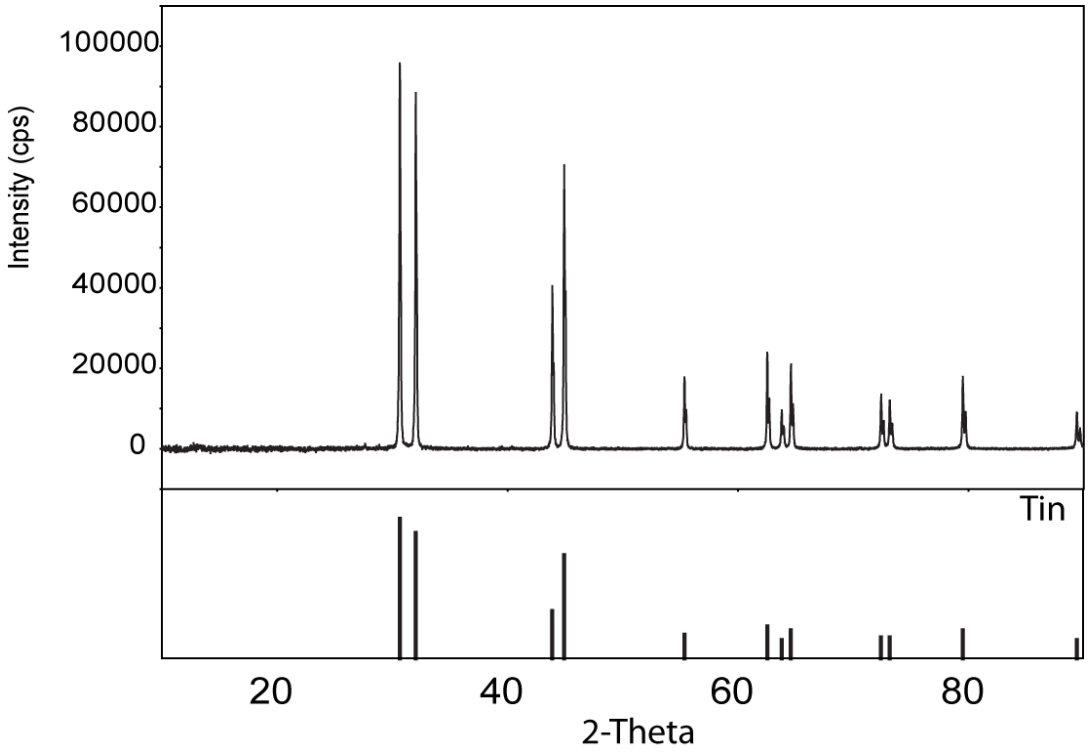

Figure A1.2 Powder X-ray diffraction pattern of tin product from reduction of $Sn(iPrO)_4$ by by $LiB(Et)_3H$ in THF at room temperature.

Since THF was shown to be an alternative to methanol in chemical reduction, cyclic voltammograms for each Sn complex in THF were recorded in a similar manner to those in methanol. The solvent did not show the same breakdown where its current density increased beyond that estimated for the concentration of the analyte in solution, so THF was found to be as stable at the potentials of interest for these precursors as it was for Pt and Pb in Chapter 3. However, the tin precursors were equally unsuitable for electroanalytical measurements of the types featured in Chapter three, much like $Pt(COD)Me_2$. As shown in Figure A1.3, the cathodic current kept increasing on consecutive sweeps. This would indicate that there is a surface

passivation reaction occurring, possibly due to SnO_x formation on the surface of the 125 μm Pt electrode. While classic metal deposition would be an acceptable phenomenon, here we see deposition of an insulating layer. Therefore, no single or double potential step experiments were attempted.

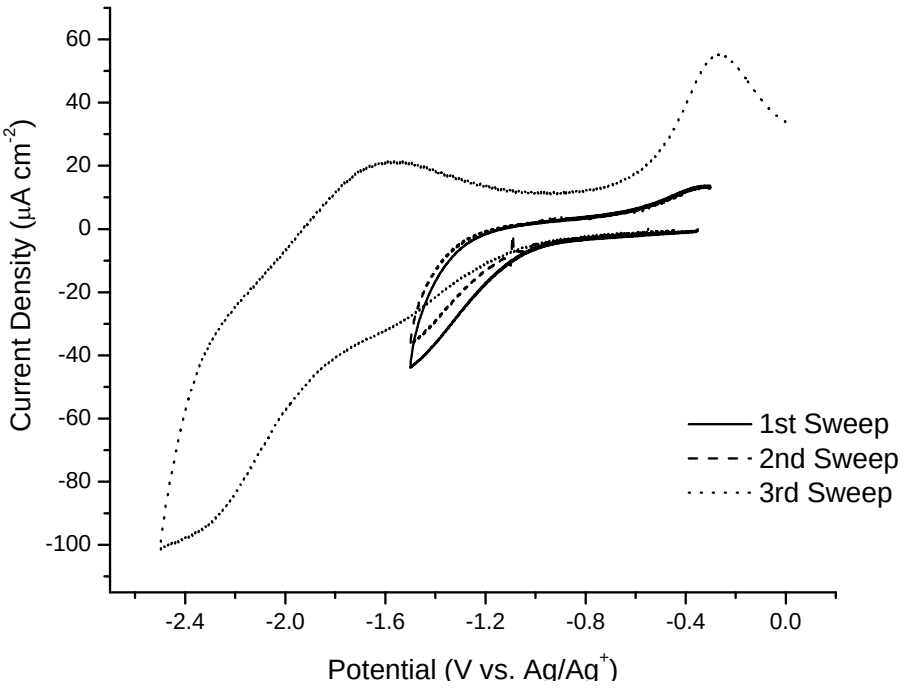

Figure A1.3 Cyclic voltammogram of 0.005 M tin (IV) isopropoxide in THF with 0.1 M TBAP on a 125 μm Pt electrode at 50 mV s^{-1}. The redox behavior for the t-butoxide shows similar unacceptable variations with increasing sweeps.

Appendix 2

Attempted Synthesis of Carbon-Supported Pd-W Alloy Nanoparticles

Background

An alternate method was devised for possible synthesis of a Pd-W binary like that shown in Chapter 4. Rather than relying on solution-based chemical reduction of Pd and W precursors to give unsupported nanoparticles, an attempt was made to modify carbon-supported palladium nanoparticles with a volatile tungsten precursor. The inspiration for this work came from Miura et al. [1], who reported the synthesis of carbon-supported PtZn by modifying Pt/C. In that reaction, as-purchased Pt/C was heated in a tube under flowing nitrogen downstream from a crucible of zinc metal. Due to the relatively high vapor pressure of Zn at elevated temperatures, zinc vapor reacted with the Pt to form the 1:1 intermetallic PtZn. This method avoids many of the nanoparticle synthesis pitfalls described in this dissertation, such as concerns about ligand and reducing agent adsorption, and eventually determining how to adhere the nanoparticles to a support. No washing steps are needed, and the particles are already dispersed on carbon. Unfortunately, tungsten has one of the lowest vapor pressures at a given temperature of any metal, and attempting the same vapor transport route as zinc would be folly. However, $W(CO)_6$ sublimes at 67°C, and decomposes to W and 6 CO above 150°C. The literature [2] has taken advantage of these properties in order to make tungsten nanoparticles supported on alumina for chemical catalysis applications by first heating $W(CO)_6$ slowly to sublime it onto the support, then rapidly raising the temperature to decompose it to W. The main concern for this synthesis would of course be the homogeneity of the final product. There is no assurance whatsoever that the tungsten, if it does decompose to the neutral metal, would be in close enough proximity to the Pd to diffuse into it. Only a specific Pd-

$(WCO)_6$ interaction could be the hope for success. This experiment mostly serves as an exercise in considering alternate means of nanoparticle synthesis beyond solution-phase chemical reduction.

Experimental

Palladium on carbon (20wt% Pd on Vulcan XC-72) was purchased from BASF and heated under flowing nitrogen at 300°C for eight hours prior to use. Tungsten hexacarbonyl was purchased from Alrich and used as received. Pd/C (0.0105 g) and $W(CO)_6$ (0.0071 g) were mixed together in a mortar and pestle in an inert-atmosphere glovebox, then sealed under vacuum in a fused silica tube. The tube was heated at 70°C for eight hours, and then the oven was turned off an allowed to cool. The tube was taken back into the glovebox, opened, and the contents were placed in an alumina crucible inside a silica tube with valve-operated stoppers at each end. The tube was then placed in a cool tube furnace, nitrogen was flowed through for 2 hours, and then the temperature was raised to 350°C over three hours. After those three hours, the heat was shut off, and the tube cooled to room temperature under flowing nitrogen. The product was characterized by XRD, microprobe, and rotating disk voltammetry as described in the main experimental chapters of this dissertation.

Results and Discussion

The X-ray diffraction showed the expected Pd structure, and need not be shown here. It was identical to the pattern seen for the starting material, and was never expected to deviate from that for reasons discussed in Chapter 4. Microprobe analysis found that the product was mostly palladium, with unquantifiable carbon signal. However, there were areas which appeared tungsten rich. The left side of Figure A2.1 shows a micrograph of the product, while the right shows the same micrograph in composition mode, where the microprobe has been set to exaggerate

contrast based on atomic number, where W (Z = 74) is expected to show more brightly than Pd (Z = 46) or C (Z = 6). The tungsten-rich area is easily seen, and is approximately 2 μm in diameter, which is too large an aggregate for it to be Pd standing out with respect to a carbon background. There is every reason to conclude that the $W(CO)_6$ did not sublime evenly over the Pd/C, but rather remained buried inside the Pd/C or sublimed downstream in the tube as nitrogen flowed.

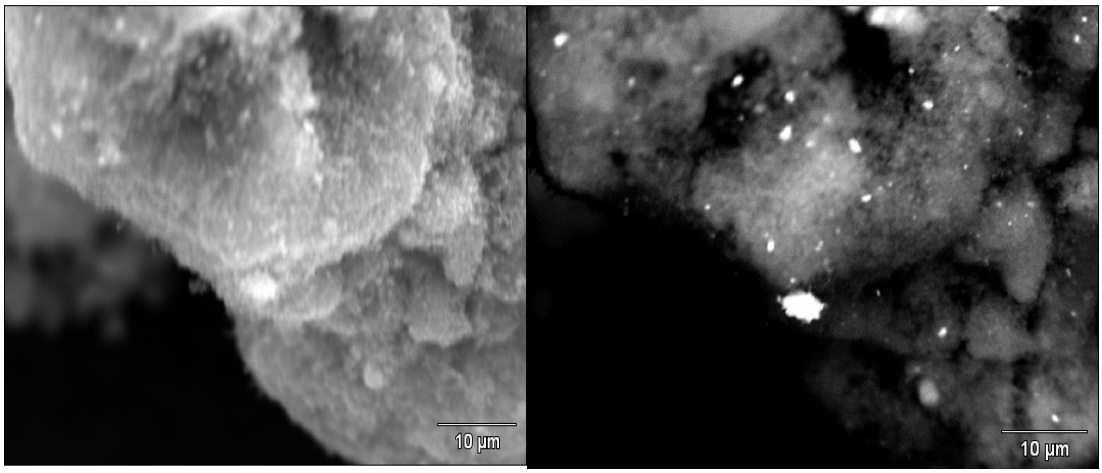

Figure A2.1 SEM of the same area of the Pd-W/C product under normal mode (left) and high-contrast composition mode (right). The bright speck in the center of the right image is visible in the left, and corresponds to high W content.

The ORR activity under the same conditions used in Chapter 4 is shown in Figure A2.2. The oxygen reduction current has a poor onset potential in the first and second sweeps (+0.76 V vs. RHE), which electrochemical cleaning improves dramatically until it reaches the value of the original BASF catalyst itself. Clearly the addition of tungsten hexacarbonyl only impedes the activity of the as-purchased catalyst when used in the manner described above. It is possible that alternate precursors and methods could be devised to realize the goal of making this binary

alloy by modifying a carbon-supported nanoparticle, but this method was not pursued further for the purposes of this dissertation.

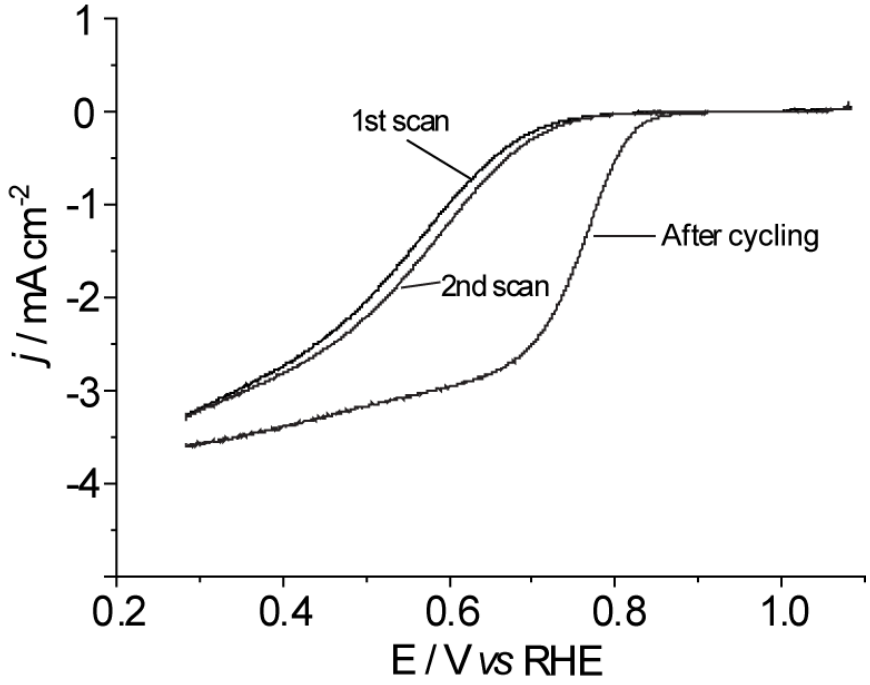

Figure A2.2 ORR polarization curves for Pd-W/C product with oxygen-saturated 0.1M HClO4 solution at 5 mVs^{-1} and 1600 rpm. Cycling the potential between the upper and lower potential boundaries at 50 mVs^{-1} for 20 minutes increases the activity to the values for as-purchased Pd/C (not shown).

REFERENCES

1. Miura, A., et al., *Synthesis of Intermetallic PtZn Nanoparticles by Reaction of Pt Nanoparticles with Zn Vapor and Their Application as Fuel Cell Catalysts.* Chemistry of Materials, 2009. **21**(13): p. 2661-2667.
2. Alvarez-Merino, M.A., et al., *Tungsten catalysts supported on activated carbon - I. Preparation and characterization after their heat treatments in inert atmosphere.* Journal of Catalysis, 2000. **192**(2): p. 363-373.